

CHEMO-MECHANICAL CHARACTERIZATION OF PHASE-SEPARATED DENTIN
ADHESIVES

By

[Copyright 2013]

Ranganathan Parthasarathy

Submitted to the graduate degree program in Bioengineering and the Graduate Faculty of the
University of Kansas in partial fulfillment of the requirements for the degree of Doctor of
Philosophy.

Chairperson Dr Anil Misra

Chairperson Dr Paulette Spencer

Dr Stevin Gehrke

Dr Jennifer Laurence

Dr Sarah Kieweg

Dr Qiang Ye

Date Defended: April 4, 2013

The Dissertation Committee for Ranganathan Parthasarathy
certifies that this is the approved version of the following dissertation:

CHEMO-MECHANICAL CHARACTERIZATION OF PHASE-SEPARATED DENTIN
ADHESIVES

Chairperson: Dr Anil Misra

Chairperson Dr Paulette Spencer

Date approved: April 4, 2013

ABSTRACT

The premature failure of composite dentin restorations can be traced to the adhesive–dentin (a/d) interface. The continuity, stability and mechanical properties of the dentin adhesive polymer in the interface depend on its composition and morphology. The adhesive is composed of a hydrophilic/hydrophobic monomer pair, which phase separates upon interaction with dentinal water, resulting in variable chemical composition and pore structure of the adhesive in the interface. The phase separation has been quantified using a ternary monomer-water phase diagram. The polymerization of the monomer phases, composition and pore structure of the resulting polymer phases were investigated. A novel micro-poromechanical constitutive model was developed to model the polymer mechanical, swelling and transport behavior while accounting for polymer-water interaction and pore pressure. The model was then used to characterize polymer formulations along the phase boundary. Parametric studies were performed to illustrate flow-dependent mechanical behavior of hydrophilic polymers.

Experimental observations showed negligible amount of crosslinker in hydrophilic-rich phases and identified the cut-off point on the phase boundary to achieve significant polymerization. The results also quantified the composition of polymers formed along the phase boundary. Crosslink density and hydrophilicity were identified as the critical parameters which determined the sorption, swelling, diffusion and poromechanical behavior of the polymer phases. These two parameters were found to depend on the phase chemical composition. Effects of external environment and confinement on the flow-dependent mechanical behavior have also been studied parametrically for hydrophilic polymers. The combination of experimental results and micro-poromechanical modeling provide structure-property relationships obtained from first

principles, which will aid in adhesive design and analysis of the adhesive-dentin interface performance.

ACKNOWLEDGEMENTS

First of all, I would like to thank Dr. Anil Misra, Dr. Paulette Spencer and Dr. Qiang Ye for their invaluable support, guidance and patience at all times. I could not have completed this project without their help and guidance.

I also like to thank Dr. Stevin Gehrke, Dr. Sarah Kieweg and Dr. Jennifer Laurence for serving on my committee and providing me excellent suggestions and guidance.

I would also like to thank Dr. Jonggu Park and again Dr. Qiang Ye for introducing and guiding me with the experimental work involving chemistry.

I wish to thank Viraj Singh for his excellent suggestions and help throughout my stay at the Bioengineering Research Center. I also thank Dr. Orestes Marangos, Dr. Shiping Huang and Farhana Abedin for their help and support during the course of this project. I also thank Jenny Ding, Ann Rundquist and all the lab assistants who helped me at various times.

Finally, I wish to express gratitude to my family, who are the inspiration for me to do this work.

This research is supported in part by: United States USPHS Research Grant NIH/NIDCR DE014392 (PS), NIH/NIDCR DE022054 (PS) and United States National Science Foundation grant CMMI-1068528(AM).

CONTENTS

ABSTRACT.....	iii
CONTENTS.....	vi
1 INTRODUCTION AND LITERATURE REVIEW.....	1
1.1 Introduction.....	1
1.1.1 Clinical Relevance.....	1
1.1.2 Adhesive Function.....	1
1.1.3 Preparation of Adhesive- Dentin Interface and Hybrid layer.....	2
1.1.4 Phase Separation.....	3
1.1.5 Degree of Polymerization and Polymerization Kinetics.....	4
1.1.6 Diffusion Behavior and Water Sorption.....	4
1.1.7 Chemo-Poro-Visco-Elastic Mechanical Properties.....	5
1.2 Significance.....	6
1.3 Specific Aims:.....	7
1.3.1 Characterization of Monomer Properties.....	8
1.3.2 Characterization of Polymer Properties:.....	8
1.3.3 Mechanical Modeling:.....	9
1.3.4 Innovation.....	9
1.3.5 Rationale for specific aim 1: Characterization of Monomer Properties.....	10
1.3.6 Rationale for specific aim 2: Characterization of Polymer Properties.....	11
1.3.7 Rationale for specific aim 3: Mechanical Modeling.....	12
1.4 Summary (General):.....	13
1.5 Relevance:.....	13

2	CHARACTERIZATION OF DENTIN ADHESIVE SYSTEM USING A TERNARY PHASE DIAGRAM.....	23
2.1	Introduction	23
2.2	Materials and Methods.....	25
2.2.1	Materials and nomenclature.....	25
2.2.2	Miscibility Experiment	26
2.2.3	Phase Separation Experiment	26
2.2.4	Calibration of FTIR spectra	27
2.2.5	Degree of conversion	28
2.2.6	Polymerization kinetics.....	29
2.2.7	Chemical composition	30
2.2.8	Morphology.....	31
2.3	Results and discussion.....	31
2.3.1	Miscibility testing	31
2.3.2	Chemometrics based calibration of FTIR spectra.....	32
2.3.3	Phase composition	32
2.3.4	Degree of conversion	34
2.3.5	Polymerization kinetics.....	35
2.3.6	Polymer phase composition	36
2.3.7	Polymer porosity.....	37
2.4	Conclusions	38

3	EXPERIMENTAL ANALYSIS AND STRUCTURE-PROPERTY RELATIONSHIPS FOR MODEL DENTIN ADHESIVE POLYMERS FORMED ON THE WATER-ADHESIVE PHASE BOUNDARY	51
3.1	Introduction	51
3.2	Materials and methods	54
3.2.1	Materials	54
3.2.2	Methods.....	54
3.3	Results	60
3.3.1	Degree of Conversion, Density, partition coefficients and Density of Leachables	60
3.3.2	Mechanical Properties.....	61
3.3.3	Crosslink density.....	64
3.3.4	Water Sorption and Swelling.....	65
3.3.5	Viscoelastic Properties.....	66
3.3.6	Glass Transition Temperature.....	67
3.4	Conclusion.....	68
4	MICROMECHANICAL MODEL FOR THE EQUILIBRIUM CONFIGURATION OF DENTIN ADHESIVE POLYMERS FORMED ON THE WATER-ADHESIVE PHASE BOUNDARY	79
4.1	Introduction	79
4.2	Materials and experimental methods.....	82
4.2.1	Materials	82
4.2.2	Methods.....	82
4.3	Mathematical model.....	87

4.3.1	Micro-poro-mechanical model.....	89
4.3.2	Chemical potential of the saturated polymer	92
4.3.3	Swelling and elastic modulus of saturated polymer	93
4.3.4	Numerical model calibration.....	94
4.4	Results and discussion.....	97
4.4.1	Experimental measurements	97
4.4.2	Model calculations	99
4.4.3	Meso-scale parameters.....	100
4.4.4	Macromechanical properties.....	102
4.5	Summary and Conclusions.....	103
5	DIFFUSION COEFFICIENTS OF WATER AND LEACHABLES IN METHACRYLATE-BASED CROSSLINKED POLYMERS USING ABSORPTION EXPERIMENTS.....	115
5.1	Introduction	115
5.2	Materials and methods	117
5.2.1	Materials	117
5.2.2	Methods.....	118
5.3	Results	126
5.3.1	Degree of Conversion, Density, partition coefficients and Density of Leachables 126	
5.3.2	Absorption experiments and simulation using mathematical model	128
5.4	Discussion	129
5.4.1	Factors affecting diffusion and partition coefficients	129
5.4.2	Effect of co-monomer structure	132

5.5	Conclusions	135
6	MICROMECHANICS BASED MODEL FOR DIFFUSION IN HYDROPHILIC POLYMERS	153
6.1	Introduction	153
6.2	Materials and methods	156
6.2.1	Materials	156
6.2.2	Methods.....	156
6.3	Mathematical Model	158
6.3.1	Micro-poro-mechanical model.....	159
6.3.2	Swelling and elastic modulus of saturated polymer	162
6.3.3	Chemical Potential	163
6.3.4	Two-dimensional diffusion model.....	165
6.4	Results and discussion.....	170
6.4.1	Sorption and swelling kinetics.....	170
6.4.2	Dependence of diffusion coefficient on composition	171
6.4.3	Dependence of diffusion process on crosslink density.....	172
6.5	Conclusion.....	173
7	POROMECHANICS PARAMETERS OF FLUID-SATURATED CHEMICALLY ACTIVE FIBROUS MEDIA DERIVED FROM A MICROMECHANICAL APPROACH.....	185
7.1	Introduction	185
7.2	Micromechanical model.....	190
7.2.1	Case 1: ($\dot{\epsilon} \neq 0, \dot{p} = 0$)	191
7.2.2	Case 2: ($\dot{\epsilon} = 0, \dot{p} \neq 0$)	196

7.2.3	Superposition of Case 1 and Case 2.....	197
7.3	Transport Model and Chemical Potential.....	198
7.4	Comparison of Drained and Undrained Compression	201
7.4.1	Loading Conditions.....	201
7.5	Results and Discussions	203
7.5.1	Fiber Stress and Induced Anisotropy	203
7.5.2	Stress-Strain and Pore Pressure-Water Content.....	204
7.5.3	Evolution of Stiffness and Poromechanical Parameters	206
7.5.4	Effect of Fiber Nonlinearity	208
7.5.5	Unconfined Drained Monotonic Compression	209
7.5.6	Creep Response at Different Stress-Levels.....	212
7.5.7	Creep Response under Varying Bath Molarity.....	214
7.5.8	Effect of Confinement on Creep Behavior	216
7.5.9	Stress Relaxation under Variable External Bath Molarity.....	217
7.6	Summary and Conclusions.....	218
8	CONCLUSIONS AND FUTURE WORK.....	235
8.1	Conclusions	235
8.2	Future work	236

LIST OF FIGURES

Figure 1-1 Schematic of a tooth restored with composite restoration. This figure depicts the relationship of the dentin-adhesive bond to the composite restoration (Misra, Spencer et al. 2005, Singh, Misra et al. 2011).....	18
Figure 1-2. Scanning electron micrograph of demineralized dentin matrix (which is primarily type I collagen). The holes that are distributed throughout the matrix represent the dentinal tubules. Under clinical conditions, pulpal fluid is pulsing through the dentinal tubules (Misra, Spencer et al. 2005).....	19
Figure 1-3. Visible light micrograph of dentin adhesive hybrid layer.....	20
Figure 1-4. Illustration representing adhesive phase separation and water entrapment at the dentin/adhesive interface	21
Figure 1-5. Flowchart for research proposal.....	22
Figure 2-1 Water miscibility as a function of HEMA content in the neat resin	44
Figure 2-2 Standards for (a) hydrophobic-rich or resin phase (b) hydrophilic-rich or aqueous phase	45
Figure 2-3 Water-monomer phase diagram for the dentin adhesive.....	46
Figure 2-4 Degree of conversion along phase boundary	47
Figure 2-5 Polymerization kinetics along the phase boundary measured using FTIR spectra.....	48
Figure 2-6 Raman imaging of HB45-33 (a) band ratio of aromatic ring to the C-H bond (b) optical visible light image (c) spectrum from region of low band ratio (d) spectrum from region of high band ratio	49
Figure 2-7 Micro-XCT slices of HB45-33 (a) under a magnification of 20X (b) under a magnification of 40X	50

Figure 3-1 Representative adhesive monomer formulations identified on the phase boundary of the water-adhesive ternary phase diagram. The circles represent the formulations prepared close to the phase boundary. The squares represent the corresponding neat formulations.....	71
Figure 3-2 Elastic moduli in dry and wet condition at 25°C and rubbery modulus versus the percentage of BisGMA in the corresponding neat monomer formulation (a) linear scale (b) semi-log scale	72
Figure 3-3 Apparent stress strain behavior in (a) dry and (b) wet condition at 25°C, apparent failure strain in (c) dry and (d) wet condition, (e) loss tangent over temperature sweep	73
Figure 3-4 Variation of (a) mass change with time, (b) volume change with time, (c) mass change in BisGMA, (d) volume change and (e) solubility with BisGMA under water absorption	74
Figure 3-5 Variation in viscoelastic properties of the polymer formulations with respect to BisGMA content.	75
Figure 3-6 (a) Glass transition temperature and (b) Peak loss tangent versus BisGMA (%) in the polymer formulation	76
Figure 3-7 Degree of conversion versus BisGMA (%) in the polymer formulation	77
Figure 3-8 Variation of crosslink density calculated from (a) rubbery modulus and (b) stoichiometry, with BisGMA content.....	78
Figure 4-1 (Color online) Representative adhesive monomer formulations identified on the phase boundary of the water-adhesive ternary phase diagram. The circles represent the formulations prepared close to the phase boundary. The squares represent the corresponding neat formulations.....	109
Figure 4-2 (Color online) Flowchart for model idealization	110

Figure 4-3 (Color online) Schematic of the saturated polymer for (a) sparsely crosslinked network and (b) highly crosslinked network. The red molecule belongs to the crosslinks and the black molecules to linear polymer chains. The large molecule in the polymer is a BisGMA unit and the smaller one is a HEMA unit. The blue molecules represent water in the interstitial spaces between the polymer chains. 111

Figure 4-4 (Color online) Correlations obtained from experimental measurements on polymer formulations close to the water-adhesive phase boundary 112

Figure 4-5 Variation of micromechanical properties with percentage of BisGMA 113

Figure 4-6 Correlation between derived mechanical properties and percentage of BisGMA 114

Figure 5-1 Simulated (a) diffusion of water (b) diffusion of leachables and (c) net mass change contours (g/mm³) at time t after immersion in water 144

Figure 5-2 Example of net mass change versus time curve for a polymer beam specimen 145

Figure 5-3 Variation of mass changes with time for water sorption sixteen adhesive formulation beam specimens at 37°C (the discrete points show the experimental data and the continuous curves show the fit using the mathematical model)..... 146

Figure 5-4 Correlation between diffusion and partition coefficients for all the sixteen adhesive formulations. The co-monomer name is used to represent the polymeric formulation (BH+co-monomer)..... 147

Figure 5-5 Variation of diffusion and partition coefficients with crosslink density and mole averaged LogP for the sixteen adhesive formulations. The co-monomer name is used to represent the polymeric formulation (BH+co-monomer)..... 148

Figure 5-6 Variation of diffusion and partition coefficients of water with crosslink density and LogP for group 1. The co-monomer name is used to represent the polymeric formulation (BH+co-monomer).....	149
Figure 5-7 Variation of diffusion and partition coefficients of water with crosslink density and LogP for group 2. The co-monomer name is used to represent the polymeric formulation (BH+co-monomer).....	150
Figure 5-8 Variation of diffusion coefficients of leachables with crosslink density and LogP for group 1. The co-monomer name is used to represent the polymeric formulation (BH+co-monomer).....	151
Figure 5-9 Variation of diffusion coefficients of leachables with crosslink density and LogP for group 1. The co-monomer name is used to represent the polymeric formulation (BH+co-monomer).....	152
Figure 6-1 Variation of (a) percentage change in mass of the sample (b) swelling i.e. volume of the sample with respect to its original volume.....	179
Figure 6-2 Variation of water concentration and Jacobian of deformation inside the beam cross section for (a) HB60 (b) HB75	180
Figure 6-3 Variation of water concentration and Jacobian of deformation inside the beam cross section for (a) HB60 (b) HB75 (c) HB80 and (d) HB92.5	181
Figure 6-4 Variation of diffusion coefficient with chemical composition	182
Figure 6-5 Variation of diffusion coefficient with model parameter A^s	183
Figure 6-6 Influence of model parameter A^s on the diffusion process.....	184

Figure 7-1 (a) Schematic of dry fibrous network at the microscale. (b) Schematic of saturated fibrous network at microscale by zooming in to a homogenized representative volume element at the macroscale.....	224
Figure 7-2 Fiber traction in an RVE.	225
Figure 7-3 Predicted fiber stress distribution with increasing compressive applied strains of 0%, 0.8%, 2.5% and 10% for (a) undrained and (b) drained conditions (plotted to the same scale)..	226
Figure 7-4 Evolution of stress, effective stress, porosity, volume change, pore pressures and fixed charge density under uniaxial compression for drained and undrained cases of loading..	227
Figure 7-5 Evolution of stiffness and poromechanical parameters under uniaxial compression for drained and undrained cases of loading.	228
Figure 7-6 Effect of fiber nonlinearity on drained behavior under unconfined compression. ...	229
Figure 7-7 Unconfined uniaxial drained monotonic compression: stress-strain behavior under varying external bath molarity (a, b and d), evolution of pore pressure (c), volume change (e), porosity (f), material properties (g-l), and the fiber stress distributions (m).	230
Figure 7-8 Creep response under different axial stress: strain (a, and b), pore pressures (c-e), volume change (f), material properties (g-l), and the fiber stress distributions (m).	231
Figure 7-9 Creep response under different external bath molarities: strain (a, and b), pore	232
Figure 7-10 Comparison of creep response under confined and unconfined conditions for same applied stress and external bath molarity: strain and effective stress (a, b and d), pore pressures (c and e), porosity (f), volume change (g), material properties (h-l), and the fiber stress distributions (m).....	233
Figure 7-11 Comparison of creep response under confined and unconfined conditions for same applied stress and external bath molarity: strain and effective stress (a, b and d), pore pressures (c	

and e), porosity (f), volume change (g), material properties (h-l), and the fiber stress distributions
(m)..... 234

LIST OF TABLES

Table 1-1 Nomenclature of adhesive resin monomers and polymers.....	15
Table 1-2 List of adhesive formulations.....	16
Table 1-3 List of photoinitiator formulations consisting of camphorquinone (CQ), ethyl-4-(dimethylamino) benzoate (EDMAB), diphenyliodonium hexafluorophosphate (DPIHP) and 3-(3,4-dimethyl-9-oxo-9H-thioxanthen-2-yloxy)-2-hydroxypropyl] trimethyl ammonium chloride (QTX).....	17
Table 2-1 List of co-monomers.....	40
Table 2-2 Composition of over-saturated mixtures for phase separation.....	41
Table 2-3 Goodness of fit of the calibration between FTIR spectra and component concentrations for (a) hydrophilic rich or aqueous phase (b) hydrophobic rich or resin phase, using PLS1	42
Table 2-4 Composition of hydrophilic rich or aqueous phases and hydrophobic rich or resin phases obtained from phase separation of oversaturated mixture	43
Table 3-1 List of co-monomers.....	69
Table 3-2 Percentage composition of the formulations on the phase boundary	70
Table 4-1 List of co-monomers.....	106
Table 4-2 Percentage composition by weight of the monomer formulations on the phase boundary	107
Table 4-3 Relation between micro-mechanical parameters and macro-mechanical material properties.....	108
Table 5-1 Chemical structures and experimental parameters for the polymerized dentin adhesives in group 1 (the mean values plus and minus the standard deviation of at least three replicates are shown).....	138

Table 5-2 Chemical structures and experimental parameters for the polymerized dentin adhesives in group 2 (the mean values plus and minus the standard deviation of at least three replicates are shown).....	139
Table 5-3 Chemical structures and experimental parameters for the polymerized dentin adhesives from formulations other than groups 1 and 2 (the mean values plus and minus the standard deviation of at least three replicates are shown).....	140
Table 5-4 Parameters from exponential fit for diffusion coefficients.....	141
Table 5-5 Relative contribution of crosslink density and hydrophilicity towards diffusion coefficient	142
Table 5-6 Fitted diffusion coefficients of the polymerized dentin adhesives.....	143
Table 6-1 List of co-monomers.....	177
Table 6-2 Diffusion coefficients and model parameters of the polymer formulations.....	178

1 INTRODUCTION AND LITERATURE REVIEW

1.1 Introduction

1.1.1 Clinical Relevance

Dental caries is a major public health problem and affects 60-90% of schoolchildren and the vast majority of adults. Dental amalgam is being phased out due to concerns of mercury release into the environment. The primary alternative to dental amalgam is composite. As compared to dental amalgam, the composite restoration has the advantages of better aesthetics, smaller size and structural reinforcement. However, they have a higher failure rate and increased frequency of replacement (Mjor, Dahl et al. 2000, Murray, Windsor et al. 2002, Bernardo, Luis et al. 2007, Levin, Coval et al. 2007, Soncini, Maserejian et al. 2007, Simecek, Diefenderfer et al. 2009). Replacement of failed composite restorations is an important clinical concern that has consequences like loss of healthy tooth structure, hours of lost productivity at work and/or school, and increased spending for repeated repair or replacement.

1.1.2 Adhesive Function

The composite restoration is achieved by bonding a composite resin to the tooth using an adhesive. The function of the adhesive is to (a) transfer the externally applied mechanical stress from the composite to the underlying tooth structure and (b) provide a continuous seal to the exposed collagen, protecting it from bacterial attack. Discontinuities in the adhesive–dentin interface arising from inadequate penetration, poor polymerization, and from mechanical and chemical stress create pathways over time for entry of bacterial enzymes, bacteria and oral fluids

(Spencer, Ye et al.). Experimental evidence has shown that the main factor associated with early failure of resin composite restorations is secondary caries at the margin of the adhesive–dentin (a/d) interface (Shimizu, Kitano et al. 1995, Collins, Bryant et al. 1998, Nordbo, Leirskar et al. 1998, Mjor, Dahl et al. 2000, Van Dijken 2000, Gaengler, Hoyer et al. 2001, Hickel and Manhart 2001, Mjor, Shen et al. 2002, Pallesen and Qvist 2003, Lindberg, Van Dijken et al. 2007, Opdam, Bronkhorst et al. 2007, Kubo, Kawasaki et al.). The secondary decay is linked to failure of the bond between the tooth and composite and increased levels of the cariogenic bacteria, *Streptococcus mutans*, at the perimeter of these materials. The failure of the dentin-adhesive bond can be traced to the failure of current adhesives to consistently seal and adhere to the dentin.

1.1.3 Preparation of Adhesive- Dentin Interface and Hybrid layer

The dental restoration is achieved by bonding a composite resin to the tooth using an adhesive. In brief, it involves the following steps: a) removal of the caries infected zone using a water-cooled dental handpiece; b) refinement of the cavity preparation to increase the likelihood of placing the composite on sound tooth structure; c) removal of mineralized component of dentin using acid etching; d) rinsing the acid etched surface and limited drying of the surface to leave a visibly moist demineralized dentin (primarily type I collagen) matrix; e) infiltration of the demineralized dentin with the adhesive resin and f) photo-polymerization of the resin with a visible light source. The morphological relationship of the dentin-adhesive bond to the composite restoration is shown in Figure 1-1.

After acid-etching, the depth of demineralization in the dentin is usually about 1 to 10 μm (Perdigao and Lopes 2001). As shown in Figure 1-2, the demineralized dentin matrix is primarily type I collagen that is suspended in dentinal fluid and water. It is necessary to maintain this

collagen in a hydrated state to prevent its collapse; a collapsed collagen matrix eliminates the porosity required for adhesive infiltration. The zone formed by a composite of adhesive resin with exposed demineralized collagen fibrils is called the hybrid layer. A visible light micrograph of the dentin-adhesive hybrid layer is shown in Figure 1-3. The molar concentration of the adhesive monomer has been demonstrated to decrease with depth in the hybrid layer. The composition of the adhesive resin along the hybrid layer is also not constant, with the ratio of hydrophobic to hydrophilic monomer steadily decreasing with depth (Zou, Armstrong et al. 2010).

Wetting of dentin substrate (Erickson 1992, Eick, Robinson et al. 1993) and micromechanical interlock via resin penetration and entanglement of exposed collagen fibrils (Spencer and Swafford 1999, Hashimoto, Ohno et al. 2000, Wang and Spencer 2003) are accepted as the main factors that determine the adequacy of a dentin-adhesive bond.

1.1.4 Phase Separation

During preparation of the tooth surface for adhesive application, it is difficult to control the amount of water left on the tooth. Clinicians routinely bond to naturally wet substrates such as caries affected dentin (Ito, Hashimoto et al. 2005) or deep dentin (Marshall, Marshall et al. 1997, Pereira, Okuda et al. 1999, Roulet and Degrange 2000, Wang, Spencer et al. 2006). The water content is even higher at the gingival margin, and correspondingly, the gingival margin in class II composite restorations is the most common location of bonding failures. It is highly likely that the water content on the dentin substrate is enough to cause phase separation of the adhesive into hydrophilic-rich and hydrophobic-rich phases as schematically shown in Figure 1-4 (Spencer and Wang 2002). Due to the differences in water miscibility and viscosity of the hydrophilic and hydrophobic components, they vary in their degree of penetration into the wet demineralized

dentin (Hashimoto, Ohno et al. 2000, Zou, Armstrong et al. 2010). The hydrophilic-rich phases resist diffusion of the hydrophobic crosslinking monomer and therefore, only form poorly polymerized, loosely crosslinked domains, which have poor mechanical integrity and high water sorption. The crosslink density and the corresponding mechanical and sorption properties decrease with depth of the hybrid layer towards the dentin (Spencer, Wang et al. 2000, Spencer and Wang 2002, Wang and Spencer 2003, Spencer, Wang et al. 2006, Guo, Spencer et al. 2007).

1.1.5 Degree of Polymerization and Polymerization Kinetics

Poor polymerization of hydrophilic-rich phases formed in the hybrid layer results in porosities and pathways for the transport of bacteria. In addition, poorly polymerized adhesive also leaves behind un-polymerized toxic monomer, which could leach out into the saliva. A sufficient degree of conversion of the polymer (at least 60%) is necessary for the dentin adhesive to form a solid polymer. The free-radical photo-polymerization of the monomer depends on the water content, photo-initiator content and crosslinkable monomer concentration. Hence, it is necessary to determine the concentration of crosslinking monomer necessary to achieve a sufficient degree of conversion. It is also instructive to study the polymerization kinetics because in light of the gel effect (O'Neil and Torkelson 1999), the chemical structure of the polymerized adhesive is correlated with the rate of polymerization.

1.1.6 Diffusion Behavior and Water Sorption

The importance of water transport through the dentin adhesive polymer is highlighted from the following phenomena: (a) after the adhesive is applied over the demineralized dentin and cured, it is exposed to dentinal fluid and saliva. Under such conditions the initially dry adhesive may be simultaneously exposed to moisture and external load resulting in anomalous changes in the

viscoelastic properties (Misra, Singh et al. 2011, Singh, Misra et al. 2011) (Rudakova and Zaikov 1987, Rudakova and Zaikov 1988) (b) the adhesive also undergoes mechanical softening and hydrolytic degradation due to chemical interactions between the polymer chains and water (Park, Ye et al. 2008) (b) after equilibrium has set in, the water-saturated adhesive behaves like a hydrogel and the poromechanical response to external stresses depends on the rate of fluid flow through the adhesive, or on the diffusion coefficient of water through the adhesive.

1.1.7 Chemo-Poro-Visco-Elastic Mechanical Properties

It is well known that the mechanical behavior of crosslinked hydrophilic polymers and hydrogels depend on the pore structure, pore connectivity, chemical structure and water sorption (Anseth, Bowman et al. 1996, Gong, Katsuyama et al. 2003, Berger, Reist et al. 2004). The dry solid polymer matrix is inherently viscoelastic and its properties have been quantified by our research group (Singh, Misra et al.). During water absorption, the ingress of water into the polymers plays roles both in plasticizing the solid polymer matrix (Banks and Ellis 1979, Banks and Ellis 1982, Ellis and Karasz 1984, Yiu, King et al. 2006) and in exerting pressure (Biot 1941, Cui and Abousleiman 2001, Chiarelli 2004, Hoang and Abousleiman 2009). Both these effects influence the mechanical behavior: plasticization by softening and pressure by load sharing . The pore pressure in the water- saturated polymers has two contributions; one from the chemical interaction between water and polymer, termed as osmotic pressure at equilibrium, and one due to the externally applied mechanical load, termed as mechanical pressure. Therefore, to characterize the mechanical behavior of the multi, hydrophobic-rich phase and hydrophilic-rich phase polymers, it is necessary to consider each of these effects. Further, the rate-dependent behavior of the polymer has two components (a) the viscous effects due to interaction between polymer chains and (b) the rate-dependence of mechanical behavior due to the resistance offered

to fluid flow through the polymer matrix. The chemical composition and structure of the polymer plays an important role in determining its mechanical properties and interaction with water. For instance, the diffusion coefficients in methacrylate based polymer systems have been found to be strongly correlated to hydrophilicity and crosslink density (Parthasarathy, Misra et al. 2012).

1.2 Significance

Extensive research has been performed to investigate chemical structure-property relationships in different polymers, including dentin adhesive polymers (Reinhart and Peppas 1984, Bellenger, Verdu et al. 1989, Nogueira, Ramirez et al. 2001, Ito, Hashimoto et al. 2005, Wang and Wu 2005, Yiu, King et al. 2006, Hosaka, Tagami et al. 2007, Parthasarathy, Misra et al. 2012). However, development and calibration of models that connect molecular structure to micromechanical properties and in turn to macro-scale behavior still remains a fundamental problem in engineering. The research presented in this dissertation presents such a model for the case of dentin adhesive polymers. In the a/d interface of a composite restoration, various polymer phases are formed and depending on their chemical composition, their chemo-mechanical properties vary along the interface. The research presented in this dissertation will address the following properties along the a/d interface: (a) monomer-water phase composition, (b) polymerization behavior, (c) polymer phase composition (d) water diffusion and swelling, and (e) poromechanical parameters. These relationships obtained between the mechanical and physicochemical properties and the phase composition serve to analyze the adhesive in the a/d interface. They serve as a guide for the identification and development of new dentin adhesives and can be used to obtain input adhesive material properties for finite element model of the a/d interface. In the design of adhesive co-monomers, the hydrophilicity and crosslinking properties

of the co-monomer are adjusted by polymer chemists, for example, by modifying side-chains, functional groups, or number of reactive sites to improve the miscibility and phase separation behavior. The material model developed in the dissertation can be used to obtain diffusion coefficients, calculate water sorption and swelling, and predict flow-dependent mechanical behavior using the crosslink density and hydrophilicity. The chemo-mechanical properties obtained from the material model can be used to simulate the mechanical performance of the adhesive, while considering loading as well as water diffusion. The objectives of decreasing monomer phase separation, water sorption and diffusion, while maintaining the mechanical properties in wet and dry conditions are critical elements in achieving a more robust and stable a/d interface. Based on current understanding, a more uniform and stable interface would extend fatigue life (Singh, Misra et al. 2011), improve crosslink density and reduce porosity which leads to bacterial and enzymatic infiltration and ultimately extend the life of the composite restoration. The experimental and modeling techniques described here can also be used to test other polymer systems interacting with water in their monomer and polymer states.

1.3 Specific Aims:

The effectiveness and durability of the a/d interface is dependent on the physicochemical and mechanical properties of the adhesive which a) protects the prepared tooth from the surrounding environment and b) transfers the applied chemo-mechanical load from the composite to healthy dentin. Water sorption, plasticization, leaching, degradation, enzymatic and bacterial attack and their effects on the mechanical properties are all strongly dependent on the adhesive composition in terms of hydrophilic-hydrophobic monomer ratio, initiator concentration and porous structure.

The overall hypothesis of this research work is that the chemical composition of a water-adhesive monomer phase boundary adequately describes the water sorption, water

diffusion and poromechanical properties of the multi-phase adhesive polymer formed in the a/d interface. The goal of this dissertation is to define the chemical composition of different monomer phases using phase diagrams and determine structure-property relationships between the chemical composition of the different monomer phases and the physicochemical and mechanical properties of the polymerized phases.

The following specific aims will be addressed. Figure 1-5 shows a flowchart of the specific aims. Table 1-1, Table 1-2 and Table 1-3 give the nomenclature of adhesive resin monomers and polymers, list of adhesive formulations with acronyms and list of photoinitiator formulations respectively.

1.3.1 Characterization of Monomer Properties

This is to determine miscibility and phase separation behavior of HBX-NRM, degree of polymerization, polymerization kinetics and influence of photo-initiator for HBX-WM-APM. The first hypothesis to be tested is that the miscibility and phase separation can be expressed as functions of the neat monomer composition. The second hypothesis to be tested is that the polymerization behavior of the monomer phases can also be defined as a function of monomer phase composition. The characterization of monomer properties has been discussed in chapter 1 of the dissertation.

1.3.2 Characterization of Polymer Properties:

This is to characterize the pore structure, pore size distribution, connectivity of pores and chemical compositions of different phases in HB45-33P. The hypothesis to be tested is that the pore structure and composition of HB45-33P can be expressed in terms of the composition of

HB45-33-APM and HB45-33-RPM. The characterization of polymer properties has been discussed in chapter 1 of the dissertation.

1.3.3 Mechanical Modeling:

To determine and compare the chemo-poro-mechanical properties along the phase boundary of the monomer-water phase diagram. The hypothesis to be tested is that the diffusion coefficients and the mechanical properties of the polymer phases in both wet and dry conditions can be expressed as a function of the chemical composition along the phase boundary. The mechanical modeling has been detailed in chapters 2, 3, 6 and 7 of the dissertation. The diffusion of water through the polymer phases has been discussed in chapters 4 and 5 of the dissertation.

1.3.4 Innovation

In dental research, a phase diagram has been used for the first time to represent the entire range of possible monomer mixtures formed in the a/d interface from interaction of adhesive monomer with water and a methodology for determination of the phase diagram has been developed. Methodologies have been proposed to investigate solvent-induced and polymerization-induced phase separation. A chemo-poro-mechanical model using granular micromechanics has been developed to model the hydrophilic adhesive phases. The calibration of the material model is performed using simple mass change and volume change experiments along with three-point bending. The resulting model is used to predict poromechanical behavior. In the material model, fiber network micromechanics are integrated into a poromechanics framework to fit the effects of chemical structure and fluid flow into a single model. Further, the influence of the crosslink density on the water diffusion into the polymer has been quantified.

1.3.5 Rationale for specific aim 1: Characterization of Monomer Properties

The phases formed in the a/d interface are influenced by the mixing of the adhesive monomer with the fluid in the dentinal tubules. The mixing can take place by a combination of diffusion, convective and turbulent phenomena, resulting in a) decrease in infiltration of the hydrophobic monomer with depth, resulting in the adhesive becoming increasingly water-rich towards the dentin matrix (Zou 2007) and b) formation of phase separated multi-phase polymer (Spencer and Wang 2002). By virtue of ‘a’ and ‘b’, the hydrophilic-hydrophobic adhesive mixture can combine in different ratios with different water concentrations, to yield various polymer phases. The uniformity in chemical composition of the hybrid layer, which is critical to achieve optimal fatigue life (Singh, Misra et al. 2011), is strongly dependent on the penetration of both the hydrophobic and hydrophilic adhesive constituents and the phase separation behavior of the adhesive formulation mixture with water. The adhesive penetration and phase separation behavior are determined by the miscibility of the adhesive co-monomers with water. A study of adhesive phase separation is necessary to quantify the chemical composition of the resulting phases, obtained when the resin monomer mixture is over-saturated with water. The chemical composition of the separated phases, in turn, governs the degree of polymerization, porosity, and mechanical properties of the different polymer phases and their composites formed in the hybrid layer. The hydrophilic-rich phases represent the upper extreme of water concentration and lower extreme of crosslinkable monomer (hydrophobic) in the hybrid layer. Loosely crosslinked domains are susceptible to higher water sorption and consequent increase in plasticization, leaching and degradation. Therefore, it is necessary to study the polymerization kinetics and final degree of conversion, especially for the hydrophilic-rich phase components of the adhesive

resin, since sufficient polymerization rate, degree of conversion and crosslinkable content in the hydrophilic-rich phase indicates sufficient polymerization throughout the hybrid layer.

1.3.6 Rationale for specific aim 2: Characterization of Polymer Properties

The hybrid layer is composed of a composite of various phases of polymers with varying pore structure and chemical composition with the demineralized collagen. The mechanical properties of the different polymer phases are critical for the stability, extended fatigue life and protection to the exposed collagen. The study of the time and rate dependent mechanical behavior of the adhesive is important in view of the variable loading rates in the mouth. The fluid diffusion through the polymer-matrix, water sorption characteristics of the polymer and intrinsic polymer viscoelasticity are all factors that influence the time and rate dependent mechanical behavior of these polymer phases (Ito, Hashimoto et al. 2005, Chiaraputt, Mai et al. 2008, Ye, Wang et al. 2009, Misra, Singh et al. 2011, Singh, Misra et al. 2011). These characteristics, in turn, are dependent on chemical composition and pore structure (Parthasarathy, Misra et al. 2012). Therefore, it is important to identify the pore structure and chemical composition of the various polymer phases formed in the hybrid layer. Micro-X-ray tomography has been extensively used to in the fields of material science and engineering to determine the 3-D structure and porosity at micro-scales. It has also been used in our lab to reconstruct the 3-D structure of dentin adhesive polymers (Parthasarathy, Misra et al. 2012). Raman spectroscopy has been used to characterize the chemical composition of dentin adhesives (Zou, Armstrong et al. 2010). The differences in homogeneity pore structure, and pore size distribution can be observed using this technique.

1.3.7 Rationale for specific aim 3: Mechanical Modeling

As explained in specific aim 2, the mechanical properties of the polymer phases in the hybrid layer are time and rate dependent. In order to quantify the material properties that govern this time and rate dependency, a constitutive model incorporating the features of polymer matrix viscoelasticity, flow-dependent viscoelasticity and influence of water sorption on polymer matrix properties becomes necessary. Though constitutive models that incorporate poroelasticity and fiber network distributions have been developed (Huang, Mow et al. 2001, Nia, Han et al. 2012), they are either focused on the poromechanical behavior of saturated, swollen hydrogels (Biot 1941, Hoang and Abousleiman 2009, Hoang and Abousleiman 2012, Wang and Hong 2012) or on the diffusion properties of polymers (Anderson and Quinn 1974, Pusch and Walch 1982, Reinhart and Peppas 1984, Lustig and Peppas 1987, Colton, Satterfield et al. 2004). Further, the models focused on the development of poromechanical behavior do not explicitly consider the effect of chemical structure. For modeling dentin adhesives, a single model accounting for the diffusion, swelling, dry to wet transition and resulting poromechanical behavior is necessary. The various polymer phases in this study, in particular, the hydrophilic-rich phases can be considered as free-swollen, crosslinked networks. Therefore, the material model for these polymers has been constructed which computes the macro-scale poromechanical behavior by superposition of polymer matrix with interstitial water. The polymer-polymer and polymer-water interactions are explicitly incorporated in the model using parameters. This model has been used by our group to explain the rate dependent behavior of soft tissue such as condylar cartilage (Parthasarathy, Misra et al. 2011).

1.4 Summary (General):

The project is aimed at characterization and chemo-mechanical modeling of polymers formed from saturated/oversaturated mixtures of dentin adhesive monomers with water. The following steps are carried out: 1. Development of a phase diagram for the monomer components and water based on chemometric analysis using FTIR spectra, 2. Determination of the morphology, pore structure and pore size distribution of relevant polymer phases using 3D micro X-Ray computer tomography, 3. Qualitative study of the chemical composition and polymer-phase distribution using micro-Raman imaging analysis, 4. Development of mechanical model by incorporation of homogenized polymer matrix into a poro-mechanics framework. 5. Estimation of chemo-poro-mechanical properties along the adhesive-water phase boundary using swelling equilibrium, 6. Estimation of the diffusion coefficient of water in the polymer phases using mass change experiments and 7. Simulation of monotonic and creep experiments under wet and dry conditions using calibrated chemo-poro-mechanical model. The results of the characterization will provide the basis for the determination of the model parameters porosity, density, local constants and diffusion coefficients.

1.5 Relevance:

In composite resin restorations, the weak link is the hybrid layer which is a composite of demineralized collagen and phase-separated dentin adhesive. The longevity of the composite restoration depends on the physicochemical and mechanical properties of the hybrid layer, and in turn, on the various polymer phases in the hybrid layer. The methodology described in this dissertation is applied to characterize these dentin adhesive polymer phases formed in the presence of water. The application of the research methodology will assist in developing dentin adhesive systems that are more water compatible without sacrificing mechanical properties.

Such results can help to choose adhesives which will improve the life of composite restorations, potentially avoiding the need for repeated restoration replacement, which decreases the need for a more complex restoration and risk of eventual tooth loss.

Control Adhesive Formulation	Standard methacrylate-based adhesive system of 45/55 wt% 2-hydroxyethyl methacrylate (HEMA)/ 2, 2-bis[4-(2-hydroxy-3-methacryloxypropoxy)phenyl]-propane (BisGMA)
Photoinitiator Systems	Different photo-initiator systems are tested based on camphorquinone (CQ), ethyl-4-(dimethylamino) benzoate (EDMAB) and diphenyliodonium hexafluorophosphate (DPIHP)
Polymer Phases	Four categories of polymer systems - a) neat adhesive resin formed without the presence of water, b) hydrophobic-rich phase formed after phase separation in water, c) hydrophilic-rich

Table 1-1 Nomenclature of adhesive resin monomers and polymers

Sample	Monomer abbreviation*	Polymer abbreviation*
Neat adhesive with HEMA to BisGMA in the mass ratio X:(100-X)	HBX-NRM	HBX-NRP
Neat adhesive with water percent at miscibility limit	HBX-PB	HB-RPP
Oversaturated mixture of neat adhesive with W mass percent of water	HBX-WM	HBX-WP
Hydrophilic-rich phase oversaturated mixture	HBX-WM-APM	HBX-WM-APP
Hydrophobic-rich phase oversaturated mixture	HBX-WM-RPM	HBX-WM-RPM

Table 1-2 List of adhesive formulations

Abbreviation for photoinitiator system	% Composition by Mass ^a			
	CQ	EDMAB	DPIHP	QTX
2PI	0.5	0.5	0	0
3PI	0.5	0.5	0.5	0
4PI	0.25	0.5	0.5	0.25

Table 1-3 List of photoinitiator formulations consisting of camphorquinone (CQ), ethyl-4-(dimethylamino) benzoate (EDMAB), diphenyliodonium hexafluorophosphate (DPIHP) and 3-(3,4-dimethyl-9-oxo-9H-thioxanthen-2-yloxy)-2-hydroxypropyl] trimethyl ammonium chloride (QTX)

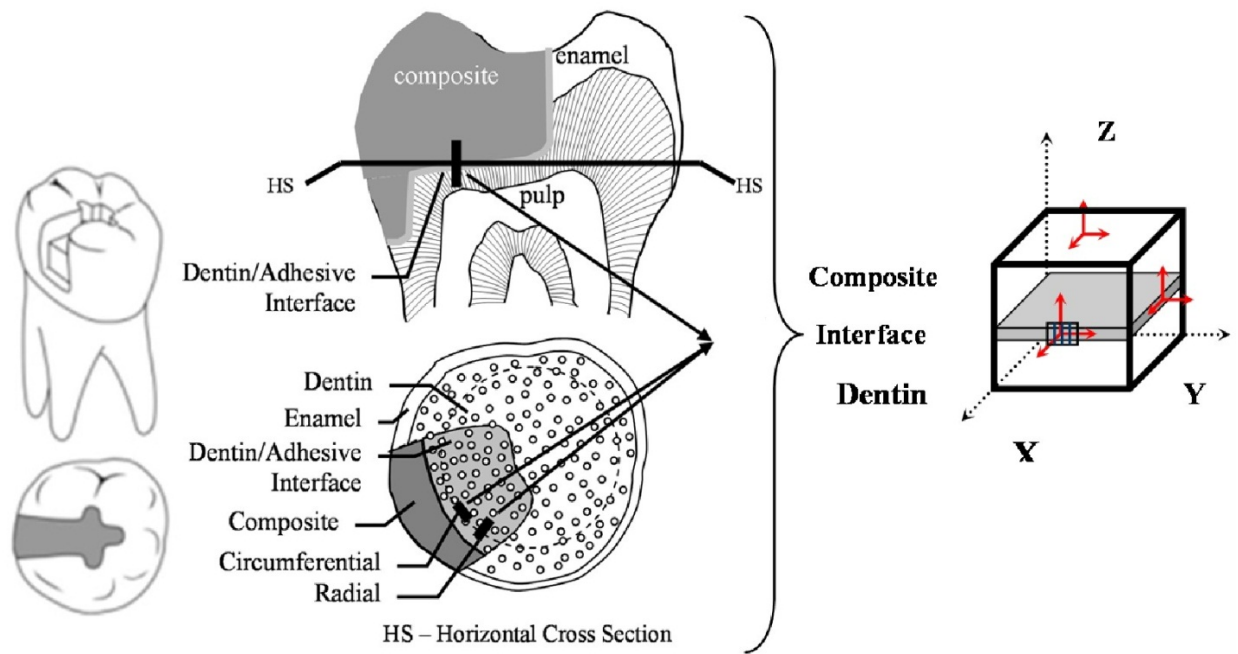


Figure 1-1 Schematic of a tooth restored with composite restoration. This figure depicts the relationship of the dentin-adhesive bond to the composite restoration (Misra, Spencer et al. 2005, Singh, Misra et al. 2011)

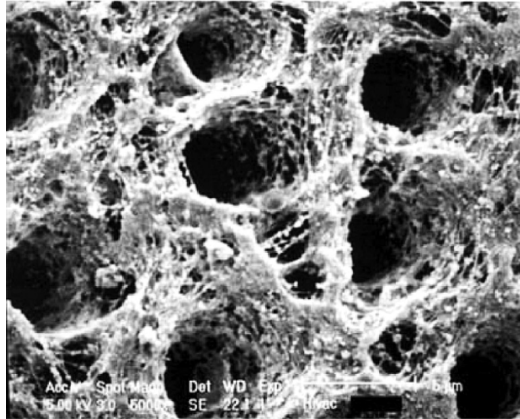


Figure 1-2. Scanning electron micrograph of demineralized dentin matrix (which is primarily type I collagen). The holes that are distributed throughout the matrix represent the dentinal tubules. Under clinical conditions, pulpal fluid is pulsing through the dentinal tubules (Misra, Spencer et al. 2005)



Figure 1-3. Visible light micrograph of dentin adhesive hybrid layer

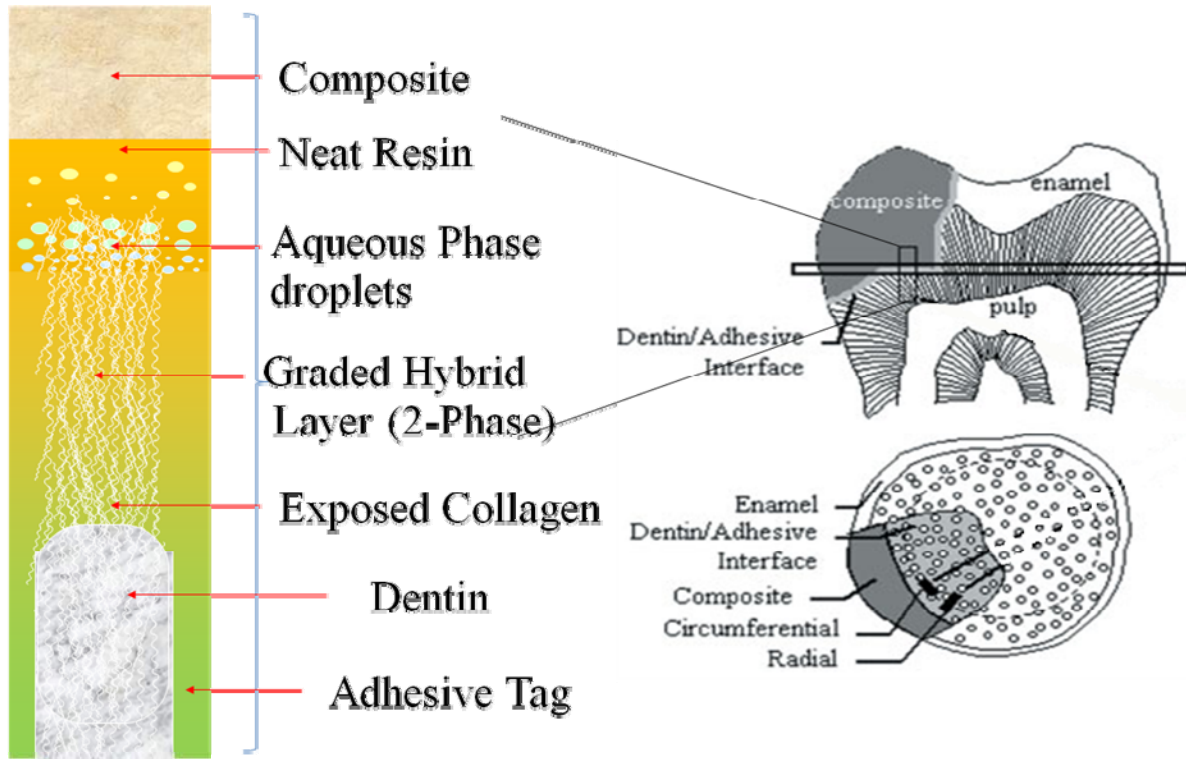


Figure 1-4. Illustration representing adhesive phase separation and water entrapment at the dentin/adhesive interface

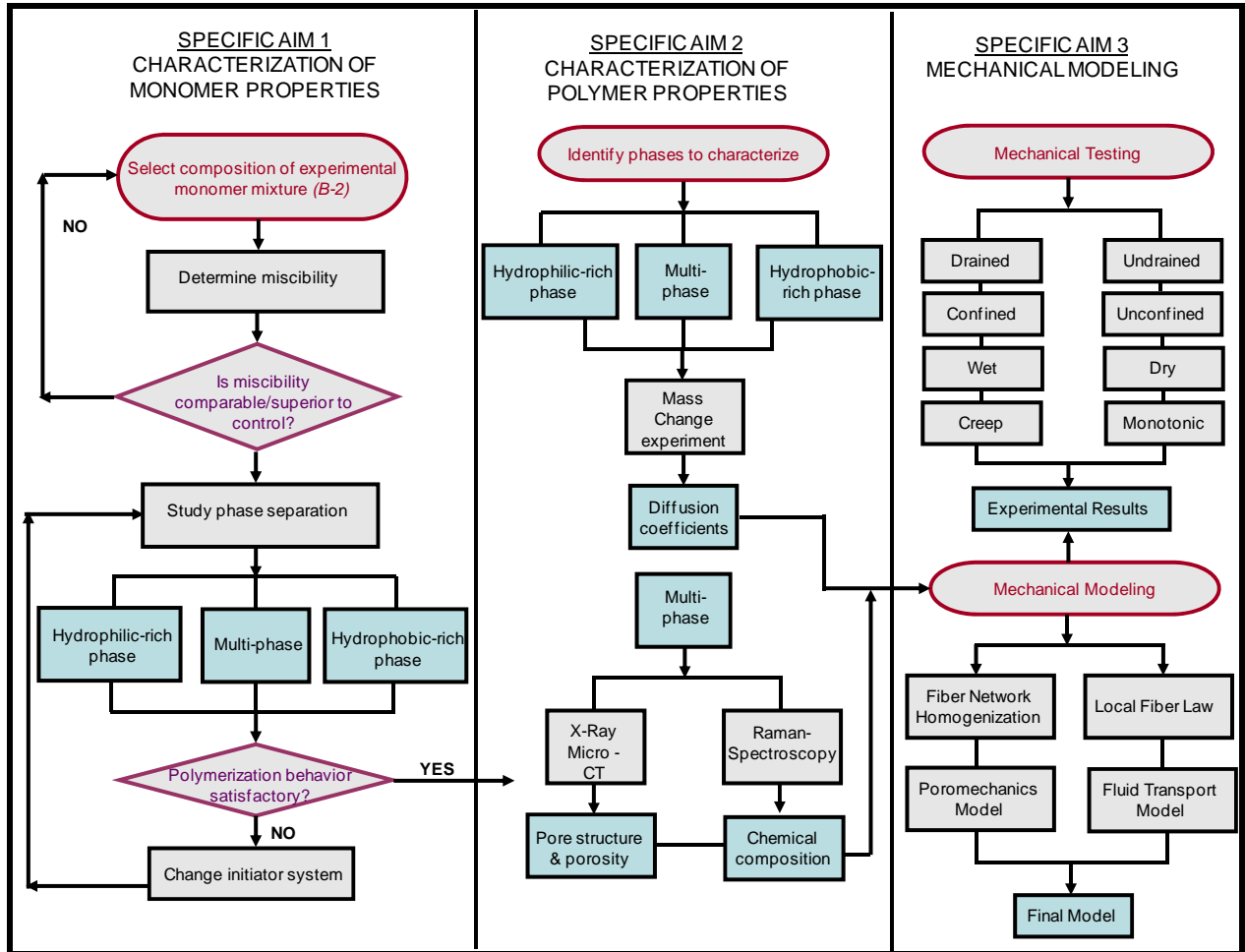


Figure 1-5. Flowchart for research proposal

2 CHARACTERIZATION OF DENTIN ADHESIVE SYSTEM USING A TERNARY PHASE DIAGRAM

Due to limited penetration and phase separation, commercial dentin adhesives consisting of a hydrophobic/hydrophilic monomer pair such as BisGMA /HEMA undergo phase separation and compositional change in adhesive dentin interfaces upon interaction with water and dentinal fluid. Consequently, the adhesive in the restoration varies in composition and morphology throughout the interface, thus affecting its chemical and mechanical properties, which influence its ability to transfer mechanical load and offer protection to exposed collagen. We have modeled the variability in composition of the adhesive monomer using a ternary adhesive-water phase diagram. We also determine the polymerization of the adhesive along the phase boundary, and study the nature of adhesive polymer polymerized in the presence of water. The results quantify the variability in adhesive monomer composition, and its effect on the resulting adhesive polymer. This type of investigation provides a thorough understanding of the composition and properties of the adhesive in the adhesive dentin interface.

2.1 Introduction

Commercial dentin adhesives use a hydrophobic/hydrophilic monomer pair such as BisGMA (Bisphenol A glycerolate (1 glycerol/phenol) dimethacrylate)/ HEMA (2-hydroxyethyl methacrylate) to simultaneously achieve a) adequate monomer penetration through hydrated pore spaces in demineralized dentin and b) adequate polymerization and polymer stiffness via crosslinking to transfer mechanical load and protect exposed collagen from bacterial and enzymatic attack. The monomer penetration takes place through a combination of convection and diffusive transport. However, due to differences in water solubility and viscosity of the

component monomers, such a system undergoes phase separation with limited infiltration of the hydrophobic monomer into the pore spaces filled with water and dentinal fluid, and experimental evidence of the same has been well established (Spencer and Wang 2002, Zou 2007, Spencer, Ye et al. 2010, Zou, Armstrong et al. 2010, Toledano, Yamauti et al. 2012). In this process, several adhesive polymer phases are formed in the adhesive-collagen hybrid layer, primarily composed of BisGMA, HEMA and pore-spaces (Spencer and Wang 2002). Research across several fields in polymer chemistry has demonstrated that the chemo-mechanical properties of crosslinked polymers are strongly correlated to their chemical composition and structure (Bellenger, Verdu et al. 1989, Ito, Hashimoto et al. 2005, Wang and Wu 2005, Hosaka, Tagami et al. 2007, Lou, Robisson et al. 2012, Parthasarathy, Misra et al. 2012, Sun, Zhao et al. 2012). The formation and composition of these polymer phases are strongly affected by their composition in the monomeric state.

The interaction of the hydrophilic/hydrophobic monomer pair with water falls under the research category of ternary liquid-liquid phase equilibria, which has been extensively studied both experimentally and theoretically for several systems (Vriens and Medcalf 1953, Renon and Prausnitz 1968, Brandani, Chianese et al. 1985, Pappa, Kontogeorgis et al. 1997, Zhang, Chai et al. 2004, Mazzobre, RomÃ¡n et al. 2005, Senol 2006). However, till date, only one such investigation on the liquid-liquid phase equilibrium of the adhesive monomer-water system has been performed (Ye, Park et al. 2011). In this work, a partial phase diagram for the monomer-water system was developed and interpreted. The present work extends this investigation by (1) construction and validation of a complete phase diagram (2) investigation of monomer conversion along the phase boundary (3) investigation of polymer kinetics along the phase boundary (4) determination of chemical composition and morphology for the phase separated

polymerized adhesive. We have constructed the phase boundary separating the miscible and immiscible portions of the system, identified criteria for polymerization of the adhesive, and determined the phase composition in polymerized adhesive systems.

In the subsequent discussion, we first briefly present our chemometrics-based approach using FTIR-ATR spectra for identification of separated phases from an oversaturated monomer-water mixture. We then construct the phase diagram using experimental data and validate it using independent measurements from HPLC and miscibility tests. Finally, we present results for the chemical composition of adhesive polymer formed from an oversaturated monomer-water mixture.

2.2 Materials and Methods

2.2.1 Materials and nomenclature

The model adhesive consisted of mixtures of 2-hydroxyethylmethacrylate (HEMA, Aldrich, Milwaukee, WI) and 2,2-bis[4-(2-hydroxy-3-methacryloxy-propoxy)phenyl]-propane (BisGMA, Aldrich, Milwaukee, WI) in several mass ratios. Deionized water was used for all the experiments. All the operations were carried out in triplicate and at ambient temperature (24 ± 1 °C). The adhesive monomer mixture not containing any water is called a neat resin. Neat resin containing X percent of HEMA and (100-X) percent of BisGMA is denoted as HBX-NR. When the neat resin is diluted with water up to its miscibility limit, it is denoted as HBX-PB where PB refers to phase boundary.

2.2.2 Miscibility Experiment

The miscibility of the adhesive with water is determined using turbidity limits. Approximately 0.5 g of neat resin containing HEMA/BisGMA in a known ratio is transferred into a brown vial. Deionized water is added in increments of 1 μl till turbidity is observed visually. The water concentration at this point is recorded as w_1 . The mixture is back titrated by adding neat resin in increments of 1 μl till turbidity is eliminated. The water concentration is recorded as w_2 . The miscibility limit is calculated using the average water concentration of the forward and backward titrations i.e. $(w_1 + w_2)/2$.

2.2.3 Phase Separation Experiment

HEMA/BisGMA monomer mixtures are prepared in the following ratios a) 75:25 and b) 25:75 to represent highly hydrophilic and highly hydrophobic regions. The neat resin HBX is diluted with known quantities of water to form oversaturated mixtures. The final compositions of the mixtures are shown in Table 2-1. Our earlier work (Ye, Park et al. 2011, Under Review) investigated phase separation for HEMA/BisGMA mass ratios of 45/55. The compositions of the mixtures in this work are chosen to build upon the data presented in (Ye, Spencer et al. 2011) and complete the phase diagram.

After deionized water is added to the neat resin, the mixture is sonicated for 1 minute to yield a well dispersed turbid mixture, which is separated using centrifugation for 20 minutes (1400g, 22°C). Centrifugation yields a denser hydrophobic-rich phase or resin phase, denoted as HBX-W-RPM, and a lighter hydrophilic rich phase or aqueous phase, denoted as HBX-W-APM, which are separated using a pipette and stored in brown vials for immediate use. Here, W is the percentage of water added to the neat resin HBX. FTIR spectra are collected for each phase at a resolution of 4 cm^{-1} , scan range of 4000 to 650 cm^{-1} , and 10 full-range scans per spectrum using

an FTIR spectrometer (Spectrum 400, PerkinElmer) and analyzed to extract the percentage composition using a calibration of spectra with respect to standards of known composition. The corresponding polymer formulations formed by polymerization of HBX-W-RPM and HBX-W-APM are denoted as HBX-W-RPP and HBX-W-APP.

2.2.4 Calibration of FTIR spectra

The calibration between the FTIR spectra and the component concentrations is developed using Beer's Law i.e. the existence of a linear relationship between the spectral intensity and the concentration of the corresponding component. The standards used for developing the calibration are shown in Figure 2-2. Separate spectral standards are chosen for hydrophilic rich and hydrophobic rich spectra since Beer's law is not necessarily linear for very large or very small component concentrations; the hydrophilic rich phases contain very small concentrations of BisGMA and the hydrophobic rich phases contain very small concentrations of water. Moreover, given the complexity in the molecular structures of the components, interaction between the different electronic vibrations could induce non-linearity into Beer's Law (Griffiths and De Haseth 2007). However, based on the experimental evidence presented in this paper, it has been verified that a piecewise linear assumption gives a satisfactory fit.

Several multivariate regression techniques are available to solve for the regression constants; we use the technique of partial least squares (PLS) since it not only solves the problem of collinearity between the spectral data, but also explains a maximum of the covariance between transformed spectra and the component concentrations (Wold, Sjoström et al. 2001). Since there is high collinearity in the information contained in a spectrum, but the concentrations of the three components HEMA, BisGMA and water in a mixture are independent, the technique PLS1 is used, where only the covariate is decomposed into a product of scores and latent vectors, and the

dependent variable is used in its original form. The goodness of fit of the calibration is verified by using the standard error of estimate (SEE) and the standard error of prediction (SEP), which is shown for each component in Table 2-3. The calibration is then used to predict unknown component concentrations from the FTIR spectra.

2.2.5 Degree of conversion

Resin mixtures used to study the degree of conversion are prepared by addition of photo-initiator to the neat monomer mixture and diluting the mixture to the miscibility limit. The following two-component visible light photoinitiators (all from Aldrich, Milwaukee, WI) were used in this work: camphoroquinone (CQ, 0.5wt%) and ethyl-4-(dimethylamino)benzoate (EDMAB, 0.5wt%). In order to simulate the clinical conditions, the photo-initiator is added during preparation of the neat resin and not after dilution. The degree of conversion (DC) was determined by Raman spectrometer as described previously (Park, Ye et al. 2009). In brief, LabRAM ARAMIS Raman spectrometer (LabRAM HORIBA Jobin Yvon, Edison, New Jersey) was used with a HeNe laser ($\lambda=633$ nm, a laser power of 17 mW) as an excitation source. The instrument settings were as follows: 200 μm confocal hole, 150 μm wide entrance slit, 600 gr/mm grating, and 10x objective Olympus lens. Data processing was performed using LabSPEC 5 (HORIBA Jobin Yvon). The samples were mounted on a computer-controlled, high-precision x-y stage. To determine the DC, spectra of the unpolymerized resins and rectangular beam samples were acquired over a range of 700 – 1800 cm^{-1} . The changes of the band height ratios of the aliphatic C=C double bond peak at 1640 cm^{-1} and the aromatic C=C at 1610 cm^{-1} (phenyl) in both the cured and uncured states were monitored. The DC was calculated as follows, based on the decrease in the intensity band ratios before and after light curing.

$$DC(\%) = \left(1 - \frac{R_{cured}}{R_{uncured}}\right) \times 100 \quad (2.1)$$

where R = band height at 1640 cm⁻¹/band height at 1610 cm⁻¹. All experiments were carried out in triplicate and the results were averaged.

2.2.6 Polymerization kinetics

The neat resin mixtures used to study the polymerization kinetics are prepared by addition of the two-component photoinitiators and diluted to the miscibility limit. In this experiment, to eliminate the effect of photoinitiator content, additional photoinitiator is added after dilution to make the total photoinitiator content up to 0.5%. The polymerization kinetics is investigated using time series of FTIR-ATR spectra collected using an FTIR spectrometer (Spectrum TimeBase, PerkinElmer). Heavy water (D₂O) is used instead of H₂O to avoid overlap of water and monomer/polymer spectral peaks. The rate of spectrum collection is approximately 1 for every 0.4~0.6 seconds. About 50 μL of the liquid resin is placed on the Perkin Elmer Spectrum 400 ATR crystal and a plastic coverslip is immediately placed over the liquid and sealed on all four sides using scotch tape to prevent evaporation. After 50 spectra are collected by the TimeBase software, UV-vis light (550 mW/cm²) is turned on for 40 s to polymerize the sample. Spectra are continuously collected by the software for 4 hours or until equilibrium is reached. The degree of conversion of the polymer with respect to time is measured using the ratio of the C=C peak (1638 cm⁻¹) with respect to either the aromatic peak (1608 cm⁻¹) or with respect to the C=O peak (1716.5 cm⁻¹). This ratio decreases as the polymerization reaction proceeds and the proportion of C=C bonds in the mixture decreases.

2.2.7 Chemical composition

The investigation of polymerization and composition is performed using micro-Raman spectroscopy on polymerized samples of HB45-33. The water content was chosen arbitrarily as 33% and does not represent the clinical condition, since the exact amount of water in the demineralized dentin is not known. The oversaturated monomer mixture HB45-33 is filled into aluminum molds, covered with a glass slide and polymerized using a hand-held LED light (Spectrum 800, Dentsply, Milford, DE, USA) of irradiance 550 mW/cm^2 , wavelength 512 nm and area 6.25 mm^2 for 40s. After 24 hours, the glass slide is removed and the specimen is stored in a vacuum oven in the presence of a drying agent (freshly dried silica gel) at 37°C . Following polymerization, the glass slide is removed and the specimens were placed at the focus of a 100X objective of an optical microscope (Nikon ME 600, Melville, NY, USA) and the Raman spectra were collected using a Raman imaging system (LabRAM HORIBA Jobin Yvon, Edison, New Jersey), equipped with Olympus lenses and a liquid-nitrogen-cooled CCD detector. The optical microscope allowed for visual identification of the position at which the Raman spectrum was obtained. The excitation source was a HeNe laser ($\lambda=633 \text{ nm}$, a laser power of 17 mW) as an excitation source. The estimated power at the laser was 100 mW after passing through the bandpass filter and condensing optics and 3 mW power was incident on the sample. Data was collected from various points on the surface of the sample to obtain several spectra which could represent the range of composition of the sample. The following peaks are used for identification of the corresponding groups: 1608 cm^{-1} for aromatic ring of BisGMA, 1456 cm^{-1} for C-H and 1638 cm^{-1} for C=C. The band ratio of the aromatic ring to the C-H bond is used as a measure of the percentage of BisGMA in the sample.

2.2.8 Morphology

The microscale morphologies of cured cylindrical specimens of HB45-33 are observed using three-dimensional (3D) Micro X-ray Computer Tomography (MicroXCT-400, Xradia Inc. Concord, CA). Computer tomography (CT) facilitates viewing of an object in 3D and allows selection of virtual slices up to a resolution of 1 μm , thus illustrating the bulk structure of heterogeneous materials. The transmission X-ray imaging of the samples are performed using an X-ray tube with a tungsten anode setting of 50 kV at 6 W with an optical magnification of 20X. The 3D images are then be re-constructed with the help of software “XM Reconstructor 8.0” using 2160 images taken at 15 s exposure time per image. The 3D images reveal the pore structure and connectivities.

2.3 Results and discussion

2.3.1 Miscibility testing

The water miscibility for neat resins prepared with varying ratios of HEMA to BisGMA is tested and plotted against the HEMA percentage in the neat resin. An exponential curve fits the data well ($R^2 = 0.99$) in the range when the HEMA content is less than 98% i.e. the BisGMA content is greater than 2%. As expected, the water solubility increases with the HEMA proportion in the neat resin. This can be verified by comparing the values of LogP for HEMA (LogP = 0.47) and BisGMA (LogP = 5.09) calculated using commercial software (ChemBioDraw Ultra, PerkinElmer).

2.3.2 Chemometrics based calibration of FTIR spectra

The phase diagram is obtained using the calibration between composition and FTIR spectra. The goodness of fit for the calibration is shown in Table 2-3. Both the SEE and SEP are small compared to the mean component concentration. In addition, the values of SEE and SEP are close to each other, indicating high confidence in the regression coefficients determined. The collinearity in spectra was also greatly reduced as only about 5-8 latent vectors were sufficient to explain more than 99% of the variance in the concentration of each component. The method offers the advantages of rapid technique, use of complete information from spectra, limited time and effort for sample preparation, spectra collection and analysis.

2.3.3 Phase composition

Figure 2-3 shows the phase diagram for the ternary system of water, HEMA and BisGMA. The phase boundary is constructed using the exponential fit to the miscibility plot. Tie lines have been obtained for 4 oversaturated water-resin mixtures whose compositions are shown in Table 2-2. The end points of the tie line lie on the exponential fit curve; thus the results from the phase separation and miscibility testing validate each other. Upon phase separation, the oversaturated mixtures form two distinct phases: a hydrophilic-rich phase primarily containing HEMA and water, and a hydrophobic rich phase, rich in BisGMA. The experimentally determined composition of these separated phases is shown in Table 2-4. The data for HB45 was obtained as part of earlier work (Ye, Park et al. 2011, Under Review). The phase separation described in this section can be classified as solvent-induced phase separation (SIPS) (Oh and Rey 2000).

The hydrophilic-rich phases contain a very low mass fraction of BisGMA. The mass fraction of BisGMA in a phase is critical because BisGMA is the component that increases the crosslink density and the hydrophobicity of the polymer. These two characteristics are the main factors

responsible for limiting the water sorption (Parthasarathy, Misra et al. 2012) and consequent reduction of mechanical stiffness. This aspect has been elaborated in chapters 3 and 4.

The phase separation behavior of the water-monomer system is simplified because BisGMA and water are nearly immiscible (Kim and Chung 2005, Ye, Park et al. 2011, Under Review). This is also verified by observing that the end points of the tie lines representing hydrophilic-rich phase have less than 1% BisGMA (detection limit). Consequently, in regions excepting extremely low water concentration or extremely low BisGMA concentration, the behavior is well defined by the relative solubility of HEMA in water to HEMA in BisGMA. From the relative partitioning of HEMA between hydrophilic-rich and hydrophobic rich phases, it can be concluded that HEMA is preferentially dissolved in BisGMA as compared to water. Similar results were also observed from phase separation tests on HB45-NR (Ye, Park et al. 2011, Under Review).

The proportion of HEMA to BisGMA used in the commercial adhesive is 45 to 55. However, as the adhesive infiltrates the wet tubules in the demineralized dentin, a) the proportion of BisGMA in the adhesive decreases and b) the absolute quantity of adhesive infiltrating the demineralized dentin decreases (Spencer and Wang 2002, Zou 2007, Zou, Armstrong et al. 2010). As a consequence, the resulting monomer phases formed in the adhesive dentin interface could lie anywhere on the phase boundary. The phase boundary represents the limit of dilution with water for a monomer phase. Further, we note that each point in the two-phase region of the phase diagram represents a mixture of two phases given by the end points of the tie line. The proportion of each phase in the mixture is inversely proportional to its distance from the point representing the two phase mixture. Therefore, the phase boundary can be utilized to study all possible phases that form in the adhesive dentin interface.

2.3.4 *Degree of conversion*

The adhesive transfers mechanical stress and protects the exposed dentin collagen from bacterial and enzymatic attack. Sufficient degree of conversion of the monomer phase is required to convert the monomer mixture into a polymer with the mechanical properties of a solid, so that the adhesive can satisfy its function. Further, we note that insufficient polymerization can result in the leaching of HEMA and BisGMA into the mouth leading to toxic effects (Schweickl, Spagnuolo et al. 2006). Therefore, a study of the degree of conversion along the phase boundary is critical. The degree of conversion along the phase boundary obtained using Raman spectroscopy is shown in Figure 2-4. For the samples on the phase boundary to the left of HB5-PB, the degree of conversion of the phases is negligibly small. Beyond HB7.5-PB, the degree of conversion is substantial. We hypothesize that the factors that determine the degree of conversion are a) photo-initiator content b) dilution and c) BisGMA content. The photo-initiator is necessary to generate free radicals that initiate the polymerization reaction, and if its concentration is too low, the polymerization reaction cannot initiate. If the dilution is too high, it decreases the solubility of the hydrophobic photo-initiator in hydrophilic-rich phases, and also decreases the probability of propagation of the reaction by chain elongation, since the concentration of monomer molecules is lowered by dilution. The BisGMA content is important since the presence of BisGMA increases the rate since crosslinking increases the viscosity of gels and slows down the termination (gel effect). We note that studying each of these factors in isolation is not straightforward and requires substantial experimental work. We also note that the formulations are described

2.3.5 *Polymerization kinetics*

In order to a) validate the results observed using Raman spectroscopy, b) observe the time rate of conversion and c) identify the critical region on the phase boundary where polymerization increases, the polymerization kinetics and degree of conversion were studied using FTIR-ATR spectroscopy. The results for HB100 to HB92.5 are shown in Figure 2-5. The results again show that only the samples on the phase boundary lying to the right of HB95-PB polymerize adequately and thus validate the result observed using Raman spectroscopy. Further, it is observed that the polymerization reaction initiates in all the cases for the duration in which the curing light is turned on. However, only the samples to the right of HB95-PB continue to polymerize even after the curing light is turned off. For the hydrophilic-rich phases HB95-PB, HB94-PB and HB92.5-PB, the rate of polymerization after the curing light is turned off is much slower as compared to formulations in the hydrophobic-rich side of the phase diagram. For example, the polymerization kinetics of HB45-RPP, shown in Figure 2-5, reveals a much higher rate of polymerization as compared to the hydrophilic-rich phases. This is again because the gel-effect, which is much higher for hydrophobic-rich formulations due to increased viscosity, greatly slows down the rate of termination of the reaction. It is important to note that the rate of polymerization and the final crosslink density are both associated with the BisGMA content of the monomer phase. A monomer transforming to a crosslinked polymer will also demonstrate a higher gel effect as compared to its transformation to a linear polymer. From the results, it is clear that the polymerization kinetics study is important in particular for hydrophilic-rich phases, which may be formed during the penetration of adhesive monomer into the dentinal fluid. Further study is necessary to isolate and identify the factors which are responsible for polymerization.

2.3.6 *Polymer phase composition*

Spectra from different regions in the polymerized sample of HB45-33 were extracted to study the contrast between hydrophilic-rich and hydrophobic-rich phases formed in the sample and to study the degree of conversion of the aqueous phases formed in the sample. The polymer phases formed contain HEMA and BisGMA in various ratios. After sonication, the monomer mixture HB45-33 consists of the separated phases HB45-33-APM and HB45-33-RPM. In order to compare the composition of HB45-33 polymer with the separated phases HB45-33-RPM and HB45-33-APM, micro-Raman imaging was applied to HB33-45 polymer. The band ratio of the aromatic (1608 cm^{-1}) to the C-H (1453 cm^{-1}) bands is used as a quantitative estimate of the percentage of BisGMA in the polymer. For HB-RPM, the band ratio is 1.33. HB-APM contains BisGMA below the detection limit of 1%, so the band ratio can be taken to be approximately zero. However, the band ratios obtained from HB45-33 polymer lie below 1.33. A representative band ratio image containing phases with distinctly different composition is shown in Figure 2-6(a). The band ratio varies from 0.5 to 1.3 within the region of study of about $12.5 \times 14\ \mu\text{m}$. The reason for the formation of a wide range of ratios is combination of polymerization-induced phase separation (PIPS) (Doane, Golemme et al. 1988, West 1988, Sperling 1997, Oh and Rey 2000) and solvent-induced phase separation (Oh and Rey 2000). The phase boundary separating the single and two or multi-phase regions in the polymeric state is not the same as the water-monomer phase boundary. The phase boundary for the water-monomer phase diagram represents the equilibrium between BisGMA, HEMA and water in their monomer state. However, the miscibility of water in a polymer of HEMA and BisGMA is different from the corresponding monomer mix. Therefore, as the polymerization propagates the solubility of water in the monomer-polymer mix decreases and after the polymerization is complete, the

equilibrium reached would represent a porous polymer that contains part of the water dissolved in the polymer matrix, and part of it phase-separated from the matrix. An optical image of the sample, shown in Figure 2-6(b), has similarities with the band ratio image obtained from micro-Raman imaging. However, due to the two dimensional nature of the optical image, it is difficult to distinguish the optical contrast produced by pore spaces from that produced by different phases.

2.3.7 Polymer porosity

A microXCT three dimensional image of the HB45-33 polymer reveals a porous structure formed from the evaporation of both dissolved and phase-separated water. The “pores” left behind after the evaporation of dissolved water are spaces between the polymer chains and are of sizes much smaller than 1 μm ; they cannot be imaged using microXCT. However, the pores left behind after evaporation of phase-separated water are in the range of microns, and are well captured by microXCT. Micro-XCT slices of a sample of HB45-33 are shown in Figure 2-7. The pore sizes range from a few microns to more than 50 μm . The pore size distribution is dependent on the energy supplied to sonicate the oversaturated monomer mixture. Data has been collected for the flow rate and fluid pressure of pulpal fluid in demineralized dentin (Ciucchi, Bouillaguet et al. 1995). However, in order to determine the exact pore sizes formed under clinical conditions, an accurate modeling of the dynamics of fluid flow and mixing with adhesive monomer is required. The estimate of pore sizes obtained here represents an approximation of these phenomena and can be used as a first estimate for poromechanical analysis of the adhesive polymers.

2.4 Conclusions

In clinical practice, wet bonding is essential to prevent collapse of the collagen network in the demineralized dentin and maintain adequate porosity for adhesive infiltration. However, phase separation and compositional change of adhesive with penetration is an important factor which affects the structure and properties, and eventually the failure of the adhesive dentin interface. The phase separation and compositional change resulting from adhesive monomer-water interaction in adhesive dentin interfaces has not been adequately investigated. As a consequence, sufficiently detailed compositional information is not available for further design steps such as mechanical characterization and synthesis of new monomer molecules. In this paper, we have quantified the monomer-water interaction using a ternary adhesive-water phase diagram and investigated the polymerization and polymer phases formed along the phase boundary. The development of the phase diagram is based upon the concept of ternary liquid-liquid phase equilibrium that is well established for several systems.

The phase diagram demonstrates that the hydrophilic-rich phases to the left of HB95-PB on the ternary phase boundary in Figure 2-3 do not polymerize sufficiently, thus indicating the potential consequences in terms of protection provided to the exposed dentin collagen and mechanical load transfer. Poor polymerization can also result in the leaching of unpolymerized monomers into the mouth, causing toxicity (Park, Eslick et al. 2011). The polymerization kinetics is strongly influenced by the gel effect, which in turn depends on the BisGMA concentration in the phase. Thus, consideration of hydrophilic-rich phase polymerization becomes an important criterion in adhesive monomer design. We also conclude that monomer-water mixtures in the two-phase region of the phase diagram yield multi-phase polymers upon polymerization. The process is a combination of both SIPS and PIPS. Part of the dissolved water phase separates

during the polymerization process and leaves behind a structure with macro-pores of sizes that vary from sub-micron to a few hundred microns.

The experimental methodology described in this paper can be used to characterize the chemical composition and morphology of any monomer-polymer system. In recent years, finite element analysis has been utilized to model the mechanical behavior of dentin adhesive interfaces and obtain estimates of failure stress or strain (Ausiello, Apicella et al. 2002, Misra, Spencer et al. 2004, Magne 2007, Singh, Misra et al. 2011). However, these models can be improved by inclusion of aspects such as composition variation, porosity and poromechanical effects. The incorporation of such properties in the constitutive equations used to describe the materials will establish a direct link between the chemistry and mechanics of the dentin adhesive interface.

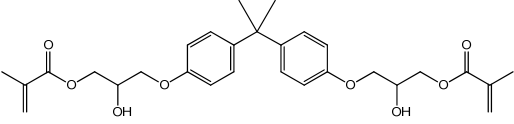
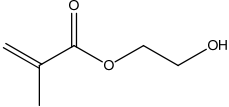
	Co-monomer chemical formula/name	Co-monomer Structure
Hydrophobic dimethacrylate	BisGMA	
Hydrophilic methacrylate	HEMA	

Table 2-1 List of co-monomers

Nomenclature	Mass Fractions		
	BisGMA	HEMA	Water
HB75-37.5	0.15625	0.46875	0.375
HB75-60	0.1	0.3	0.6
HB25-30	0.525	0.175	0.3
HB25-75	0.1875	0.0625	0.75
HB45-16	0.385	0.315	0.3
HB45-33	0.1375	0.1125	0.75
HB45-50	0.385	0.315	0.3

Table 2-2 Composition of over-saturated mixtures for phase separation

(a)

Property	LV's	% Variance	SEE	SEP	Mean value
HEMA	5	99.74	0.01334	0.01407	0.4733
BisGMA	6	99.98	0.004597	0.004809	0.2575
Water	5	99.84	0.01249	0.01323	0.2692

(b)

Property	Lv's	%Variance	SEE	SEP	Mean value
HEMA	6	100	0.00225	0.002348	0.532
BisGMA	8	99.66	0.00063	0.000702	0.008988
Water	5	99.99	0.00238	0.002428	0.459

Table 2-3 Goodness of fit of the calibration between FTIR spectra and component concentrations for (a) hydrophilic rich or aqueous phase (b) hydrophobic rich or resin phase, using PLS1

Nomenclature	HYDROPHILIC-RICH PHASE			Nomenclature	HYDROPHOBIC-RICH PHASE		
	HEMA	BisGMA	Water		HEMA	BisGMA	Water
HB75-37.5-APM	29.8 ± 0.3	BDL	69.2 ± 0.8	HB75-37.5-RPM	55.9 ± 0.1	22.7 ± 0.0	21.8 ± 0.1
HB75-60-APM	22.5 ± 0.2	BDL	76.1 ± 1.1	HB75-60-RPM	50.1 ± 0.1	36.0 ± 0.3	14.5 ± 0.4
HB25-30-APM	8.8 ± 0.4	BDL	90.3 ± 0.1	HB25-30-RPM	21.0 ± 0.2	74.6 ± 1.2	4.8 ± 1.2
HB25-75-APM	3.8 ± 0.1	BDL	95.7 ± 0.5	HB25-75-RPM	13.1 ± 0.3	83.6 ± 0.2	3.5 ± 0.1
HB45-16-APM	18.3 ± 0.8	BDL	81.6 ± 0.6	HB45-16-RPM	33.1 ± 0.3	58.9 ± 0.4	7.9 ± 0.2
HB45-33-APM	16.8 ± 0.7	BDL	83.1 ± 0.8	HB45-33-RPM	37.4 ± 0.3	53.9 ± 0.3	8.6 ± 0.2
HB45-50-APM	14.7 ± 1.2	BDL	85.3 ± 1.1	HB45-50-RPM	39.7 ± 0.4	50.8 ± 0.5	9.5 ± 0.3

BDL: Below detection limit

Table 2-4 Composition of hydrophilic rich or aqueous phases and hydrophobic rich or resin phases obtained from phase separation of oversaturated mixture

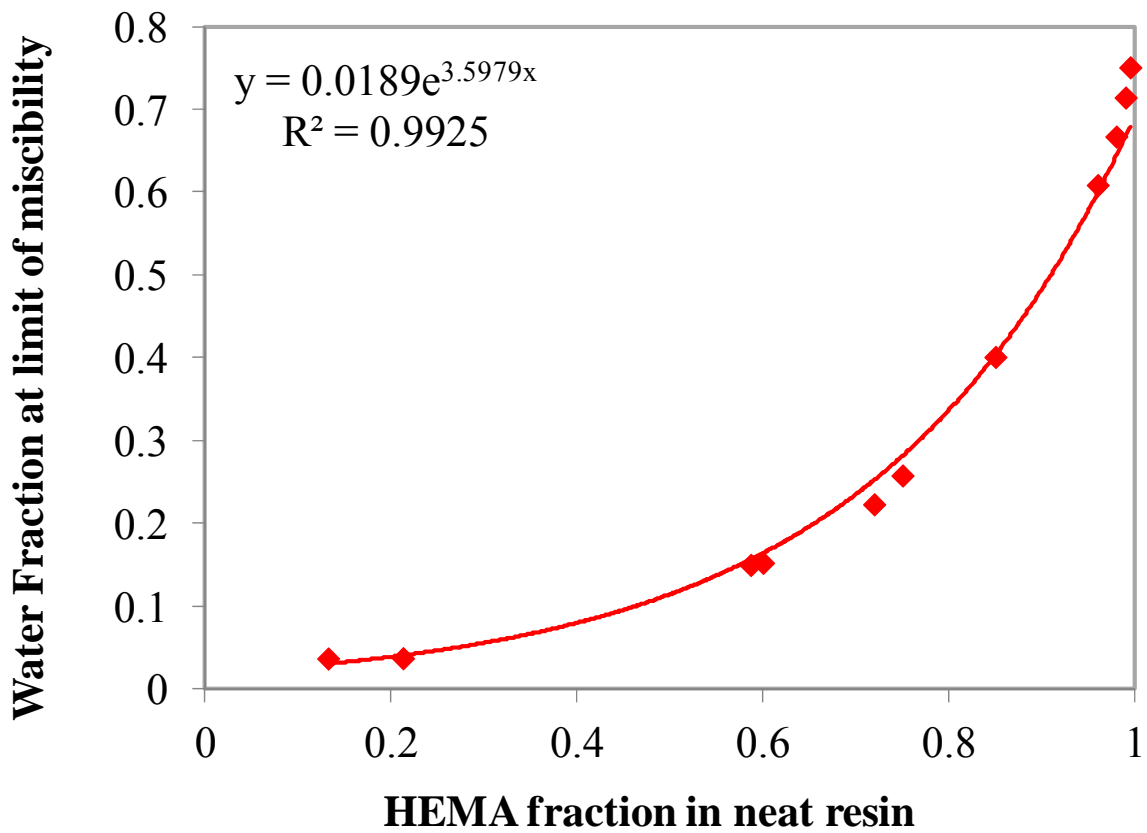


Figure 2-1 Water miscibility as a function of HEMA content in the neat resin

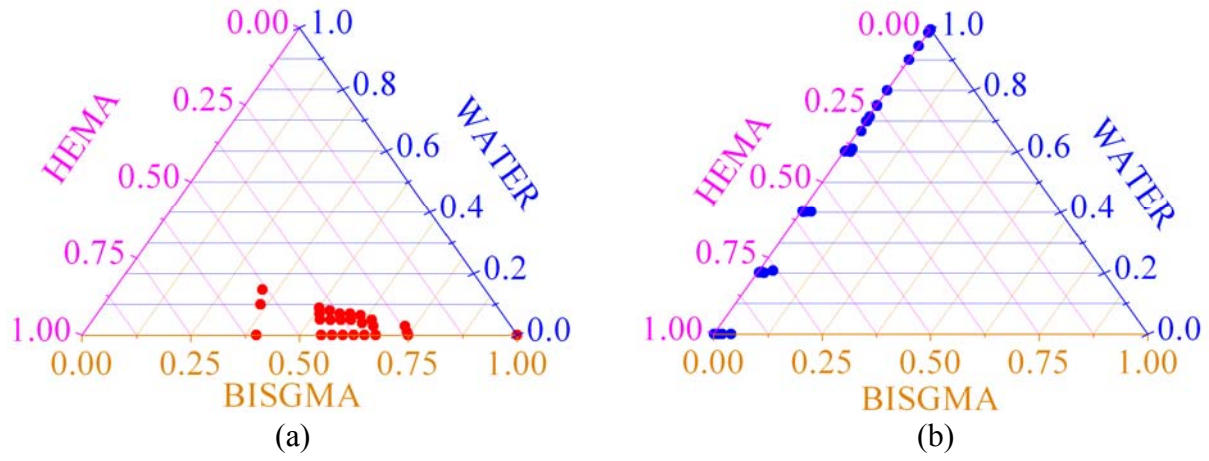


Figure 2-2 Standards for (a) hydrophobic-rich or resin phase (b) hydrophilic-rich or aqueous phase

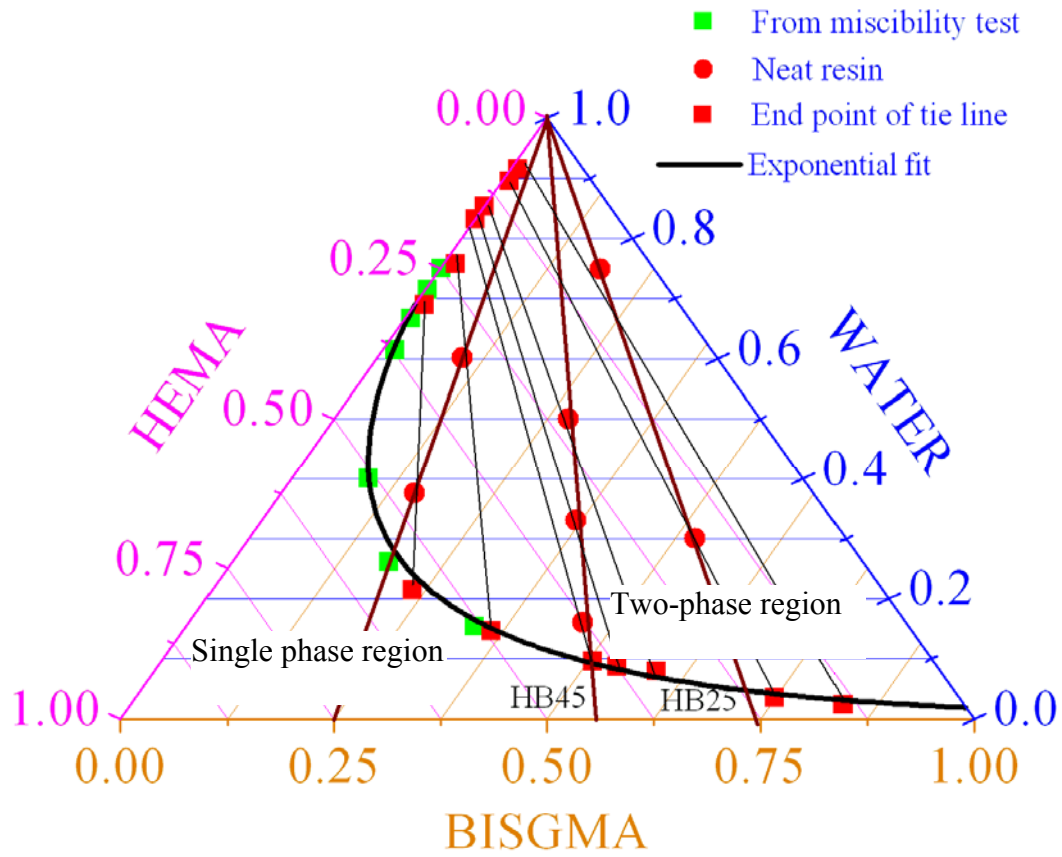


Figure 2-3 Water-monomer phase diagram for the dentin adhesive

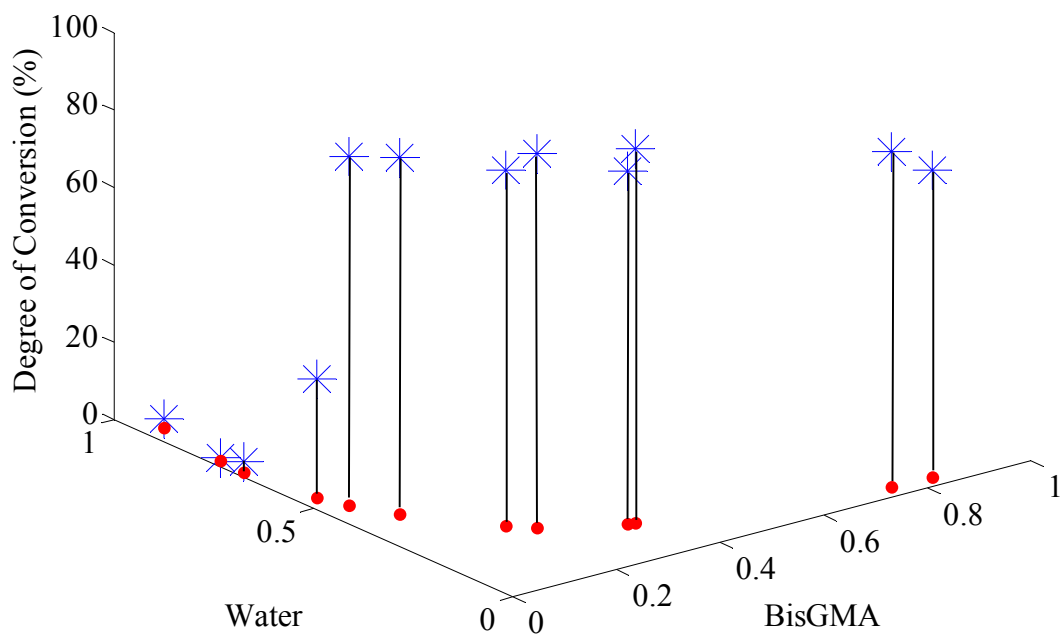


Figure 2-4 Degree of conversion along phase boundary

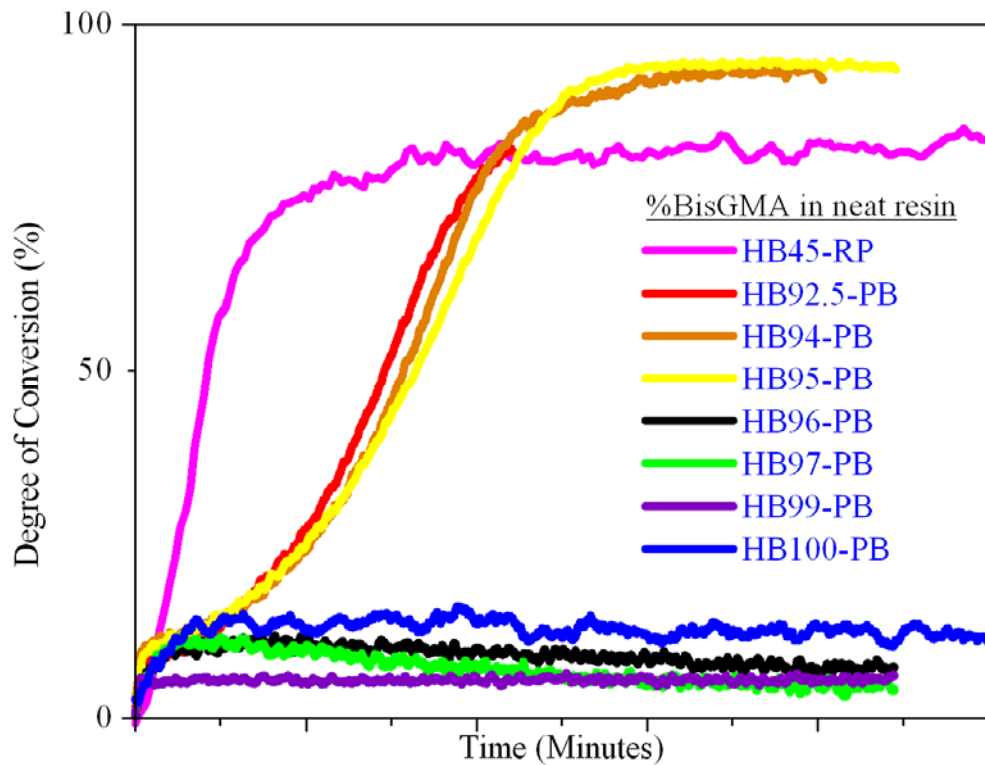


Figure 2-5 Polymerization kinetics along the phase boundary measured using FTIR spectra

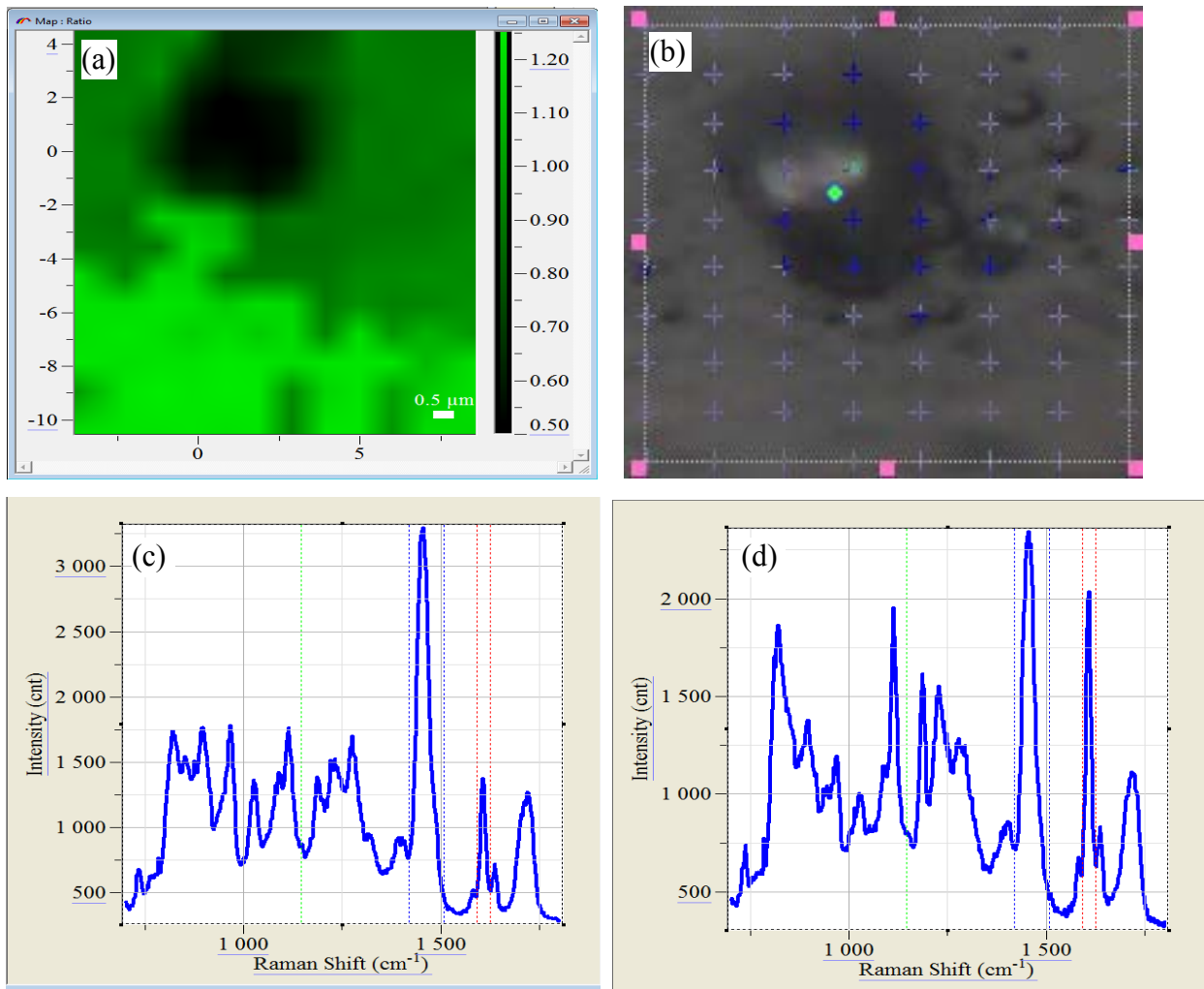


Figure 2-6 Raman imaging of HB45-33 (a) band ratio of aromatic ring to the C-H bond (b) optical visible light image (c) spectrum from region of low band ratio (d) spectrum from region of high band ratio

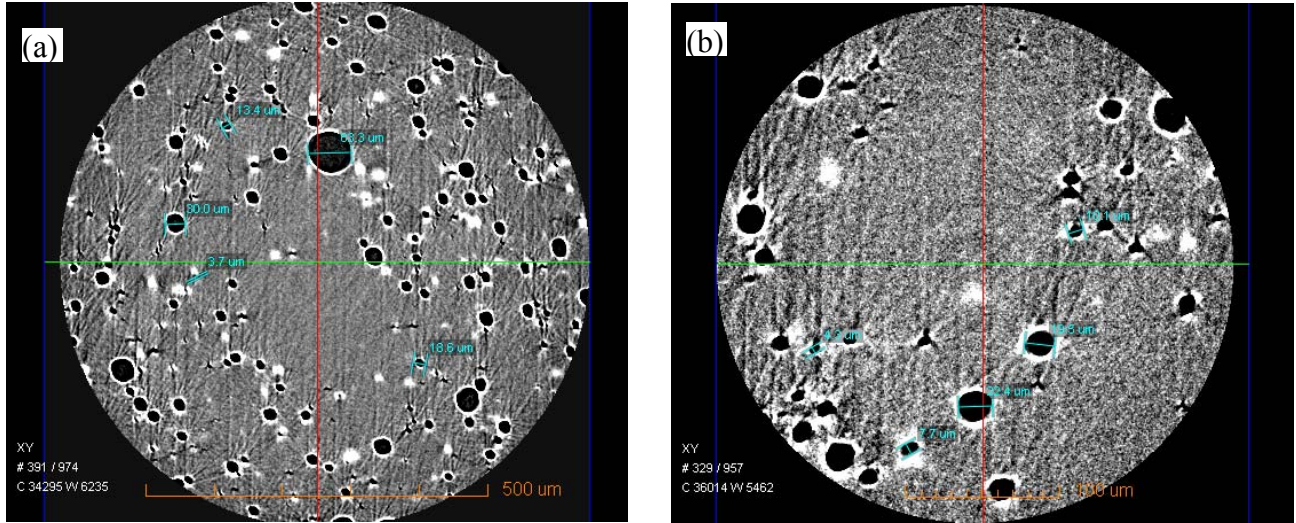


Figure 2-7 Micro-XCT slices of HB45-33 (a) under a magnification of 20X (b) under a magnification of 40X

3 EXPERIMENTAL ANALYSIS AND STRUCTURE-PROPERTY RELATIONSHIPS FOR MODEL DENTIN ADHESIVE POLYMERS FORMED ON THE WATER- ADHESIVE PHASE BOUNDARY

Dentin adhesive systems are composed of hydrophilic and hydrophobic components. During their application to the wet, oral environment, dentin adhesives can experience composition change and phase separation which compromises the quality of the hybrid layer. The various polymer phases formed in the hybrid layer have been classified according to their chemical composition in the monomer state using a ternary adhesive-water phase diagram. These phases have been characterized in terms of their water sorption, crosslink density and elastic modulus in wet and dry states. The structure-property relationships obtained are useful in overall analysis of the dentin-adhesive bond and serve as an aid in the synthesis of novel co-monomers for dentin adhesives.

3.1 Introduction

The lack of effective and durable dentin adhesives is generally considered one of the major problems with the use of composites in direct restorative dentistry. The primary factor in the premature failure of moderate to large composite restorations is secondary decay at the margins of the restorations, which is 3.5 times higher as compared to amalgams (Bernardo, Luis et al. 2007). The composite restoration is achieved by bonding a composite resin to the tooth using an adhesive. It is formed by infiltration of demineralized dentin collagen with adhesive that is photo-polymerized to form a hybrid layer. The ideal hybrid layer is expected to provide a continuous and stable connection between the adhesive and subjacent dentin, while the adhesive

surrounding the demineralized collagen is expected to protect it from degradation by bacterial enzymes, oral fluids and bacteria in the mouth. However, the hybrid layer has been identified to be the weak link in a composite restoration.

Commercial dentin adhesive systems are composed of two monomer components - hydrophilic and hydrophobic. In the monomer state, the adhesive must be hydrophilic enough to achieve integration with the wet, demineralized dentin matrix. The polymerized adhesive must be relatively hydrophobic to avoid swelling and sorption of oral fluids. To provide durable function in the mouth, the optimal dentin adhesive must possess a hydrophilic/hydrophobic balance. In this paper, we study dentin adhesive systems formed using the hydrophilic/hydrophobic monomer pair of HEMA/BisGMA, which is the major component of commercial dentin adhesives. The penetration of the adhesive into the wet demineralized dentin may take place by phenomena such as spontaneous diffusion, and convection resulting from external energy during application, gravity or surface tension. Since the hydrophobic component BisGMA is also more viscous, it transports slower through both diffusion as well as convection, as compared to the hydrophilic component. In the wet, oral environment, the hydrophilic/hydrophobic monomer composition of these dentin adhesives can experience change due to phase separation (Ye, Park et al. 2011, Parthasarathy, Misra et al. 2012) which compromises the quality of the hybrid layer. Hence, subsequent photo-polymerization results in an adhesive-collagen hybrid layer where the composition of the adhesive changes along the depth of the hybrid layer (Zou 2007, Zou, Armstrong et al. 2010). In previous work, we utilized a ternary phase diagram to represent the monomer distribution in the hybrid layer (Ye, Park et al. 2011). Assuming both diffusion and convection to influence to influence the transport of the adhesive monomer into the porous

demineralized dentin, the composition of the adhesive in the hybrid layer can be effectively represented by the phase boundary on the ternary phase diagram.

Our previous work has shown that the mechanical property of the adhesive not only affects the overall bond or shear strength but has a profound influence on the load transfer mechanism at the dentin-adhesive (a/d) interface and its fatigue life (Misra, Spencer et al. 2004, Misra, Spencer et al. 2005, Singh, Misra et al. 2011). In addition, the change in the mechanical property of the adhesive with time can result in a gradual loss of the mechanical integrity of the a/d interface. The absorption of water by the adhesive polymer and leaching of unpolymerized monomer from the adhesive are linked to mechanical softening (Ito, Hashimoto et al. 2005, Wang and Wu 2005) and hydrolytic degradation with time. The visco-plastic properties of the adhesive, in particular, change anomalously with water content under loading (Misra, Singh et al. 2011, Singh, Misra et al. 2011). In an earlier study, we identified that hydrophilicity and crosslink density are two important independent variables which affect the water sorption and diffusion into methacrylate-based crosslinked polymers (Parthasarathy, Misra et al. 2012). There is concern that the effects of such liquid uptake and hydrolytic degradation may lead to a shortened service life of dental restorations. There is also concern of biological effects elicited by the species evolved from dentin resin restorations, thus requiring the effects of liquid uptake to be investigated (Ferracane 2006). Consequently, the development of structure-property relationships along the water-adhesive phase boundary is crucial for an understanding of the mechanical behavior of dentin adhesives formed in the hybrid layer. The aim of the current study is to measure and correlate the following chemo-mechanical properties along the phase boundary with the corresponding chemical composition: water sorption, swelling, equilibrium elastic modulus under wet and dry conditions, crosslink density, failure and viscoelastic properties.

3.2 Materials and methods

3.2.1 Materials

The “model” methacrylate based dentin adhesive monomer formulations were prepared as mixtures of BisGMA (Bisphenol A glycerolate (1 glycerol/phenol) dimethacrylate), 2-hydroxyethylmethacrylate (HEMA, 99%) and deionized water. They were purchased from Sigma Chemical Co., St. Louis, MO, USA. The chemical structures of the co-monomers are shown in Table 1. The monomers were purchased from Sigma Chemical Co., St. Louis, MO, USA. The following three-component visible light photoinitiators (all from Aldrich, Milwaukee, WI) were used in this work: camphoroquinone (CQ, 0.5wt%), ethyl-4-(dimethylamino)benzoate (EDMAB, 0.5wt%) and diphenyliodonium hexafluorophosphate (DPIHP, 0.5wt%) without further purification. The concentration of the photoinitiator component is calculated with respect to the total amount of monomer. All materials were used as received.

3.2.2 Methods

Preparation of neat adhesive resins

Monomer mixtures in the following mass ratios of HEMA to BisGMA were added along with a 3 component photo-initiator system (0.5 mass percent of camphorquinone (CQ), ethyl-4-dimethylamino benzoate (EDMAB) and diphenyl iodonium phosphate (DPIHP)) into brown vials: a) 0.3:0.7 b) 0.6:0.4 c) 0.7:0.3 d) 0.75:0.25 e) 0.8:0.2 f) 0.925:0.075 and g) 0.95:0.05 (HEMA/BisGMA) . The monomer-initiator mixtures in the brown vials were mixed using vortex mixers and shakers until they completely dissolved in each other to give a homogeneous adhesive resin. The neat resins have been represented on the ternary phase diagram using squares as shown in Figure 3-1. A weighing balance with a resolution of 0.01 mg (Mettler Toledo,

X205 dual range) was used to weigh each component and was used for all weight measurements described henceforth.

Determination of water solubility of neat adhesive resins

About 1 g of each neat resin was weighed into a brown vial and water was added in increments of approximately 0.01 g until the mixture is visually observed to be turbid. The percentage of water in the mixture is noted (w_1). The mixture is then back-titrated using the neat resin till the turbidity disappears and the percentage of water in the mixture is noted (w_2). The water miscibility is calculated as the average of w_1 and w_2 . The procedure can be represented on the ternary phase diagram as moving along the line of constant monomer ratio starting at the neat resin (square point) towards the intersection of the phase boundary with the line, which represents the limit of miscibility for that monomer ratio.

Preparation of polymer samples from monomer-water formulations on phase boundary

Water equivalent to about 2-3 percentages below the miscibility limit is added to each neat resin and mixed till fully dissolved. The water content was chosen to lie within the miscibility limit to prevent formation of any defects from polymerization induced phase separation at the scale of study. The composition of these formulations has been represented using circles on the ternary phase diagram as shown in Figure 3-1. Square beams with a side of 1 mm and a length of at least 10 mm were prepared for each formulation by casting these prepared adhesive resins into glass-tubing molds (Fiber Optic Center Inc, #CV1012, Vitrocom Round Capillary Tubing of Borosilicate Glass). The resins were injected into the tubing using a micro-pipette and light polymerized with a LED light curing unit of intensity 250 mW/cm^2 and area 6.25 mm^2 for 9s (LED Curebox, Prototech, and Portland, OR). The polymerized samples were stored in dark at room temperature for two days to provide adequate time for post-cure polymerization. The

samples were subsequently extracted from the glass tubing and stored in a vacuum oven in the presence of a drying agent (freshly dried silica gel) at 37°C.

Degree of Conversion

The degree of conversion (DC) was determined by Raman spectrometer as described previously (Park, Ye et al. 2009). In brief, LabRAM ARAMIS Raman spectrometer (LabRAM HORIBA Jobin Yvon, Edison, New Jersey) was used with a HeNe laser ($\lambda=633$ nm, a laser power of 17 mW) as an excitation source. The instrument settings were as follows: 200 μm confocal hole, 150 μm wide entrance slit, 600 gr/mm grating, and 10x objective Olympus lens. Data processing was performed using LabSPEC 5 (HORIBA Jobin Yvon). The samples were mounted on a computer-controlled, high-precision x-y stage. To determine the DC, spectra of the unpolymerized resins and rectangular beam samples were acquired over a range of 700 – 1800 cm^{-1} . The changes of the band height ratios of the aliphatic C=C double bond peak at 1640 cm^{-1} to the aromatic C=C at 1610 cm^{-1} (phenyl) in both the cured and uncured states were monitored. The DC was calculated as follows, based on the decrease in the intensity of band ratios before and after light curing.

$$DC(\%) = \left(1 - \frac{R_{\text{cured}}}{R_{\text{uncured}}} \right) \times 100 \quad (3.1)$$

where R = band height at 1640 cm^{-1} /band height at 1610 cm^{-1} . All experiments were carried out in triplicate over each sample area and across samples and the results were averaged.

Mechanical testing

Mechanical tests were performed using a three-point bending apparatus with 10 mm beam span on a Bose Electroforce 3200 tester. Loading was applied at a rate of 0.001 mm/sec or equivalently in terms of the elastic strains at the rate of 75 $\mu\text{/sec}$. For the mechanical test in dry condition, the polymer beam samples were used as prepared. For wet testing, the samples were

stored in water at 37°C for at least 5 days and up to 15 days until the samples were completely saturated and no further change in mass was observed. Average stress-strain curves were obtained and used to calculate the elastic modulus from the linear region using at least three samples for each formulation under dry and wet conditions, respectively.

Dynamic Mechanical Analysis

The measurement of glass transition temperature and apparent rubbery modulus was carried out using dynamic thermomechanical analysis (DMA Q800, TA Instruments, New Castle, USA) in a 3-point bending configuration. The analysis has been described previously (Park, Ye et al. 2009). The frequency used to measure the storage modulus was 1 Hz with amplitude of 15 μm and a pre-load of 0.01 N. The storage modulus was measured across 0°C to 250°C using a temperature sweep conducted at 3°C/min. The glass transition temperature was identified from the peak of the loss tangent – temperature curve. The storage modulus decreased with temperature and reached an asymptote, which was taken to be the apparent rubbery modulus of the polymer.

Determination of crosslink density

Assuming the adhesive polymers to obey Flory's rubber elasticity theory (Flory 1953), the effective crosslink density, ν_e in moles/ m^3 was calculated as shown below.

$$\nu_e = \frac{E'}{3RT_g} \quad (3.2)$$

where E' is the apparent rubbery modulus, T_g is the glass transition temperature of the polymer, and the universal gas constant $R = 8.31 \text{ J K}^{-1} \text{ mol}^{-1}$.

The stoichiometric crosslink density ν_s in moles/m³ was calculated from the mole percentage of the crosslinker and the degree of conversion as follows. The degree of conversion was assumed to be uniform for BisGMA and HEMA segments.

$$\nu_s = \frac{100b(DC)\rho}{M_b} \quad (3.3)$$

Where b is the percentage of BisGMA in the polymer, DC is the percentage degree of conversion, ρ is the polymer density and M_b is the molar mass of BisGMA.

Determination of LogP

The LogP values (ratio of solubility in octanol to solubility in water) for each of the comonomers and the model adhesives are determined using ChemBioDraw Ultra 12.0 (CambridgeSoft from Perkin Elmer). The LogP value for each model adhesive formulation is determined using the mole fraction-average of individual monomer values as shown below:

$$\text{LogP}_{Total} = x_{HEMA} \text{LogP}_{HEMA} + x_{BisGMA} \text{LogP}_{BisGMA} + x_{co-monomer} \text{LogP}_{co-monomer} \quad (3.4)$$

Alternatively, the overall LogP could also be calculated based on the mass fractions of each monomer in the formulation.

Absorption Experiment

Multiple beam specimens are used to study the water sorption behavior of each formulation. Distilled, deionized water (HPLC grade, W5SK-4, Fisher Scientific, Fair Lawn, NJ, USA) is used throughout the experiments. The beam specimens are placed into a vacuum chamber for drying until a constant weight w_1 is obtained. The specimens are then immersed in water and stored at room temperature. At fixed time intervals (1, 2, 3, 5, 7, 11, 24, 36, 48, 60, 72, 108, 144, 216, and 324h), the specimens are retrieved, blotted dry to remove excess liquid, weighed in air (w_2), and returned to the liquid bath. If the specimens are not yet saturated (attain constant

mass), data is collected at additional intervals spaced 24 hours apart till constant mass is reached. After these measurements were complete, the specimens are dried in the vacuum chamber until a constant weight (w_3) was obtained. The values (%) for mass change (W_{mc}), solubility (W_{su}) and water sorption (W_{sp}) were calculated as follows:

$$W_{mc} (\%) = \frac{w_2 - w_1}{w_1} \quad (3.5)$$

$$W_{su} (\%) = \frac{w_1 - w_3}{w_1} \quad (3.6)$$

$$W_{sp} = W_{mc} + W_{su} \quad (3.7)$$

Swelling Experiment

The beam specimens used in the absorption experiment described above were placed into a vacuum chamber for drying until a constant mass was obtained. The specimens were then weighed in air (w_{1a}) and weighed under distilled, deionized water (w_{1b}). The measurement under water is performed within about 10 seconds to avoid any absorption of water during the process. The weight under water is equal to the weight in air minus the buoyancy force exerted by the water. The specimens were then immersed in water and stored at room temperature. At fixed time intervals (5 minutes, 10 minutes, 20 minutes, 40 minutes, 1 hour, 2 hours, 3 hours, 5 hours, 7 hours, 10 hours, 24 hours, 36 hours, 48 hours and 72 hours), the specimens were retrieved, blotted dry to remove excess liquid, weighed in air (w_{2a}), weighed in water (w_{2w}), and returned to the liquid bath. If the specimens are not yet saturated (attain constant mass), data is collected at additional intervals spaced 24 hours apart till constant mass is reached. The volume of the sample is calculated using the weights in air and water as shown below.

$$V_n = \alpha \frac{w_{na} - w_{nw}}{\rho_w - \rho_a} \quad (3.8)$$

where V_n is the volume of the sample, w_{na} is the weight of the sample in air, w_{nw} is the weight of the sample in water for the n^{th} measurement, and $\alpha=0.99985$ is a factor to account for air buoyancy. $\rho_w=1 \text{ g/cm}^3$ and $\rho_a=0.0012 \text{ g/cm}^3$ are the densities of water and air respectively. The values (%) for mass change in air (W_{ma}) and volume change expressed using the Jacobian of deformation, J was calculated as follows:

$$W_{mc} (\%) = \frac{w_{2a} - w_{1a}}{w_{1a}} \quad (3.9)$$

$$J_n = \frac{V_n}{V_1} \quad (3.10)$$

3.3 Results

The concentrations of water, BisGMA and HEMA in any of the monomer formulations in Table 3-2 are related via the ternary phase boundary shown in Figure 3-1; accordingly the chemical composition of a monomer formulation can be defined by one of the three components. We also know that crosslink density and hydrophilicity have been determined to be the key factors which determine the chemo-mechanical behavior of methacrylate-based polymers (Parthasarathy, Misra et al. 2012). For these reasons, we choose to study the results with respect to the percentage BisGMA in the formulations.

3.3.1 Degree of Conversion, Density, partition coefficients and Density of Leachables

Table 3-1 gives the degree of conversion (DC), polymerized adhesive density, and partition coefficient of water and density of leachables in polymerized adhesive. The DC of all the polymerized dentin adhesives was found to be in the range 87% to nearly 100%. As the free radical polymerization proceeds, microgels of polymer form with certain amount of dissolved monomer and water within them and are separated from the remaining monomer-water mixture.

Further propagation of the polymerization reaction is limited by the diffusion of the reactive species from the monomer-water mixture into the microgel, which depends on the viscosity of the resin. The presence of water in the monomer resin decreases the viscosity, thereby increasing the propagation of the polymerization reaction and the degree of conversion.

The densities of all the dentin adhesives were close to 1.2 g/cm^3 . The LogP values have been calculated as described earlier, and vary from 1.07 to 1.80. They are used as an indicator of hydrophilicity. The solubility values range from 0.00 to 4.82%. They are found to be uncorrelated to the degree of conversion values. However, a weak trend of decrease in solubility with LogP can be observed. This is consistent with the fact that more hydrophilic formulations are also more likely to leach out. Uniform samples were obtained as shown by the small standard deviation of all measured quantities.

3.3.2 *Mechanical Properties*

Figure 3-2 shows a comparison of the elastic moduli of the polymers in dry, wet and rubbery elastic conditions. The elastic moduli under dry and wet conditions are measured at room temperature (25°C), while the rubbery modulus is measured at the glass transition temperature. The elastic moduli in both dry and wet conditions show an increasing trend with the percentage of BisGMA in the monomer formulation. Under dry conditions, the elastic modulus increases non-linearly with BisGMA content. Under wet conditions, the modulus is negligibly small up to about 20% BisGMA and follows a sigmoidal relationship with the BisGMA content in the polymer. The rubbery modulus also increases with BisGMA content. For up to about 20% BisGMA content, we observe that the rubbery modulus is in the neighborhood of the modulus under wet conditions; beyond this value, the elastic modulus in the wet condition follows a different slope with BisGMA content.

In the dry condition, the strong hydrogen bonding between HEMA and BisGMA polymer segments is responsible for the elastic stiffness. The plasticizing effect of water is responsible for lowering the elastic modulus in the wet condition. The polymer-solvent interaction responsible for plasticization is closely related to the water solubility in the monomer. Dissolution of HEMA monomer in water is energetically feasible and takes place spontaneously by breaking of HEMA-HEMA hydrogen bonds and formation of HEMA-water hydrogen bonds. However, dissolution of BisGMA in water is not energetically feasible because of the hydrophobic effect caused by the bulky aromatic groups and the large non-polar part of the BisGMA molecule. In the wet condition, when the percentage of BisGMA is below 20, the adhesive behaves like an elastomer because the BisGMA segments are too far from each other to interact via hydrogen bonding. However, at BisGMA contents greater than 20%, the BisGMA segments interact with each other through hydrogen bonds which are not spontaneously plasticized by water due to the hydrophobic effect. Due to the presence of these BisGMA-BisGMA hydrogen bonds, the behavior of the polymer in the wet condition is much stiffer than that predicted by rubbery elasticity. Correlations between wet moduli and solubility parameters have been obtained for dentin adhesives (Hosaka, Tagami et al. 2007). As the BisGMA content increases further, the polymer approaches a network structure.

Figure 3-3 (a) and (b) show the apparent stress strain behavior in both dry and wet conditions of the polymer formulations along the water-adhesive phase boundary. The increasing yield stress with BisGMA content is because of increasing density of hydrogen bonds as well as covalent crosslinks. In the dry condition, we observe that the polymers with an intermediate quantity of BisGMA show significant plastic deformation at yield for the formulations; they experience ductile failure. The polymers with either very low or very high percentage of BisGMA

experience brittle failure. Figure 3-3(c) shows the variation of apparent failure strain with BisGMA in the dry condition. The apparent failure strain increases, peaks and then falls with increase in BisGMA content. Typically, glassy polymers fail by a combination of mechanisms: bond breaking, which is typically associated with brittle failure and microshear band formation, which is typically associated with ductile failure and takes place by a viscous flow process (Haward and Young 1997). Bond breakage appears to be the primary mode of failure between HEMA segments, as indicated by the relatively brittle failure for the polymers with low BisGMA contents. For very high BisGMA contents, the scope for viscous flow is very less because of decreased free volume and high covalent crosslink density; hence the mode of failure is brittle. The variation of apparent failure strain with BisGMA content is similar to that of loss modulus with BisGMA (see section 3.4). The loss modulus also represents the extent of energy absorbed by viscous flow; thus it is correlated to the extent of ductile failure. From Figure 3-3 (e), we observe two transitions, one as a shoulder in the loss tangent graph, and the other at a much higher temperature around 160°C. The significance of the shoulder increases with increase in BisGMA concentration. We hypothesize that the inter-molecular hydrogen bonds between HEMA segments, which control the behavior at low BisGMA concentrations are well below their glass transition (~160°C) at room temperature. Thus, we observe highly brittle failure at low BisGMA concentrations. On the other hand, the second transition is observed in polymers with higher BisGMA concentrations. This transition is much closer to room temperature; hence is strongly associated with viscous flow at yield as opposed to the glass transition associated with the hydrogen bonds. Therefore, the corresponding polymer samples exhibit ductile failure. The relation between the yield stress and transition processes have been studied earlier for other polymers (Bauwens 1972).

Figure 3-3 (d) shows the variation of apparent failure strain with BisGMA in the wet condition. In the wet state, the HEMA-HEMA hydrogen bonds have been dissolved or plasticized by water and their contribution to the yield stress is lost, thus decreasing its magnitude. As the BisGMA content decreases, the stress-strain behavior increasingly becomes like that of an elastomer at low BisGMA contents. At higher BisGMA contents, the viscous flow phenomenon is still present due to the hydrogen bonding between BisGMA segments; for HB80 onwards, the viscous flow is negligible, the polymer chains are completely mobile and the behavior is close to that of an elastomer.

3.3.3 Crosslink density

Figure 3-8 shows both the effective crosslink density ν_e and the stoichiometric crosslink density ν_s . Both these measures increase with BisGMA since it is the crosslinking monomer, but we observe that the stoichiometric prediction based on the degree of conversion is close to the values predicted from the rubbery modulus for BisGMA content up to about 20%, showing that the material is indeed rubbery elastic. For BisGMA content greater than 20%, the effective crosslink density is much higher than the stoichiometric crosslink density. Several reasons could contribute to this phenomena: a) the restriction of chain motion due to strong non-covalent interactions between the BisGMA segments b) the contribution of the non-covalent interactions to the stiffness c) the decrease in free volume for chain motion due to large size of BisGMA segments and d) the inadequacy of the affine rubbery elasticity as the chain length decreases with increase in BisGMA content.

3.3.4 Water Sorption and Swelling

Figure 3-4 (a) and (b) show the variation in water sorption and swelling with time for all the polymer formulations. Figure 3-4 (c) and (d) show the variation in equilibrium water sorption and swelling with BisGMA content. We observe that the equilibrium water sorption and swelling decrease with BisGMA content. The water sorption values range from more than 70% in the most hydrophilic polymer (7.5% BisGMA) to less than 10% in the most hydrophobic polymer (70% BisGMA). The decrease in water sorption can be well fit ($R^2=0.97$) by an exponential function. The increased stiffness of the polymer with BisGMA under wet conditions, as well as the decrease in hydrophilicity with BisGMA content are responsible for the reduction in swelling and water sorption. The reduction in water sorption for methacrylate-based polymers with increased stiffness and decreased hydrophilicity has been shown earlier (Parthasarathy, Misra et al. 2012). Further, we observe that the rate of water sorption and swelling also decrease with BisGMA content i.e. the diffusion coefficient of water in the polymer decreases with BisGMA content. Since this decrease again corresponds to increased stiffness and reduced hydrophilicity with BisGMA, it is qualitatively consistent with the Eyring's transition state theory (Eyring 1936, Glasstone, Laidler et al. 1941, Hirschfelder, Curtiss et al. 1954, Eyring and Ree 1961, Park and Crank 1968), where the free energy for activation of diffusion depends on the hydrophilicity and network stiffness (Krongauz 2010), which is a function of interaction density of covalent and non-covalent bonds.

The solubility values range from ~0% at 85% BisGMA to 4.74% at 5% BisGMA. The decrease in solubility with increase in BisGMA content, shown in Figure 3-4(e), could be attributed to increase in hydrophilicity since hydrophilic leachables are more easily leached out in water (Parthasarathy, Misra et al. 2012). The solubility is not significantly influenced by the degree of

conversion since the degree of conversion decreases with BisGMA content while the solubility also decreases with BisGMA content. This also shows that a majority of the unpolymerized monomer is likely to be BisGMA rather than HEMA.

3.3.5 *Viscoelastic Properties*

From Figure 3-6(a), we observe that the storage modulus increases rapidly from 7.5 to 20% BisGMA and then stays nearly constant. Figure 3-6(b) shows that the loss modulus goes through a peak and then decreases with BisGMA content. The loss tangent $\tan \delta$, given by the ratio of the loss to storage modulus and shown in Figure 3-6(c) decreases with BisGMA content. The increase in storage modulus is for similar reasons as the increase in elastic modulus (see Figure 3-2), due to increase in non-covalent interactions and covalent bonds with BisGMA. It is interesting to observe that the increase in storage modulus beyond 20% BisGMA is minimal while the increase in elastic modulus continues up to about 70% BisGMA. This difference is likely due to the fact that the storage moduli were measured at a frequency of 1 Hz and amplitude 15 μm i.e. at a rate of loading of 15 $\mu\text{m}/\text{sec}$, which is 15 times faster than the 1 $\mu\text{m}/\text{sec}$ loading rate used to obtain the elastic moduli from three-point bending. At higher rate of loading, the polymer chains are less mobile and contribute more to the storage modulus.

Since we study the viscoelastic properties at 25°C, which is well below the glass transition temperature, the viscous contribution arises from the small scale movement of the polymer chains, which depends on the available free volume (Schapery 2000, Boudenne, Ibos et al. 2011). The available free volume decreases with increasing BisGMA content because of increased interaction density and the steric effects from the large size of BisGMA; hence we observe a decrease in the loss tangent. This increase in interaction density and decrease in available free volume for chain motion is likely nonlinear with BisGMA; the effects are steep up

to about 20% BisGMA and shallower beyond. In support of this argument, the storage modulus and the elastic modulus also have a steeper rise up to about 20% BisGMA.

The loss modulus depends on the mobility of polymer chains and the frictional resistance to rearrangement of polymer chains under applied stress or strain. The initial increase in the loss modulus up to about 20% BisGMA reflects increasing frictional resistance when sufficient mobility is available for the chains to rearrange. The decrease in loss modulus beyond about 20% BisGMA is because the chains become increasingly immobile with increasing BisGMA content, which is also reflected in the increasing elastic modulus (see Figure 3-2).

3.3.6 Glass Transition Temperature

The glass transition temperature, shown in Figure 3-6(a), increases with percentage BisGMA and goes through a maximum before decreasing. The glass transition occurs at the temperature when a majority of the polymer chains have the maximum free volume and mobility while the material is still viscoelastic. Beyond the glass transition, the material becomes rubbery and the chain mobility contributes to rubbery elasticity, rather than a viscous component of viscoelasticity.

Initially, as BisGMA increases, the mobility of polymer chains is suppressed due to steric effects and increase in non-covalent and covalent bonds leading to an increase in T_g . However, with further increase in BisGMA content, a larger fraction of the polymer becomes bound together by covalent crosslinks and the chain length of the mobile portions decreases. Therefore, the glass transition of the polymer requires lesser energy and the polymer becomes rubbery at a smaller temperature. The decrease in proportion of mobile chains is also reflected in the decrease in peak loss tangent shown in Figure 3-6(b). Corresponding to the increased covalent crosslink density, we note that the rubbery modulus is higher at higher BisGMA contents (see Figure 3-2).

3.4 Conclusion

The properties of the model dentin adhesive polymer formed along the phase boundary were studied as a function of their composition, or position on the ternary water-adhesive phase diagram. A dependence of both elastic and viscoelastic mechanical properties on the BisGMA content, in other words the polymer phase composition was observed. The plasticizing effect of water on these polymers has been explained in terms of the covalent crosslink density. The polymer phase composition determines the fundamental properties of crosslink density and hydrophilicity, which in turn govern the mechanical and sorption behavior.

While the water-adhesive phase diagram provides a comprehensive description of the water-compatibility and solubility of the monomer adhesive resin, the structure-property relationships provide the corresponding chemo-mechanical properties. Such a database could be used to identify key properties and work with the chemical structure to improve mechanical behavior in wet conditions while maintaining or improving the monomer solubility and phase-separation behavior. As part of future work, a micro-poro-mechanical model will be developed to describe the swollen equilibrated state of these polymer phases. The diffusion coefficients for the polymer phases along the phase boundary will also be obtained. These properties further build upon the material database required to model the behavior of a hybrid layer.

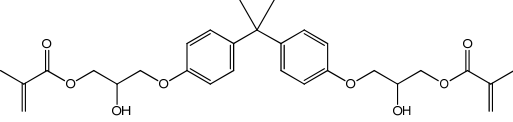
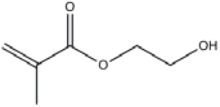
Co-monomer chemical formula/name	Co-monomer Structure
BisGMA	
HEMA	

Table 3-1 List of co-monomers

Purity: (a) = 98%, (b) 95%, and (c) 85% (mixture of isomers), all other monomers are reagent grade.

Supplier: ¹ Sigma Chemical Co., St. Louis, MO, USA.

	BisGMA	HEMA	Water
HB15	83.3	14.70	2.00
HB30	66.51	28.51	4.98
HB45	50.05	40.95	9.00
HB60	34.8	52.20	13.00
HB70	24.45	57.05	18.50
HB75	19.5	58.50	22.00
HB80	14	56.00	30.00
HB92.5	3.75	46.25	50.00
HB95	2.2	41.80	56.00

Table 3-2 Percentage composition of the formulations on the phase boundary

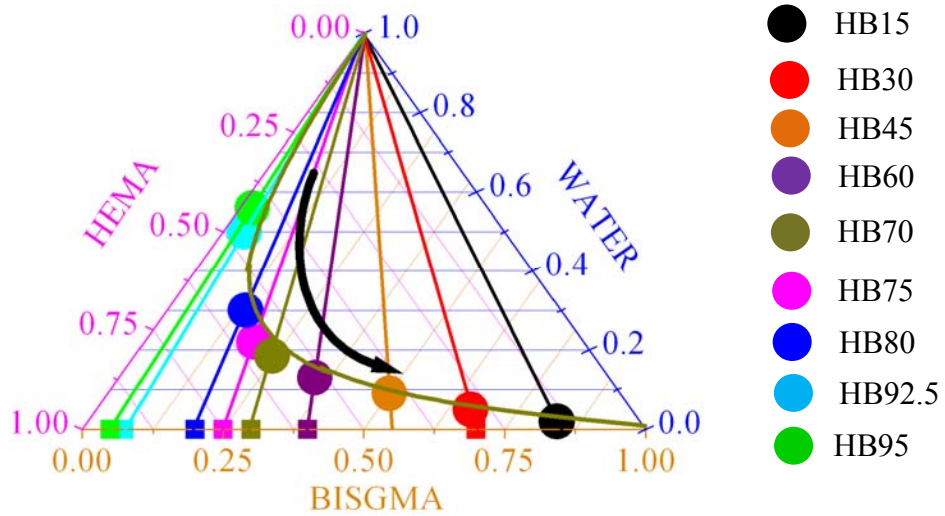


Figure 3-1 Representative adhesive monomer formulations identified on the phase boundary of the water-adhesive ternary phase diagram. The circles represent the formulations prepared close to the phase boundary. The squares represent the corresponding neat formulations.

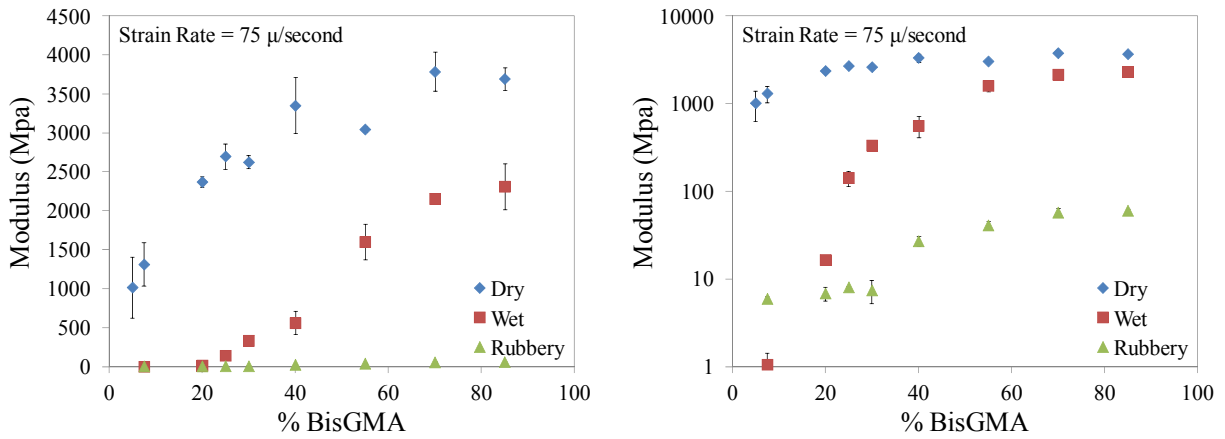


Figure 3-2 Elastic moduli in dry and wet condition at 25°C and rubbery modulus versus the percentage of BisGMA in the corresponding neat monomer formulation (a) linear scale (b) semi-log scale

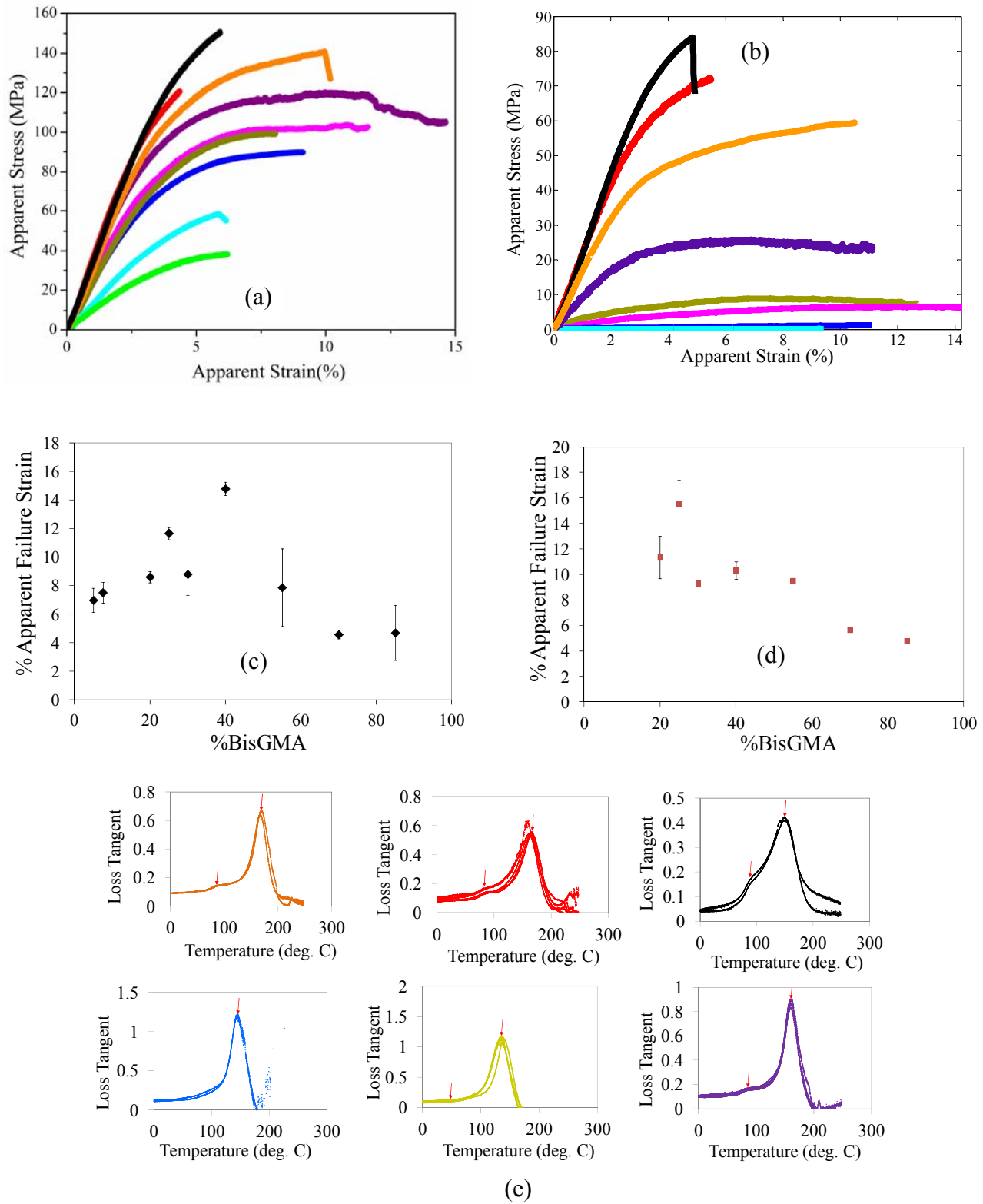


Figure 3-3 Apparent stress strain behavior in (a) dry and (b) wet condition at 25°C, apparent failure strain in (c) dry and (d) wet condition, (e) loss tangent over temperature sweep

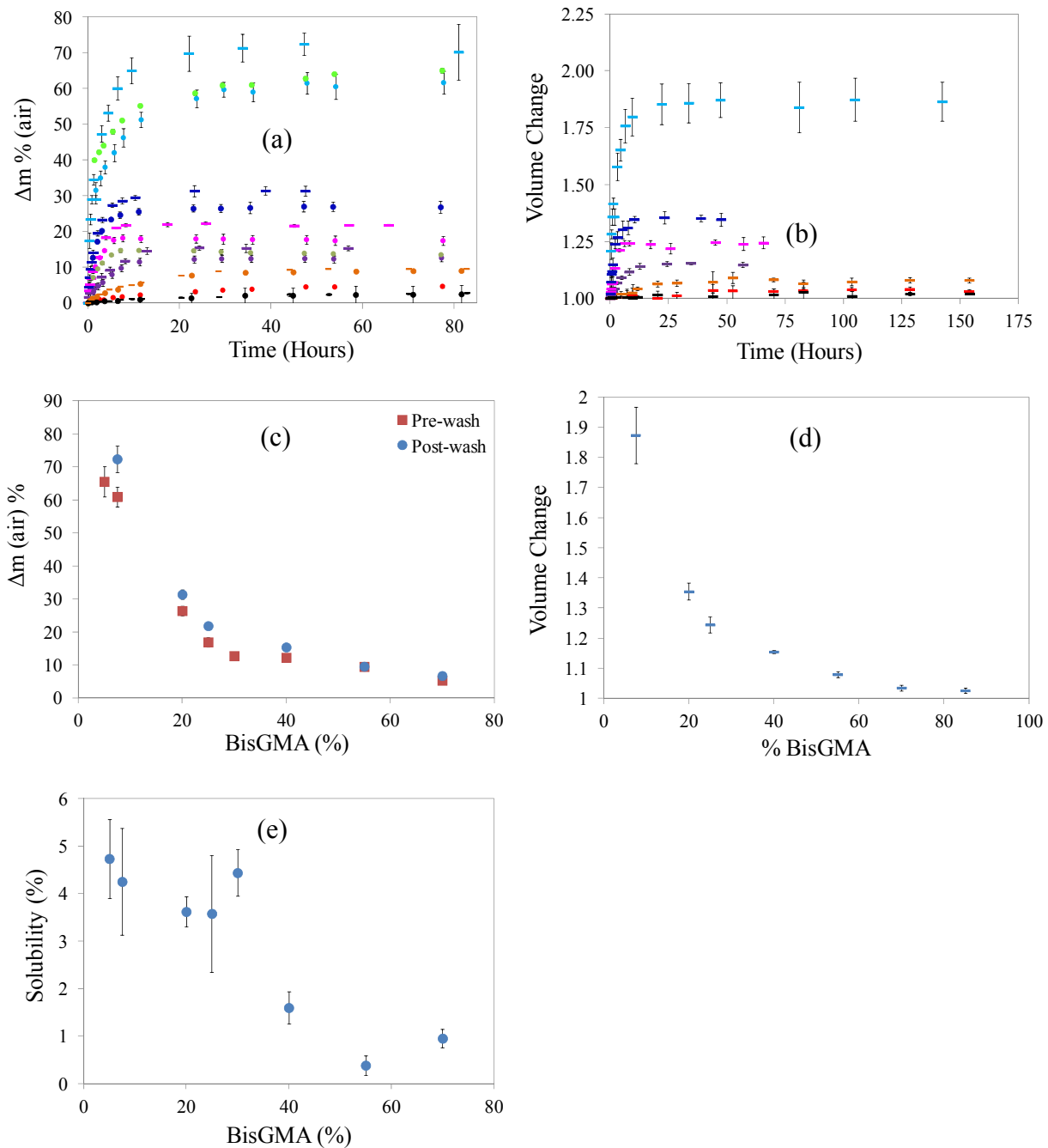


Figure 3-4 Variation of (a) mass change with time, (b) volume change with time, (c) mass change in BisGMA, (d) volume change and (e) solubility with BisGMA under water absorption

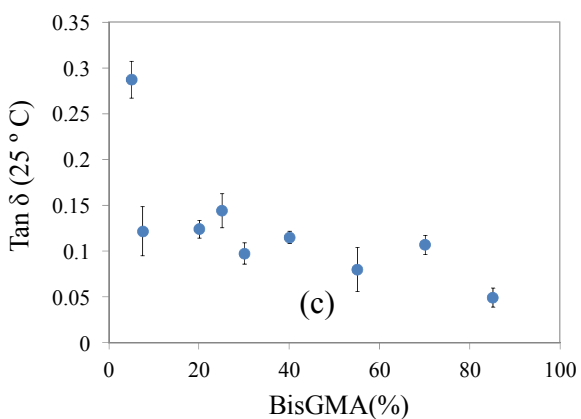
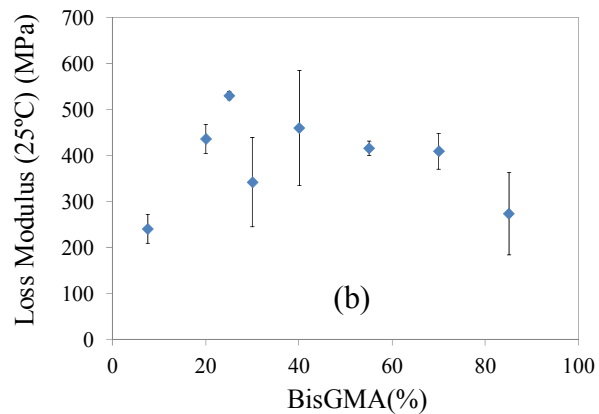
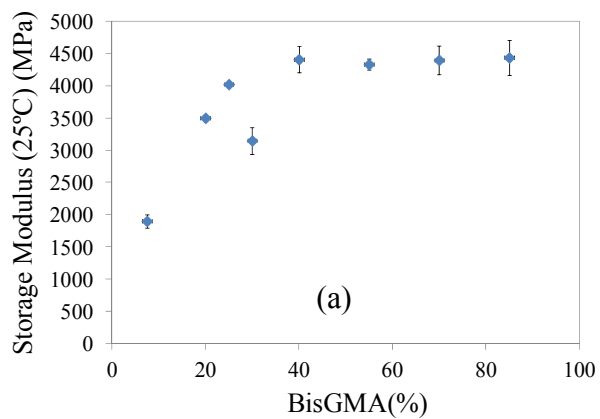


Figure 3-5 Variation in viscoelastic properties of the polymer formulations with respect to BisGMA content.

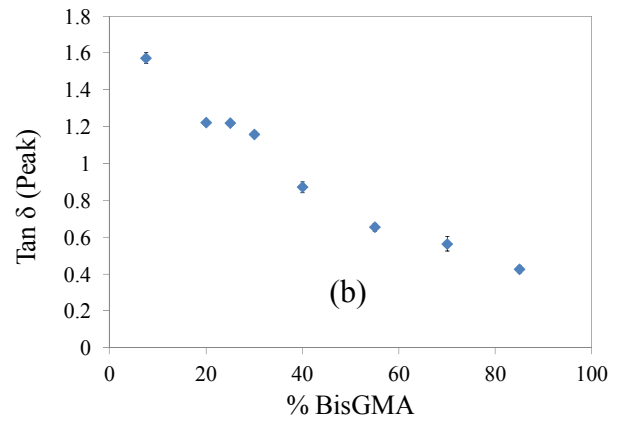
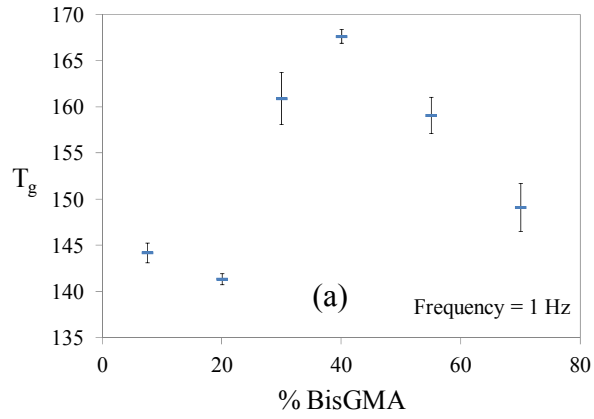


Figure 3-6 (a) Glass transition temperature and (b) Peak loss tangent versus BisGMA (%) in the polymer formulation

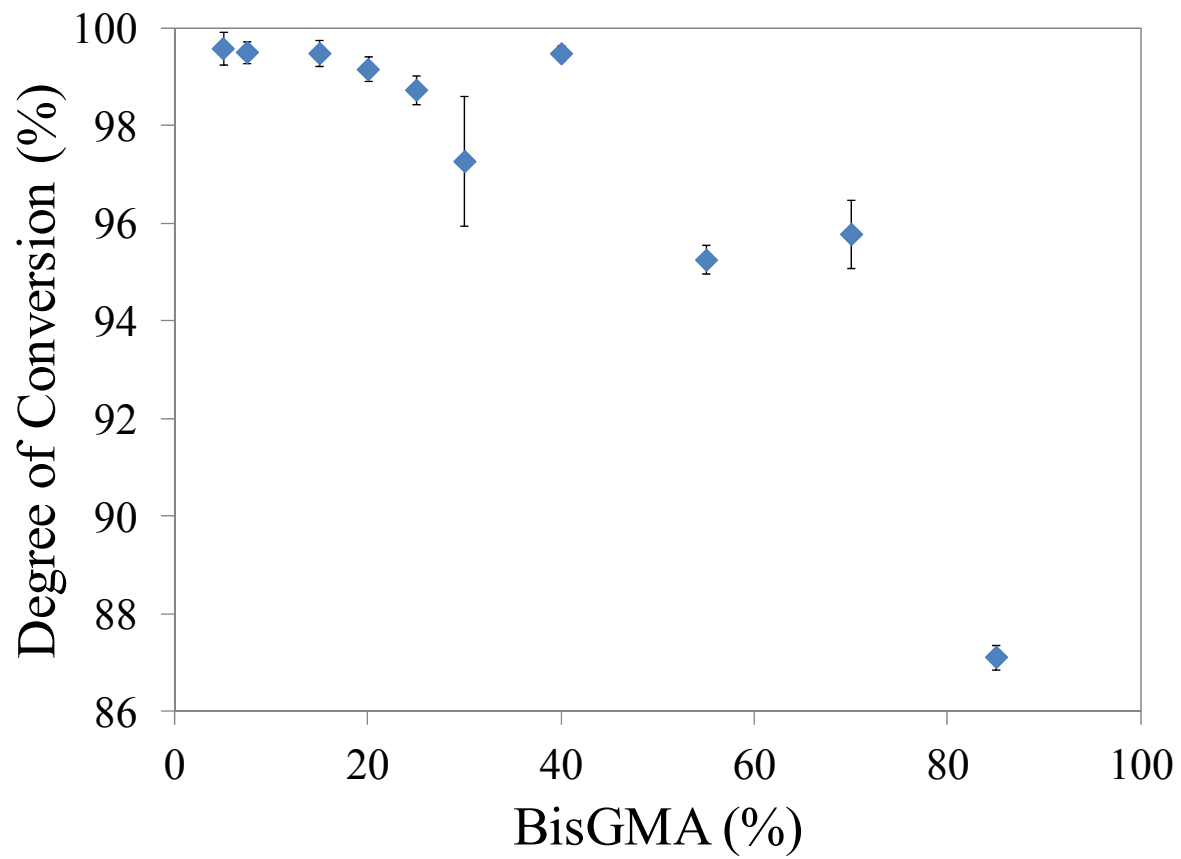


Figure 3-7 Degree of conversion versus BisGMA (%) in the polymer formulation

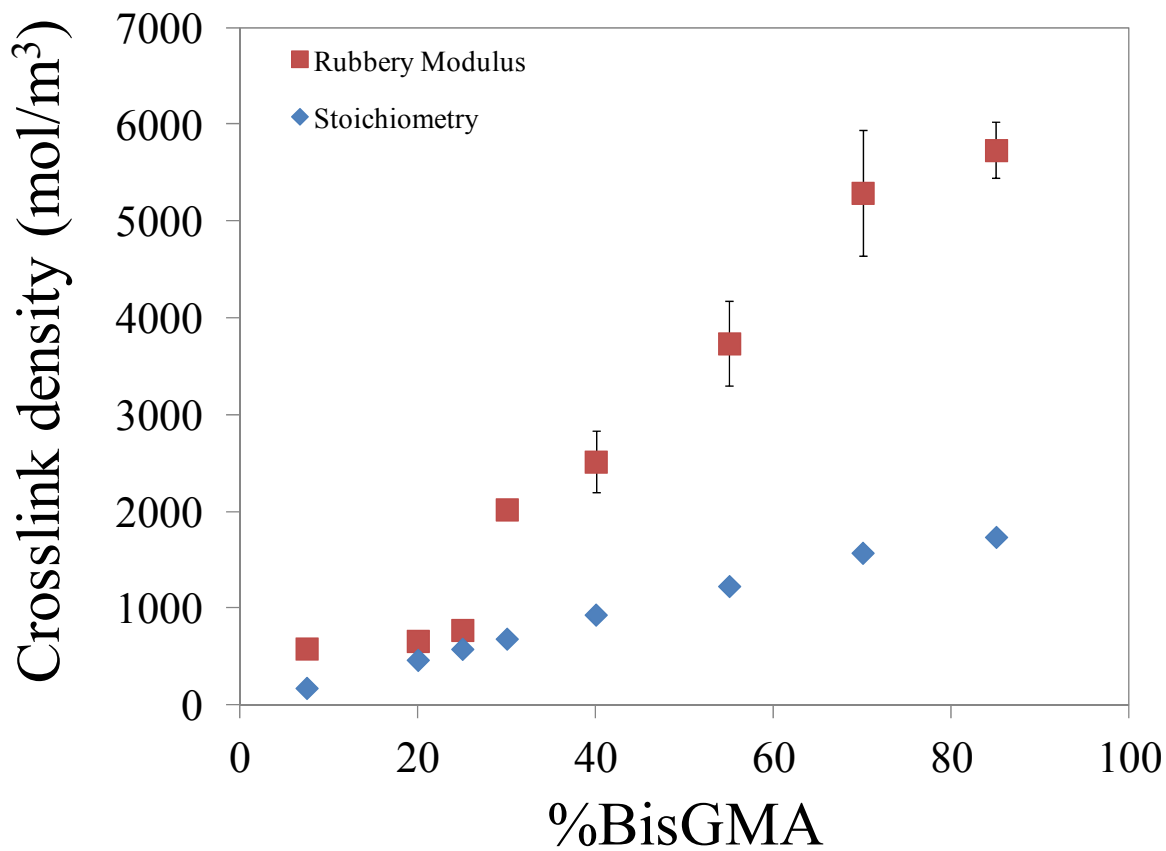


Figure 3-8 Variation of crosslink density calculated from (a) rubbery modulus and (b) stoichiometry, with BisGMA content

4 MICROMECHANICAL MODEL FOR THE EQUILIBRIUM CONFIGURATION OF DENTIN ADHESIVE POLYMERS FORMED ON THE WATER-ADHESIVE PHASE BOUNDARY

During their application to the wet, oral environment, dentin adhesives can experience composition change and phase separation which compromises the quality of the hybrid layer. The chemical composition of polymer phases formed in the dentin-adhesive hybrid layer has been represented using a ternary water-adhesive phase diagram. These phases have been characterized using a micromechanical model incorporating poro-mechanical effects and polymer-solvent thermodynamics. The polymer free volume, interaction parameter and density of crosslink stiffness are the model parameters. The variation of the model parameters and model-predicted polymer properties has been studied as a function of composition along the phase boundary. The resulting structure-property correlations provide insight into interactions occurring at the molecular level in the saturated polymer system. These correlations can be used to obtain input properties for mechanical modeling of the hybrid layer, and are expected to aid in the design and improvement of water-compatible dentin adhesive polymers.

4.1 Introduction

Polymers formed from hydrophilic/hydrophobic monomer pairs have been used in a variety of biomedical applications such as bioadhesives, artificial organs, prostheses, drug delivery systems and orthopedic materials. The polymer properties are strongly correlated to its chemical composition and network structure. Particularly, the phase separation, water sorption, associated swelling, water diffusion, mechanical properties and biocompatibility of these materials

significantly influence their functional performance. The dentin adhesive systems used in composite tooth restorations, like many other bioadhesive systems, are also composed of hydrophobic/hydrophilic organic monomer mixtures. In composite tooth restorations, adhesive systems formed of hydrophilic/hydrophobic monomer mixtures infiltrate into the wet, demineralized collagen of the tooth to form a collagen-adhesive composite known as the hybrid layer. One of the major factors that affects the stability and durability of the hybrid layer is inadequate penetration of the adhesive and its physical separation into individual phases. The presence of water in wet demineralized dentin is a major detrimental factor for dentin adhesives used to bond composite restorations. It is well accepted that the hybrid layer is the weakest link in the adhesive-dentin bond (Spencer, Ye et al. 2010).

In dentin adhesive systems the hydrophobic/hydrophilic monomer pair serves the following functions: a) in the monomer state, the adhesive hydrophilicity aids in its integration with the wet, demineralized dentin matrix, while b) in the polymerized state, adhesive hydrophobicity leads to lower sorption of oral fluids and endows adequate stiffness to minimize swelling. Thus, to provide durable function in the mouth, the optimal dentin adhesive must possess a hydrophilic/hydrophobic balance. However, in the wet, oral environment, dentin adhesives can experience composition change and phase separation. The penetration of the adhesive into the wet demineralized dentin may take place by a combination of diffusion and convection resulting from external energy during adhesive application on the dentin substrate. Since the hydrophobic component is also more viscous, it transports slower through both diffusion as well as convection, as compared to the hydrophilic component. Hence, subsequent photopolymerization results in an adhesive-collagen hybrid layer where the composition of the adhesive changes spatially, particularly along the depth of the hybrid layer. Both, phase

separation (Ye, Park et al. 2011, Under Review, Parthasarathy, Misra et al. 2012) and limited infiltration of the hydrophobic component along the depth of the hybrid layer (Zou 2007, Zou, Armstrong et al. 2010), have been experimentally observed in dentin adhesive interfaces.

The possible monomer phases formed in the hybrid layer by the mixing of the hydrophobic/hydrophilic adhesive monomer pair with water can be represented by the phase boundary of an adhesive-dentin ternary phase diagram (Ye, Park et al. 2011). Phase separation and adhesive composition changes in the monomer state affect both the hydrophilicity and stiffness of the adhesive polymer phases. The hydrophilicity and stiffness are the major factors that control the chemo-mechanical behavior of the adhesive polymer, which has a profound influence on the load transfer mechanism at the dentin-adhesive (a/d) interface and its fatigue life (Misra, Spencer et al. 2004, Misra, Spencer et al. 2005, Singh, Misra et al. 2010, Singh, Misra et al. 2011). Further, it has been observed that the visco-plastic properties of the adhesive change anomalously with water content under loading (Misra, Singh et al. 2011, Singh, Misra et al. 2011, Singh, Misra et al. 2013). In addition, the hydrophilicity and crosslink density have been identified to be two important independent variables which affect the water sorption and diffusion into methacrylate-based crosslinked polymers (Parthasarathy, Misra et al. 2012).

The aim of this paper is to characterize and understand the variation of polymer phase chemo-mechanical properties along the adhesive-dentin phase boundary. A suite of mechanical tests and swelling experiments were performed on five different polymer formulations whose water-hydrophilic-hydrophobic compositions lie close to the phase boundary. A micro-chemo-poro-mechanical model was developed to describe the swelling behavior of these polymer formulations. The experimental data was used to obtain the variation of model parameters with chemical composition. Additional experimental evidence was collected to independently

confirm the variation in the model parameters. The model parameters were then used to predict estimates of Poisson's ratio and bulk modulus. The model parameters and predicted results were qualitatively and quantitatively studied with respect to the chemical composition along the phase boundary. The resulting structure-property relationships give insight into the influence of chemical composition on the variation of chemo-mechanical properties along the phase boundary.

4.2 Materials and experimental methods

4.2.1 Materials

Methacrylate based dentin adhesive monomer formulations were prepared as mixtures of BisGMA (Bisphenol A glycerolate (1 glycerol/phenol) dimethacrylate), 2-hydroxyethylmethacrylate (HEMA, 99%) (Sigma Chemical Co., St. Louis, MO, USA.) and deionized water. The chemical structures of the co-monomers are shown in Table 1. The following three-component visible light photoinitiators (all from Aldrich, Milwaukee, WI) were used in this work: camphoroquinone (CQ, 0.5wt%), ethyl-4-(dimethylamino)benzoate (EDMAB, 0.5wt%) and diphenyliodonium hexafluorophosphate (DPIHP, 0.5wt%). The concentration of the photoinitiator component was calculated with respect to the total amount of monomer. All materials were used as received.

4.2.2 Methods

Preparation of neat adhesive resins

Monomer mixtures in the following mass ratios of HEMA to BisGMA were added along with a 3-component photo-initiator system (0.5 mass percent of camphorquinone (CQ), ethyl-4-

dimethylamino benzoate (EDMAB) and diphenyl iodonium phosphate (DPIHP)) into brown vials: a) 0.3:0.7 b) 0.6:0.4 c) 0.7:0.3 d) 0.75:0.25 e) 0.8:0.2 f) 0.925:0.075 and g) 0.95:0.05 (HEMA:BisGMA). The monomer-initiator mixtures in the brown vials were prepared using vortex mixers and shakers to obtain a homogeneous adhesive resin. The neat resins are represented on the ternary phase diagram using squares as shown in Figure 4-1. A weighing balance with a resolution of 0.01 mg (Mettler Toledo, X205 dual range) was used to weigh each component and was used for all weight measurements described henceforth.

Determination of water solubility of neat adhesive resins

About 1g of each neat resin was weighed into a brown vial and water was added in increments of approximately 0.01 g until the mixture was visually observed to be turbid. The percentage of water in the mixture was noted (w_1). The mixture was then back-titrated using the neat resin till the turbidity disappeared and the percentage of water in the mixture was noted (w_2). The water solubility was calculated as the average of w_1 and w_2 . The procedure is represented on the ternary phase diagram as moving along the line of constant monomer ratio starting at the neat resin (square point) towards the intersection with the phase boundary line, which represents the limit of solubility for that monomer ratio.

Preparation of polymer samples from monomer-water formulations on phase boundary

Water equivalent to about 2-3 percentages below the solubility limit is added to each neat resin and mixed till fully dissolved (see Table 2). The water content was chosen to lie within the solubility limit to minimize polymerization induced phase separation at the scale of this study. The composition of these formulations has been represented using circles on the ternary phase diagram as shown in Figure 4-1. The direction of increasing hydrophobicity or decreasing hydrophilicity along the phase boundary has been indicated using a black arrow. Square beams

with a side of 1 mm and a length of at least 10 mm were prepared for each formulation by casting these prepared adhesive resins into glass-tubing molds (Fiber Optic Center Inc, #CV1012, Vitrocom Round Capillary Tubing of Borosilicate Glass). The resins were injected into the tubing using a micro-pipette and light polymerized with a LED light curing unit of irradiance 250 mW/cm² and area 6.25 mm² for 9s (LED Curebox, Prototech, and Portland, OR). The wavelength of the curing light is in the range of 450 nm. The polymerized samples were stored in dark at room temperature for two days to provide adequate time for post-cure polymerization. The samples were subsequently extracted from the glass tubing and stored in a vacuum oven in the presence of a drying agent (freshly dried silica gel) at 37°C.

Degree of Conversion

The degree of conversion (DC) was determined by Raman spectrometer as described previously (Park, Ye et al. 2009). In brief, LabRAM ARAMIS Raman spectrometer (LabRAM HORIBA Jobin Yvon, Edison, New Jersey) was used with a HeNe laser ($\lambda=633$ nm, a laser power of 17 mW) as an excitation source. The instrument settings were as follows: 200 μm confocal hole, 150 μm wide entrance slit, 600 gr/mm grating, and 10x objective Olympus lens. Data processing was performed using LabSPEC 5 (HORIBA Jobin Yvon). The samples were mounted on a computer-controlled, high-precision x-y stage. To determine the DC, spectra of the unpolymerized resins and rectangular beam samples were acquired over a range of 700 – 1800 cm^{-1} . The changes of the band height ratios of the aliphatic C=C double bond peak at 1640 cm^{-1} and the aromatic C=C at 1610 cm^{-1} (phenyl) in both the cured and uncured states were monitored. The DC was calculated as follows, based on the decrease in the intensity band ratios before and after light curing.

$$DC(\%) = \left[1 - \frac{R_{\text{cured}}}{R_{\text{uncured}}} \right] \times 100 \quad (4.1)$$

where $R = \text{band height at } 1640 \text{ cm}^{-1} / \text{band height at } 1610 \text{ cm}^{-1}$. All experiments were carried out in triplicate over each sample area and across samples and the results were averaged.

Absorption and swelling experiment

Multiple beam specimens were used to study the water sorption behavior of each formulation. Distilled, deionized water (HPLC grade, W5SK-4, Fisher Scientific, Fair Lawn, NJ, USA) was used throughout the experiments. The specimens were first pre-washed by immersing in water for 10 days to remove any leachable matter. The beam specimens were then placed into a vacuum chamber for drying until they reach constant mass. The specimens were then re-immersed in water and stored at room temperature. The weight under water is equal to the weight in air minus the buoyancy force exerted by the water. The time interval for data collection varied from 10 minutes during the beginning of the experiment to 24 hours. After each time interval, the specimens were retrieved, blotted dry to remove excess liquid, weighed in air, weighed in water, and returned to the water bath. The measurement under water was performed within about 10 seconds to avoid any absorption of water during the process. The volume of the sample was calculated using the mass in air and water as shown below.

$$V = \alpha \frac{m_a - m_w}{\rho_w - \rho_a} \quad (4.2)$$

where V is the volume of the sample, m_a is the mass of the sample in air, m_w is the mass of the sample in water, and $\alpha=0.99985$ is a factor to account for air buoyancy. $\rho_w=1 \text{ g/cm}^3$ and $\rho_a=0.0012 \text{ g/cm}^3$ are the densities of water and air respectively. The sample mass density ρ was calculated as follows.

$$\rho = \frac{m_a}{m_a - m_w} (\rho_w - \rho_a) + \rho_a \quad (4.3)$$

The measured fractional mass change in air, Δm_a , and in water, Δm_w , was obtained as

$$(\Delta m_a)_{meas} = \frac{m_a - m_{a0}}{m_{a0}}; \quad \text{and} \quad (\Delta m_w)_{meas} = \frac{m_w - m_{w0}}{m_{w0}} \quad (4.4)$$

and the volume change expressed as the Jacobian of the deformation, J was calculated as follows:

$$J = \frac{V}{V_0} \quad (4.5)$$

where m_{a0} , m_{w0} and V_0 are the initial sample mass and volume, respectively.

Dynamic Mechanical Analysis

The measurement of glass transition temperature and storage modulus in the rubbery state was carried out using dynamic mechanical analysis (DMA Q800, TA Instruments, New Castle, USA) in a 3-point bending configuration. The analysis has been described previously (Park, Ye et al. 2009). The frequency used to measure the storage modulus was 1 Hz with amplitude of 15 μm and a pre-load of 0.01 N. The applied displacements and measured loads were converted to stresses and strains using the equations of elastic beam theory for long slender beams undergoing small deformations. The storage modulus was measured across 0°C to 250°C using a temperature sweep. The temperature sweep was conducted at 3°C/min. The glass transition temperature was identified from the peak of the $\tan \delta$ – temperature curve. The storage modulus decreased with temperature and reached an asymptote at the glass transition temperature. This asymptotic storage modulus was taken to be the apparent rubbery modulus of the polymer. The covalent crosslink density was calculated based on Flory’s rubber elasticity theory (Flory 1953, Krongauz 2010) as shown below:

$$\nu_e = \frac{E'}{3RT} \quad (4.6)$$

where E' is the apparent rubbery modulus measured from the rubbery plateau, and the universal gas constant $R = 8.31 \text{ J K}^{-1}\text{mol}^{-1}$. Eq. (4.6) is based on the rubber elasticity theory. It is not valid for high degrees of cross linking, but has been used when the storage modulus in the rubbery region is in the range of 2×10^6 and 2×10^8 Pa (Krongauz 2010). Eq. (4.6) has been used widely to estimate the crosslink density of polymeric materials. The stoichiometric crosslink density ν_s in moles/m³ was calculated from the mole percentage of the crosslinker and the degree of conversion as follows. The degree of conversion was assumed to be uniform for BisGMA and HEMA segments.

$$\nu_s = \frac{100b(DC)\rho}{M_b} \quad (4.7)$$

Where b is the percentage of BisGMA in the polymer, DC is the percentage degree of conversion, ρ is the polymer density and M_b is the molar mass of BisGMA.

Mechanical testing

Mechanical tests were performed using a three-point bending apparatus with 10 mm beam span on a Bose Electroforce 3200 tester. The samples which were completely saturated and swollen after the absorption and swelling experiment were used for this test. Loading was applied at a rate of 0.001 mm/sec or 7.5 μ /sec. Average stress-strain curves ($n=3$) were obtained and used to calculate the elastic modulus from the linear region for each formulation under dry and wet conditions, respectively.

4.3 Mathematical model

A number of theories to model the elasticity of a polymer network have been developed, such as the kinetic or statistical theory of rubber elasticity, and the phenomenological Mooney-Rivlin type models and their variations (Horkay and McKenna 2007). It is well accepted that the

macro-scale properties of a material are significantly influenced by the interaction between representative units. For example, granular micromechanics theory has been used to derive bounds of elastic moduli for granular materials using inter-particle contacts (Misra and Chang 1993, Chang, Chao et al. 1995) and more recently, to derive constitutive equations for rate-dependent visco-damage behavior, including loading induced anisotropy, based upon inter-granular force-displacement relationships (Misra and Singh 2013). Thus, constitutive models that relate the externally applied action to the molecular-scale parameters have an advantage for describing the mechanical behavior of polymer networks because they enable mechanical responses to be estimated from the knowledge of the molecular structure (Horkay and McKenna 2007). In this paper, we treat the adhesive polymer to possess a pseudo-granular structure in which the grain-interactions represent the average behavior of the covalent bonds between segments in the linear polymer chain, the covalent crosslinks between segments in two different polymer chains, non-covalent hydrogen bonds, van der Waals interactions, entanglements, and other physical interactions. The proposed approach provides a feasible meso-scale method to relate the macro-scale properties to molecular-scales for materials whose micro-structure and local interactions are ill-defined (Misra, Marangos et al. 2013, Misra and Singh 2013). The term meso-scale has been used to refer to a scale smaller than the micro-scale but much larger than the size of a polymer segment (molecular scale), such that a representative volume element at the meso-scale contains several thousand polymer segments. We modeled the wet adhesive polymer using a three-step procedure by applying a) granular micromechanics (Chang, Chao et al. 1995) to model the elastic behavior of the polymer network, b) a self-consistent homogenization of the (homogenized) polymer network with the pore space to obtain the homogenized porous polymer stiffness, and c) the poro-mechanical approach to obtain the behavior of the saturated polymer by

superposing the (homogenized) porous polymer with the interstitial water. A schematic depiction of the modeling procedure is shown in Figure 4-2(a) to (c). In addition, a schematic depiction of the idealization for cases of low and high crosslink density is shown in Figure 4-3(a) and (b), respectively.

4.3.1 *Micro-poro-mechanical model*

In the first step (see Figure 4-2(a)), the theoretically dense wet polymer network was homogenized using the granular micromechanics approach which assumes the system to be composed of grains interacting in both the normal and shear directions. In this approach, the stress tensor was obtained in terms of the tensor product of the interaction force vector and the vector joining the centroid of pseudo-grains (Misra, Marangos et al. 2013). The resultant expression for the stress tensor has similarities to the microscopic stress description utilized for reptation models of polymers (see for example Section 5.3 (Doi 1996)). Using the granular micromechanics approach, the following expression for Young's modulus and Poisson's ratio can be derived for isotropic systems subjected to isotropic loading, under the so called "static hypothesis" for expressing inter-granular forces in terms of the stress tensor (Chang, Chao et al. 1995).

$$E^s = 10A^s \left(\frac{\alpha^s}{2+3\alpha^s} \right) \quad (4.8)$$

$$\nu^s = \frac{1-\alpha^s}{2+3\alpha^s} \quad (4.9)$$

where E^s and ν^s are the elastic modulus and Poisson's ratio of the polymer network, A^s is a meso-scale parameter proportional to the inter-granular stiffness in the normal direction and the number density of inter-granular interactions, and α^s is the ratio of the transverse to normal inter-

granular stiffness. Formulae relating other forms of macro-scale material properties to meso-scale parameters are given in Table 3. The “static hypothesis” approach is derived by relating the macro-scale strain to the local displacements through least square fitting (Chang, Chao et al. 1995) in order to capture the non-affine local deformations observed in these material systems (Wen, Basu et al. 2012).

In the second step (see Figure 4-2(b)), the polymer network was homogenized with the porous space using the self-consistent approximation (Misra, Marangos et al. 2013) to obtain the 4th-order stiffness tensor C_{ijkl} of the porous polymer as shown below.

$$C_{ijkl} = C_{ijkl}^s - \phi C_{ijmn}^s H_{mnkl}^\phi \quad (4.10)$$

where H^ϕ is the strain concentration tensor in the pore space determined by using the equivalent inclusion technique (Eshelby 1957), and ϕ is the porosity of the polymer. The stiffness tensor C_{ijkl}^s was written in terms of E^s and ν^s given in Eqs. (4.8) and (4.9) as

$$C_{ijkl}^s = \lambda^s \delta_{ij} \delta_{kl} + \mu^s (\delta_{ik} \delta_{jl} + \delta_{il} \delta_{jk}) \quad (4.11)$$

where λ^s and μ^s can be determined from formulae in Table 3, and δ_{kl} is the Kronecker delta. We have used the tensor notation for the development of the mathematical model, thus the subscripts in this section follow the tensor summation convention. For the saturated swollen polymer, the pore spaces were assumed to be spherical for simplicity in the absence of well-defined morphological information. The Eshelby tensor S for spherical inclusion in isotropic medium is given as (Mura 1987)

$$S_{ijkl} = \frac{(5\nu-1)}{15(1-\nu)} \delta_{ij} \delta_{kl} + \frac{(4-5\nu)}{15(1-\nu)} (\delta_{ik} \delta_{jl} + \delta_{il} \delta_{jk}) \quad (4.12)$$

where ν is the Poisson's ratio of the homogenized porous polymer . The strain concentration tensor H^ϕ for the pore space is then calculated as follows (Misra, Marangos et al. 2013):

$$H_{ijkl}^\phi = \left(I_{ijkl} - S_{ijkl} \right)^{-1} \quad (4.13)$$

where $I = (\delta_{ij} \delta_{kl})$ is the identity tensor.

In step three (see Figure 4-2(c)); we superposed the homogenized porous polymer phase with the fluid phase following the procedure described in (Misra, Marangos et al. 2013) after considering large deformation. We thus obtained the incremental overall constitutive equation for the saturated polymer in a poroelastic framework as follows.

$$\dot{\sigma}_{ij} = -\delta_{rs} L_{rs} \bar{\sigma}_{ij} + C_{ijkl} \dot{\epsilon}_{kl} + \bar{\sigma}_{jm} L_{im} + \bar{\sigma}_{im} L_{jm} - B_{ij} \dot{p} \quad (4.14)$$

$$\dot{\zeta} = B_{kl} \dot{\epsilon}_{kl} + \Gamma \dot{p} \quad (4.15)$$

where $\dot{\sigma}_{ij}$ is the stress rate, $\bar{\sigma}_{ij}$ is the stress in the polymer phase, L_{im} is the velocity gradient of the saturated polymer, $\dot{\epsilon}_{kl}$ is the strain rate, \dot{p} is the fluid pressure rate, $\dot{\zeta}$ is the volumetric rate of water uptake with respect to the volume of the saturated polymer, and B_{ij} and Γ are the poromechanics constants. B_{ij} and Γ were obtained in a straightforward manner using self-consistent homogenization as:

$$B_{ij} = \phi \delta_{mn} H_{mnij}^\phi \quad (4.16)$$

$$\Gamma = B_{kl} \left(C_{ijkl}^s \right)^{-1} (B_{kl} - \phi \delta_{kl}) + \frac{\phi}{K_f} \quad (4.17)$$

where K_f is the bulk modulus of water. The poromechanics constant B measures the ratio of water volume squeezed out to the volume change of the saturated polymer under (idealized) conditions of flow under zero pressure. B_{ij} is called the effective stress coefficient and represents the proportion of the applied load carried by the fluid. Γ is a compliance parameter which

measures the amount of water which can be forced into the saturated polymer under pressure while the volume is kept constant. Γ is a measure of the combined fluid-solid compressibility. It is noteworthy that the value of B_{ij} is not unity and both B_{ij} and Γ depend on the stiffness of the porous polymer and the polymer network. Under the assumption of negligible change in water density, $\zeta = \dot{\gamma}_w$ where $\dot{\gamma}_w$ is the increment in water volume fraction in the saturated polymer.

4.3.2 Chemical potential of the saturated polymer

Water absorption and swelling is determined by the mechanical properties as well as the chemical potential of the water in the polymer. The chemical potential of water in a polymer relative to chemical potential of pure water has been derived by (Flory 1953). Here, we used a modified form written as:

$$\mu = RT \left[\ln(\gamma_w) + (1 - \gamma_w) + \chi(1 - \gamma_w)^2 \right] + \Psi(\gamma_w - V_{\phi 0}) \bar{p} \frac{M_w}{\rho_w} \quad (4.18)$$

where μ is the chemical potential difference between the water inside the polymer and pure water, henceforth referred to as chemical potential, R is the universal gas constant ($=8.314 \text{ JK}^{-1} \text{ mol}^{-1}$), T is the temperature, γ_w is the water volume fraction, \bar{p} is the effective fluid pressure in

the polymer given as $\bar{p} = \int B_{ij} \delta_{ij} \dot{p}$, $\frac{M_w}{\rho_w}$ is the partial molar volume of water in the polymer, M_w

the molecular weight and ρ_w the mass density of water, χ is the polymer-water interaction parameter, $V_{\phi 0}$ is the initial free volume in the polymer and Ψ is the Heaviside step function such

that $\Psi(\gamma_w - V_{\phi 0}) = 0$ when $\gamma_w < V_{\phi 0}$ and $\Psi(\gamma_w - V_{\phi 0}) = 1$ when $\gamma_w \geq V_{\phi 0}$. The effective fluid

pressure \bar{p} at equilibrium when the chemical potential difference vanishes, $\mu=0$, is identified as

the osmotic pressure. We note that the first term in Eq.(4.18) represents the free energy

resulting from the entropy and enthalpy of mixing, while the second term represents the contribution from elastic deformation. The Heaviside step function was introduced in the second term to account for the initial free volume, V_{ϕ_0} , defined as that fractional volume of the polymer which needs to be saturated before the interstitial water develops pressure as the result of the elastic swelling of the polymer structure. In literature, the free volume has been defined as the volume not occupied by the polymer molecules but constituting a part of the bulk volume of the overall polymer solid or polymer/diluent system (Yasuda, Peterlin et al. 2003). The free volume in a polymer has also been defined equivalently as the volume occupied by openings between the polymer chains where the solvent molecules can pass through (Amsden 1998, Yasuda, Peterlin et al. 2003). Our definition is consistent with those from literature since the fluid pressure and corresponding stress in the polymer is created only when there is resistance to any further increase in space between the chains beyond the initially empty space.

4.3.3 Swelling and elastic modulus of saturated polymer

We assume that the swelling under stress-free condition, wherein the increment of external stress, $\dot{\sigma}_{ij} = 0$, is isotropic, that is $\dot{\epsilon}_{ij} = \epsilon \delta_{ij}$ and $B_{ij} = B \delta_{ij}$. Furthermore, for the swelling experiments performed on beams whose length is much larger than the cross sectional dimensions plane strain conditions may be assumed. Solving Eq. (4.14) and (4.15) under these conditions, we obtained the following relationship applicable to our experiments

$$\dot{p} = \left[\frac{C_{1111} + C_{1122}}{2B^2 + \Gamma(C_{1111} + C_{1122})} \right] \dot{\gamma}_w \quad (4.19)$$

$$\dot{\epsilon} = \left[\frac{B}{2B^2 + \Gamma(C_{1111} + C_{1122})} \right] \dot{\gamma}_w \quad (4.20)$$

where the stress correction terms involving the velocity gradient, L_{ij} , vanish for the condition of plane strain. The volume change expressed as the Jacobian of the deformation, J is related to the isotropic strain as

$$\frac{\dot{J}}{J} = 2\dot{\epsilon} \quad (4.21)$$

Further, we note that the rate of loading for mechanical testing performed in this study is orders of magnitude faster than the rate of water diffusion (or drainage) in the beam samples. Therefore, the loading can be considered as undrained and $\dot{\zeta} = 0$. Solving Eq. (4.14) and (4.15) for this condition gives a relationship for the undrained stiffness in term of the drained stiffness C_{ijkl} , used in Eqs. (4.19) and (4.20), and poromechanics constants B_{ij} as follows

$$C_{ijkl}^u = C_{ijkl} + \frac{B_{ij}B_{kl}}{\Gamma} \quad (4.22)$$

4.3.4 Numerical model calibration

Eqs. (4.18) through (4.22) allows us to relate the macroscopic experimental measurements, that is the undrained elastic modulus, the mass change in air, the mass change in water and the volume change to the local (meso-scale) parameters A^s , $V_{\phi 0}$ and χ . However, a numerical solution of these coupled nonlinear equations is required for the calibration of the meso-scale parameters. To this end, we minimized the following objective error function

$$e(A^s, V_{\phi 0}, \chi) = \left(\frac{\Delta m_a - (\Delta m_a)_{meas}}{(\Delta m_a)_{meas}} \right)^2 + \left(\frac{\Delta m_w - (\Delta m_w)_{meas}}{(\Delta m_w)_{meas}} \right)^2 + \left(\frac{J - J_{meas}}{J_{meas}} \right)^2 + \left(\frac{E^u - E_{meas}^u}{E_{meas}^u} \right)^2 \quad (4.23)$$

subject to the constraints

$$A^s > 0, 0 < V_{\phi 0} < 1, \chi > 0 \quad (4.24)$$

where the change of mass in air

$$\Delta m_a = \frac{\rho_w V_\phi}{m_{a0}}, \quad (4.25)$$

the change of mass in water

$$\Delta m_w = \frac{\rho_w (V_\phi - V + V_0)}{m_{w0}} \quad (4.26)$$

the jacobian J is given by Eq.(4.21), and the undrained elastic modulus is given by Eqs.(4.19), (4.19) and (4.22). We further note that under saturation the water volume fraction, $\gamma_w = \phi = \frac{V_\phi}{V}$, and at equilibrium the chemical potential given by Eq. (4.18) must vanish, thus yielding the required relationship for determining V , V_ϕ , J and E^u , that are needed in Eq.(4.23). However, the effective fluid pressure, \bar{p} , the drained stiffness, C_{ijkl} , and the poromechanics constants B_{ij} and Γ are unknown at equilibrium. Further, the relationship between the effective fluid pressure and the water volume fraction given by Eq. (4.19) is in an incremental form. Therefore, Eq. (4.18) was solved incrementally for the equilibrium condition, $\mu = 0$. At each increment, the water volume fraction and effective pressure in Eq.(4.18) were solved using the iterative Newton's method for which we defined the residual at the end of increment $t + \Delta t$ as follows

$$f(\gamma_w^{t+\Delta t}) = \mu^{t+\Delta t} - \left(RT \left[\ln(\gamma_w^{t+\Delta t}) + (1 - \gamma_w^{t+\Delta t}) + \chi(1 - \gamma_w^{t+\Delta t})^2 \right] + \bar{p}^{t+\Delta t} \frac{M_w}{\rho_w} \right) \quad (4.27)$$

and expanded in Taylor's series as:

$$f(\gamma_w^{t+\Delta t}) = f(\gamma_w^{t+\Delta t})^i + \Delta \gamma_w^{t+\Delta t} \left(\frac{\partial f}{\partial \gamma_w^{t+\Delta t}} \right)^i \quad (4.28)$$

where $\Delta \gamma_w^{t+\Delta t}$ is the correction in the i -th iteration of increment $t + \Delta t$. Setting the residual in Eq. (4.28) to zero, we get

$$\Delta\gamma_w^{t+\Delta t} = \frac{f(\gamma_w^{t+\Delta t})^i}{K_T^i} \quad (4.29)$$

where the tangent

$$K_T^i = -\left(RT \left[\frac{1}{\gamma_w^{t+\Delta t}} - 1 - 2\chi(1 - \gamma_w^{t+\Delta t}) \right] + \Omega \frac{M_w}{\rho_w} \right), \quad (4.30)$$

$\Omega = B \left[\frac{C_{1111} + C_{1122}}{2B^2 + \Gamma(C_{1111} + C_{1122})} \right]$, and the increment of effective fluid pressure $\Delta\bar{p}^{-t+\Delta t}$ was

calculated as $\Delta\bar{p}^{-t+\Delta t} = \Omega\Delta\gamma_w^{t+\Delta t}$. At the end of the i -th iteration, we updated the water volume fraction as follows till convergence

$$\gamma_w^{t+\Delta t} = \gamma_w^{t+\Delta t} + \Delta\gamma_w^{t+\Delta t} \quad (4.31)$$

The above numerical scheme was implemented using the following 3 steps:

Step 1: To initiate the calculations, we utilized the following initial estimates of meso-scale parameters: (1) $A^s = 5E^u$, where E^u is the undrained modulus obtained from the mechanical experiment and the relationship between E and A from Table 3 is used with $\alpha^s = 1$; (2) the initial free volume, $V_{\phi 0}$, is taken as a small number typically < 0.1 ; and (3) $\chi = 0.5$ which are similar to the published results for polyHEMA (Tauer, Ali et al. 2005, Xu, Goponenko et al. 2008).

Step 2: For the case of $\gamma_w < V_{\phi 0}$, that is prior to the saturation of the initial free volume, the water pressure is zero and chemical potential, μ , can be obtained from Eq. (4.18) directly for given γ_w . For $\gamma_w = V_{\phi 0}$ the chemical potential μ^0 is also obtained from Eq. (4.18) by substituting $\bar{p}^{-0} = 0$. For $\gamma_w \geq V_{\phi 0}$, the solution was based upon the procedure outlined in Eqs.

(4.27)-(4.31), where the chemical potential was updated using a uniform increment, $\Delta\mu = -\frac{\mu^0}{N}$,

and N was chosen to be sufficiently large to obtain converged solutions with minimal iterations. For each increment and within each iteration, the values of C_{ijkl} , B_{ij} , Γ were updated using Eq.(4.10), Eq. (4.16)and Eq. (4.17) where $\phi = \gamma_w$. We note that Eq. (4.10) is non-linear in ϕ since H_{ijkl}^ϕ and S_{ijkl} depend on the Poisson's ratio, ν , therefore, Eqs.(4.10), (4.12) and (4.13) were simultaneously solved using an optimization scheme, such as Levenberg-Marquardt scheme to determine, ν , and subsequently C_{ijkl} , B_{ij} and Γ .

Step 3: Once the equilibrium values of γ_w , \bar{p} , C_{ijkl} , B_{ij} , Γ were obtained at $\mu^{t+\Delta t} = 0$, the change of mass in air (Eq.(4.25)), change of mass in water (Eq.(4.26)), Jacobian of deformation and undrained elastic moduli were calculated at equilibrium and substituted into Eq. (4.23)to calculate the error $e(A^s, V_{\phi 0}, \chi)$. The error function was minimized using linear search optimization to determine A^s , $V_{\phi 0}$ and χ , where step 2 is utilized in each iteration to obtain the equilibrium values as indicated above.

4.4 Results and discussion

4.4.1 Experimental measurements

For the subsequent discussion, we use the nomenclature HBN to denote the formulations described in Table 2, where H represents HEMA, B represents BisGMA and N is the percentage of HEMA in the neat resin. For example, HB60 is the formulation corresponding to the yellow circle in Figure 4-1 and prepared by diluting the neat resin corresponding to the yellow square with water. Since the composition of the formulations on the phase boundary follows a well-defined curve, the composition on the phase boundary is fully defined by the percentage of one of the components. We describe our results with respect to percentage of BisGMA in the resin.

We note that to reduce the time and amount of data collection the following four formulations – HB30, HB60, HB75, HB80 and HB92.5 were chosen to perform the absorption and swelling experiments. Time varying data was collected for HB60, HB75, HB80 and HB92.5, while the data for HB30 was collected after equilibrium was reached. Figure 4-4 shows experimental data for the formulations prepared close to the phase boundary, represented by circles on the ternary water-adhesive phase diagram as shown in Figure 4-1. Figure 4-4 (a) to (d) show experimental data from water sorption and swelling while Figure 4-4 (e) and (f) show data from mechanical testing.

From Figure 4-4 (a) and (b) we observe that the rate of diffusion of water into the polymer, as well as the rate of swelling was seen to decrease with increase in BisGMA along the phase boundary. The final water sorption and swelling at equilibrium are also observed to decrease with increase in BisGMA as seen from Figure 4-4 (c) and (d). Figure 4-4 (e) shows that the covalent crosslink density obtained using Eq. (4.6) increased with BisGMA content. Finally, we see from Figure 4-4 (f), that both the dry and wet moduli increase with percentage of BisGMA, although the wet moduli were significantly smaller than the dry moduli.

The water sorption shown in Figure 4-4 (c) was found to be greater after pre-washing, which is likely due to the free volume created by washing away leachables. Further, the decrease in magnitude and the rate of water sorption in Figure 4-4 (a) and (c) with BisGMA is expected as discussed in our previous work (Parthasarathy, Misra et al. 2012), since with increasing BisGMA there is an increase in density of covalent crosslinks, non-covalent interactions and hydrophobicity. The difference in the dry and wet moduli shown in Figure 4-4 (f) is also expected as these polymers experience partial plasticization of non-covalent interactions upon imbibing water (Singh, Misra et al. 2013). It is noteworthy, however, that the rubbery moduli

which were used here for the covalent crosslink densities determination ranged from ~6 MPa to 50 MPa. These values are two orders of magnitude smaller than the elastic moduli under both wet and dry conditions as shown in Figure 4-4 (f). Traditionally, the contributions of covalent crosslinks are expected to govern the polymer stiffness in the rubbery stage, while the non-covalent bonds contribute significantly to the stiffness at the room temperature (Safranski and Gall 2008, Ashby and Jones 2012). In fact, the crosslink density calculated using stoichiometric method was found to be even smaller than that obtained using Eq. (4.6) indicating that the non-covalent interactions play a controlling role for these polymers even at the rubbery state. Further, the large difference in the rubbery modulus and the room temperature modulus suggests that in these polymers the non-covalent interactions dominate in both the wet and dry conditions. These findings also underlines the significance of the micro-poro-mechanical model described in section 4.3.1, since the stiffness calculated from this model accounts for the contribution from not only the covalent crosslinks between polymer segments but also the non-covalent hydrogen bonds, van der Waals interactions, entanglements, and other physical interactions.

4.4.2 Model calculations

We applied the numerical model calibration described in section 4.3.4 to the macro-scale experimental measurements to obtain the meso-scale parameter A^s , the initial free volume $V_{\phi 0}$, and the interaction parameter χ . In addition, we computed the Poisson's ratio, bulk modulus and Lamé's constants (see Table 3) and poromechanics constants using Eqs. (4.16) and (4.17) under undrained conditions at equilibrium. Finally we obtained the meso-scale parameters A^u and α^u for the saturated porous polymer under undrained conditions at equilibrium from C_{ijkl}^u using the

formulae in Table 3. The variations of these properties with respect to percentage BisGMA were then examined to understand the structure-property relationships.

4.4.3 *Meso-scale parameters*

Figure 4-5(a) shows the variation of the initial free volume of the polymer with changing BisGMA concentration along the phase boundary. The free volume in a polymer depends on the available space between polymer chains, which is affected by a number of factors such as a) the nature of bonds between the polymer segments, b) the volume and distribution of water that was dissolved in the monomer mixture, c) evaporation of this dissolved water from the sample during curing, and d) the size distribution of the polymer segments. BisGMA increases the covalent crosslink density as well as the non-covalent interactions between the polymer segments. The presence of crosslinking may restrict the packing of chains and decrease the free volume (Khonakdar, Morshedian et al. 2003). So, the decrease in free volume from HB80 to HB30 may be attributed to this increased density of interactions. However, we observe that the free volume of HB92.5 is lower than that of HB80, HB75 and HB60. This is possibly due to a decrease in free volume caused by a greater retention of the water molecules dissolved in the monomer, as bound water in the polymer, given the relatively high hydrophilicity of this formulation. We hypothesize that the influence of packing density on the free volume arising due to the dissimilar sizes of BisGMA and HEMA segments is outweighed by the other factors discussed here. Further, in Figure 4-5(b) we show the equilibrium porosity, ϕ , or volumetric water content, γ_w . The volumetric water content depends upon both the hydrophobicity and the polymer network stiffness, and decreases with BisGMA content in a nonlinear fashion. We observe from Eq. (4.18) that under equilibrium conditions when $\mu=0$, γ_w has a nonlinear dependence on the fluid

pressure as well as on χ , which is representative of hydrophobicity. The fluid pressure in turn depends on the polymer network stiffness C_{ijkl} , as represented in Eq. (4.19). At low BisGMA content, the network stiffness is small and the hydrophobicity is low leading to high water absorption. The water absorption decreases with BisGMA content and asymptotes to around 7 percent.

The dimensionless interaction parameter χ , originally introduced in (Flory 1942) and (Huggins 1941) characterizes the energy of mixing of the solvent and polymer. The relationship between the polymer-water interaction parameter χ with the BisGMA content is shown in Figure 4-5(c). Overall, χ shows an increasing relationship with the percentage of BisGMA. The interaction parameter, χ depends on the following factors: a) interactions between water molecules and the polymer molecules by virtue of its definition, b) crosslink density of the polymer network, and c) the packing of the polymer chains and the overall structure. In particular, it is known that the χ for crosslinked polymer exceeds that of the corresponding un-crosslinked polymer (Freed and Pesci 1989). We observe the value of χ (1.26) for HB30 to be significantly higher than the χ (0.68) for HB92.5. An increasing trend of χ with the weight percent of the crosslinker was found in a study by (Wang and Wu 2005) for swelling experiments on polymers formed from a hydrophobic/hydrophilic monomer pair. Since HB30 is significantly higher in monomer hydrophobicity as well as crosslink density as compared to HB92.5, we observe a corresponding significant difference in χ as well. The values of χ for HB80, HB75 and HB60 are not significantly different from each other, which could be due to a complex interaction between the governing factors listed above. It is also noteworthy that the monomer formulations lie along the phase boundary i.e. they contain HEMA, BisGMA as well as water. The amount and nature of water that remains in the polymer after the polymerization could also influence the variation of χ .

From Figure 4-5 (d) we observe that the meso-scale parameter A^s increases with BisGMA content. It is noteworthy that the parameter A^s represents the average stiffness and number density of interactions between polymer segments. The increase in covalent crosslink density with BisGMA is clear from Figure 4-4(e). The increase of A^s with BisGMA is not only contributed by the covalent crosslink density but also by the increase in non-covalent and other physical interactions as discussed earlier.

4.4.4 *Macromechanical properties*

Figure 4-6 (a) shows the variation of Poisson's ratio with percentage BisGMA. We observe that at low BisGMA content, wherein the contribution of crosslinking is relatively small, the Poisson's ratio tends to 0.5, which is same as that of water. It has been experimentally confirmed that the Poisson's ratio of hydrogels with low crosslink density is indeed close to 0.5. For example, (Johnson, Bauer et al. 2004) determined the Poisson's ratio of poly-HEMA hydrogel to be 0.42 ± 0.03 at pH 2.8 and 0.45 ± 0.12 at pH 12 and (Boudou, Ohayon et al. 2006) found Poisson's ratios of 0.48 ± 0.012 for relatively low crosslink density. It is noteworthy that the experimental determination of Poisson's ratio of hydrogels often involves specialized image analysis techniques. Based upon the optimization scheme described in step 2 of section 3.4, we determined a Poisson's ratio of 0.489 at 7.5% BisGMA, which lies in the range of the experimental observations. The variation in bulk modulus with BisGMA content is also shown in Figures 6(b). Though the bulk modulus increases with the percentage of BisGMA, we observe that the bulk modulus for the saturated polymer is much lower than that of water or the dry polymer, which suggests that these materials cannot be modeled using simple mixture theories. The high value of Poisson's ratio and the low value of the bulk modulus at low BisGMA content are due to the low drained stiffness of the resultant highly porous polymer

network. Particularly for the Poisson's ratio, the contributions of the poromechanical parameters dominate in the undrained conditions.

Figure 4-6 (c) and (d) show the variation of the poromechanical parameters B and Γ with respect to the BisGMA content. The decreasing value of B implies that the role of the fluid pressure in resisting the applied load decreases with the BisGMA percentage. The decreasing value of Γ indicates decrease in overall compressibility of the saturated polymer with increase in BisGMA. The decrease in overall compressibility is attributed to increased covalent, non-covalent and physical interactions, as well as reduced water volume fraction leading to reduced plasticization with increase in BisGMA. Figure 4-6 (e) and (f) give the variation of the Lamé's constants for reference. The Lamé's constants are an alternative method to express the material elastic constants. We particularly note that the shear modulus tends to zero at low BisGMA content.

4.5 Summary and Conclusions

The dentin adhesives used in composite restorations polymerize in the presence of water and thus vary in their spatial composition, spanning about ten microns from the dentin end to the composite polymer end. Generally, these adhesives are a conglomerate of many angstrom-scale structural units, which interact through various covalent bonds forming linear as well as crosslinks and non-covalent interactions such as van der Waals, hydrogen bonds, hydrophobic and electrostatic interactions. Their molecular structure is typically deduced by polymer chemists based on the information from their chemistry of polymerization. Though the molecular structure of the monomers and the polymerization mechanism is qualitatively understood, the details of their meso-scale (sub-micron scale) structure, composed of polymer chains crosslinked at intervals and entanglements is not known. Due to the large number of atoms in a meso-scale, and the ill-defined knowledge of meso-structure and molecular

interactions, there are severe limitations to atomistic-scale modeling (both molecular dynamics and *ab-initio*) of these material systems.

Therefore, in this paper we adopted the granular micromechanics approach, in which the material is treated as a granular system whose grain interactions represent the average behavior of the various molecular-scale interactions. In addition, we included chemo-poro-mechanical effects using a meso-scopic chemical potential and Biot's poromechanical methodology for incorporating the pore-fluid pressure. The developed model was applied to investigate the chemo-poro-mechanical properties of dentin adhesive polymer phases formed along the ternary adhesive-water phase boundary. These dentin adhesive polymer phases represent the composition of adhesive monomer applied to wet demineralized dentin. Water sorption, swelling, static and dynamic mechanical tests were performed. An optimization procedure was developed to determine the meso-scale model parameters using the experimentally measured sorption, swelling and elastic behaviors. These model parameters are identifiable with molecular scale interactions. The variation of these parameters along the phase boundary quantifies the effect of crosslink density and hydrophobicity on the chemo-poro-mechanical properties. It is noteworthy that the trends predicted by the model agreed with independent experimental measurements and with chemical compositions. The model was used to predict additional mechanical properties like Poisson's ratio and bulk modulus, which are difficult to measure experimentally. Further, we obtained insights into possible mechanisms at the molecular scale that are responsible for the bulk material properties.

In the field of restorative dentistry, an intuitive approach based on experience is often used by polymer chemists to identify or design new co-monomer adhesive molecules to meet multiple target criteria such as water sorption and elastic modulus. We expect that the chemo-mechanical

model introduced in this paper will enhance this approach by providing a stronger link between polymer chemistry and the macro-scale chemo-mechanical properties. Further, the model parameters have been determined along the adhesive-dentin phase boundary. These model parameters can be used for describing the hybrid layer mechanical properties for input into finite element models of dentin-adhesive interfaces. The model can also be extended to incorporate polymer rate-dependent behavior such that the fluid-flow and the intrinsic viscous effects can be distinguished resulting in a more comprehensive description of the mechanical behavior of these materials.

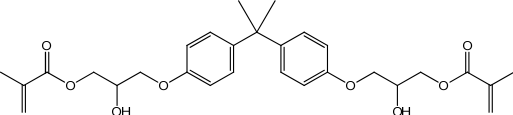
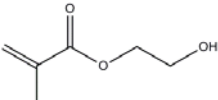
Co-monomer chemical formula/name	Co-monomer Structure
BisGMA	
HEMA	

Table 4-1 List of co-monomers

	BisGMA (%)	HEMA (%)	Water (%)	Solubility (%)
HB30	66.51	28.51	4.98	6.69
HB60	34.8	52.2	13	15.2
HB70	24.45	57.05	18.5	21.1
HB75	19.5	58.5	22	24.8
HB80	14	56	30	32.5
HB92.5	3.75	46.25	50	53.8

Table 4-2 Percentage composition by weight of the monomer formulations on the phase boundary

Macro-mechanical property		(A, α)
Elastic modulus	E	$A \left(\frac{\alpha}{2+3\alpha} \right)$
Poisson's Ratio	ν	$\frac{1-\alpha}{2+3\alpha}$
Bulk modulus	K	$\frac{2A}{3}$
Shear modulus	μ	$5A \left(\frac{\alpha}{3+2\alpha} \right)$
Lame's first parameter	λ	$A \left(\frac{1+\alpha}{2+3\alpha} \right)$

Table 4-3 Relation between micro-mechanical parameters and macro-mechanical material properties

Note: Superscripts s and u used in the text refer to the theoretically dense wet polymer network and the saturated swollen polymer under undrained conditions.

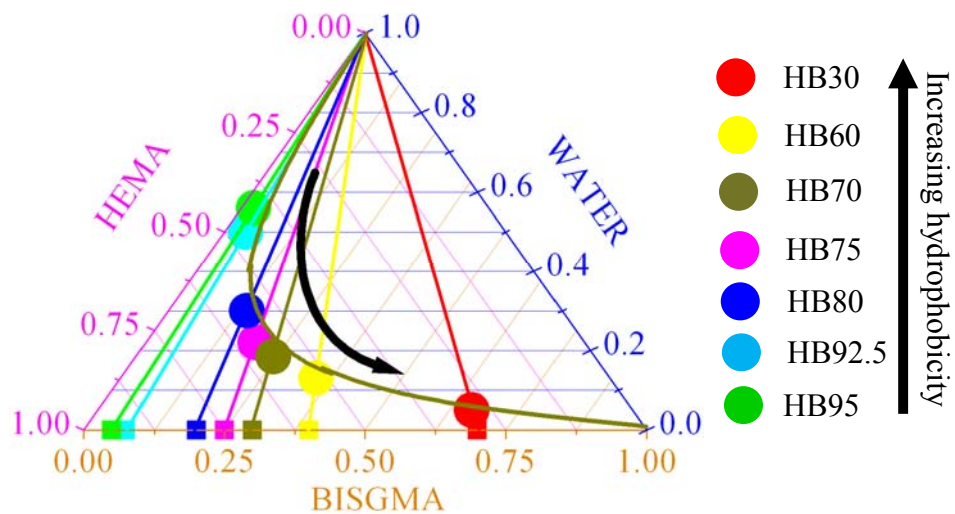


Figure 4-1 (Color online) Representative adhesive monomer formulations identified on the phase boundary of the water-adhesive ternary phase diagram. The circles represent the formulations prepared close to the phase boundary. The squares represent the corresponding neat formulations.

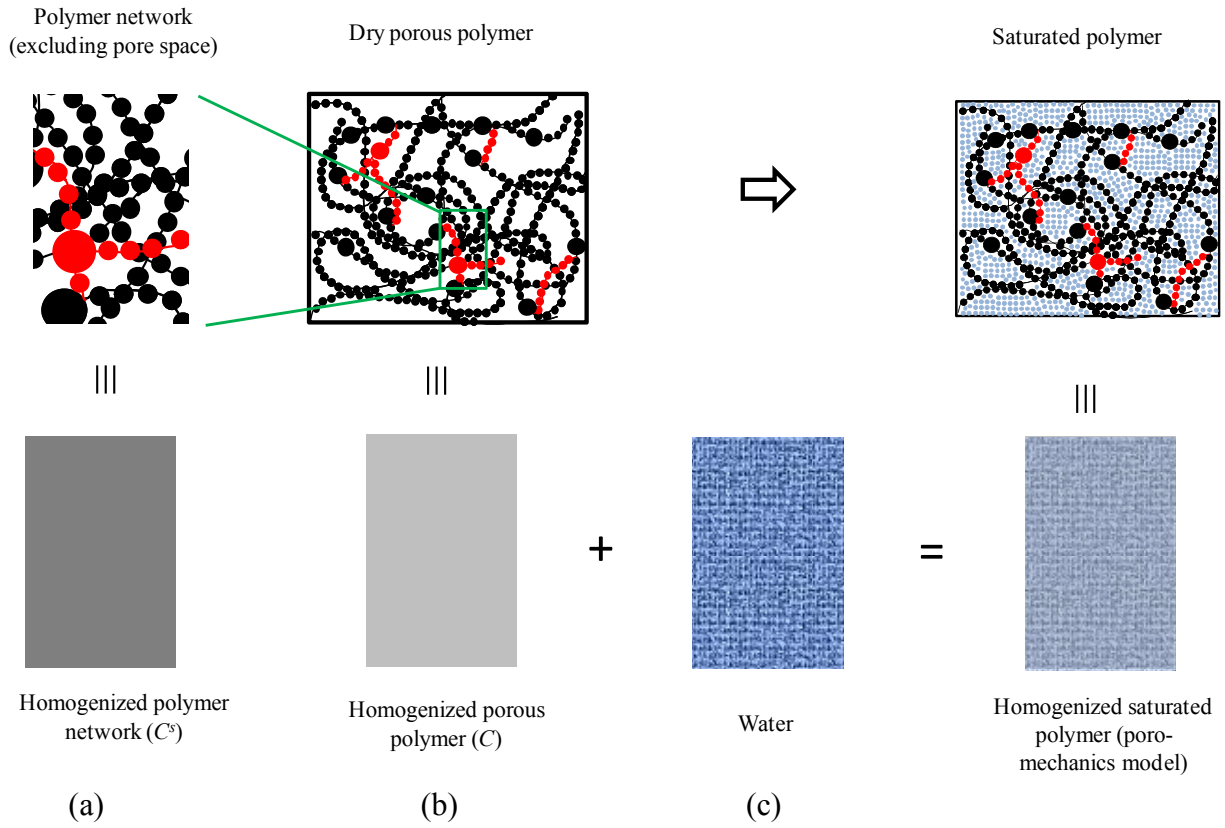


Figure 4-2 (Color online) Flowchart for model idealization

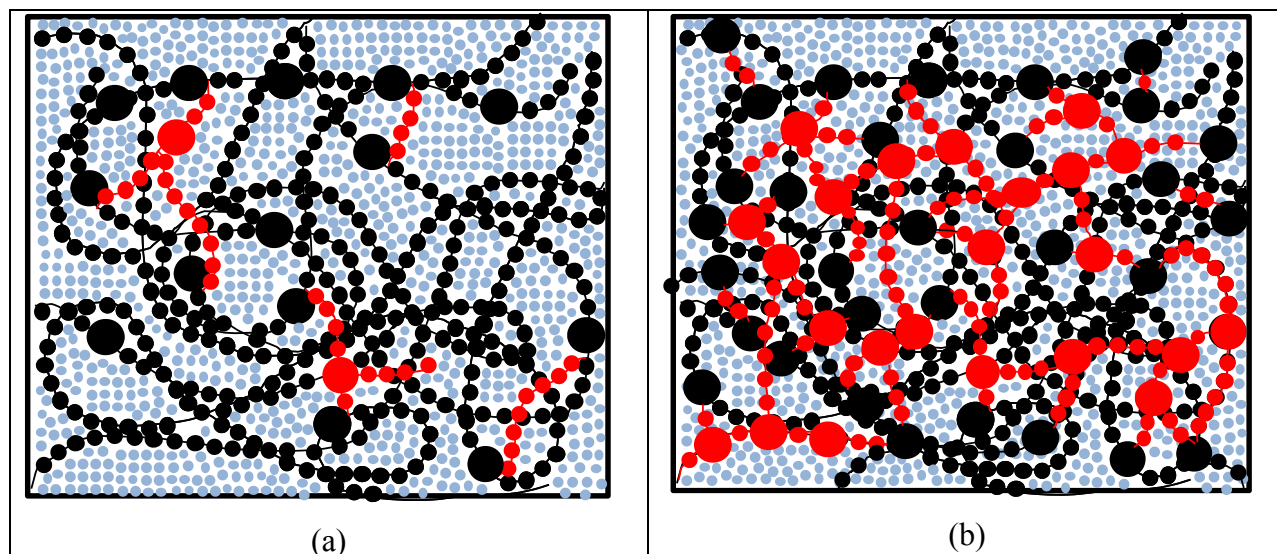


Figure 4-3 (Color online) Schematic of the saturated polymer for (a) sparsely crosslinked network and (b) highly crosslinked network. The red molecule belongs to the crosslinks and the black molecules to linear polymer chains. The large molecule in the polymer is a BisGMA unit and the smaller one is a HEMA unit. The blue molecules represent water in the interstitial spaces between the polymer chains.

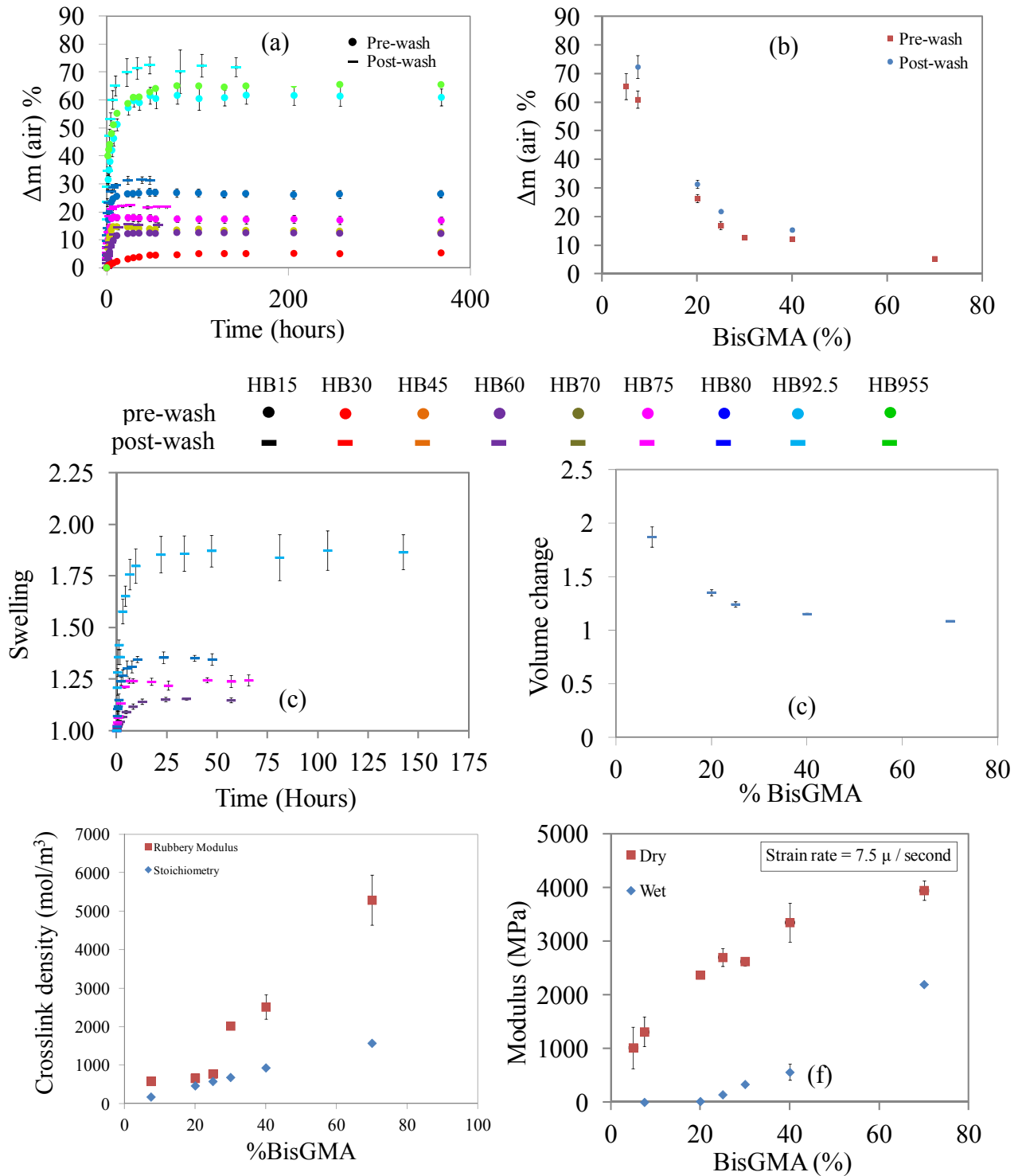


Figure 4-4 (Color online) Correlations obtained from experimental measurements on polymer formulations close to the water-adhesive phase boundary

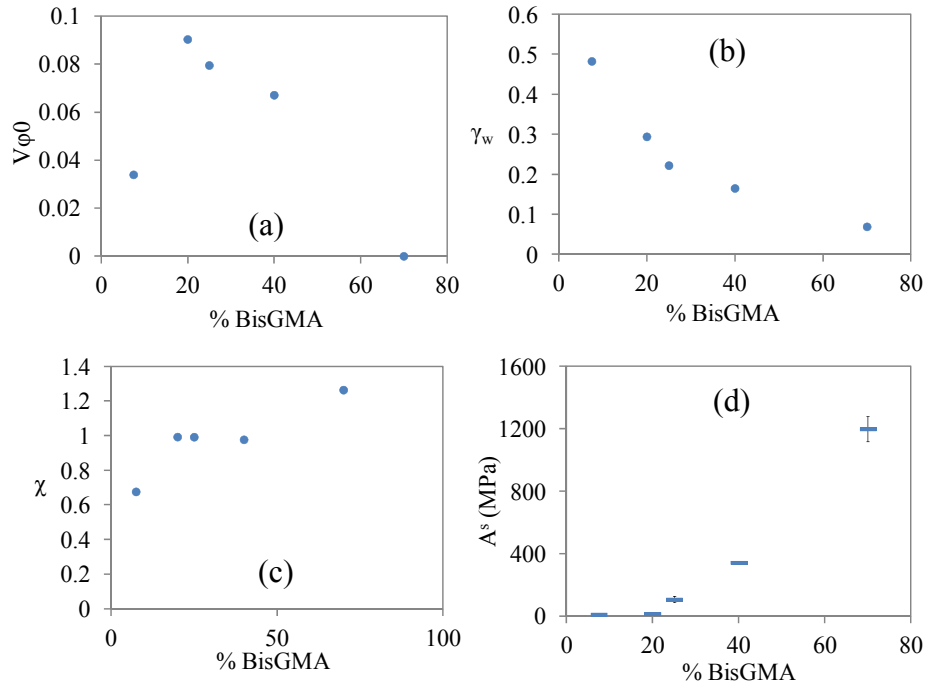


Figure 4-5 Variation of micromechanical properties with percentage of BisGMA

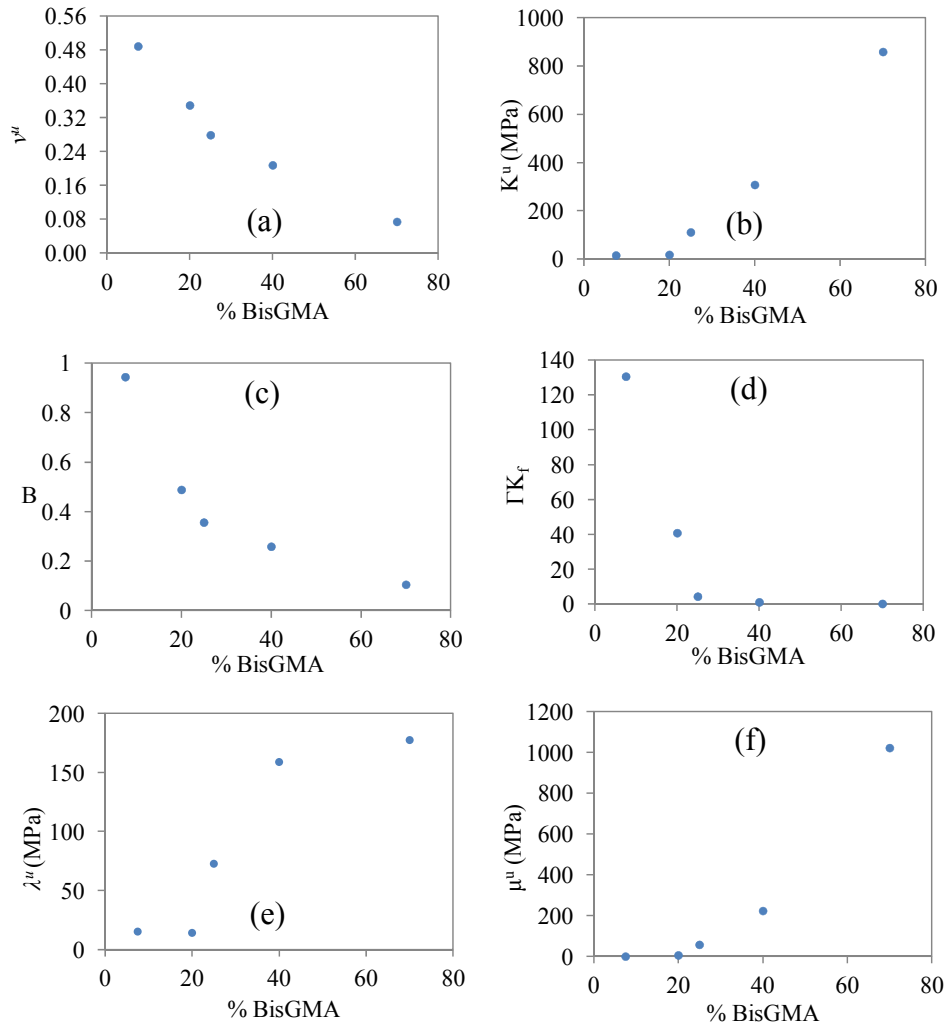


Figure 4-6 Correlation between derived mechanical properties and percentage of BisGMA

5 DIFFUSION COEFFICIENTS OF WATER AND LEACHABLES IN METHACRYLATE-BASED CROSSLINKED POLYMERS USING ABSORPTION EXPERIMENTS

The diffusion of water into dentin adhesive polymers and leaching of unpolymerized monomer from the adhesive are linked to their mechanical softening and hydrolytic degradation. Therefore, diffusion coefficient data are critical for the mechanical design of these polymeric adhesives. In this study, diffusion coefficients of water and leachables were obtained for sixteen methacrylate-based crosslinked polymers using absorption experiments. The experimental mass change data was interpreted using numerical solution of the two-dimensional diffusion equations. The calculated diffusion coefficients varied from $1.05 \times 10^{-8} \text{ cm}^2/\text{sec}$ (co-monomer TMTMA) to $3.15 \times 10^{-8} \text{ cm}^2/\text{sec}$ (co-monomer T4EGDMA). Correlation of the diffusion coefficients with crosslink density and hydrophilicity showed an inverse trend ($R^2 = 0.41$). The correlation of diffusion coefficient with crosslink density and hydrophilicity are closer for molecules differing by simple repeat units ($R^2 = 0.95$). These differences in the trends reveal mechanisms of interaction of the diffusing water with the polymer structure.

5.1 Introduction

The lack of effective and durable dentin adhesives is generally considered one of the major problems with the use of composites in direct restorative dentistry. Previous work has shown that the mechanical property of the adhesive not only effects the overall bond or shear strength but has a profound influence on the load transfer mechanism at the dentin-adhesive (a/d) interface and its fatigue life (Misra, Spencer et al. 2004, Misra, Spencer et al. 2005, Singh, Misra et al. 2011). In addition, the change in the mechanical property of the adhesive with time can

result in a gradual loss of the mechanical integrity of the a/d interface. The absorption of water by the adhesive polymer and leaching of unpolymerized monomer from the adhesive are linked to mechanical softening and hydrolytic degradation. Diffusion of water coupled with mechanical action can lead to various forms of failure such as brittle destruction or softening without loss of integrity (Rudakova and Zaikov 1987, Rudakova and Zaikov 1988). The viscoelastic properties of the adhesive, in particular, change anomalously with water content under loading (Misra, Singh et al. 2011, Singh, Misra et al. 2011). The rate at which these phenomena take place is directly dependent on the diffusion coefficients of water and leachable products in the polymer network of the cured adhesive.

The objective of the present work is to characterize the diffusion coefficients of water and leachable products for “model” methacrylate based dentin adhesives. To this end, absorption experiments were performed on 16 polymer formulations to record their mass change behavior. The experiments for this characterization are performed using deionized water in which the polymer structure interacts with the water molecule alone. These experiments are expected to provide a baseline data for future studies in simulated oral conditions. Diffusion experiments on dentin adhesives using water have also been conducted by other researchers (Sideridou and Papanastasiou 2007, Sideridou and Karabela 2008, Sideridou, Karabela et al. 2008, Costella, Trochmann et al. 2010, Sideridou and Karabela 2011). The dentin adhesive resins were prepared using 15 candidate co-monomers along with HEMA (2-hydroxyethyl methacrylate) and BisGMA (Bisphenol A glycerolate (1 glycerol/phenol) dimethacrylate). In the past, similar mass change measurements have been performed to determine the diffusion coefficient of water in polymers and dentin adhesives (Unemori, Matsuya et al. 2003, Malacarne, Carvalho et al. 2006, Sideridou and Karabela 2008, Costella, Trochmann et al. 2010, Tham, Chow et al. 2010, Hill and

Whittaker 2011). In these references, one-dimensional diffusion using Crank's solution for the fractional solute absorption was applied to disc specimens. In comparison, in the present paper, parallelepiped beam specimens have been utilized, which allows complementary measurements, including mechanical properties, on the same specimen. Since by nature, diffusion depends upon the sample geometry and boundary conditions, Crank's solution cannot be used to interpret ~~our~~ the measurements obtained, and a two-dimensional simulation of the diffusion process is required. The two-dimensional diffusion equations, describing combined water and leachable products diffusion, are solved using a finite difference scheme. The diffusion coefficients were determined using a nonlinear optimization to fit the measured mass change data. The obtained diffusion coefficients were correlated with the polymer crosslink density and hydrophilicity. It was found that crosslink density and hydrophilicity, which are closely related to the co-monomer structure, are the key parameters that control the diffusion phenomena for these polymers.

5.2 Materials and methods

5.2.1 Materials

The 16 “model” methacrylate based dentin adhesives were prepared as mixtures of BisGMA (Bisphenol A glycerolate (1 glycerol/phenol) dimethacrylate) and 2-hydroxyethylmethacrylate (HEMA, 99%) along with additional co-monomers. The co-monomers used were ethylene glycol dimethacrylate (EGDMA, 98%), 1,3-butanediol dimethacrylate (1,3-BDMA), 1,4-butanediol dimethacrylate (1,4-BDMA, 98%), bisphenol A ethoxylated dimethacrylate (BisEMA), diethylene glycol dimethacrylate (DEGDMA, 95%), 1,3-glycerol dimethacrylate (GDMA, 85%, mixture of isomers), triethylene glycol dimethacrylate (TEGDMA, 95%), trimethylolpropane trimethacrylate (TMTMA), diurethane dimethacrylate (UDMA, mixture of

isomers), tetraethylene glycol dimethacrylate (T4EGDMA), 1,6-hexanediol dimethacrylate (1,6-HDMA), were purchased from Sigma Chemical Co., St. Louis, MO, USA. Co-monomers glyceryl trimethacrylate (GTMA), pentaerythritol trimethacrylate (PETMA) and pentaerythritol dimethacrylate (PEDMA) were purchased from Monomer-Polymer and Dajac Labs, Trevose, PA, USA. Co-monomer neopentyl glycol dimethacrylate (NGDMA) was purchased from Sartomer, Exton, Pennsylvania, USA. The chemical structures of the co-monomers are shown in Table 5-1. The following three-component visible light photoinitiators (all from Aldrich, Milwaukee, WI) were used in this work: camphoroquinone (CQ, 0.5wt%), ethyl-4-(dimethylamino)benzoate (EDMAB, 0.5wt%) and diphenyliodonium hexafluorophosphate (DPIHP, 0.5wt%) without further purification. The concentration of the photoinitiator component is calculated with respect to the total amount of monomer. All materials were used as received.

5.2.2 *Methods*

Preparation of adhesive resins

Resin mixtures with a mass ratio of 45/30/25 (HEMA/BisGMA/co-monomer) with a 3 component photo-initiator system (0.5 mass percent of camphorquinone (CQ), ethyl-4-dimethylamino benzoate (EDMAB) and diphenyl iodonium phosphate (DPIHP) were prepared in brown vials using each of the co-monomers listed in the Materials section. The resin mixture with a mass ratio of 45/55 (HEMA/BisGMA) and 3 component photo-initiator system was used as a control. The preparation of the adhesive resin mixture using the control has been described previously (Singh, Misra et al. 2010). The resin mixtures were continuously shaken and sonicated at room temperature for 48 hours until a homogeneous mix was obtained.

Preparation of adhesive polymer beams

Square beams with a side of 1 mm and a length of at least 10 mm were prepared for each comonomer formulation by casting the prepared adhesive resins into glass-tubing molds (Fiber Optic Center Inc, #CV1012, Vitrocom Round Capillary Tubing of Borosilicate Glass). The adhesive resins were injected into the tubing using a micro-pipette and light polymerized with a LED light curing unit of intensity 250 mW/cm² and area 6.25 mm² for 9s (LED Curebox, Prototech, and Portland, OR). The polymerized samples were stored in dark at room temperature for two days to provide adequate time for post-cure polymerization. The samples were subsequently extracted from the glass tubing and stored in a vacuum oven in the presence of a drying agent (freshly dried silica gel) at 37°C.

Degree of Conversion

The degree of conversion (DC) was determined by Raman spectrometer as described previously (Park, Ye et al. 2009). In brief, LabRAM ARAMIS Raman spectrometer (LabRAM HORIBA Jobin Yvon, Edison, New Jersey) was used with a HeNe laser ($\lambda=633$ nm, a laser power of 17 mW) as an excitation source. The instrument settings were as follows: 200 μm confocal hole, 150 μm wide entrance slit, 600 gr/mm grating, and 10x objective Olympus lens. Data processing was performed using LabSPEC 5 (HORIBA Jobin Yvon). The samples were mounted on a computer-controlled, high-precision x-y stage. To determine the DC, spectra of the unpolymerized resins and rectangular beam samples were acquired over a range of 700 – 1800 cm^{-1} . The changes of the band height ratios of the aliphatic C=C double bond peak at 1640 cm^{-1} and the aromatic C=C at 1610 cm^{-1} (phenyl) in both the cured and uncured states were monitored. The DC was calculated as follows, based on the decrease in the intensity band ratios before and after light curing.

$$DC(\%) = \left[1 - \frac{R_{cured}}{R_{uncured}} \right] \times 100 \quad (5.1)$$

where R = band height at 1640 cm⁻¹/band height at 1610 cm⁻¹. All experiments were carried out in triplicate and the results were averaged.

Density Measurements

The densities of the vacuum dried adhesive polymers were measured using an analytical weighing balance with a resolution of 0.01 mg (Mettler Toledo, X205 dual range). The densities were obtained using the mass of the sample in air and in water as follows:

$$\rho = \frac{A}{A-B}(\rho_0 - \rho_L) + \rho_L \quad (5.2)$$

ρ =Density of sample, A=Weight of sample in air, B=Weight of sample in the auxiliary liquid (water), ρ_0 =Density of the auxiliary liquid (water), and ρ_L =Air density (0.0012 g/cm³). As can be seen, equation (2) incorporates an adjustment for the buoyancy provided by air.

Dynamic Mechanical Analysis

The measurement of glass transition temperature and apparent rubbery modulus was carried out using dynamic mechanical analysis (DMA Q800, TA Instruments, New Castle, USA) in a 3-point bending configuration. The analysis has been described previously (Park, Ye et al. 2009). The frequency used to measure the storage modulus was 1 Hz with amplitude of 15 μ m and a pre-load of 0.01 N. The storage modulus was measured across 0°C to 250°C using a temperature sweep. The temperature sweep was conducted at 3°C/min. The glass transition temperature was identified from the peak of the tan δ – temperature curve. The storage modulus decreased with temperature and reached an asymptote at the glass transition temperature. This asymptotic storage modulus was taken to be the apparent rubbery modulus of the polymer. The crosslink

density was calculated based on Flory's rubber elasticity theory (Krongauz 2010) as shown below:

$$\nu_e = \frac{E'}{3RT_g} \quad (5.3)$$

where E' is the apparent rubbery modulus, T_g is the glass transition temperature of the polymer, and the universal gas constant $R = 8.31 \text{ J K}^{-1}\text{mol}^{-1}$. Equation (3) is based on the kinetic rubber elasticity theory. It is not valid for high degrees of cross linking, but can be used when the storage modulus in the rubbery region is in the range of 2×10^6 and 2×10^8 Pa (Krongauz 2010). The storage moduli measured for the polymer formulations in this study were found to lie within this range. Therefore, equation (3) was applied to calculate the crosslink density.

Determination of LogP

The LogP values (ratio of solubility in octanol to solubility in water) for each of the co-monomers and the model adhesives were determined using ChemBioDraw Ultra 12.0 (CambridgeSoft from Perkin Elmer). The LogP value for each model adhesive formulation is was determined using the mole fraction-average of individual monomer values as shown below:

$$\text{LogP}_{\text{Total}} = x_{\text{HEMA}} \text{LogP}_{\text{HEMA}} + x_{\text{BisGMA}} \text{LogP}_{\text{BisGMA}} + x_{\text{co-monomer}} \text{LogP}_{\text{co-monomer}} \quad (5.4)$$

Alternatively, the overall LogP could also be calculated based on the mass fractions of each monomer in the formulation.

Absorption Experiment

Multiple beam specimens were used to study the water sorption behavior of each formulation. Distilled, deionized water (HPLC grade, W5SK-4, Fisher Scientific, Fair Lawn, NJ, USA) was used throughout the experiments. The beam specimens were placed into a vacuum chamber for drying until a constant mass m_1 was obtained. The specimens were then immersed in water and

stored in an incubator (Fischer Scientific – Isotemp incubator) at 37°C. At fixed time intervals (3, 5, 24, 48, 96, 168, and 240h), the specimens were retrieved, blotted dry to remove excess liquid, weighed (m_2), and returned to the liquid bath. The values (%) for mass change (W_{mc}), solubility (W_{su}) and water sorption (W_{sp}) were calculated as follows:

$$W_{mc} (\%) = \frac{m_2 - m_1}{m_1} \quad (5.5)$$

$$W_{su} (\%) = \frac{m_1 - m_3}{m_1} \quad (5.6)$$

$$W_{sp} = W_{mc} + W_{su} \quad (5.7)$$

Two-dimensional diffusion model

For the methacrylate based polymers, that can be described as low to moderately hydrophilic at low activities, Fick's law of diffusion and Henry's law for equilibrium sorption are known to be applicable (Ghi, Hill et al. 1997, ThomINETTE, Gaudichet-Maurin et al. 2007). Therefore, the diffusion of water into the adhesive polymer beam and the diffusion of unpolymerized monomer into the surrounding water are were both modeled using Fick's law. A similar method has been used by previous researchers to model mass change of methacrylate based polymers in water in a 1-dimensional context (Sideridou and Papanastasiou 2007, Sideridou and Karabela 2008).

For the water diffusion into the polymer matrix, Fick's law and the equation of continuity can be written as follows in terms of the local flux (\vec{j}), the diffusion coefficient (D_w) and the water concentration as mass per unit volume (u) :

$$\vec{j} = -D_w \vec{\nabla} u \quad (5.8)$$

$$\frac{\partial u}{\partial t} + \vec{\nabla} \cdot \vec{j} = 0 \quad (5.9)$$

Equations (8) and (9) can be combined into:

$$\frac{\partial u}{\partial t} = D_w \nabla^2 u \quad (5.10)$$

which was solved for the concentrations, u , under specified boundary and initial conditions. Since beam shaped samples with large aspect ratio are used, the end effects can be neglected and the problem can be simplified to be a planar diffusion process in a square domain. A central difference scheme is was used to discretize space coordinates and a backward difference scheme is was used to discretize time as follows.

$$\nabla^2 u \approx \frac{u_{i+1,j}^{t+1} - 2u_{i,j}^{t+1} + u_{i-1,j}^{t+1}}{(\Delta x)^2} + \frac{u_{i,j+1}^{t+1} - 2u_{i,j}^{t+1} + u_{i,j-1}^{t+1}}{(\Delta y)^2} \quad (5.11)$$

$$\frac{\partial u}{\partial t} \approx \frac{u_{i,j}^{t+1} - u_{i,j}^t}{\Delta t} \quad (5.12)$$

Where Δx and Δy are discretized intervals in space and Δt is the discretization in time.

Introducing equations (11) and (12) into equation (1), the discretized equation is was obtained as:

$$-\alpha_x [u_{i-1,j}^{t+1} + u_{i+1,j}^{t+1}] + [1 + 2\alpha_x + 2\alpha_y] u_{i,j}^{t+1} - \alpha_y [u_{i,j-1}^{t+1} + u_{i,j+1}^{t+1}] = u_{i,j}^t \quad (5.13)$$

$$\alpha_x = \frac{D_w \Delta t}{(\Delta x)^2} \quad (5.14)$$

$$\alpha_y = \frac{D_w \Delta t}{(\Delta y)^2} \quad (5.15)$$

Equation (13) is was then rearranged by assembling the two dimensional matrices u^t and u^{t+1} into vectors containing the concentrations by moving right to left along the matrix and concatenating all the rows. The matrix form of the equation was obtained as shown in equation (16).

$$KDw_{ij} u_j^{t+1} = u_j^t \quad (5.16)$$

where KDw_{ij} are the diffusion multipliers obtained from equation (13). The boundary

conditions state that the edges of the square are instantaneously saturated with water whose value

is given by Henry's law constants defined as dimensionless partition coefficients. To this end it is noted that the water sorption reaches a saturation value after 10 days (240 hours) of immersion. The partition coefficient was taken as the ratio of the concentration of water in the polymer at greater than 10 days (saturation) to the concentration of water in pure state.

$$H = \frac{c_s}{c_w} \quad (5.17)$$

where c_w is the mass per unit volume of pure water and c_s is the mass of water per unit volume of polymer when the polymeric matrix is saturated with water. The initial conditions state that the polymer sample interior is free of water at time $t=0$.

Because free-radical polymerization can vary the density of crosslinks in methacrylate-based polymers, the resulting spatial heterogeneity may facilitate the entrapment of residual monomers into the microgels, which will be leached out easily (Malacarne, Carvalho et al. 2006). It can be assumed that the elution was not a long-term process because of the small amount of components and the quick releasing at the early stage. Most of these leachable species are eluted quickly from polymerized resins within a few days (Ferracane 2006). It was assumed that the diffusion coefficients of these hydrophilic leachables are similar and could be treated as integrity for the model so that the difference in overall diffusion of leachables from those crosslinked copolymers can be compared in a straightforward manner. The unreacted hydrophobic components in the polymer diffused in a negligible amount into the aqueous solution during the time of absorbance experiments (Ye, Park et al. 2008, Ye, Park et al. 2011, Under Review). Sideridou et al. have also reported (Sideridou, Karabela et al. 2008) that a significant amount of hydrophobic monomer (BisGMA) still remained in the resins even after the second water sorption following a sorption-desorption cycle.

A similar approach as discussed above was used to solve the diffusion equation for the transport of leachable products from the polymer beam into the water. The governing differential equations and their discretized forms for diffusion of leachable products were written in an identical manner to equations (8)-(16), and shown in the Appendix. The diffusion of the leachable products was modeled with an equivalent diffusion coefficient D_L , which is a function of the diffusion coefficients and the weight fractions of potential hydrophilic leachables like unreacted monomers, initiator, additives and low molecular weight species (Kostoryz, Dharmala et al. 2009). The weights are the mass fractions of these products in the total mass of leachables. The boundary conditions state that the edges of the square leach out the leachables instantaneously and are at a zero concentration of leachable. The initial conditions state that leaching has not started at time $t=0$ in the polymer matrix interior. The total density of leachable in the polymer at $t=0$ was taken as the calculated total mass of leached product per unit volume of the polymer after 10 days.

The net mass change at a time, t , and a location, j , was given by the superposition of the mass increase due to the diffusion of water obtained from equation (16) and the mass decrease due to leaching given by equation (28) as shown in equation (18).

$$m_j^t = u_j^t + v_j^t \quad (5.18)$$

The simulated diffusion and net mass change at some time t following immersion in water are illustrated in Figure 1. Thus, the total mass change of the polymer per unit volume is given by the summation of the elemental mass changes over all the elements in the square cross-section.

$$M_j^t = \sum_j (u_j^t + v_j^t) \Delta x_j \Delta y_j \quad (5.19)$$

The percentage mass change was given by the total mass change per unit volume scaled by the density of the polymer as depicted in Figure 2. The diffusion coefficients for water and leachables for each polymer formulation were determined by minimizing the sum of squares error between the simulated mass change shown in equation (19) and the experimentally observed mass change described in section 2.2.7. The Nedler-Mead simplex direct search method was used for the optimization.

5.3 Results

5.3.1 Degree of Conversion, Density, partition coefficients and Density of Leachables

Clearly, the chemical structure of methacrylate monomers used in this study has an important role in the behavior of diffusion and partition coefficients. Therefore, a subset of the polymer formulations was collected into 2 groups and the remaining were studied individually. Group 1 consisted of co-monomers with different lengths of ethylene oxide unit between methacrylate groups. Group 2 consisted of co-monomers with different number of aliphatic carbons (branched or straight chain) between the methacrylate groups. Table 5-1, Table 5-2 and Table 5-3 give the degree of conversion (DC), polymerized adhesive density, partition coefficient of water and density of leachables in polymerized adhesive for group 1, group 2 and the remaining formulations, respectively. The range of variation obtained in the various physical, chemical and mechanical properties indicates that the data is suitable for understanding chemical structure-property trends. Small standard deviation in the measured properties was obtained for each formulation showing the uniformity of sample preparation and experimental methods.

The DC of all the polymerized dentin adhesives was found to be in the narrow range of 83% to 93%. The solubility values ranged from 0 to 4.82%. The solubility was found to be uncorrelated

to the degree of conversion. However, a weak trend of decrease in solubility with LogP was observed. This trend is consistent with the fact that more hydrophilic formulations are also more likely to leach out. The water sorption of the different formulations varied from 6.74 to 12.21 %. The densities of all the dentin adhesives were close to 1.2 g/cm³. The water sorption values, scaled with the corresponding densities were converted into partition coefficients, as described in section 2.2.8. The LogP values were calculated as described in section 2.2.6 and found to vary from 1.07 to 1.8. The LogP values decrease with the hydrophilicity of the co-monomers, as expected. BH+PEDMA with two hydroxyl groups in PEDMA has the lowest LogP. It is noteworthy, though, that BH+PEDMA also has a relatively low diffusion coefficient. In group 1, BH+EGDMA has the lowest value of sorption and highest values for rubbery modulus and crosslink density. The sorption values, rubbery modulus and crosslink density respectively decrease, increase and increase with the number of ethylene oxide chains and the hydrophilicity indicated by LogP. The glass transition temperature did not show a clear trend. In group 2, the solubility and sorption were seen to decrease with the crosslink density. 1, 6-HDMA, which has an open chain structure, has the lowest crosslink density and the highest values for sorption and solubility. BH+1, 3-BDMA where 1,3-BDMA has a branched chain structure, has the highest rubbery modulus, glass transition temperature and crosslink density. The rubbery modulus is significantly lower for the formulation with its structural isomer, 1, 4-BDMA due to its open chain structure. The solubility is again, observed to be lower for both 1, 3 and 1, 4-BDMA. Among the other formulations, the trimethacrylate monomers are found to increase the crosslink density, as expected. GTMA has the highest crosslink density and correspondingly, the lowest sorption and solubility.

5.3.2 Absorption experiments and simulation using mathematical model

Absorption results for all the model adhesives up to 10 days are shown in Figure 3. The absorption curves are characterized by a peak and a post-peak reduction to a final equilibrium mass change. It can be observed that the measured peak mass change data typically occurred at ~24 hrs and the asymptote was reached at ~100 hrs. The post-peak reduction is attributable to diffusion of leachables, which are expected to have a smaller diffusion coefficient due to their size. Clearly, the water diffusion coefficients would be under-estimated, if they were based on water sorption data alone (i.e., increases in wet mass). Since net increase in wet mass must occur simultaneously with loss of dry mass due to simultaneous solubilization of unreacted monomers, the true water absorption is greater than the measured mass change. The observed peak in the mass change curve was found to be absent in the results for a pre-washed control sample (unpublished data). This shows that the loss of leachables is the only factor contributing to this peak. Similar findings have been reported by other investigators (Sideridou and Karabela 2008).

The fitted percentage mass change curves for the various dentin adhesive polymer formulations are also shown in Figure 3. It can be seen that a good match (R^2 ranges from 0.88 to 0.996) is obtained between the simulated and measured mass change for most of the dentin adhesives, which shows that Fickian diffusion is a reasonable assumption for methacrylate based polymers. Table 5-6 gives the fitted diffusion coefficients of water and leachable products in the polymerized adhesives. The diffusion coefficients of water were found to range from 1.06 to 3.15×10^{-8} cm²/s. These values are similar to those reported in the literature for other methacrylate based dentin adhesives (Sideridou, Karabela et al. 2008, Costella, Trochmann et al. 2010). The diffusion coefficients of leachables were found to be generally an order of magnitude

smaller than the diffusion coefficients of water. However, they exhibited a larger range from 6.41×10^{-10} to 2.21×10^{-8} cm²/s.

5.4 Discussion

The control dentin adhesives used in this work were a mixture of a modern hydrophobic component (BisGMA) and hydrophilic components (HEMA). The composition was based on conventional dentin adhesives (Pashley and Zhang 1998, Spencer and Wang 2002). There is concern that the effects of liquid uptake and hydrolytic degradation may lead to a shortened service life of dental restorations. There is also concern regarding the biological effects elicited by the species evolved from dentin resin restorations, thus requiring the effects of liquid uptake to be investigated (Ferracane 2006).

The different model adhesive formulations were tested as candidate dentin adhesives. The coefficients of diffusion for water and for leachables in the polymer network are closely linked to the failure of the adhesive through mechanical softening and hydrolytic degradation. Since the adhesives function at the normal temperature of the human body, the absorption experiments were performed at 37 degrees Celsius. The diffusion coefficients for water transport and leaching have been determined for each of the co-monomer formulations. The diffusion coefficients were correlated to the crosslink density and hydrophilicity of the polymers.

5.4.1 Factors affecting diffusion and partition coefficients

The factors which can influence the diffusion coefficient of a solvent in crosslinked polymers have been studied by various researchers (Amsden 1998, Wu, Joseph et al. 2009, Krongauz 2010). It has been reported that the diffusion of a solvent through a crosslinked polymer network is not only due to diffusion through narrow channels. Solvent diffusion also involves restriction

of polymer chain motion and interaction of the solvent with the functional groups in the polymer structure (Yiu, King et al. 2006, Krongauz 2010). The diffusion takes place because of the difference in chemical potential or difference in Gibbs free energy between the solvent in the polymer and the pure solvent. The Gibbs free energy can be separated into two components – the free energy of mixing and the energy associated with expansion of the polymer network. The expansion of the network is related to the restriction of polymer chain motion by crosslinks and the free energy of mixing can be represented by the Flory interaction parameter. The formation of hydrogen bonds of the diffusing water with specific sites on the polymer network can also significantly influence the value of the diffusion and partition coefficients. Swelling of the polymer is another factor which can decrease diffusion rate since diffusion in swollen polymers is almost always slower than diffusion in pure solvent (Krongauz 2010). Intra-molecular hydrogen bonds in the polymer may also play a significant role (Bellenger, Verdu et al. 1989). In addition, there could be other factors specific to certain molecular structures.

Previous investigators have explained the diffusion and partition coefficient behavior either by the free-volume theory which accounts for the phenomenon of the solute molecule diffusing through the pore spaces or by the interaction theory which accounts for the interaction of the solute molecule with the chemical structure and the formation of hydrogen bonds at specific sites during the diffusion process (Bellenger, Verdu et al. 1989, Unemori, Matsuya et al. 2003, Yiu, King et al. 2006).

The data is analyzed first for the effect of site-specific hydrogen bond formation. Figure 4 shows that the diffusion coefficient and partition coefficient have a positive correlation when all the polymer formulations are considered together (with $R^2 = 0.86$ for a linear fit to the data). This shows that when the entire data set is considered together, the contribution of site-specific

hydrogen bonds is minimal on an average i.e. the influence of water molecules fixing to specific sites during the process of diffusion is minimal.

The data is then analyzed with respect to the diffusion dependence on interaction with the polymer functional groups and expansion of polymer network. The interaction of the solute with the functional groups in the polymer is represented using mole average LogP (hydrophilicity) and the effect and stiffness of polymer network structure is represented by crosslink density, obtained from DMA analysis. Diffusion coefficient and partition coefficient both show a decreasing trend with LogP and with crosslink density as shown in Figure 5. The negative correlation of diffusion and partition coefficient with crosslink density is not unexpected since the activation enthalpy associated with the polymer fraction-dependent portion of the swollen network increases with crosslink density (Krongauz 2010). Similarly, the negative correlation between diffusion coefficient, partition coefficient and LogP is attributable to an increase in the interaction energy, with hydrophobicity or LogP.

Based on Krongauz et al. (Krongauz 2010), the diffusion coefficients of small molecules in crosslinked polymers have an exponential dependence on the polymer-solvent interaction energy as well as the free energy of polymer chain extension. Therefore, the variation in diffusion coefficients can be modeled using an exponential dependence on the hydrophilicity as well as the crosslink density as shown in equation (20).

$$D_w = Ce^{A*CLD+B*(LogP)} \quad (5.20)$$

where CLD= crosslink density, A, B and C = fitting constants. Table 5-4 gives the fitting constants and the goodness of fit parameter R^2 for the entire set of polymers, group 1 and group 2 polymers, respectively. The inverse trend of diffusion coefficient with crosslink density and LogP can be observed from the negative values of A and B when the fit is made for the entire dataset and confirms the trends observed in Figure 5. Since the data involves co-monomer

molecules that have different structures and functional groups there is considerable scatter in the data as shown by the low R^2 (= 0.41). The values of AxCLD and BxLogP can be observed to compare the relative their relative contributions in describing the diffusion coefficient.

5.4.2 Effect of co-monomer structure

Properties of formulations from groups 1 and 2 with the chemical structures of the corresponding co-monomers are shown in Table 5-1 and Table 5-2. The remaining formulations are shown in Table 5-3. The relationships of diffusion and partition coefficient with crosslink density and LogP are shown in Figures 6 and 7 for groups 1 and 2, respectively. In group 1, the diffusion and the partition coefficients, were both seen to decrease with logP value, which is inversely proportional to hydrophilicity as shown in Figures 6(c) and (d). This effect can be explained based on the fact that increasing hydrophilicity aids in decreasing the activation energy required for diffusion by helping the water molecules to overcome the attractive forces between themselves. Similar relationships were also observed by Yiu *et al.* and Malacarne *et al.* (Malacarne, Carvalho et al. 2006, Yiu, King et al. 2006). On the other hand the diffusion and the partition coefficients, were not observed to show any specific trend with crosslink density. The crosslink density values of BH+DEGDMA, BH+TEGDMA and BH+T4EGDMA were not significantly different ($p=0.285$) from each other. Therefore, the observed difference in diffusion (and partition) coefficients may be mainly attributed to the differences in hydrophobicity (LogP). BH+EGDMA has a much higher crosslink density than the other three formulations in the group. However, the diffusion and partition coefficients of BH+EGDMA are still observed to follow the same trend as the other three in their dependence on LogP. This also shows that the effect of crosslink density on diffusion and partition coefficients is minimal for this group and the majority of the dependence is on the hydrophobicity. A comparison of the values of (BxLogP)

and (AxCLD) in group 1, shown in Table 5-5, further confirms that the majority of the variance in data in this group can be explained using hydrophilicity. Also, since the partition and diffusion coefficients show similar trends for this group, these results may be interpreted to suggest that the formation of site specific hydrogen bonds is minimal (Unemori, Matsuya et al. 2003, Yiu, King et al. 2006).

From the values of (AxCLD) and (BxLogP) for group 2, shown in Table 5-5, it is observed that, similar to group 1, the hydrophilicity has a stronger influence on the diffusion behavior as compared to the crosslink density. However, the percentage of variance in the diffusion coefficients explained by crosslink density and hydrophilicity is less than group 1. This is expected since the co-monomer chemical structures in group 1 differ by a simple repeating unit of ethylene oxide, while those in group 2 differ in a more complex way. A major difference in group 2 is that the diffusion coefficient shows a positive correlation with LogP, or a negative correlation with hydrophilicity. This phenomenon may be due to various confounding factors discussed subsequently.

It is seen from Figures 7(a) and 7(b) that the diffusion coefficient and partition coefficient decrease with the crosslink density. However, by comparing the contributions of crosslink density and hydrophilicity for this group from Table 5-5, and noting the positive sign of A, this decrease may be termed not causal. The diffusion coefficients of BH+1,3-BDMA, BH+1,4-BDMA and BH+EGDMA are similar while that of BH+1,6-HDMA is substantially different from these three and from BH+NGDMA. The variation of the partition coefficients with hydrophilicity is not straightforward. From Figures 7(a) and 7(b) it can be seen that BH+NGDMA has a much lower diffusion coefficient than BH+1,6-HDMA though they are close in terms of both crosslink density and hydrophilicity. The lower diffusion coefficient could also

is likely due to the branched chain structure of BH+NGDMA as compared to the straight chain structure of BH+1,6-HDMA. Thus, in some cases, the packing density, or free volume, which is dependent upon the chemical structure, might also play an important role in determining the diffusive behavior of water. In this case, there could be a more complex interplay of the diffusing water with these polymeric structures, possibly involving hydrogen bonding. In addition, Figure 4 shows that the diffusion coefficients do not show an increasing trend with the partition coefficient, considering the pairs of 1,6-HDMA and NGDMA or 1,3-BDMA, 1,4-BDMA and EGDMA, which may again point to possible bonding of the diffusing water molecule with the polymeric structure. Other comparisons can also be made based upon similarity of chemical structures from Table 5-3. For instance, the co-monomer molecules of BH+GDMA and BH+PEDMA have similar chemical structures. However, the former resin molecule contains two hydroxyl groups in comparison to one hydroxyl group in BH+GDMA. In similarity to group 2, the diffusion coefficient and partition coefficient of BH+PEDMA is much lower than that of BH+GDMA. In this case, the formation of internal polymer-water hydrogen bonds within the polymer network which could restrict the movement as well as accumulation of water through the polymer network can play a significant role. This is the likely reason why PEDMA appears as an outlier on the overall plots of diffusion and partition coefficients versus LogP. The formulations BH, BH+BisEMA and BH+UDMA showed a similar trend as observed by others (Sideridou and Karabela 2008).

The diffusion coefficients of the leachables of the polymers are seen to follow similar but not exactly the same trends as the diffusion coefficients of water in the polymer. For comparison the diffusion coefficients of the leachables for groups 1 and 2 are shown in Figures 8 and 9. The diffusion coefficients for the leachables are seen to be an order of magnitude less than the

diffusion coefficients for water. It has been observed that the diffusivity of a solute through a crosslinked polymer structure decreases exponentially with solute size, as recently observed by Zustiak *et al.* (Zustiak and Leach 2011). The leached products probably consist of unpolymerized monomer and filler material, which are large molecules compared to water. Also, the similarity in the trends of the diffusion coefficient of water as well as diffusion coefficient of leachables supports the assumption that the unreacted hydrophobic components in the polymer diffused in a negligible amount into the aqueous solution during the time of the absorbance experiments. The difference in order of magnitude may be attributed to the size of the effusing molecules.

5.5 Conclusions

The agreement between the measured and fitted mass change data of the polymer formulations shown in Figure 3 indicate that the diffusion of water as well as leachables within the polymer network is predominantly Fickian in nature. Based on the observed trends, the diffusion coefficients, crosslink density and hydrophilicity were found to be suitable predictors of diffusion in methacrylate based crosslinked polymers. A study of the exponential fit between the diffusion coefficients and the predictors revealed their relative influence on the diffusion coefficients. In general, the hydrophilicity is found to have a greater influence on the diffusion behavior of water in methacrylate based dentin adhesive polymers investigated in this paper. The approximately linear positive correlation brought out between diffusion and partition coefficients indicates that the formation of hydrogen bonds of the solute with the polymeric structure during diffusion is minimal. Some of the polymer formulations have been grouped based on chemical structure of the co-monomer.

There is ongoing research in our group towards the identification of suitable dentin adhesives for composite restorations. It has been shown that the phenomenon of anomalous or accelerated creep occurs only when there is diffusion of the solvent into the polymer matrix and not when the sample is in a dry or fully saturated state (Singh, Misra et al. 2011). Further, the extent of anomalous creep is directly influenced by the rate of sorption of solvent into the polymer matrix (Habeger, Coffin et al. 2001). To this end, the diffusion coefficients calculated in this paper will aid in the mechanical design of the adhesive based composite restoration under dynamic loading. The trends developed for the variation of the diffusion coefficient with crosslink density and hydrophilicity will assist in development of structure-property relationships and identification of candidate monomers for development of these dentin adhesives.

Appendix:

The diffusion of leachables is explained in a similar way to water diffusion. The governing equations for leaching are given in terms of the local flux (\vec{j}), the diffusion coefficient (\bar{D}) and the concentration of leachable (v) as follows:

$$\vec{j} = -D_L \bar{\nabla} v \quad (5.21)$$

$$\frac{\partial v}{\partial t} + \bar{\nabla} \cdot \vec{j} = 0 \quad (5.22)$$

$$\nabla^2 v \approx \frac{v_{i+1,j}^{t+1} - 2v_{i,j}^{t+1} + v_{i-1,j}^{t+1}}{(\Delta x)^2} + \frac{v_{i,j+1}^{t+1} - 2v_{i,j}^{t+1} + v_{i,j-1}^{t+1}}{(\Delta x)^2} \quad (5.23)$$

$$\frac{\partial v}{\partial t} \approx \frac{v_{i,j}^{t+1} - v_{i,j}^t}{\Delta t} \quad (5.24)$$

$$-\beta_x [v_{i-1,j}^{t+1} + v_{i+1,j}^{t+1}] + [1 + 2\beta_x + 2\beta_y] v_{i,j}^{t+1} - \beta_y [v_{i,j-1}^{t+1} + v_{i,j+1}^{t+1}] = v_{i,j}^t \quad (5.25)$$

$$\beta_x = \frac{D_L \Delta t}{(\Delta x)^2} \quad (5.26)$$

$$\beta_y = \frac{D_L \Delta t}{(\Delta y)^2} \quad (5.27)$$

Assembling the system of discretized equations gives the form shown below.

$$KDL_{ij}v_j^{t+1} = v_j^t \quad (5.28)$$

KDL_{ij} are the diffusion (leachable) multipliers obtained from equation (25).

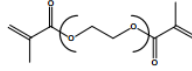
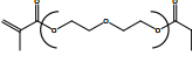
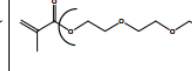
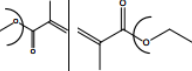
Group 1				
Chemical Name	Ethylene glycol dimethacrylate	Diethylene glycol dimethacrylate	Triethylene glycol dimethacrylate	Tetraethylene glycol dimethacrylate
Abbreviation	EGDMA	DEGDMA	TEGDMA	T4EGDMA
Degree of Conversion (%)	88.0±0.0	92.5 ±0.8	92.7±0.6	92.5±0.8
Sorption (%)	7.4±0.17	8.59±0.09	9.03±0.3	12.2±0.98
Solubility (%)	1.8±0.34	0.9±0.21	0.6±0.17	3.53±0.95
Rubbery Modulus (x 10 MPa)	108±8.06	38.8±3.21	35.3±5.77	38.5±6.82
Glass transition temperature (°C)	130.7±7.7	152.8±0.7	141.1±1.1	131.2±2.6
Crosslink Density (molm ⁻³)	10719.3±205.6	3660±319	3420±587	3820±753
Partition Coefficient	0.09±0.0022	0.107±0.0012	0.109±0.0091	0.146±0.0
Density (g/cm ³)	1.238±0.01	1.242±0.01	1.204±0.05	1.232±0.01
Leachable Density (x 10 ⁻² g/cm ³)	2.23±0.44	1.12±0.27	0.72±0.23	4.36±1.21
Log P (mol avg.)	1.295	1.243	1.203	1.175
D of water (x 10 ⁻⁸ cm ² /sec)	1.36	1.891	2.16	3.148
D of leachable (x 10 ⁻⁹ cm ² /sec)	2.184	3.162	1.733	3.526

Table 5-1 Chemical structures and experimental parameters for the polymerized dentin adhesives in group 1 (the mean values plus and minus the standard deviation of at least three replicates are shown).

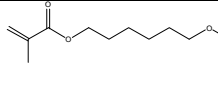
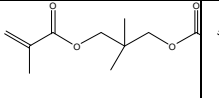
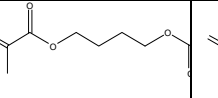
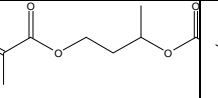
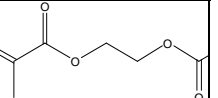
Group 2					
Chemical Name	1,6-hexanediol dimethacrylate	Neopentyl glycol dimethacrylate	1,4-butanediol dimethacrylate	1,3-butanediol dimethacrylate	Ethylene glycol dimethacrylate
Abbreviation	1,6-HDMA	NGDMA	1,4-BDMA	1,3-BDMA	EGDMA
Degree of Conversion (%)	91.5±0.9	88.5±3.0	91.7±0.4	89.6±0.1	88.2±0.5
Sorption (%)	9.25±0.48	9.95±0.98	6.9±0.15	7.2±0.04	7.40±0.17
Solubility (%)	2.66±0.27	2.75±0.75	0.80±0.26	0.9±0.05	1.80±0.34
Rubbery Modulus (x 10 MPa)	56.9±9.9	54.9±7.93	81.8±5.69	154.0±2.57	108±8.06
Glass transition temperature (°C)	150.0±4.8	168.3±2.0	147.8±4.3	153.7±2.6	130.7±7.7
Crosslink Density (molm ⁻³)	5400±111	4990±779	7790±771	18500±1840	10800±1440
Partition Coefficient	0.112±0.00	0.107±0.0045	0.084±0.0018	0.088±0.00	0.09±0.0022
Density (g/cm ³)	1.208±0.01	1.208±0.02	1.221±0.01	1.222±0.00	1.238±0.01
Leachable Density (x 10 ⁻² g/cm ³)	3.21±0.35	3.32±0.97	0.98±0.33	1.10±0.06	2.23±0.44
LogP (mol avg.)	1.543	1.524	1.4	1.372	1.295
D of water (x 10 ⁻⁸ cm ² /sec)	1.721	1.497	1.358	1.406	1.36
D of leachable (x 10 ⁻⁹ cm ² /sec)	7.456	4.634	7.931	1.026	2.184

Table 5-2 Chemical structures and experimental parameters for the polymerized dentin adhesives in group 2 (the mean values plus and minus the standard deviation of at least three replicates are shown).


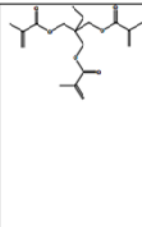
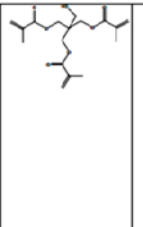

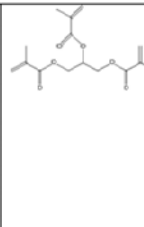
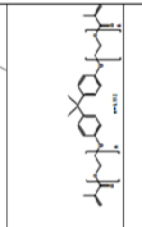
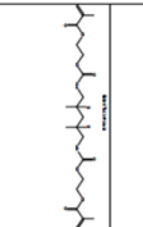
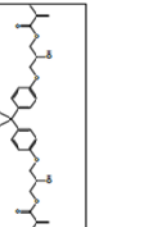
Other monomers								
Chemical Name	Pentaerythritol dimethacrylate	Trimethylolpropane trimethacrylate	Pentaerythritol trimethacrylate	1,3-glycerol dimethacrylate	Glyceryl trimethacrylate	Bisphenol A ethoxylate dimethacrylate	Diurethane dimethacrylate	Bisphenol A-glycerolate dimethacrylate
Abbreviation	PEDMA	TMTMA	PETMA	GDMA	GTMA	BisEMA	UDMA	BisGMA
Degree of Conversion (%)	88.4±0.9	85.9±1.9	84.0±1.5	89.6±0.4	84.2±1.6	93.4±0.4	92.8±0.3	88.0±0.0
Sorption (%)	9.25±0.09	6.93±0.26	10.2±0.44	9.89±0.53	6.74±0.09	7.51±0.2	7.61±0.2	7.5±0.12
Solubility (%)	2.88±0.45	2.00±0.05	4.82±0.96	1.10±0.27	1.00±0.14	1.10±0.26	0±0.16	0.3±0.02
Rubbery Modulus (x 10 MPa)	55.3±5.68	186±25.4	122±18.4	69.8±9.57	38.8±3.21	18.9±1.75	22.6±2.53	24.1±3.14
Glass transition temperature (°C)	154.7±8.2	156±2.6	155.2±4.1	166.0±1.2	164.2±3.3	111.1±1.9	130.6±0.8	142.0±1.8
Crosslink Density (molm ⁻³)	5190±807	17400±266	11400±2050	6830±923	26400±190	1980±216	2250±264	2330±333
Partition Coefficient	0.102±0.0019	0.087±0.0013	0.113±0.0115	0.124±0.0015	0.085±0.0019	0.092±0.0028	0.092±0.0025	0.105±0.0037
Density (g/cm ³)	1.204±0.01	1.236±0.01	1.227±0.06	1.257±0.01	1.259±0.01	1.224±0.2	1.215±0.01	1.206±0.02
Leachable Density (x 10 ⁻² g/cm ³)	3.47±0.57	2.47±0.07	5.91±1.44	1.38±0.34	1.26±0.19	1.35±0.33	0.00±0.00	0.36±0.02
Log P (mol avg.)	1.067	1.529	1.276	1.166	1.373	1.767	1.800	1.738
D of water (x 10 ⁻⁶ cm ² /sec)	1.532	1.060	2.542	2.382	1.172	1.563	1.334	1.882
D of leachable (x 10 ⁻⁶ cm ² /sec)	4.445	3.048	7.33	22.13	1.769	0.6412	2.003	0.7882

Table 5-3 Chemical structures and experimental parameters for the polymerized dentin adhesives from formulations other than groups 1 and 2 (the mean values plus and minus the standard deviation of at least three replicates are shown).

	A	B	C	R ²
All Formulations	-2.5E-05	-0.66971	5.25 x 10 ⁻⁸	0.411774
Group1	1.62E-05	-7.37943	1.62 x 10 ⁻⁴	0.945942
Group 2	1.67E-06	0.851354	4.27 x 10 ⁻⁹	0.703179

Table 5-4 Parameters from exponential fit for diffusion coefficients

Sample	Crosslink Density (molm ⁻³)	LogP (mol avg)	A x CLD	B x LogP
Group 1				
C + EGDMA	10719.3	1.2953	0.1736534	9.5589374
C + DEGDMA	3645.4	1.2427	0.0590549	9.1705939
C + TEGDMA	3410.0	1.2034	0.0552418	8.8805204
C + T4EGDMA	3807.5	1.1745	0.0616807	8.6672397
Group 2				
C + 1,6- HDMA	5382.1	1.5426	0.0898807	1.3132946
C + NGDMA	4978.3	1.5237	0.0831374	1.2971794
C + 1,4-BDMA	7771.5	1.4000	0.1297844	1.1919078
C + 1,3-BDMA	5595.8	1.3720	0.0934505	1.1680462
C + EGDMA	10719.3	1.2953	0.179013	1.1028006

Table 5-5 Relative contribution of crosslink density and hydrophilicity towards diffusion coefficient

	Diffusion coefficient of water (cm ² /sec)	Diffusion coefficient of leachable (cm ² /sec)
BH-Control	1.881E-08	7.831E-09
T4EGDMA	3.150E-08	3.530E-09
NGDMA	1.496E-08	4.634E-09
PETMA	2.542E-08	7.330E-09
PEDMA	1.531E-08	4.445E-09
1,6-HDMA	1.721E-08	7.467E-09
EGDMA	1.360E-08	2.184E-09
DEGDMA	1.891E-08	3.161E-09
TEGDMA	2.160E-08	1.733E-09
GDMA	2.382E-08	2.212E-08
GTMA	1.172E-08	1.769E-09
1,3-BDMA	1.406E-08	1.026E-09
1,4-BDMA	1.358E-08	7.931E-10
BisEMA	1.563E-08	6.412E-10
TMTMA	1.060E-08	3.048E-09
UDMA	1.334E-08	2.003E-09

Table 5-6 Fitted diffusion coefficients of the polymerized dentin adhesives

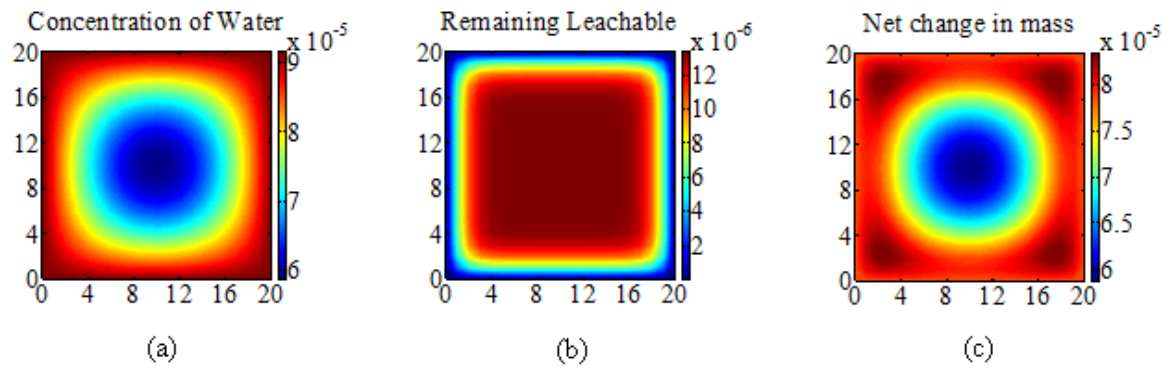


Figure 5-1 Simulated (a) diffusion of water (b) diffusion of leachables and (c) net mass change contours (g/mm^3) at time t after immersion in water

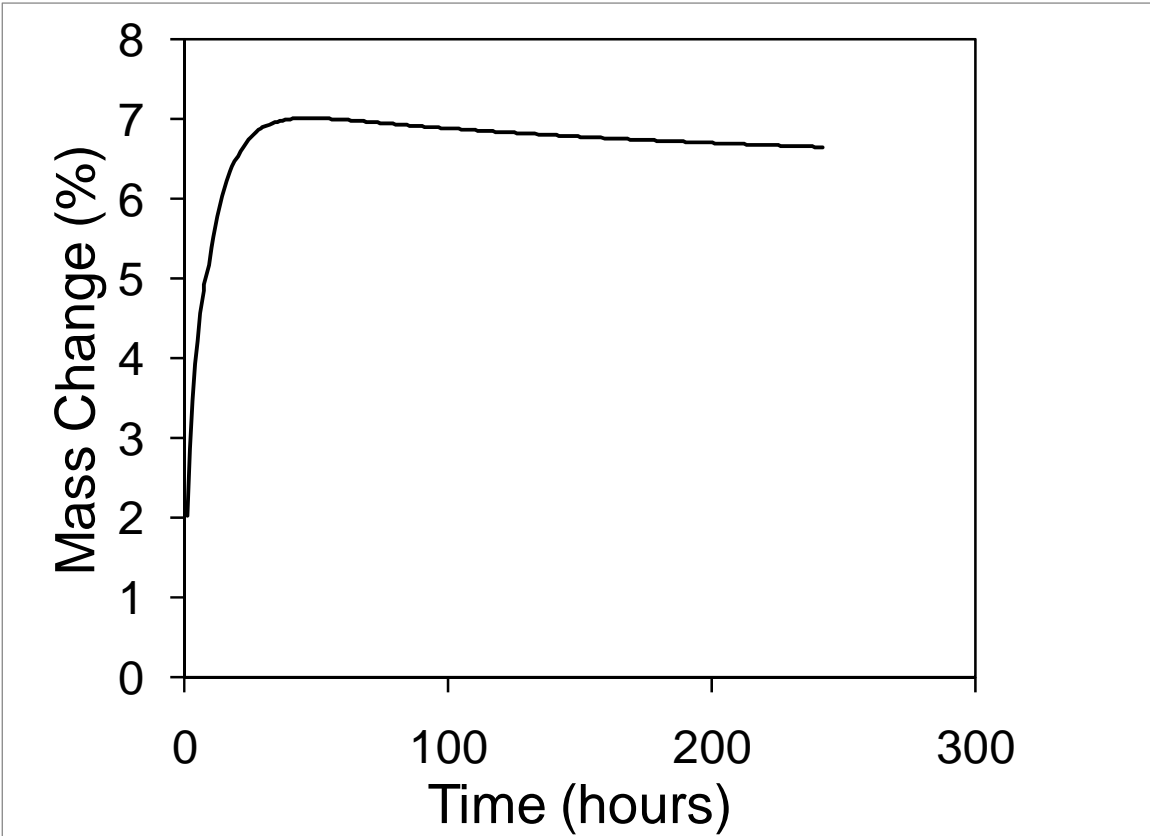
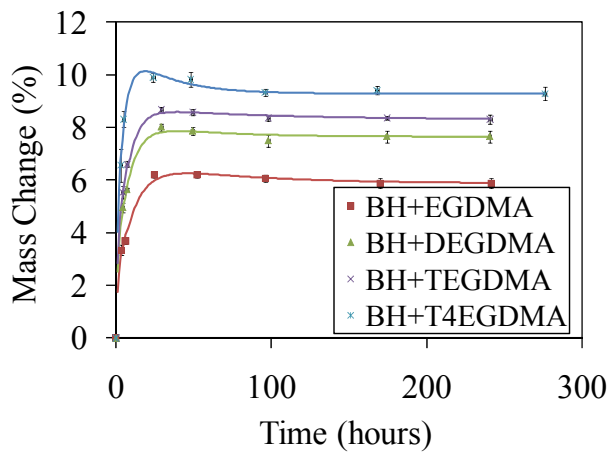
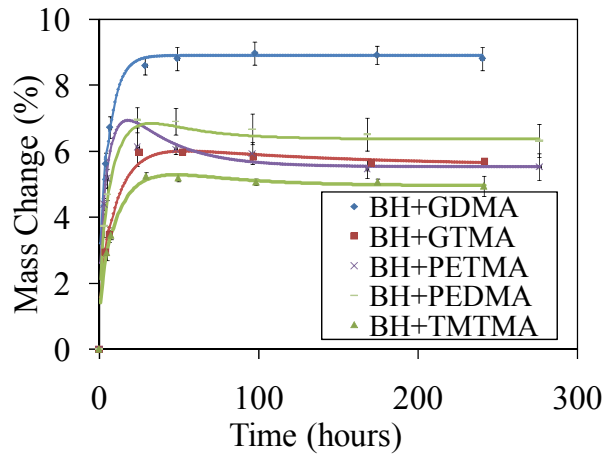


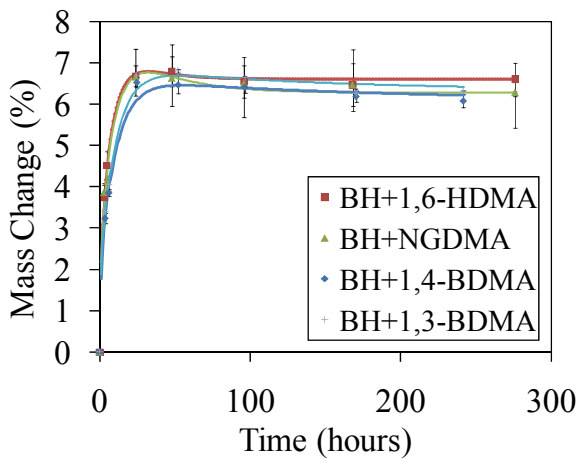
Figure 5-2 Example of net mass change versus time curve for a polymer beam specimen



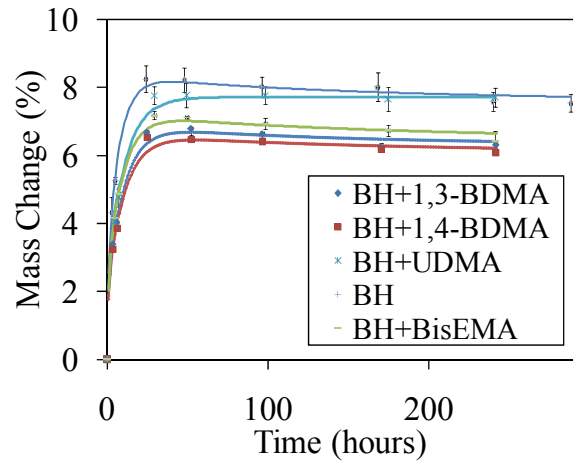
(a)



(b)



(c)



(d)

Figure 5-3 Variation of mass changes with time for water sorption sixteen adhesive formulation beam specimens at 37°C (the discrete points show the experimental data and the continuous curves show the fit using the mathematical model)

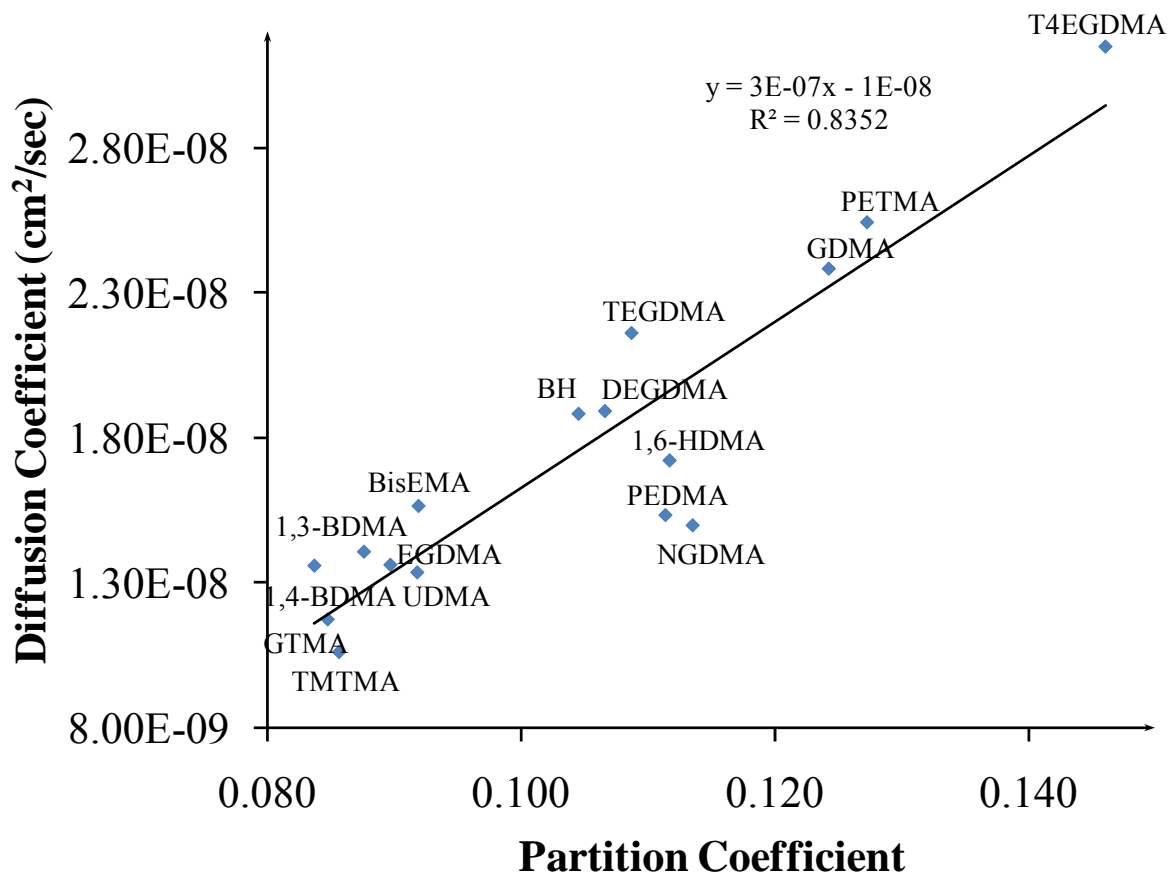


Figure 5-4 Correlation between diffusion and partition coefficients for all the sixteen adhesive formulations. The co-monomer name is used to represent the polymeric formulation (BH+co-monomer)

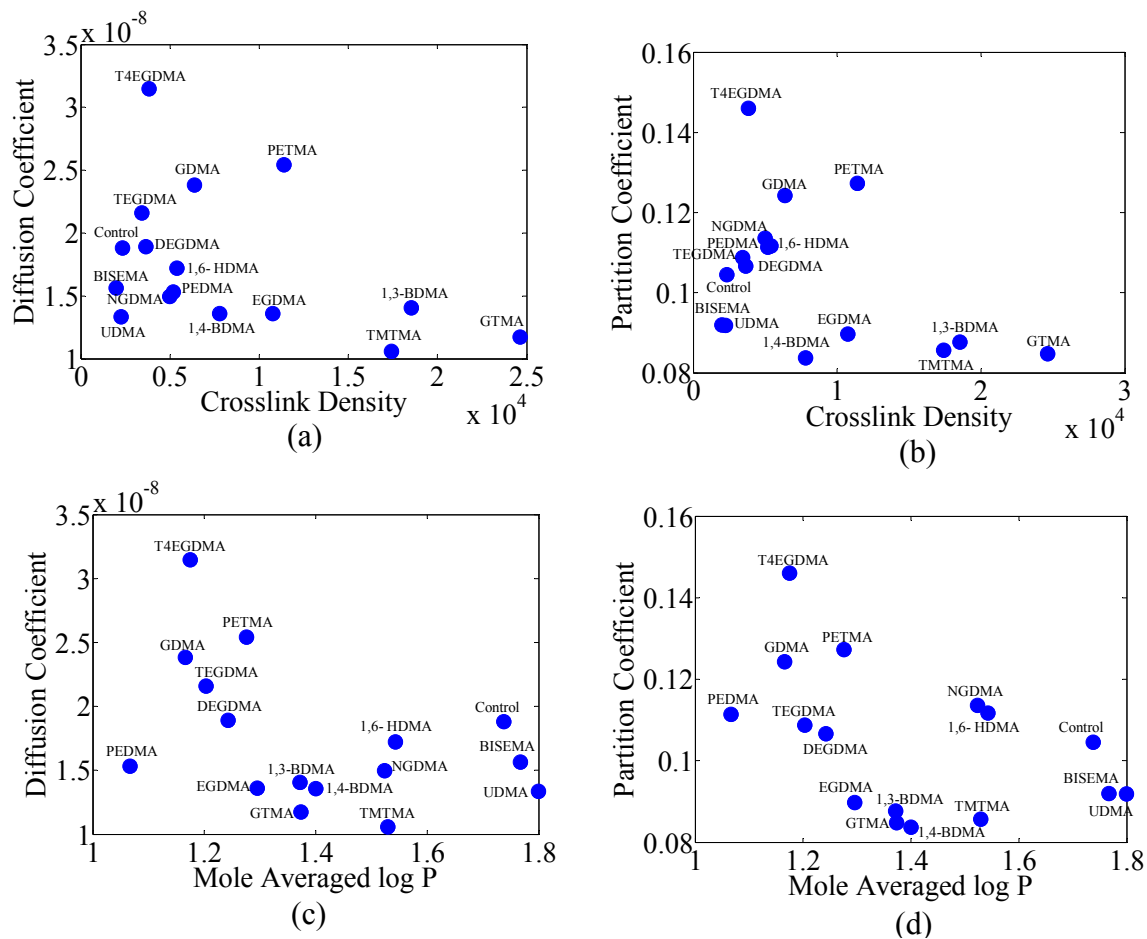


Figure 5-5 Variation of diffusion and partition coefficients with crosslink density and mole averaged LogP for the sixteen adhesive formulations. The co-monomer name is used to represent the polymeric formulation (BH+co-monomer)

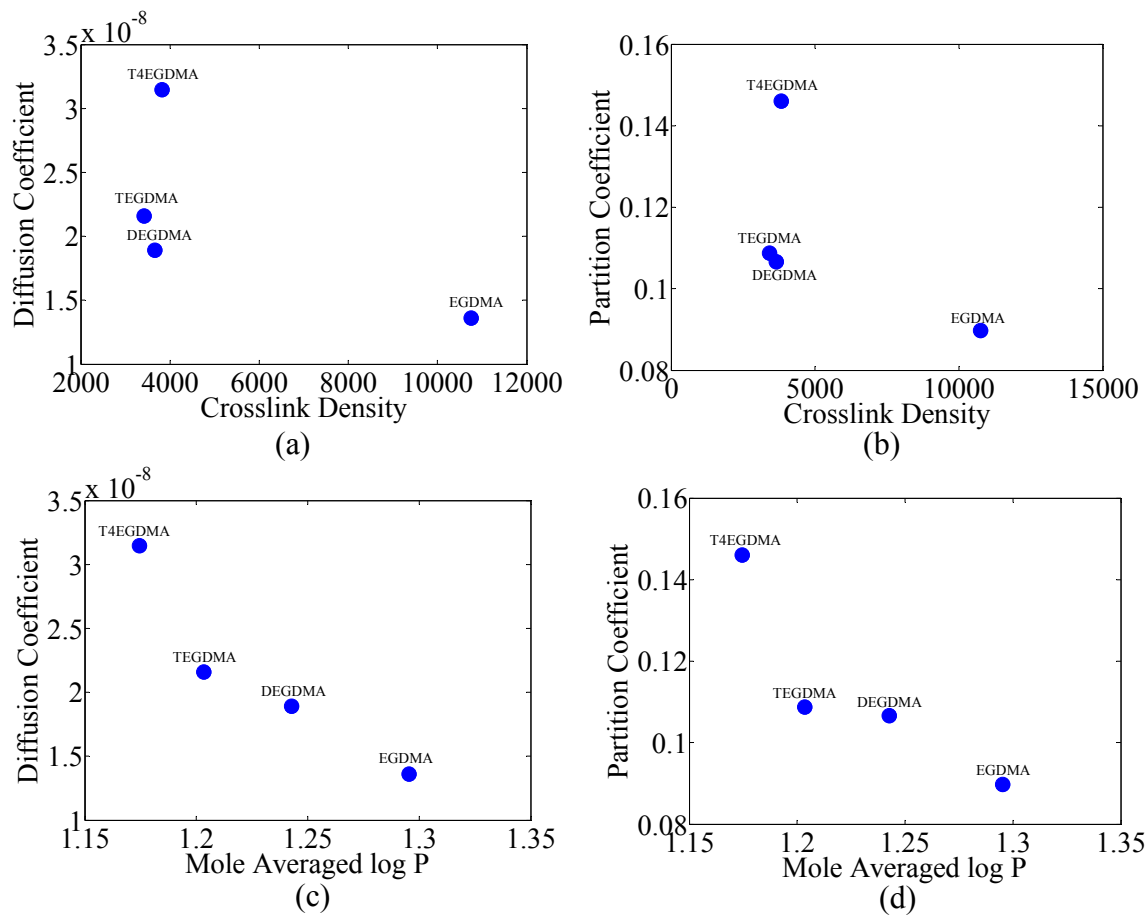


Figure 5-6 Variation of diffusion and partition coefficients of water with crosslink density and LogP for group 1. The co-monomer name is used to represent the polymeric formulation (BH+co-monomer).

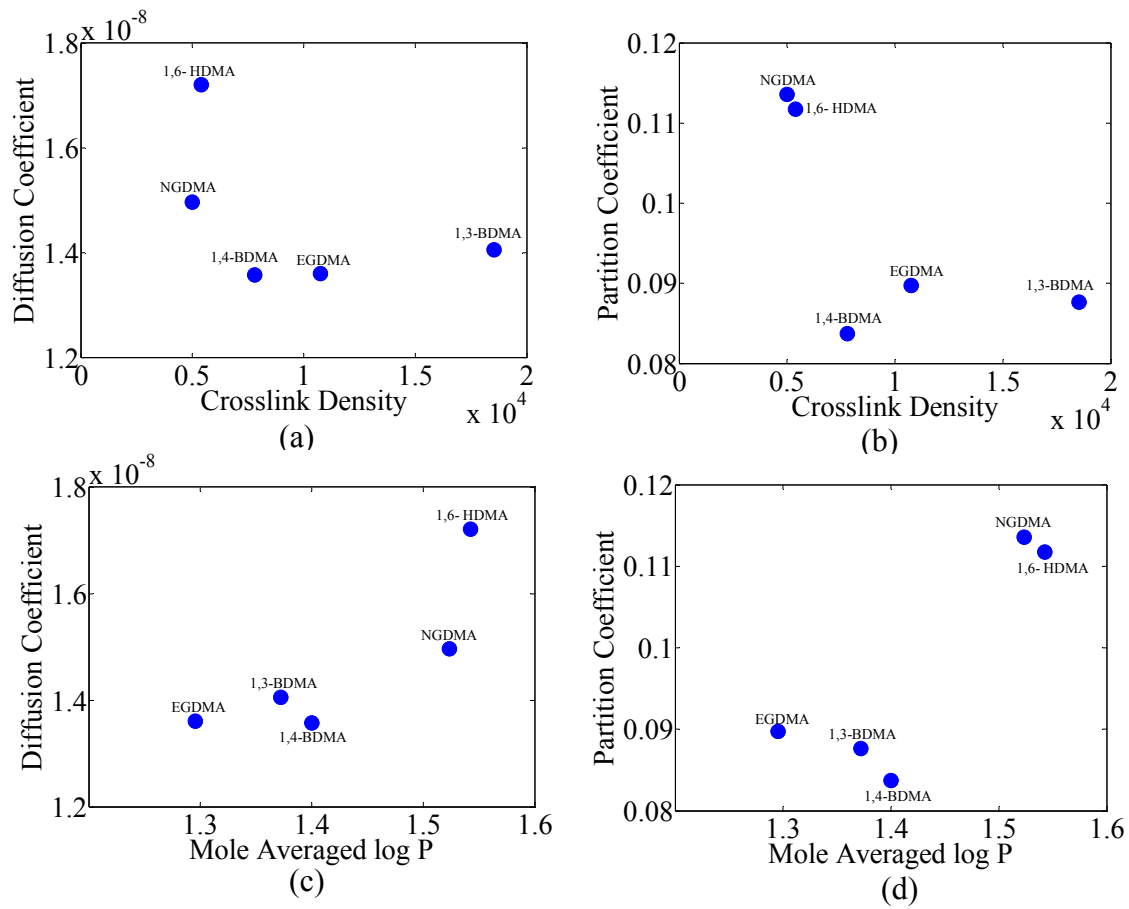


Figure 5-7 Variation of diffusion and partition coefficients of water with crosslink density and LogP for group 2. The co-monomer name is used to represent the polymeric formulation (BH+co-monomer)

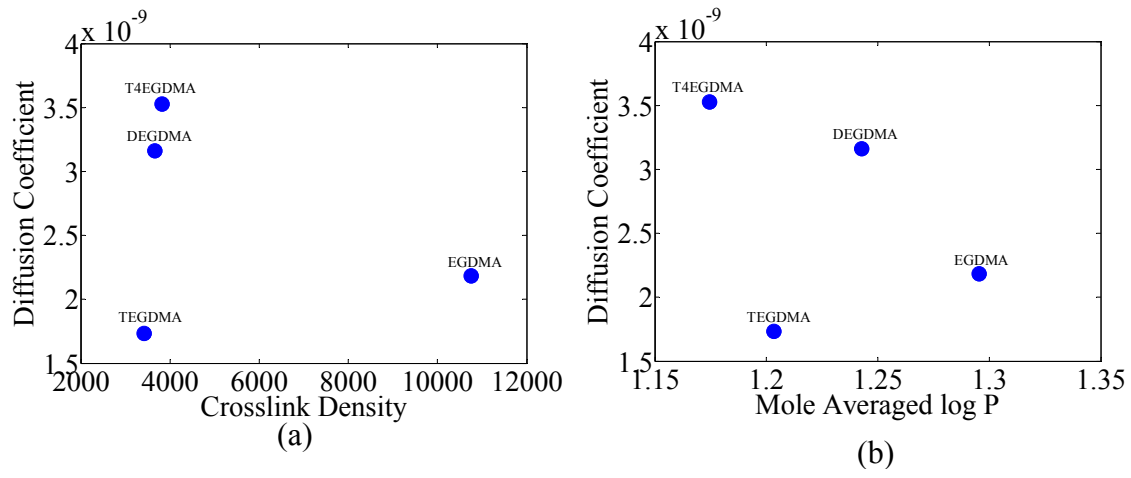


Figure 5-8 Variation of diffusion coefficients of leachables with crosslink density and LogP for group 1. The co-monomer name is used to represent the polymeric formulation (BH+co-monomer)

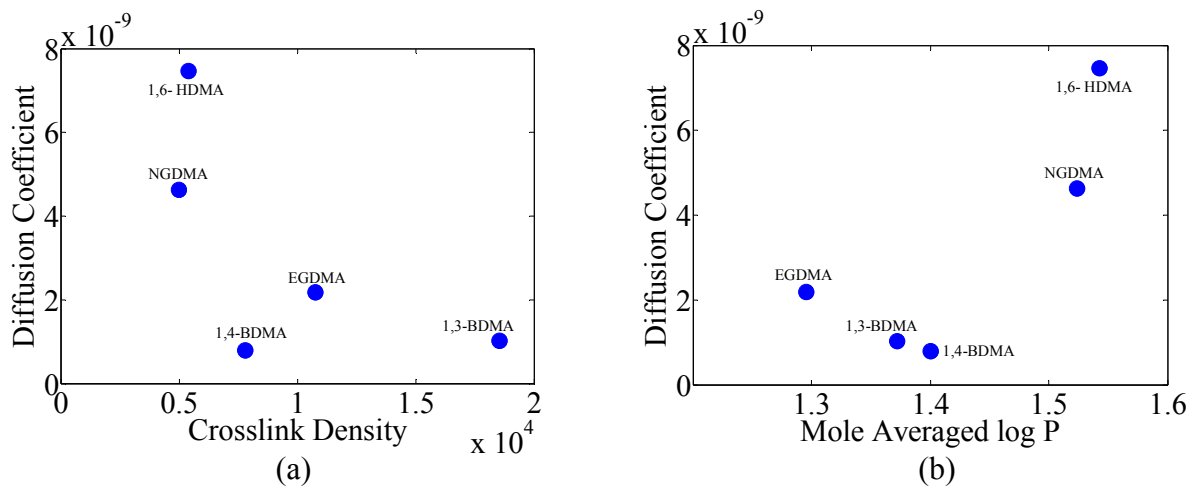


Figure 5-9 Variation of diffusion coefficients of leachables with crosslink density and LogP for group 1. The co-monomer name is used to represent the polymeric formulation (BH+co-monomer)

6 MICROMECHANICS BASED MODEL FOR DIFFUSION IN HYDROPHILIC POLYMERS

The diffusion of water in polymers and its consequence on their mechanical behavior remains a problem of interest with applications in diverse areas of engineering. In this paper, we have developed an approach that couples micromechanical modeling of polymer matrices with the Flory-Rehner theory swelling theory for obtaining the diffusion coefficients of water for Fickian diffusion in hydrophilic polymers. The micromechanical approach uses homogenization to account for the effect of molecular interactions on the macro-scale behavior of the polymer matrix and uses superposition to account for pore pressure. The model successfully predicts the swelling of the polymer resulting from water absorption. We have also focused on the effect of the polymer stiffness and chemistry on the diffusion process. To that end, we obtain the diffusion coefficients for four polymer formulations with monotonically varying crosslink density and hydrophilicity. The calculated coefficients follow the Eyring theory with respect to their relationship with crosslink density. To further investigate the diffusion process, we perform a parametric study which demonstrates a dual role played by the crosslink density (a) its effect on the diffusion path and (b) its contribution to the mechanical part of the free energy.

6.1 Introduction

Hydrophilic crosslinked polymers are widely used in biomedical industry as media for drug delivery, heart-valve replacements; adhesive dentistry and are being considered for applications like artificial cartilage. They are also used for separation of migrating molecules and for diffusion-controlled release of active molecules (Rosoff 1989). In such applications, their interaction with water or biological fluids has significant impact on their functionality. In

particular, the diffusion of water through these polymers impacts their physical and mechanical properties, and therefore requires a fundamental study. The understanding of diffusion through crosslinked polymers and its effective modeling continues to be a challenging problem even with contributions spanning several decades. Early investigation focused on the diffusion dependence on molecular and pore structure (Anderson and Quinn 1974, Pusch and Walch 1982, Colton, Satterfield et al. 2004). The pioneering work related to diffusion through crosslinked polymers is attributed to Peppas, who developed a theory to predict the diffusion coefficient of solutes in water-swollen crosslinked polymers based on Eyring's theory (Reinhart and Peppas 1984). This theory accounted for the influence of factors like free volume, crosslink density and molecular weight between crosslinks. Peppas also developed a theory for diffusion and swelling in crosslinked polymers which incorporated relaxation of the polymer chains and a distinction between glassy and rubbery phases (Lustig and Peppas 1987). The coupled effect of external stress and moisture diffusion on the degradation in mechanical properties of polymers has also been investigated (Rudakova and Zaikov 1987, Rudakova and Zaikov 1988, Singh, Misra et al. 2011). All the above mentioned theories have focused on the mechanisms of diffusion and interaction of the solvent or penetrant with the polymer matrix and consequent plasticization or degradation.

On the other hand, with the rise in popularity of hydrogels and articular cartilage research, there has been a lot of focus on the poroelastic and poroviscoelastic mechanical behavior of fully saturated and swollen polymers. Accordingly, constitutive models have been developed that operate in the realm of fully saturated networks or polymers (Biot 1956, Huang, Mow et al. 2001, Hoang and Abousleiman 2009, Hoang 2011, Hoang and Abousleiman 2012, Wang and Hong 2012). However, there are certain applications, for example dentin adhesives, where polymers are subject to solvent interaction in their dry, glassy condition with or without external

loading, and also experience mechanical loading in their saturated swollen condition. For such applications, a constitutive model that can predict both a) swelling in the partially rubbery state and b) poromechanical behavior in the saturated swollen state becomes necessary. The efforts along this line of approach have been relatively few. For example, the diffusion of moisture into fiber reinforced organic matrix composites under external load was modeled by (Sar, Freour et al. 2012). A constitutive model and finite element implementation for diffusion influenced by mechanical damage for polymer matrix aircraft components was developed by (Roy and Xu 2001). A poromechanics based model has been used to study the transport of moisture and water vapor in deformable food materials (Dhall and Datta 2011, Rakesh and Datta 2013). However, there are differences in the way Fick's Law is applied, when the diffusion is established to be Fickian. Some of these researchers use the concentration gradient as the driving force for diffusion in favor of the more fundamental chemical potential gradient, which incorporates the effects of polymer hydrophilicity as well as crosslink density.

The present work provides a model that describes solvent diffusion into polymers using Fick's Law and the mechanical equilibrium using a poromechanics framework. In particular, (1) the influence of hydrophilicity and fluid pressure on the chemical potential is accounted for using the Flory-Rehner swelling theory (Flory 1942, Flory 1953), (2) poromechanical based constitutive law is introduced for the saturated polymer to relate the fluid pressure with the polymer matrix stress (3) discrete effects at a smaller scale are retained by using micromechanics, while also introducing the influence of interaction density, (4) a numerical solution is developed and implemented to model diffusion of water into dentin adhesive polymers.

In the subsequent discussion, we first briefly present the expression for the chemical potential. Secondly, we describe the conservation laws and the constitutive equations for the polymer matrix and write the governing differential equation (GDE) for the diffusion. We then provide

the numerical procedure utilizing Newton-Raphson method for evaluating the solution to the GDE. We then demonstrate application of the model by fitting experimental data for water absorption into dentin adhesive polymers and validate the approach by comparison with volume change measurements. We also perform a parametric study of the influence of crosslink density on the diffusion process. The results provide insight into the dual role played by crosslink density in the diffusion process.

6.2 Materials and methods

6.2.1 Materials

Four methacrylate based polymer formulations were prepared as mixtures of BisGMA (Bisphenol A glycerolate (1 glycerol/phenol) dimethacrylate), 2-hydroxyethylmethacrylate (HEMA, 99%) and water. The chemical structures of the monomers are shown in Table 6-1. The following three-component visible light photoinitiators (all from Aldrich, Milwaukee, WI) were used in this work: camphoroquinone (CQ, 0.5wt%), ethyl-4-(dimethylamino)benzoate (EDMAB, 0.5wt%) and diphenyliodonium hexafluorophosphate (DPIHP, 0.5wt%) without further purification. The concentration of the photoinitiator component is calculated with respect to the total amount of monomer. All materials were used as received.

6.2.2 Methods

Preparation of polymer beams

Resin mixtures with the following mass ratios of HEMA/BisGMA were prepared in brown vials: a) 60/40 b) 75/25 c) 80/20, and d) 92.5/7.5. A 3 component photo-initiator system (0.5 mass percent of camphorquinone (CQ), ethyl-4-dimethylamino benzoate (EDMAB) and diphenyl iodonium phosphate (DPIHP) was added. The mixture is then diluted with water up to 2 to 3

percentages below the solubility limit. The mixture is sonicated for 48 hours at room temperature. Using each resin mixture, square beams with a side of 1 mm and a length of at least 10 mm were prepared for each co-monomer formulation by casting the prepared resins into glass-tubing molds and light polymerized with a LED light curing unit for 40 seconds. The polymerized samples were stored in dark at room temperature for two days to provide adequate time for post-cure polymerization. The samples were subsequently extracted from the glass tubing and stored in a vacuum oven in the presence of a drying agent (freshly dried silica gel) at 37°C for 48 hours. The preparation of the polymer beams has been explained in detail in earlier work (Parthasarathy, Misra et al. 2012). The polymer formulations are named as “HBx” where x is the percentage of HEMA in the polymer.

Water absorption experiment

Multiple beam specimens were used to study the water sorption behavior of each formulation. Distilled, deionized water (HPLC grade, W5SK-4, Fisher Scientific, Fair Lawn, NJ, USA) was used throughout the experiments. The beam specimens are stored in water for 10 days so that any leachables such as unpolymerized monomers could be leached out by water. Subsequently, the beams are stored in a vacuum oven in the presence of a drying agent (freshly dried silica gel) at 37°C for 48 hours or until constant weight is obtained. The beams are then immersed in water at room temperature. The weight in air (w_{na}) and weight in water (w_{nw}) are recorded for each specimen at the beginning of the experiment and the following times after: 5 minutes, 10 minutes, 20 minutes, 40 minutes, 1 hour, 2 hours, 3 hours, 5 hours, 7 hours, 10 hours, 24 hours, 36 hours, 48 hours and 72 hours. The subscript n stands for the n^{th} reading. If the specimens are not yet saturated (attain constant mass), data is collected at additional intervals spaced 24 hours apart till constant mass is reached. The following quantities are then calculated:

Mass change in air:

$$\Delta w_{na} = w_{na} - w_{0a} \quad (6.1)$$

Mass change in water:

$$\Delta w_{nw} = w_{nw} - w_{0w} \quad (6.2)$$

Volume of the sample:

$$V_n = \alpha \frac{w_{na} - w_{nw}}{\rho_w - \rho_a} \quad (6.3)$$

Jacobian for volume change:

$$J_n = \frac{V_n}{V_0} \quad (6.4)$$

where the balance correction factor to account for air buoyancy $\alpha=0.99985$, density of water $\rho_w = 1 \text{ g/cm}^3$ and density of air $\rho_a=0.0012 \text{ g/cm}^3$. The percentage mass change of the sample is given as follows. The total fractional mass change of the sample can be calculated as $(w_{fa} - w_{0a}) / w_{0a}$, where w_{fa} is the final mass of the sample.

6.3 Mathematical Model

A number of theories to model the elasticity of a polymer network have been developed, such as the kinetic or statistical theory of rubber elasticity, and the phenomenological Mooney-Rivlin type models and their variations (Horkay and McKenna 2007). It is well accepted that the macro-scale properties of a material are significantly influenced by the interaction between representative units. For example, granular micromechanics theory has been used to derive bounds of elastic moduli for granular materials using inter-particle contacts (Misra and Chang 1993, Chang, Chao et al. 1995) and more recently, to derive constitutive equations for rate-dependent visco-damage behavior, including loading induced anisotropy, based upon inter-granular force-displacement relationships (Misra, Marangos et al. 2013). Thus, constitutive models that relate the externally applied action to the molecular-scale parameters have an

advantage for describing the mechanical behavior of polymer networks because they enable mechanical responses to be estimated from the knowledge of the molecular structure (Horkay and McKenna 2007). In this paper, we treat the adhesive polymer to possess a pseudo-granular structure in which the grain-interactions represent the average behavior of the covalent bonds between segments in the linear polymer chain, the covalent crosslinks between segments in two different polymer chains, non-covalent hydrogen bonds, van der Waals interactions, entanglements, and other physical interactions. The proposed approach provides a feasible meso-scale method to relate the macro-scale properties to molecular-scales for materials whose micro-structure and local interactions are ill-defined (Misra, Marangos et al. 2013, Misra and Singh 2013). The term meso-scale has been used to refer to a scale smaller than the micro-scale but much larger than the size of a polymer segment (molecular scale), such that a representative volume element at the meso-scale contains several thousand polymer segments. We modeled the wet adhesive polymer using a three-step procedure by applying 1) granular micromechanics (Chang, Chao et al. 1995) to model the elastic behavior of the polymer network, 2) a self-consistent homogenization of the (homogenized) polymer network with the pore space to obtain the homogenized porous polymer stiffness, and 3) the poro-mechanical approach to obtain the behavior of the saturated polymer by superposing the (homogenized) porous polymer with the interstitial water. A schematic depiction of the modeling procedure is shown in Figure 2. In addition, a schematic depiction of the idealization for cases of low and high crosslink density is shown in Figure 3(a) and (b), respectively.

6.3.1 Micro-poro-mechanical model

In the first step, the theoretically dense wet polymer network was homogenized using the granular micromechanics approach which assumes the system to be composed of grains interacting in both the normal and shear directions. In this approach, the stress tensor was

obtained in terms of the tensor product of the interaction force vector and the vector joining the centroid of pseudo-grains (Misra, Marangos et al. 2013). The resultant expression for the stress tensor has similarities to the microscopic stress description utilized for reptation models of polymers (see for example Section 5.3 (Doi 1996)). Using the granular micromechanics approach, the following expression for Young's modulus and Poisson's ratio can be derived for isotropic systems subjected to isotropic loading, under the so called "static hypothesis" for expressing inter-granular forces in terms of the stress tensor (Chang, Chao et al. 1995).

$$E^s = 10A^s \left(\frac{\alpha^s}{2 + 3\alpha^s} \right) \quad (6.5)$$

$$\nu^s = \frac{1 - \alpha^s}{2 + 3\alpha^s} \quad (6.6)$$

where E^s and ν^s are the elastic modulus and Poisson's ratio of the polymer network, A^s is a meso-scale parameter proportional to the inter-granular stiffness in the normal direction and the number density of inter-granular interactions, and α^s is the ratio of the transverse to normal inter-granular stiffness. Formulae relating other forms of macro-scale material properties to meso-scale parameters are given in Table 3. The "static hypothesis" approach is derived by relating the macro-scale strain to the local displacements through least square fitting (Chang, Chao et al. 1995) in order to capture the non-affine local deformations observed in these material systems (Wen, Basu et al. 2012).

In the second step, the polymer network was homogenized with the porous space using the self-consistent approximation (Misra, Marangos et al. 2013) to obtain the 4th-order stiffness tensor C_{ijkl} of the porous polymer as shown below.

$$C_{ijkl} = C_{ijkl}^s - \phi C_{ijmn}^s H_{mnkl}^\phi \quad (6.7)$$

where H^ϕ is the strain concentration tensor in the pore space determined by using the equivalent inclusion technique (Eshelby 1957), and ϕ is the porosity of the polymer. The stiffness tensor C_{ijkl}^s was written in terms of E^s and ν^s given in Eqs. (6.5) and (6.6) as

$$C_{ijkl}^s = \lambda^s \delta_{ij} \delta_{kl} + \mu^s (\delta_{ik} \delta_{jl} + \delta_{il} \delta_{jk}) \quad (6.8)$$

where λ^s and μ^s can be determined from formulae in Table 3, and δ_{kl} is the Kronecker delta. We have used the tensor notation for the development of the mathematical model, thus the subscripts in this section follow the tensor summation convention. For the saturated swollen polymer, the pore spaces were assumed to be spherical for simplicity in the absence of well-defined morphological information. The Eshelby tensor S for spherical inclusion in isotropic medium is given as follows (Mura 1987).

$$S_{ijkl} = \frac{(5\nu - 1)}{15(1 - \nu)} \delta_{ij} \delta_{kl} + \frac{(4 - 5\nu)}{15(1 - \nu)} (\delta_{ik} \delta_{jl} + \delta_{il} \delta_{jk}) \quad (6.9)$$

where ν is the Poisson's ratio of the homogenized porous polymer. The strain concentration tensor H^ϕ for the pore space is then calculated as follows (Misra, Marangos et al. 2013):

$$H_{ijkl}^\phi = (I_{ijkl} - S_{ijkl})^{-1} \quad (6.10)$$

where $I = (\delta_{ij} \delta_{kl})$ is the identity tensor.

In step three, we superposed the homogenized porous polymer phase with the fluid phase following the procedure described in (Misra, Marangos et al. 2013) after considering large deformation. We thus obtained the incremental overall constitutive equation for the saturated polymer in a poroelastic framework as follows.

$$\dot{\sigma}_{ij} = -\delta_{rs} L_{rs} \bar{\sigma}_{ij} + C_{ijkl} \dot{\epsilon}_{kl} + \bar{\sigma}_{jm} L_{im} + \bar{\sigma}_{im} L_{jm} - B_{ij} \dot{p} \quad (6.11)$$

$$\dot{\zeta} = B_{kl} \dot{\epsilon}_{kl} + \Gamma \dot{p} \quad (6.12)$$

where $\dot{\sigma}_{ij}$ is the stress rate, $\bar{\sigma}_{ij}$ is the stress in the polymer phase, L_{im} is the velocity gradient of the saturated polymer, $\dot{\varepsilon}_{kl}$ is the strain rate, \dot{p} is the fluid pressure rate, $\dot{\zeta}$ is the volumetric rate of water uptake with respect to the volume of the saturated polymer, and B_{ij} and Γ are the poromechanics constants. B_{ij} and Γ were obtained in a straightforward manner using self-consistent homogenization as:

$$B_{ij} = \phi \delta_{mn} H_{mnij}^{\phi} \quad (6.13)$$

$$\Gamma = B_{kl} \left(C_{ijkl}^s \right)^{-1} (B_{kl} - \phi \delta_{kl}) + \frac{\phi}{K_f} \quad (6.14)$$

where K_f is the bulk modulus of water. The poromechanics constant B measures the ratio of water volume squeezed out to the volume change of the saturated polymer under (idealized) conditions of flow under zero pressure. B_{ij} is called the effective stress coefficient and represents the proportion of the applied load carried by the fluid. Γ is a compliance parameter which measures the amount of water which can be forced into the saturated polymer under pressure while the volume is kept constant. Γ is a measure of the combined fluid-solid compressibility. It is noteworthy that the value of B_{ij} is not unity and both B_{ij} and Γ depend on the stiffness of the porous polymer and the polymer network. Under the assumption of negligible change in water density, $\dot{\zeta} = \dot{\gamma}_w$ where $\dot{\gamma}_w$ is the increment in water volume fraction in the saturated polymer.

6.3.2 Swelling and elastic modulus of saturated polymer

We assume that the swelling under stress-free condition, wherein the increment of external stress, $\dot{\sigma}_{ij} = 0$, is isotropic, that is $\dot{\varepsilon}_{ij} = \varepsilon \delta_{ij}$ and $B_{ij} = B \delta_{ij}$. Furthermore, for the swelling experiments performed on beams whose length is much larger than the cross sectional

dimensions plane strain conditions may be assumed. Solving Eq. (6.11) and (6.12) under these conditions, we obtained the following relationship applicable to our experiments

$$\dot{p} = \left[\frac{C_{1111} + C_{1122}}{2B^2 + \Gamma(C_{1111} + C_{1122})} \right] \dot{\gamma}_w \quad (6.15)$$

$$\dot{\varepsilon} = \left[\frac{B}{2B^2 + \Gamma(C_{1111} + C_{1122})} \right] \dot{\gamma}_w \quad (6.16)$$

where the stress correction terms involving the velocity gradient, L_{ij} , vanish for the condition of plane strain. The volume change expressed as the Jacobian of the deformation, J is related to the isotropic strain as

$$\frac{\dot{J}}{J} = 2\dot{\varepsilon} \quad (6.17)$$

Further, we note that the rate of loading for mechanical testing performed in this study is orders of magnitude faster than the rate of water diffusion (or drainage) in the beam samples. Therefore, the loading can be considered as undrained and $\dot{\zeta} = 0$. Solving Eq. (6.11) and (6.12) for this condition gives a relationship for the undrained stiffness in term of the drained stiffness C_{ijkl} , used in Eqs. (6.15) and (6.16), and poromechanics constants B_{ij} as follows

$$C_{ijkl}^u = C_{ijkl} + \frac{B_{ij}B_{kl}}{\Gamma} \quad (6.18)$$

6.3.3 Chemical Potential

Water absorption and swelling is determined by the mechanical properties as well as the chemical potential of the water in the polymer. The chemical potential of water in a polymer relative to chemical potential of pure water has been derived by (Flory 1953). Here, we used a modified form written as:

$$\mu = RT \left[\ln(\gamma) + (1-\gamma) + \chi(1-\gamma)^2 \right] + \Psi(\gamma - V_{\phi 0}) \bar{p} \frac{M}{\rho} \quad (6.19)$$

where μ is the chemical potential difference between the water inside the polymer and pure water, henceforth referred to as chemical potential, R is the universal gas constant ($=8.314 \text{ JK}^{-1} \text{ mol}^{-1}$), T is the temperature, γ_w is the water volume fraction, \bar{p} is the effective fluid pressure in the polymer given as $\bar{p} = \int B_{ij} \delta_{ij} \dot{p}$, $\frac{M}{\rho}$ is the partial molar volume of water in the polymer, M_w the molecular weight and ρ_w the mass density of water, χ is the polymer-water interaction parameter, V_{ϕ_0} is the initial free volume in the polymer and Ψ is the Heaviside step function such that $\Psi(\gamma - V_{\phi_0}) = 0$ when $\gamma < V_{\phi_0}$ and $\Psi(\gamma - V_{\phi_0}) = 1$ when $\gamma \geq V_{\phi_0}$. The effective fluid pressure \bar{p} at equilibrium when the chemical potential difference vanishes, $\mu=0$, is identified as the osmotic pressure. We note that the first term in Eq. (6.19) represents the free energy resulting from the entropy and enthalpy of mixing, while the second term represents the contribution from elastic deformation. The Heaviside step function was introduced in the second term to account for the initial free volume, V_{ϕ_0} , defined as that fractional volume of the polymer which needs to be saturated before the interstitial water develops pressure as the result of the elastic swelling of the polymer structure. In literature, the free volume has been defined as the volume not occupied by the polymer molecules but constituting a part of the bulk volume of the overall polymer solid or polymer/diluent system (Yasuda, Peterlin et al. 2003). The free volume in a polymer has also been defined equivalently as the volume occupied by openings between the polymer chains where the solvent molecules can pass through (Amsden 1998, Yasuda, Peterlin et al. 2003). Our definition is consistent with those from literature since the fluid pressure and corresponding stress in the polymer is created only when there is resistance to any further increase in space between the chains beyond the initially empty space.

6.3.4 Two-dimensional diffusion model

It is well established that the nature of fluid transport through polymers depends on the relative magnitudes of the characteristic times for stress-relaxation and solvent diffusion (Lustig and Peppas 1987). The characteristic stress relaxation time for methacrylate-based polymers is of the order of a few minutes, while the characteristic diffusion time for square beams of methacrylate-based polymers with a side of 1 mm is more than 30 hours. Since the stress relaxation time is several orders of magnitude smaller than the characteristic diffusion time, we defined the fluid flow according to Fick's law as shown below.

$$\vec{j}_w = -\frac{DMc_w}{RT} \vec{\nabla} \mu \quad (6.20)$$

The conservation of the fluid mass was written as follows using a Lagrangian description.

$$\frac{\partial}{\partial t}(\rho_w \gamma) = -\nabla \cdot (\vec{j}_w) \quad (6.21)$$

where \vec{j}_w is the local flux of water.

where D is the diffusion coefficient and $c_w = \frac{\rho_w \gamma}{M_w}$ is the molar concentration of the fluid.

Neglecting the change in fluid density, Eq. (6.20) and (6.21) was combined into:

$$\frac{\partial \gamma}{\partial t} = \frac{D}{RT} \left(\gamma \vec{\nabla}^2 \mu + \vec{\nabla} \gamma \cdot \vec{\nabla} \mu \right) \quad (6.22)$$

From calculations on our polymers, we found the first derivative product terms to be negligibly small in comparison to the second derivative terms. Hence, the governing equation for diffusion mass transfer reduced to the following.

$$\frac{\partial \gamma}{\partial t} = \frac{D}{RT} \left(\gamma \vec{\nabla}^2 \mu \right) \quad (6.23)$$

Taking the time derivative on both sides of Eq. (6.19), the rate of change of water content at a material point was expressed in terms of the rate of change of the chemical potential difference.

$$\frac{\partial \gamma}{\partial t} = \frac{\frac{\partial \mu}{\partial t}}{RT \left[\frac{1}{\gamma} - 1 - 2\chi(1-\gamma) \right] + \Psi(\phi_{FV} - \gamma) \frac{\Omega M}{\rho}} \quad (6.24)$$

Where $\Omega = \frac{B(C_{11} + C_{12})}{2B_{11}^2 + (C_{11} + C_{12})\Gamma}$

Substituting Eq. (6.24) into Eq.(6.23),

$$\frac{\partial \mu}{\partial t} = D_{eff} \nabla^2 \mu \quad (6.25)$$

$$D_{eff} = D \left(\left[1 - \gamma - 2\chi\gamma(1-\gamma) \right] + \Psi(\phi_{FV} - \gamma) \frac{\Omega\gamma M}{\rho RT} \right) \quad (6.26)$$

which was solved for the chemical potentials, μ , under specified boundary and initial conditions.

We note that the diffusion coefficient D is a function of crosslink density and hydrophilicity.

Since beam shaped samples with large aspect ratio are used, the end effects were neglected and the problem was simplified to a planar diffusion process in a square domain. A central difference scheme was used to discretize space coordinates and a backward difference scheme was used to discretize time as follows.

$$\nabla^2 \mu \approx \frac{{}^{t+\Delta t}\mu_{I+1,J} - 2{}^{t+\Delta t}\mu_{I,J} + {}^{t+\Delta t}\mu_{I-1,J}}{(\Delta x)^2} + \frac{{}^{t+\Delta t}\mu_{I,J+1} - 2{}^{t+\Delta t}\mu_{I,J} + {}^{t+\Delta t}\mu_{I,J-1}}{(\Delta y)^2} \quad (6.27)$$

$$\frac{\partial \mu}{\partial t} \approx \frac{{}^{t+\Delta t}\mu_{I,J} - {}^t\mu_{I,J}}{\Delta t} \quad (6.28)$$

Where Δx and Δy are discretized intervals in space, Δt is the discretization in time and (I, J) is the position of a node in the domain. Introducing Eq.(6.27) and Eq.(6.28) into Eq.(6.25), the discretized equation was obtained as:

$$\begin{aligned} & -{}^{t+\Delta t}\theta_x \left[{}^{t+\Delta t}\mu_{I-1,J} + {}^{t+\Delta t}\mu_{I+1,J} \right] + \left[1 + 2{}^{t+\Delta t}\theta_x + 2{}^{t+\Delta t}\theta_y \right] {}^{t+\Delta t}\mu_{I,J} \\ & -{}^{t+\Delta t}\theta_y \left[{}^{t+\Delta t}\mu_{I,J-1} + {}^{t+\Delta t}\mu_{I,J+1} \right] = {}^t\mu_{I,J} \end{aligned} \quad (6.29)$$

Where ${}^{t+\Delta t}\theta_x = \frac{D_{eff}\Delta t}{(\Delta x)^2}$ and ${}^{t+\Delta t}\theta_y = \frac{D_{eff}\Delta t}{(\Delta y)^2}$.

Eq. (6.29) was then rearranged by assembling the two-dimensional matrices ${}^t\mu$ and ${}^{t+\Delta t}\mu$ into vectors containing the chemical potentials by moving right to left along the matrix and concatenating all the rows using $i = (I-1) + J$. The matrix form of Eq. (6.29) was obtained as shown below.

$${}^{t+\Delta t}K_{ij} {}^{t+\Delta t}\mu_j = {}^t\mu_i \quad (6.30)$$

where

$${}^{t+\Delta t}K_{ij} = \left(1 + 2\left({}^{t+\Delta t}\theta_x\right)_j + 2\left({}^{t+\Delta t}\theta_y\right)_j \right) \delta_{ij} - \left({}^{t+\Delta t}\theta_x\right)_j \delta_{i(j+1)} - \left({}^{t+\Delta t}\theta_x\right)_j \delta_{i(j-1)} - \left({}^{t+\Delta t}\theta_y\right)_j \delta_{i(j-n_x)} - \left({}^{t+\Delta t}\theta_y\right)_j \delta_{i(j+n_y)}$$

The boundary conditions are $\mu=0$ at the edges of the beam and $\gamma=0$ or $\mu=-\infty$ inside the cross-section of the beam. The beam was initially dry, and then placed in water till the polymer-water system is allowed to reach equilibrium. The boundary of the beam is assumed to instantaneously reach equilibrium and the interior of the beam is initially dry resulting in the boundary conditions $\mu=0$ at the edges of the beam and the initial conditions $\gamma=0$ or $\mu=-\infty$ inside the cross-section of the beam.

Numerical solution

The numerical solution to the nonlinear equation system represented by Eq. (6.29) can be obtained in an exact form by using the definition of chemical potential from Eq.(6.19). In this

paper, we utilized the Newton-Raphson method to solve this set of nonlinear equations. We defined a residual chemical potential vector, $f\left({}^{t+\Delta t}\gamma_j\right)$, as

$$f\left({}^{t+\Delta t}\gamma_j\right) = -{}^t\mu_i + {}^{t+\Delta t}K_{ij} {}^{t+\Delta t}\mu_j \quad (6.31)$$

We expanded the residual $f\left({}^{t+\Delta t}\gamma_j\right)$ in Taylor's series with respect to the water volume fraction at the α^{th} iteration to obtain:

$$f\left({}^{t+\Delta t}\gamma_j\right) = f\left({}^{t+\Delta t}\gamma_j\right)^\alpha + \Delta\gamma_w^{t+\Delta t} \left(\frac{\partial f}{\partial \gamma_w^{t+\Delta t}} \right)^\alpha \quad (6.32)$$

where we omitted the terms of order 2 and higher. We thus obtained the increment of water volume fraction, corresponding to the residual at the end of the α^{th} iteration as:

$$\Delta^\alpha \gamma_w^{t+\Delta t} = \frac{f\left({}^{t+\Delta t}\gamma_j\right)^\alpha}{K_T^i} \quad (6.33)$$

Where the tangent

$$\begin{aligned} (K_T)_j &= -\frac{\partial f}{\partial \left({}^{t+\Delta t}\gamma_j^\alpha\right)} = -{}^{t+\Delta t}\omega_{ij}^\alpha RT \left[\ln\left({}^{t+\Delta t}\gamma_j^\alpha\right) + \left(1 - {}^{t+\Delta t}\gamma_j^\alpha\right) + \chi \left(1 - {}^{t+\Delta t}\gamma_j^\alpha\right)^2 \right] \\ &- \Psi\left({}^{t+\Delta t}\gamma_j^\alpha - V_\varphi\right) {}^{t+\Delta t}\omega_{ij}^\alpha {}^{t+\Delta t}p_j^{-\alpha} \frac{M}{\rho} - {}^{t+\Delta t}K_{ij}^\alpha RT \left[\frac{1}{{}^{t+\Delta t}\gamma_j^\alpha} - 1 - 2\chi \left(1 - {}^{t+\Delta t}\gamma_j^\alpha\right) \right] \\ &- \Psi\left({}^{t+\Delta t}\gamma_j^\alpha - V_\varphi\right) {}^{t+\Delta t}K_{ij}^\alpha {}^{t+\Delta t}\Omega \frac{M}{\rho} \end{aligned} \quad (6.34)$$

where ${}^{t+\Delta t}\omega_{ij}^\alpha = \frac{\partial \left({}^{t+\Delta t}K_{ij}^\alpha\right)}{\partial \left({}^{t+\Delta t}\gamma_w^\alpha\right)}$ and the increment of fluid pressure, given by Eq.(6.15),

$$\Delta {}^{t+\Delta t}p^{-\alpha} = \Omega {}^{t+\Delta t}\gamma_w^\alpha.$$

The expressions for ${}^{t+\Delta t}\omega_{ij}^\alpha$, ${}^{t+\Delta t}\theta_x^\alpha$ and ${}^{t+\Delta t}\theta_y^\alpha$ are shown below.

$$\left({}^{t+\Delta t}\theta_x^\alpha\right)_j = \frac{\Delta t}{(\Delta x)^2} D \left(\left[1 - {}^{t+\Delta t}\gamma_j^\alpha - 2\chi {}^{t+\Delta t}\gamma_j^\alpha (1 - {}^{t+\Delta t}\gamma_j^\alpha) \right] + \Psi(\phi_{FV} - {}^{t+\Delta t}\gamma_j^\alpha) \frac{\Omega {}^{t+\Delta t}\gamma_j^\alpha M}{\rho RT} \right),$$

$$\left({}^{t+\Delta t}\theta_y^\alpha\right)_j = \frac{\Delta t}{(\Delta y)^2} D \left(\left[1 - {}^{t+\Delta t}\gamma_j^\alpha - 2\chi {}^{t+\Delta t}\gamma_j^\alpha (1 - {}^{t+\Delta t}\gamma_j^\alpha) \right] + \Psi(\phi_{FV} - {}^{t+\Delta t}\gamma_j^\alpha) \frac{\Omega {}^{t+\Delta t}\gamma_j^\alpha M}{\rho RT} \right)$$

$${}^{t+\Delta t}\omega_{ij}^\alpha = 2 \left(\left({}^{t+\Delta t}\beta_x^\alpha \right)_j + \left({}^{t+\Delta t}\beta_y^\alpha \right)_j \right) \delta_{ij} - \left({}^{t+\Delta t}\beta_x^\alpha \right)_j \delta_{i(j+1)} - \left({}^{t+\Delta t}\beta_x^\alpha \right)_j \delta_{i(j-1)} - \left({}^{t+\Delta t}\beta_y^\alpha \right)_j \delta_{i(j-n_x)} - \left({}^{t+\Delta t}\beta_y^\alpha \right)_j \delta_{i(j+n_y)}$$

where

$${}^{t+\Delta t}\beta_x^\alpha = \frac{D\Delta t}{(\Delta x)^2} \left(\left[-1 - 2\chi + 4\chi {}^{t+\Delta t}\gamma_j^\alpha \right] + \Psi(\phi_{FV} - {}^{t+\Delta t}\gamma_j^\alpha) \frac{\Omega {}^{t+\Delta t}M}{\rho RT} \right)$$

$${}^{t+\Delta t}\beta_y^\alpha = \frac{D\Delta t}{(\Delta y)^2} \left(\left[-1 - 2\chi + 4\chi {}^{t+\Delta t}\gamma_j^\alpha \right] + \Psi(\phi_{FV} - {}^{t+\Delta t}\gamma_j^\alpha) \frac{\Omega {}^{t+\Delta t}M}{\rho RT} \right)$$

At the end of the α th iteration, we updated the water volume fraction as follows till convergence

$${}^{t+\Delta t}\gamma_j^\alpha = {}^{t+\Delta t}\gamma_j^\alpha + \Delta {}^{t+\Delta t}\gamma_j^\alpha \quad (6.35)$$

The calculation was continued until ${}^t\mu_i$ approaches a specified tolerance $\varepsilon > 0$.

Determination of diffusion coefficients

The fractional mass change of the polymer at time t is given by the summation of the elemental mass changes over all the elements j in the square cross-section as shown below.

$$M_j^t = \frac{\rho_w}{\rho_s(1-V_\phi)} L^2 \left(\sum_{\text{interior}} ({}^t\gamma_j) {}^tJ_j \Delta x \Delta y + \sum_{\text{edges}} ({}^t\gamma_j) {}^tJ_j \frac{\Delta x \Delta y}{2} + \sum_{\text{corners}} ({}^t\gamma_j) {}^tJ_j \frac{\Delta x \Delta y}{4} \right) \quad (6.36)$$

where ρ_s is the true density of the polymer material given as $\rho_s = \left(\frac{m_{0a}}{m_{0a} - m_{0w}} \right) (\rho_w - \rho_a) + \rho_w$ and

tJ_j is the Jacobian of deformation for the element j , given by Eq. (6.17).

The diffusion coefficient of water for each polymer formulation is determined by minimizing the sum of squares error between the simulated fractional mass change shown in Eq.(6.36) and

the experimentally observed fractional mass change in Eq. (6.1). The Nedler-Mead simplex direct search method was used for the optimization.

Prediction of swelling

The Jacobian of deformation for all the elements j in the square cross-section of the polymer at time t is given by the ratio of the total volume at t to the initial volume, as shown below.

$$J_j^t = \frac{1}{L^2} \left(\sum_{\text{interior}} {}^tJ_j \Delta x_j \Delta y_j + \sum_{\text{edges}} {}^tJ_j \frac{\Delta x_j \Delta y_j}{2} + \sum_{\text{corners}} {}^tJ_j \frac{\Delta x_j \Delta y_j}{4} \right) \quad (6.37)$$

The percentage mass change is given by the total mass change per unit volume scaled by the initial mass of the polymer.

6.4 Results and discussion

For the subsequent discussion, we use the nomenclature HBx to denote the formulations described in Table 2, where H represents HEMA, B represents BisGMA and x is the percentage of HEMA in the neat resin. Each formulation contains was prepared by adding water 2 to 3 percentages below the solubility limit.

6.4.1 Sorption and swelling kinetics

Figure 6-1(a) shows the mass change data for the polymer samples and the corresponding experimental fits. The model was able to fit the mass change data accurately ($R^2 = 90$ to 99%). This verified that the diffusion was Fickian in nature. The characteristic time of diffusion of water into a square polymer beam of side 1 mm was verified to be orders of magnitude larger than the characteristic stress-relaxation time for all the polymer formulations, further confirming that the diffusion is indeed Fickian. The diffusion coefficients obtained are shown in Table 2 along with the model parameters obtained from equilibrium data (see appendix for details).

The swelling of the polymers with time, shown in Figure 1(b), was also predicted accurately using the diffusion coefficients obtained ($R^2 = 89$ to 96%). Figures 2 and 3 show the contour plots of the water volume fraction, γ , and the Jacobian of deformation, J , at 2, 4 and 6 hours after the beginning of the experiment. Since the free volume must be fully saturated before the polymer starts swelling, the swelling front lags behind the wetting front as the water diffuses into the polymer for HB60, HB75 and HB80. HB95 has a much smaller free volume than the other three polymer formulations, so the wetting front and the swelling front advance almost simultaneously. As the wetting fronts from the four ends of the beam meet at the center, the water volume fraction assumes a quadratic profile with respect to the depth of the beam cross-section. Similarly, as the swelling fronts from the four ends meet, the Jacobian of deformation assumes a quadratic profile.

6.4.2 Dependence of diffusion coefficient on composition

The diffusion coefficient decreases with increase in the percentage of BisGMA, as shown in Figure 6-4. In these formulations, BisGMA is the crosslinking component since it is a dimethacrylate. Further, with increase in BisGMA, there is also an increase in density of covalent crosslinks, non-covalent interactions and hydrophobicity. It has been demonstrated that the diffusion coefficient in methacrylate-based polymers strongly depends on the hydrophilicity and the crosslink density (Parthasarathy, Misra et al. 2012). The decreasing trend of diffusion coefficient with BisGMA percent shown in Figure 6-4 agrees with those results. The drop is steep from HB80 to HB60, but shallower from HB92.5 to HB80. This is likely because as the percentage of BisGMA drops, the density and influence of covalent and non-covalent interactions falls rapidly and the behavior shifts towards a linear polymer rather than a crosslinked polymer.

6.4.3 Dependence of diffusion process on crosslink density

We note that the influence of crosslink density on the diffusion process is two-fold. It restricts the free volume and pore size where the water molecules can pass through. Before the initial free volume is filled up, this is the sole role played by the crosslink density. After the free volume is filled up, the crosslinks offer resistance to the expansion of the polymer network, thus accelerating the approach of the polymer-water system to equilibrium. Figure 6-5 shows a plot of the diffusion coefficient versus the model parameter A^s , which represents the density of both covalent and non-covalent interactions between polymer segments. The exponential dependence of the diffusion coefficient on the model parameter A^s agrees with the Eyring theory (Peppas and Reinhart 1983, Krongauz 2010) where the change in free energy corresponds to the chemical potential defined in Eq.(6.19).

To illustrate the overall effect of crosslink density on the diffusion process, we considered four formulations with varying values of parameter A^s , which represents the crosslink density. In this parametric study, we considered the free volume to be zero, interaction parameter as 0.68 to represent a relatively hydrophilic polymer, and A^s to take the values 10, 50, 100, 200, 300 and 500 MPa. For each case we determined the diffusion coefficient, D , using the exponential fit between the diffusion coefficient and parameter A^s . Figure 6-6(a) shows the variation in water volume fraction with time for each case. The increase in A^s slows down both the rate of diffusion and the final water absorption. Similarly, as observed in Figure 6-6(b), an increase in A^s slows down the swelling rate and decreases the final volume change. The dual effect of interaction density on the diffusion rate can be observed in Figure 6-6(c), which shows the change in the effective diffusion coefficient, D_{eff} , defined in Eq.(6.26). For each case, the effective diffusion coefficient has been plotted with time at each 0.05 mm along the Y axis passing through the center of the beam cross section. The initial value of the effective diffusion

coefficient is lowered by increasing the crosslink density by virtue of a decrease in the pore spaces and increase in tortuosity. The behavior of the effective diffusion coefficient beyond the initial value is affected by the resistance to swelling offered by increased crosslink density. An increased crosslink density rapidly increases the fluid pressure, speeding up the rate of increase of the chemical potential, and thereby decreasing the drop in effective diffusion coefficient as the diffusion proceeds. When A^s is low, the effective diffusion coefficient drops significantly as the contribution of For an A^s value of 300 MPa, the effective diffusion coefficient does not drop significantly over the time of diffusion, and for an A^s of 500 MPa, there is a slight increase in the effective diffusion coefficient with time.

6.5 Conclusion

Fluid flow plays a major role in the rate-dependent mechanical behavior of several materials such as soft biological tissues, hydrogels and hydrophilic polymers. Poromechanics based models have successfully been able to explain such mechanical behavior in a saturated condition. However, in certain instances, material models that can be used to explain both poromechanical behavior and solvent diffusion into the dry material become necessary. Examples of such cases include polymers in biomedical applications such as bioadhesives which have to interact with bodily fluid and carry mechanical load. In this paper, we have utilized a poromechanical model which accounts for the chemical structure of the material to study the diffusion of fluid and concomitant swelling of hydrophilic crosslinked polymers. We note that values of diffusion coefficients are necessary to model fluid flow to predict flow-dependent mechanical behavior. The model framework developed in this paper allows the use of simple mass change experiments to determine diffusion coefficients, which can be used in a poromechanical model to predict mechanical behavior of saturated polymers.

This model is based upon a methodology developed by the authors that incorporates a micromechanics based homogenization of the discrete inter-molecular interactions to arrive at the overall mechanical behavior of the polymer matrix. The fluid flow is incorporated using a poromechanics based approach. In this paper, we apply our model to describe diffusion and predict swelling. The associated boundary value problem has been solved using finite difference scheme and Newton-Raphson method. We demonstrate the ability of the model to predict swelling and describe the effect of crosslink density on the diffusion process. The procedure we use does not account for variation in gradients due to deformation of the sample; however, we note that in spite of this approximation, the model fits the sorption curves well, closely predicts the swelling and reveals insights into the mechanism of swelling.

The model incorporates coupling between the mechanical behavior and the solvent diffusion. The numerical results demonstrate the movement of the wetting front as well as the swelling front through the beam cross section. The swelling front is shown to lag because of the free volume in the polymer. The model is particularly relevant for applications where the polymer needs to be hydrophilic, but also have substantial mechanical stiffness under saturated conditions. For example, dentin adhesive polymers need a hydrophilic/hydrophobic balance to be able to penetrate water-filled pores in monomer state and carry substantial mechanical load in a wet saturated polymer state. The effect of increasing crosslink stiffness and crosslink density while maintaining a constant hydrophilicity becomes a critical input to design polymers for such applications.

Appendix: Model Calibration

The model is calibrated using the equilibrium condition at free swelling. The model parameters A^s , V_ϕ and χ are determined by fitting the equilibrium values of sorption and swelling

measurements as well as the elastic modulus measurements. The elastic modulus is measured using three-point bending at a strain rate which is much faster than the characteristic time for diffusion. To account for the large deformation and significant volume change of the sample, the deformation of a single representative volume element (RVE) is computed incrementally.

Eqs. (6.15) through (6.18) allows us to relate the macroscopic experimental measurements, that is the undrained elastic modulus, the mass change in air, the mass change in water and the volume change to the local (meso-scale) parameters A^s , $V_{\phi 0}$ and χ . However, a numerical solution of these coupled nonlinear equations is required for the calibration of the meso-scale parameters. To this end, we minimized the following objective error function

$$e(A^s, V_{\phi 0}, \chi) = \left(\frac{\Delta m_a - (\Delta m_a)_{eqbm}}{(\Delta m_a)_{eqbm}} \right)^2 + \left(\frac{\Delta m_w - (\Delta m_w)_{eqbm}}{(\Delta m_w)_{eqbm}} \right)^2 + \left(\frac{J - J_{eqbm}}{J_{eqbm}} \right)^2 + \left(\frac{E^u - E_{meas}^u}{E_{meas}^u} \right)^2 \quad (6.38)$$

subject to the constraints

$$A^s > 0, \quad 0 < V_{\phi 0} < 1, \quad \chi > 0 \quad (6.39)$$

where the change of mass in air

$$\Delta m_a = \frac{\rho_w V_{\phi}}{m_{a0}}, \quad (6.40)$$

the change of mass in water

$$\Delta m_w = \frac{\rho_w (V_{\phi} - V + V_0)}{m_{w0}} \quad (6.41)$$

The jacobian J is given by Eq.(6.17), and the undrained elastic modulus is given by Eqs.(6.15),

(6.16) and (6.18). We note that under saturation the water volume fraction, $\gamma_w = \phi = \frac{V_{\phi}}{V}$, and at

equilibrium the chemical potential given by Eq. (6.19) must vanish, thus yielding the required relationship for determining V , V_ϕ , J and E^u , that are needed in Eq.(6.38).

The error function given by Eq. (6.38) was minimized using linear search optimization to determine A^s , $V_{\phi 0}$ and χ . For each iteration, the change of mass in air and water, the Jacobian and the undrained elastic modulus are determined by solving Eq. (6.19) for the equilibrium condition $\mu=0$. The details of the model calibration have been explained in Chapter 4.

	Co-monomer chemical formula/name	Co-monomer Structure
Hydrophobic dimethacrylate	BisGMA	
Hydrophilic methacrylate	HEMA	

Table 6-1 List of co-monomers

Supplier: Sigma Chemical Co., St. Louis, MO, USA.

	$D \times 10^{12} \text{ (m}^2\text{/sec)}$	$A^s \text{ (MPa)}$	χ	V_ϕ
HB60	5.58	356.8	0.96	0.0667
HB75	18.14	104.5	1	0.0797
HB80	25.41	15.83	0.99	0.0904
HB92.5	25.92	11.70	0.68	0.0340

Table 6-2 Diffusion coefficients and model parameters of the polymer formulations

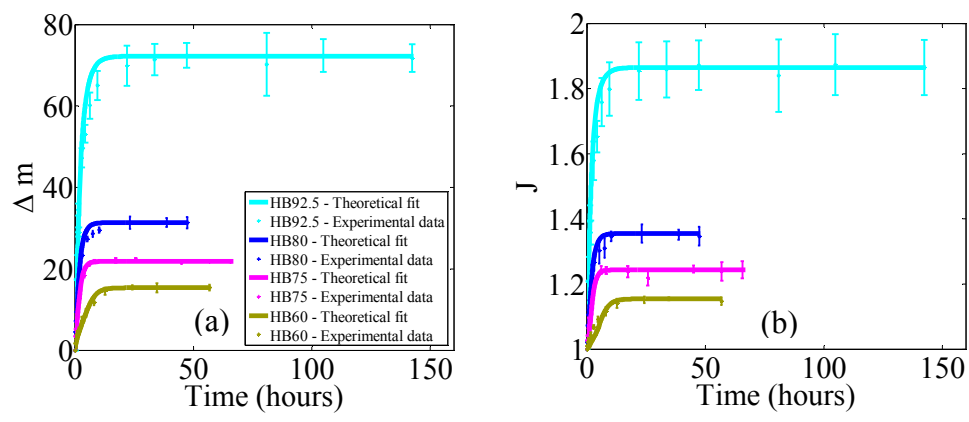


Figure 6-1 Variation of (a) percentage change in mass of the sample (b) swelling i.e. volume of the sample with respect to its original volume

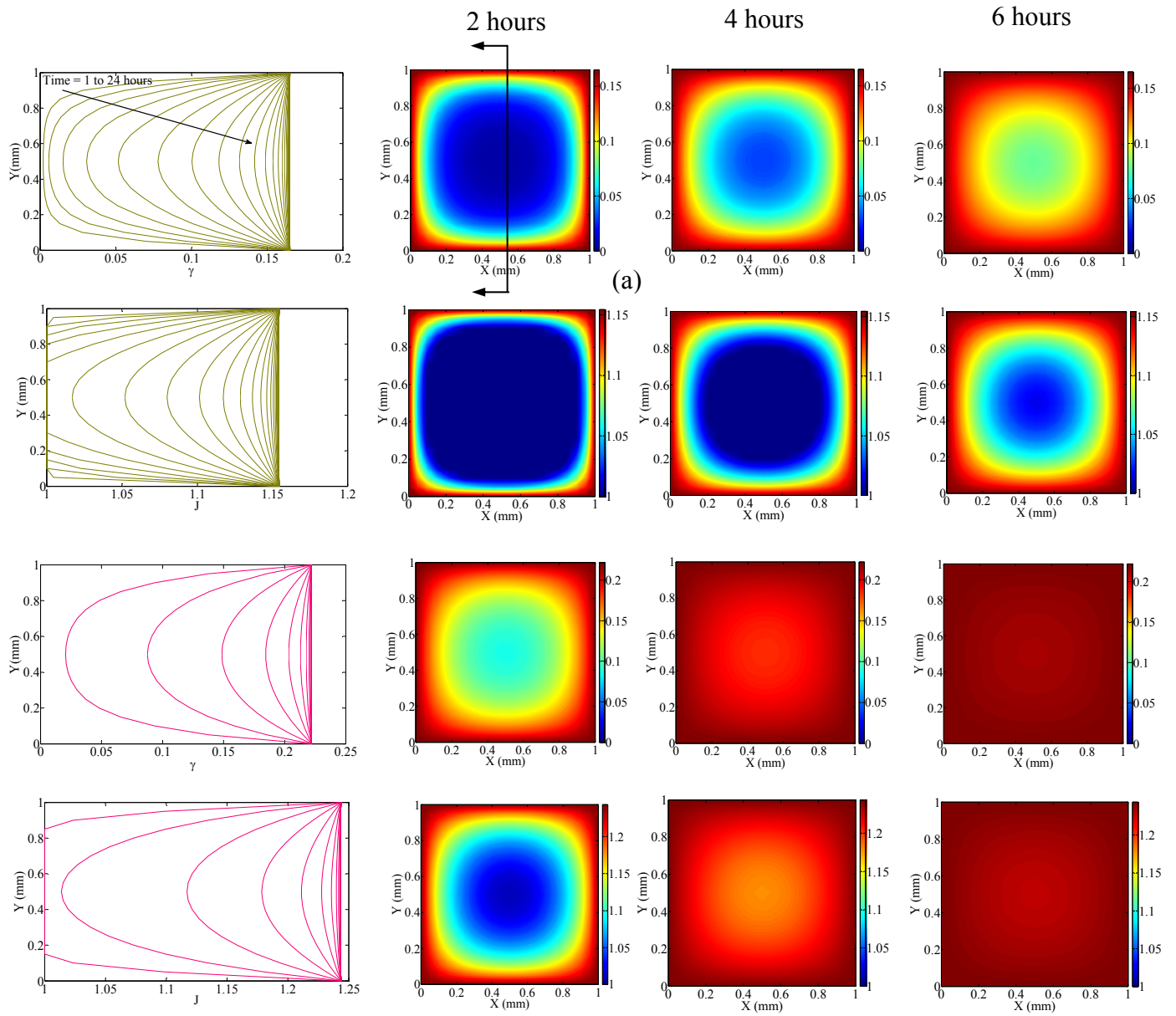


Figure 6-2 Variation of water concentration and Jacobian of deformation inside the beam cross section for (a) HB60 (b) HB75

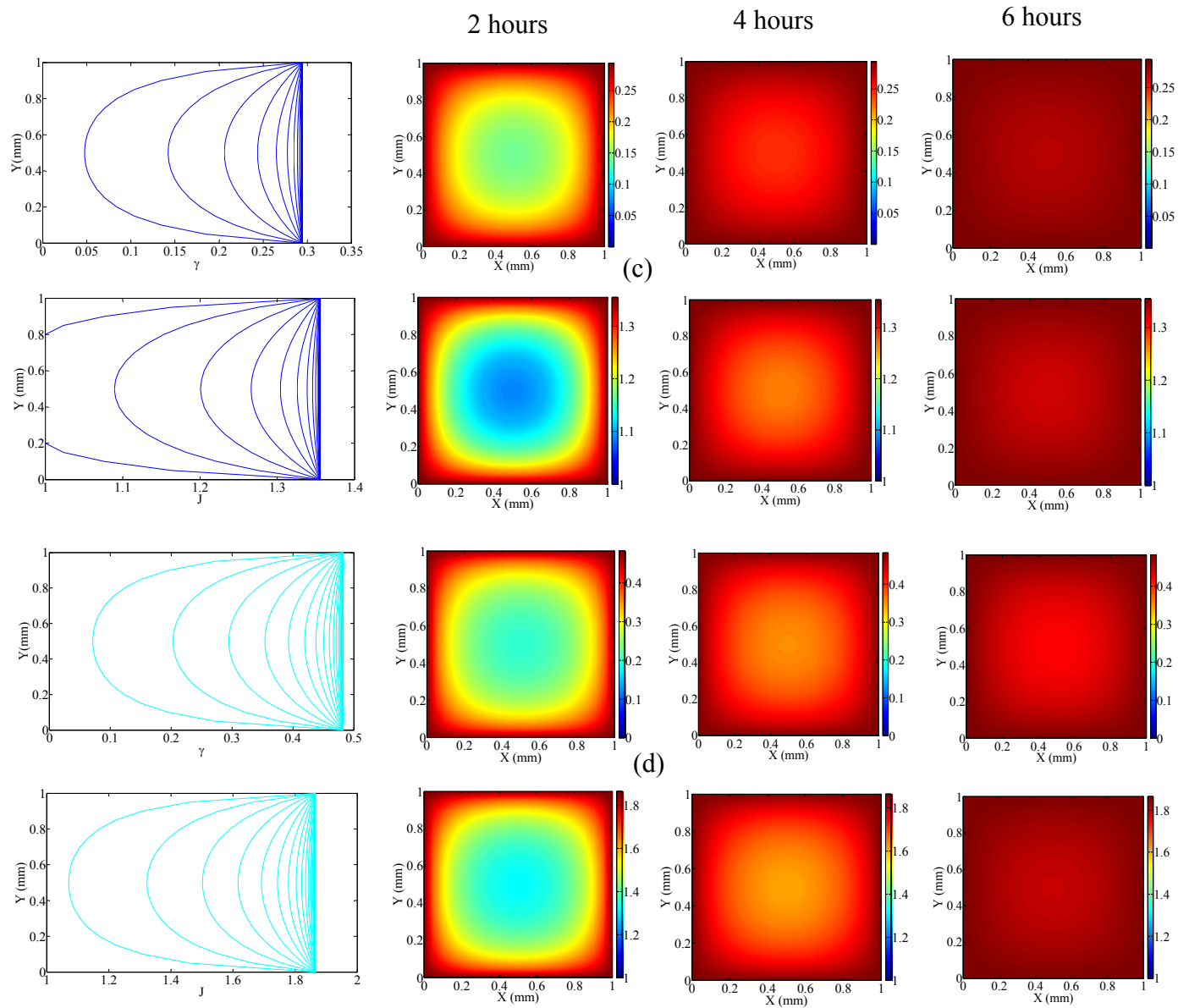


Figure 6-3 Variation of water concentration and Jacobian of deformation inside the beam cross section for (a) HB60 (b) HB75 (c) HB80 and (d) HB92.5

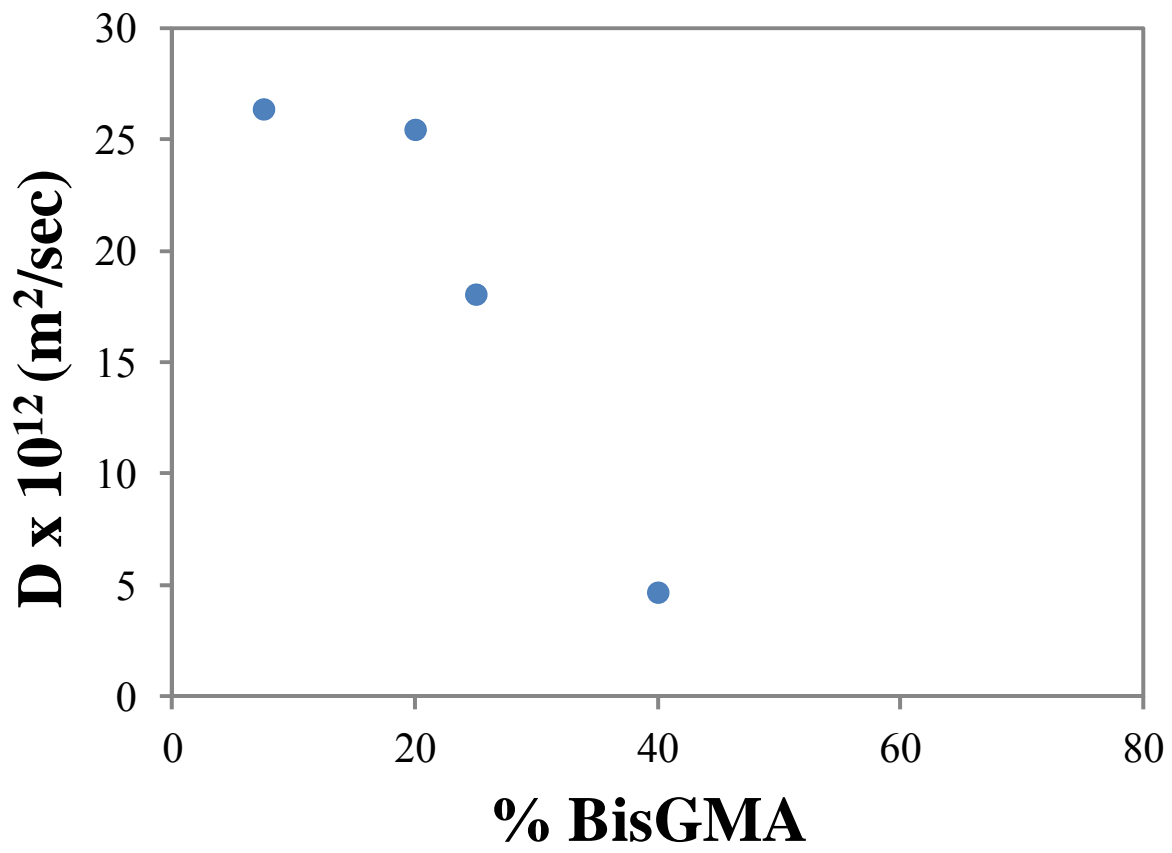


Figure 6-4 Variation of diffusion coefficient with chemical composition

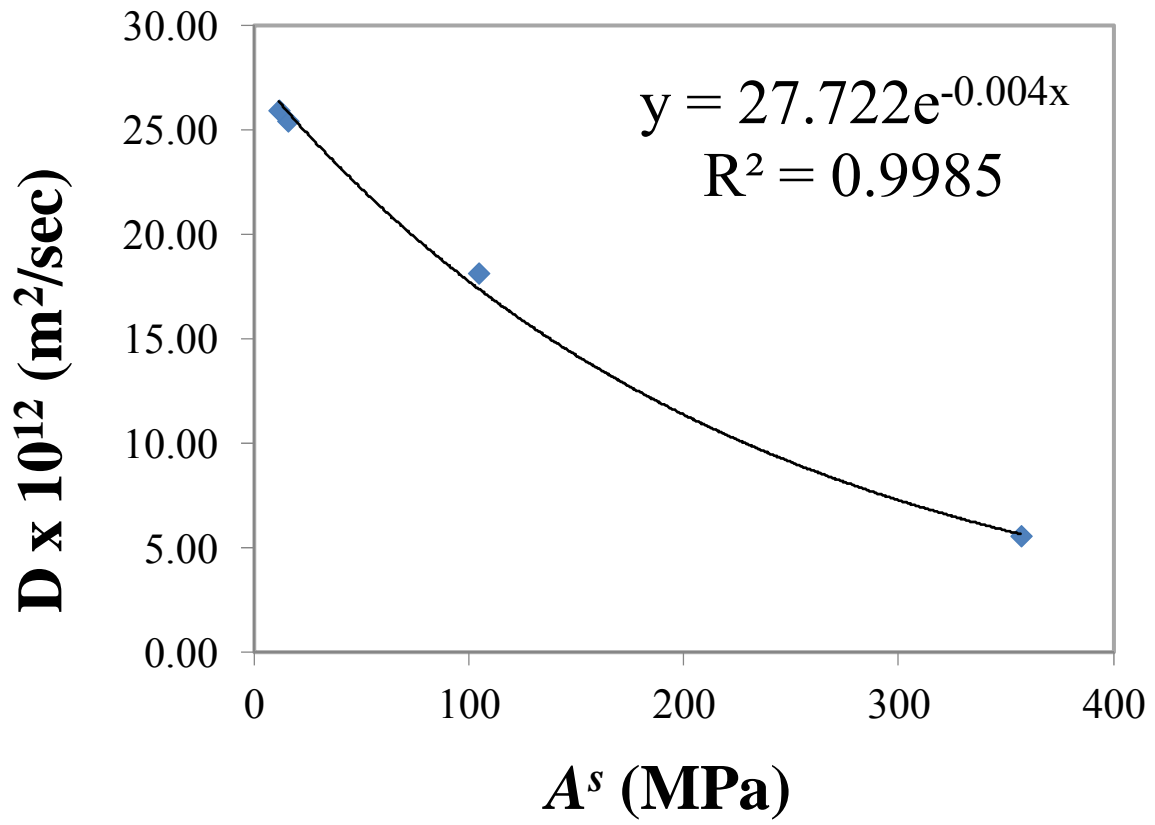


Figure 6-5 Variation of diffusion coefficient with model parameter A^s

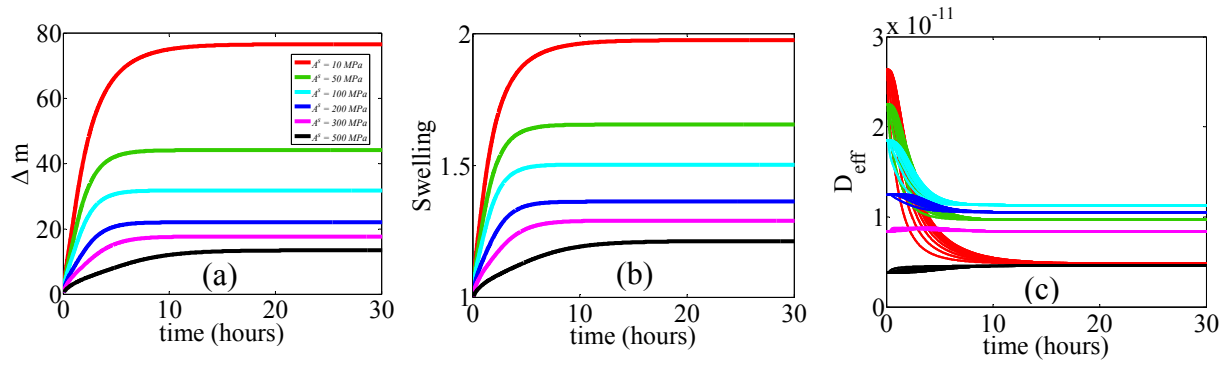


Figure 6-6 Influence of model parameter A^s on the diffusion process

7 POROMECHANICS PARAMETERS OF FLUID-SATURATED CHEMICALLY ACTIVE FIBROUS MEDIA DERIVED FROM A MICROMECHANICAL APPROACH

We have developed a micromechanics based model for chemically active saturated hydrogels that incorporates fiber network microstructure, chemical potential driven fluid flow, and microporomechanics. The stress-strain relationship of the dry polymer is first obtained by considering the fiber behavior. The constitutive relationships applicable to saturated media are then derived in the poromechanics framework using Hill's volume averaging. The advantage of this approach is that the resultant continuum model accounts for the discrete nature of the individual fibers while retaining a form suitable for porous materials. As a result, the model is able to predict the influence of micro-scale phenomena, such as the fiber pre-strain caused by osmotic effects and evolution of fiber network structure with loading, on the overall behavior and in particular, on the poromechanics parameters. Additionally, the model can describe fluid-flow related rate-dependent behavior under confined and unconfined conditions and varying chemical environments. The significance of the approach is demonstrated by simulating unconfined drained monotonic uniaxial compression under different surrounding fluid bath molarity, and fluid-flow related creep and relaxation at different loading-levels and different surrounding fluid bath molarity. The model predictions conform to the experimental observations for saturated soft fibrous materials. The method can potentially be extended to other porous materials such as bone, clays, foams and concrete.

7.1 Introduction

Fluid saturated fibrous natural and synthetic materials are ubiquitous and of interest in diverse fields. These materials are found in nature as soft biological tissues or synthesized as polymeric

hydrogels or form at the interfaces where the water in biological tissues interacts with synthetic polymeric materials. Their mechanical behavior is of interest in wide areas of biomechanics, such as growth mechanobiology (Shraiman 2005, Ateshian and Humphrey 2012), function of heart valves and other cardiovascular tissues (Cowin and Humphrey 2002, Holzapfel and Ogden 2003, Sacks, Merryman et al. 2009), temporomandibular disc and condylar cartilage (Kuboki, Shinoda et al. 1997, Detamore and Athanasiou 2003, Singh and Detamore 2008), tissue engineering scaffolds (Nowak, Breedveld et al. 2002, Luo and Shoichet 2004) and the hybrid layer of dentin-adhesive interfaces (Misra, Spencer et al. 2005). The presence of chemical activity and material non-linearity in addition to the fluid-solid mechanical interaction makes the theoretical analysis of such materials a challenging problem. These materials can be described as porous solids and modeled using principles of poromechanics pioneered by Biot (Biot 1941, Biot 1972), who developed the stress-strain relationships for infinitesimal and finite deformations of elastic soil under three-dimensional consolidation. Biot also extended his theory to viscoelastic solid matrices (Biot 1956) and his approach has since been extended to include chemical activity, material microstructure and solid matrix non-linearity. In contrast to nonporous materials, porous media require additional material properties, termed as poromechanics parameters, in order to define their mechanical behavior. The poromechanical parameters, denoted in this paper by B_{ij} and Γ , are necessary to account for the additional degrees of freedom viz. the fluid pressure and the change of fluid content. For linear isotropic materials, parameters B_{ij} and Γ correspond to the constants α and l/Q introduced by Biot (Biot 1941). An alternative method for modeling saturated fibrous network is by the use of continuum mixture theory (Truesdell and Toupin 1960). However, it has been shown (Bowen 1982, Coussy, Dormieux et al. 1998) that the Biot's poromechanics constitutive equations can be recovered from the mixture theory.

Numerous researchers have investigated the behavior of chemically active porous media using either poromechanics or mixture theory. These efforts have addressed several issues of significance to these type of materials including: chemical potential driven fluid-flow (Mow, Kuei et al. 1980, Lai, Hou et al. 1991); separation of intra and extrafibrillar waters in articular cartilage (Huyghe 1999, Loret and Simoes 2003); fibril reinforcement in cartilage (Fortin, Soulhat et al. 2000, Korhonen, Laasanen et al. 2003, Wilson , Donkelaar et al. 2004, Wilson , Donkelaar et al. 2005); collagen network structure and non-linearity (Farquhar, Dawson et al. 1990, Bursac , McGrath et al. 2000, Quinn and Morel 2007, Federico and Herzog 2008, Ateshian, Rajan et al. 2009); porous continuum for describing bone growth/resorption(Madeo, Lekszycki et al. 2011, Grillo, Federico et al. 2012, Madeo, George et al. 2012); dual-porosity poroelasticity of bone (Cowin 1999); physico-chemical forces between solid and fluid components in swelling clays (Bennethum, Murad et al. 1997); solid matrix dilatation under loading (Sciarra, dell'Isola et al. 2001); poroelasticity and viscoporoelasticity of polymeric gels (Yoon, Cai et al. 2010, Wang and Hong 2012); and second-gradient effects in porous media (dell'Isola, Guarascio et al. 2000, Madeo, Dell'Isola et al. 2008, Sciarra, Dell'Isola et al. 2008). In particular, the numerical simulation of second-gradient effects and microstructure on bio-mechanical coupling and bone remodeling has been carried out by (Madeo, George et al. 2012). As evident, a large number of these works have focused on biological soft tissues owing to the need for constitutive models which could replicate their complex material behavior and aid in modeling and interpretation of experimental studies on tissue engineering and tissue growth (Petite, Viateau et al. 2000). We note, however, that the varieties of porous media and the number of references are too numerous to include here so we have limited ourselves to cite a

selection; the reader should be able to reconstruct the literature by following the references cited therein.

Although the above cited modeling efforts incorporate a broad range of factors that affect the poromechanical behavior of chemically active fiber networks, a number of issues need further attention. For example, a kinematic assumption is used to distribute the strain between the solid and fluid phases. Further, though some of the models have incorporated microstructure, its effect on the evolution of B_{ij} and Γ has not been explicitly considered. These values also affect the pore pressures and chemical potentials generated during loading which drive the fluid flow. The fluid flow, in turn, has been found to be a common denominator governing the transport of nutrients or contaminants which affect important properties such as (a) growth and repair in tissues such as articular cartilage and (b) failure of landfills and foundations for engineering structures like roads, buildings and runways. On the other hand, in approaches that use micromechanics based approach to derive the overall poroelastic behavior, the effects of the solid phase deformation on the poromechanics parameters are explicitly incorporated (Cheng 1997, Dormieux, Molinari et al. 2002, Quiligotti, Maugin et al. 2003, Hoang 2011). Such an approach was used to model articular cartilage as an anisotropic poroelastic material and used to simulate cyclic loading (Hoang and Abousleiman 2012). However, the approach did not model the evolution of anisotropy resulting from microstructural changes to the fiber network during loading.

The present work addresses some of the issues stated above by developing a model that incorporates fiber microstructure, chemical potential driven fluid flow, and micro-poromechanics. In particular we (1) account for the discrete nature of the individual fibers

through micromechanics based homogenization, (2) relate the fiber network description to a poromechanics description, and (3) solve for rate-dependent behavior under confined and unconfined conditions and under varying chemical environments. We find that B_{ij} can deviate upto 10% or more from unity and Γ can vary significantly for these highly compressible materials during creep and relaxation, particularly at small strains. We also find that the evolution of B_{ij} and Γ , as well as that of the fiber network stiffness strongly depends on the changes in fiber microstructure during loading as well as fluid drainage. In the subsequent discussion, we first derive the stress-strain relationship for a fiber network using kinematically driven micromechanical methodology (Chang and Misra 1990, Misra and Chang 1993). We then superpose the homogenized network with the fluid phase to derive the overall constitutive relationship, including expressions for the poromechanical parameters B_{ij} and Γ . Then, we formulate the necessary transport laws for the chemical potential driven fluid flow. Finally, we simulate steady state as well as rate-dependent mechanical behavior under varying conditions of confinement and external bath molarity. We find that the model predictions show qualitatively similar behavior as that observed in experimental data for the various cases of loading presented. The model predictions have been made for articular cartilage under varying load and chemical environment. The microstructure of articular cartilage is that of a hyperelastic material (hydrogel) of low stiffness that is reinforced by a network of stiff collagen fibers. The collagen fibers cannot resist compression due to their rope-like behavior (Clark 1985, Farquhar, Dawson et al. 1990, Li, Buschmann et al. 1999, Wilson, Donkelaar et al. 2004), consequently the fiber law shown in Eq. (7.17) describes the local behavior of a collagen fiber. However, such as in a crosslinked hydrogel, the charged proteoglycan assemblies are imbedded in the collagen fiber network (Horkay 2012), hence it is difficult to model the fiber network and the gel separately. It has been demonstrated that articular cartilage loses more than 84% of its stiffness when the

collagen fiber network has been digested using collagenase (Huang, Wang et al. 2011). So, we neglect the contribution of the aggrecan hydrogel to shear stiffness and assume the stress in the hydrogel to be a hydrostatic fluid pressure. It has also been experimentally demonstrated that cartilage is primarily poroelastic rather than viscoelastic (McCutchen 1982), as proved by the significant sensitivity in equilibration times to specimen size.

7.2 Micromechanical model

We consider a porous material whose solid matrix is a fibrous network as shown schematically in Figure 1, which depicts the microscopic and continuum scales of dry and saturated fibrous porous media. In general saturated chemically active porous media have a nonlinear behavior accompanied by large strains. Therefore, we seek incremental form of Biot's constitutive equations for this media. In this paper, we treat only the nonlinearities that originate from fiber buckling, elongation dependent fiber stiffness, and charge density dependent chemical potential. Nonlinearities from dissipative processes that lead to plastic deformations will be treated in future work. In this case, linearity can be assumed for small increments in stress and strain; thus superposition is used to derive the incremental constitutive behavior. To proceed we consider the general loading increment to be a superposition of two cases. In case 1, we apply an increment of Green-Lagrange strain while the increment of interstitial fluid pressure is held zero denoted as $(\dot{\epsilon} \neq 0, \dot{p} = 0)$. In case 2, we hold the increment of Green-Lagrange strain to be zero while we apply an increment of interstitial fluid pressure denoted as $(\dot{\epsilon} = 0, \dot{p} \neq 0)$. Similar superposition has been used for modeling porous media previously (Dormieux, Molinari et al. 2002, Dormieux, Lemarchand et al. 2003, Misra, Marangos et al. 2012).

7.2.1 Case 1: ($\dot{\varepsilon} \neq 0, \dot{p} = 0$)

Fiber network stress

We first write the macroscopic Cauchy stress, σ_{ij} , of a representative volume element (RVE) of the dry fiber network as the volume average of microscopic stresses

$$\sigma_{ij} = \frac{1}{V} \int_V \sigma_{ij}^f dV \quad (7.1)$$

where V denotes the RVE and σ_{ij}^f is the stress in infinitesimal volume dV . Using Signorini's theorem (Signorini 1932) and applying Gauss' divergence rule, Eq. (4.1) can be written as (see (Chang and Misra 1989))

$$\sigma_{ij} = \frac{1}{V} \int_V \sigma_{ik}^f \frac{\partial x_j}{\partial x_k} dV = \frac{1}{V} \int_{\partial V} \sigma_{ik}^f n_k x_j dA - \frac{1}{V} \int_V \frac{\partial \sigma_{ik}^f}{\partial x_k} x_j dV \quad (7.2)$$

In the absence of body forces and inertial effects, $\frac{\partial \sigma_{ik}^f}{\partial x_k} = 0$, thus we get

$$\sigma_{ij} = \frac{1}{V} \int_{\partial V} \sigma_{ik}^f n_k x_j dA = \frac{1}{V} \int_{\partial V} t_i^f x_j dA \quad (7.3)$$

Where the traction vector $t_i^f = \sigma_{ik}^f n_k$, the position vector $x_i = R_i + r_i$, the centroid of the RVE is denoted by R_i , x_i is the position vector of one end of the intercepted collagen fiber and r_i is the radius vector of the spherical RVE as shown in Figure 2. Eq. (7.3) can now be simplified as

$$\sigma_{ij} = \frac{1}{V} \int_{\partial V} t_i^f (R_j + r_j) dA = \frac{1}{V} \int_{\partial V} t_i^f r_j dA = \frac{1}{V} \int_{\partial V} r_j df_i^f \quad (7.4)$$

since $\int_{\partial V} t_i^f R_j dA = 0$ for centro-symmetrical RVE. Further, the force acting on the infinitesimal

area dA , defined as $df_i^f = t_i^f dA$ is given by

$$df_i^f = (A^f \sigma^f(\theta, \phi) n_i) N \xi(\theta, \phi) \sin \theta d\theta d\phi \quad (7.5)$$

as the product of (1) the force in the fiber, $A^f \sigma^f n_i$, where A^f is the fiber area, σ^f is the fiber stress and n_i is a unit normal vector expressed in spherical coordinates as the triad $\langle \cos\theta, \sin\theta\cos\phi, \sin\theta\sin\phi \rangle$, and (2) the number of fibers intersecting the infinitesimal area, $dA = \sin\theta d\theta d\phi$, given by $N\xi(\theta, \phi)\sin\theta d\theta d\phi$, where $\xi(\theta, \phi)$ is the probability density of the fiber distribution along (θ, ϕ) , and N is the total number of fibers. Since the average length of a fiber is given as r , the total volume of fibers in the RVE is $NA^f r$. Expressing fiber volume in terms of the fiber volume fraction, γ_f , we get

$$NA^f r = \gamma_f V \quad (7.6)$$

Combining Eqs. (7.4), (7.5) and (7.6), with we obtain the following relationship for the RVE Cauchy stress

$$\sigma_{ij} = \gamma_f \int_{\partial V} \sigma^f(\theta, \phi) n_i n_j \xi(\theta, \phi) \sin\theta d\theta d\phi \quad (7.7)$$

We now obtain the relationship for the increment of the RVE Cauchy stress, $\dot{\sigma}_{ij}$, as follows from Eq. (7.4):

$$\dot{\sigma}_{ij} = -\frac{\dot{V}}{V^2} \int_{\partial V} df_i^f r_j + \frac{1}{V} \int_{\partial V} \dot{df}_i^f r_j + \frac{1}{V} \int_{\partial V} df_i^f \dot{r}_j \quad (7.8)$$

where the terms with over dot ($\dot{\quad}$) denote incremental quantities throughout the paper. From the definition of the Second Piola Kirchhoff stress, $df_i^f = F_{ik} df_k^{f0}$, where the force df_i^f expressed with respect to the current configuration is related to the force df_i^{f0} expressed with respect to the undeformed configuration through the deformation gradient, F_{ik} . Thus

$$\dot{df}_i^f = \dot{F}_{ik} df_k^{f0} + F_{ik} \dot{df}_k^{f0} \quad (7.9)$$

Further, from the definition of the deformation gradient, $r_j = F_{jm} r_m^0$, we get

$$\dot{r}_j = \dot{F}_{jm} r_m^0 \quad (7.10)$$

where r_m^0 is the position vector in the undeformed configuration. Eq. (7.8) can now be written as follows

$$\dot{\sigma}_{ij} = -\frac{\dot{J}}{J^2 V_0} F_{ik} \left(\int_{\partial V} df_k^{f0} r_m^0 \right) F_{jm} + \frac{1}{V} \int_{\partial V} \hat{df}_i^f r_j + \frac{1}{JV_0} \dot{F}_{ik} \left(\int_{\partial V} df_k^{f0} r_m^0 \right) F_{jm} + \frac{1}{JV_0} F_{ik} \left(\int_{\partial V} df_k^{f0} r_m^0 \right) \dot{F}_{jm} \quad (7.11)$$

where V_0 is the undeformed volume of the RVE, J is the jacobian of the deformation gradient such that $V = JV_0$, and $\hat{df}_i^f = F_{ik} \dot{df}_k^{f0}$. We note that the Cauchy stress defined in Eq. (7.4) can be expressed in terms of the Second Piola Kirchoff stress as follows

$$\sigma_{ij} = \frac{1}{J} F_{ik} S_{km} F_{jm} = \frac{1}{J} F_{ik} \left(\frac{1}{V_0} \int_{\partial V} df_k^{f0} r_m^0 \right) F_{jm} \quad (7.12)$$

Thus, Eq. (7.12) can be written as

$$\dot{\sigma}_{ij} = -\dot{J} J^{-2} F_{ik} S_{km} F_{jm} + \hat{\sigma}_{ij} + J^{-1} \dot{F}_{ik} F_{ik} S_{km} F_{jm} + J^{-1} F_{ik} S_{km} \dot{F}_{jm} \quad (7.13)$$

Using the spatial velocity gradient defined as $L_{jp} = \dot{F}_{jm} F_{mp}^{-1}$, and increment of jacobian given as $\dot{J} = \delta_{rs} L_{rs} J$, Eq. (7.13) can be written as

$$\dot{\sigma}_{ij} = -\delta_{rs} L_{rs} \sigma_{ij} + \hat{\sigma}_{ij} + \sigma_{jm} L_{im} + \sigma_{im} L_{jm} \quad (7.14)$$

From whence we obtain the well-known Truesdell stress increment

$$\hat{\sigma}_{ij} = \dot{\sigma}_{ij} + \delta_{rs} L_{rs} \sigma_{ij} - \sigma_{im} L_{jm} - \sigma_{jm} L_{im} \quad (7.15)$$

The Truesdell stress increment can be further simplified analogous to Eq. (7.7) as follows

$$\hat{\sigma}_{ij} = \frac{1}{V} \int_{\partial V} \hat{df}_i^f r_j = \gamma_f \int_{\partial V} \hat{\sigma}^f(\theta, \phi) n_i n_j \xi(\theta, \phi) \sin \theta d\theta d\phi \quad (7.16)$$

where the fiber stress increment, $\hat{\sigma}^f$, can be related to the fiber strain increment by the following

1-dimensional nonlinear constitutive equation considering a slender fiber element

$$\hat{\sigma}^f = C^f (e^f)^\alpha \dot{e}^f \quad \text{in tension; and} \quad \hat{\sigma}^f = 0 \quad \text{in compression} \quad (7.17)$$

where C^f is a constant and exponent $\alpha \geq 0$. Further, the fiber strain increment, \dot{e}^f , can be expressed in terms of the overall RVE strain increment, $\dot{\epsilon}_{kl}$, using the following kinematic assumption

$$\dot{e}^f = n_k n_l \dot{\epsilon}_{kl} \quad (7.18)$$

Thus the tangential stress-strain relationship for the RVE can be written as follows

$$\hat{\sigma}_{ij} = C_{ijkl} \dot{\epsilon}_{kl} \quad (7.19)$$

where $C_{ijkl} = \gamma_f \int_{\partial V} C^f(\theta, \phi) n_i n_j n_k n_l \xi(\theta, \phi) \sin \theta d\theta d\phi$, and for uniform probability density of the

fiber distribution, $\xi(\theta, \phi) = \frac{1}{4\pi}$. The derived relationship has similarities with those obtained

using the virtual internal bond and granular micromechanics methods (Chang and Misra 1990, Gao and Klein 1998, Misra and Yang 2010, Misra and Singh). The approach presented here can also be applied to obtain higher-order stiffness tensors of relevance to second- and higher-gradient theories (dell'Isola, Sciarra et al. 2009, Yang and Misra 2012).

Volumetric water content

For case 1 loading increment, since the fluid pressure increment is held zero, the incremental change in volumetric water content is same as the incremental change in volume of pore space, thus

$$\dot{\zeta} = \varphi \dot{\epsilon}_{ii}^\varphi \quad (7.20)$$

where $\dot{\zeta}$ is the incremental change in volumetric water content, φ is the pore volume fraction (porosity) referred to the deformed configuration at the beginning of the strain increment, and $\dot{\epsilon}_{ii}^\varphi$ is the increment of average pore space strain. We note here that the fiber volume fraction, γ_f , and porosity, φ , satisfy the relationship $\gamma_f + \varphi = 1$. Further, the incremental average pore space strain

can be expressed in terms of the average incremental Green-Lagrange strain of the RVE as follows:

$$\dot{\boldsymbol{\varepsilon}}_{ij}^{\varphi} = H_{ijkl}^{\varphi} \dot{\boldsymbol{\varepsilon}}_{kl} \quad (7.21)$$

where H_{ijkl}^{φ} is the strain concentration tensor for the pore space. The average incremental fiber strain $\dot{\boldsymbol{\varepsilon}}_{kl}^f$ can also be expressed in terms of the average incremental Green-Lagrange strain of the RVE as follows:

$$\dot{\boldsymbol{\varepsilon}}_{ij}^f = H_{ijkl}^f \dot{\boldsymbol{\varepsilon}}_{kl} \quad (7.22)$$

Following Hill's volume averaging principle expressed as

$$\dot{\boldsymbol{\varepsilon}}_{ij} = (1 - \varphi) \dot{\boldsymbol{\varepsilon}}_{ij}^f + \varphi \dot{\boldsymbol{\varepsilon}}_{ij}^{\varphi} \quad (7.23)$$

we obtain the following identity.

$$\delta_{ik} \delta_{jl} = (1 - \varphi) H_{ijkl}^f + \varphi H_{ijkl}^{\varphi} \quad (7.24)$$

Noting that the increment of the pore stress is zero, the volume average incremental stress for the RVE can be written as

$$\hat{\boldsymbol{\sigma}}_{ij} = (1 - \varphi) \hat{\boldsymbol{\sigma}}_{ij}^f \quad (7.25)$$

Now, using the constitutive relationship for the fiber material, written as $\hat{\boldsymbol{\sigma}}_{ij}^f = C_{ijkl}^f \dot{\boldsymbol{\varepsilon}}_{kl}^f$, and combining Eqs. (7.19), (7.22) and (7.25) we find

$$(1 - \varphi) H_{ijkl}^f = \left(C_{pqij}^f \right)^{-1} C_{pqkl} \quad (7.26)$$

Further, using Eqs. (7.20), (7.21), (7.24) and (7.26), the incremental change in volumetric water content, $\dot{\zeta}$, can be expressed in terms of the average incremental Green-Lagrange strain of the RVE as

$$\dot{\zeta} = \left(\delta_{ik} \delta_{jl} - \left(C_{ijkl}^f \right)^{-1} C_{ijmn} \right) \delta_{ij} \dot{\boldsymbol{\varepsilon}}_{kl} \quad (7.27)$$

7.2.2 Case 2: ($\dot{\varepsilon} = 0, \dot{p} \neq 0$)

Since the incremental strain is held zero during case 2 loading, we consider the increment of Cauchy stress given as

$$\dot{\sigma}_{ij} = -B_{ij}\dot{p} \quad (7.28)$$

where \dot{p} is the increment of the pore fluid pressure and B_{ij} is the poromechanical parameter.

Further, the incremental change in volumetric water content is given as

$$\dot{\zeta} = \left(\dot{\varepsilon}_{ii}^{\phi} + \frac{\dot{p}}{K_f} \right) \phi \quad (7.29)$$

where the first term in Eq. (7.29) arises from the volume change of the pore spaces and the second term is contributed by the fluid compressibility. In addition, the volume average incremental stress for the RVE can be written as

$$\dot{\sigma}_{ij} = (1-\phi)\dot{\sigma}_{ij}^f + \phi\dot{\sigma}_{ij}^{\phi} = (1-\phi)\dot{\sigma}_{ij}^f - \phi\dot{p}\delta_{ij} \quad (7.30)$$

Since the fiber material is expected to be considerably (order of magnitude) stiffer than the RVE such that it suffers small deformations, we assume $\dot{\sigma}_{ij}^f = C_{ijkl}^f \dot{\varepsilon}_{kl}^f$, which leads to the following relationship in light of Eq. (7.28)

$$(1-\phi)\dot{\varepsilon}_{kl}^f = (C_{ijkl}^f)^{-1} (\phi\delta_{ij} - B_{ij})\dot{p} \quad (7.31)$$

Now, using Eq. (7.23) for this case, we get

$$\phi\dot{\varepsilon}_{ii}^{\phi} = -(C_{ijkl}^f)^{-1} (\phi\delta_{ij} - B_{ij})\dot{p} \quad (7.32)$$

Thus from Eq. (7.29), the incremental change in volumetric water content is obtained as,

$$\dot{\zeta} = \left(-(C_{pqij}^f)^{-1} (\phi\delta_{pq} - B_{pq})\delta_{ij} + \frac{\phi}{K_f} \right) \dot{p} \quad (7.33)$$

7.2.3 Superposition of Case 1 and Case 2

Case 1 and 2 results, given in Eqs. (7.19), (7.27), (7.28) and (7.33), are now superposed to obtain the incremental stress-strain relationship for the general case of applied loading, $(\dot{\epsilon}, \dot{p})$, as follows.

$$\dot{\sigma}_{ij} = -\delta_{rs} L_{rs} \bar{\sigma}_{ij} + C_{ijkl} \dot{\epsilon}_{kl} + \bar{\sigma}_{jm} L_{im} + \bar{\sigma}_{im} L_{jm} - B_{ij} \dot{p} \quad (7.34)$$

$$\dot{\zeta} = \left(\delta_{ik} \delta_{jl} - (C_{ijkl}^f)^{-1} C_{ijmn} \right) \delta_{ij} \dot{\epsilon}_{kl} + \Gamma \dot{p} \quad (7.35)$$

where $\bar{\sigma}_{ij}$ is the effective stress obtained from accretion of Eq. (7.14) and

$$\Gamma = (C_{pqij}^f)^{-1} (B_{pq} - \varphi \delta_{pq}) \delta_{ij} + \frac{\varphi}{K_f} \quad (7.36)$$

It now remains to define B_{ij} , to which end we consider the following second-order virtual work expression

$$\dot{\sigma}_{ij}^2 \delta \dot{\epsilon}_{ij}^1 = \langle \dot{\sigma}_{ij}^2 \delta \dot{\epsilon}_{ij}^1 \rangle_V = (1 - \varphi) \langle \dot{\sigma}_{ij}^{f2} \delta \dot{\epsilon}_{ij}^{f1} \rangle_{V_f} + \varphi \langle \dot{\sigma}_{ij}^{\varphi 2} \delta \dot{\epsilon}_{ij}^{\varphi 1} \rangle_{V_\varphi} \quad (7.37)$$

where $\langle \cdot \rangle$ represents volume averaged quantities, and superscripts represents cases 1 and 2. In light of Eqs. (7.28), (7.30) and (7.31), Eq. (7.37) becomes

$$-B_{ij} \dot{p} \delta \dot{\epsilon}_{ij}^1 = (1 - \varphi) \dot{\sigma}_{ij}^{f1} \delta \dot{\epsilon}_{ij}^{f2} - \varphi \dot{p} \delta_{ij} \delta \dot{\epsilon}_{ij}^{\varphi 1} \quad (7.38)$$

It is straightforward to show that first term of the right-hand-side vanishes, that is $\dot{\sigma}_{ij}^{f1} \delta \dot{\epsilon}_{ij}^{f2} = 0$, by considering the second-order virtual work $\langle \dot{\sigma}_{ij}^1 \delta \dot{\epsilon}_{ij}^2 \rangle_V$. Now, using Eq. (7.21) we simplify the second-order virtual work expression in Eq. (7.38) as follows

$$B_{ij} \dot{p} \delta \dot{\epsilon}_{ij}^1 = \varphi \dot{p} \delta_{ij} H_{ijkl}^\varphi \delta \dot{\epsilon}_{kl}^1 \quad (7.39)$$

Since Eq. (7.39) must hold for all virtual strain increments, $\delta \dot{\epsilon}_{kl}^1$, we obtain the following expression for B_{ij} , using Eqs. (7.24) and (7.26),

$$B_{ij} = \left(\delta_{mi} \delta_{nj} - (C_{pqmn}^f)^{-1} C_{pqij} \right) \delta_{mn} \quad (7.40)$$

Thus Eqs. (7.34)-(7.36) can be written as follows

$$\dot{\sigma}_{ij} = -\delta_{rs} L_{rs} \bar{\sigma}_{ij} + C_{ijkl} \dot{\epsilon}_{kl} + \bar{\sigma}_{jm} L_{im} + \bar{\sigma}_{im} L_{jm} - B_{ij} \dot{p} \quad (7.41)$$

$$\dot{\zeta} = B_{ij} \dot{\epsilon}_{ij} + \Gamma \dot{p} \quad (7.42)$$

$$\Gamma = (C_{ijkl}^f)^{-1} \left[\left(\delta_{mi} \delta_{nj} - (C_{pqmn}^f)^{-1} C_{pqij} \right) \delta_{mn} - \varphi \delta_{ij} \right] \delta_{kl} + \frac{\varphi}{K_f} \quad (7.43)$$

7.3 Transport Model and Chemical Potential

When saturated chemically active fibrous media are immersed in an ionic solution, they either imbibe or exude fluid depending upon the fixed charges within the fibrous media, the molarity and the ion valencies of the surrounding fluid bath. The flow of fluid and ions can be described using the concept of electrochemical potential for ionic solutions introduced in (Guggenheim 1929). The constitutive equation for the diffusion of fluid with respect to the solid matrix can be expressed as (see also (Loret and Simoes 2007)) for a general constitutive equation for diffusion of fluids and ions):

$$\vec{j}_w = \frac{D_w}{RT} \rho_w \varphi (\vec{\nabla} \mu_w) \quad (7.44)$$

where subscript w refers to the fluid, j is the flux, ρ is the mass density, μ is the chemical potential, D is the diffusion coefficient expressed in dimensions of area per unit time, and R and T are the universal gas constant and temperature, respectively. Eq. (7.44) assumes that the diffusive flux of the ions through the fluid is much faster than the diffusive flux of the fluid through the porous medium so that ionic equilibrium is instantaneously established as compared to chemical equilibrium of the fluid phase (Lanir 1987). For a single RVE of the porous medium, Eq. (7.44) can be approximated as follows.

$$j_w = \frac{D_w}{RT} \rho_w \varphi \left(\frac{\Delta \mu_w}{l} \right) \quad (7.45)$$

where the flux is assumed to be isotropic hence expressed as a scalar, and l , representing the length scale over which the diffusion occurs, is the RVE size. We note that the fluid flow is in general, not isotropic for porous media such as articular cartilage, and changes during loading due to induced anisotropy. In addition, the diffusion coefficient also changes during loading, with applied strain, induced anisotropy and mechanical pressure (Greene, Zappone et al. 2010). However, we assume isotropic flow and a constant diffusion coefficient for ease of calculation and interpretation of the results.

The difference in fluid chemical potential which drives the flow of the fluid is written as follows (Guggenheim 1929, Overbeek 1956)

$$\Delta \mu_w = \mu_w^i - \mu_w^o = (p - p^o) v_w + RT (\ln x_w^i - \ln x_w^o) \quad (7.46)$$

where superscript i and o denote inside and outside of the porous material, respectively, x_w is the mole fraction, v_w is the partial molar volume, and p is the partial pressure. For dilute solutions, the above equation may be simplified as follows (Overbeek 1956).

$$\Delta \mu_w = (p - p^o) v_w + RT v_w (2C_o - C_{Na^+}^i - C_{Cl^-}^i) \quad (7.47)$$

where $C_{Na^+}^i$ and $C_{Cl^-}^i$ are the concentrations of the Na^+ cations and Cl^- anions inside the porous material, respectively, while C_o is the concentration of either ion in the surrounding fluid bath. Since the ionic equilibrium is instantaneously established, equating the chemical potentials of the sodium and chloride ions and applying the Donnan equilibrium condition (Overbeek 1956) gives the following.

$$C_{Na^+}^i C_{Cl^-}^i = C_o^2 \quad (7.48)$$

The concentrations of ions in the surrounding fluid bath are assumed to be constant since its volume is much larger compared to the porous medium. Electroneutrality inside the porous material can now be written as follows:

$$C_{Na^+}^i - C_{Cl^-}^i - C_F = 0 \quad (7.49)$$

where C_F is the fixed charge density of the porous material. Using equations (7.48) and (7.49), Eq. (7.47) can be simplified as

$$\Delta\mu_w = (p - p^o)v_w - RTv_w \left[\left(\frac{1}{4}C_F^2 + C_o^2 \right)^{1/2} - C_o \right] \quad (7.50)$$

Taking the pressure in the surrounding fluid bath $p^o=0$, the chemical potential difference can be rewritten as

$$\Delta\mu_w = (p - p^c)v_w \quad (7.51)$$

where p^c is identified as the Donnan's osmotic pressure given by

$$p^c = RT \left[\left(\frac{1}{4}C_F^2 + C_o^2 \right)^{1/2} - C_o \right] \quad (7.52)$$

Hence, Eq. (7.45) can be written as follows.

$$j_w = K_{ww}(p - p^c) \quad (7.53)$$

where $K_{ww} = \frac{D_w \rho_w \phi v_w}{RTl}$ is an effective mass transfer coefficient. We observe that the chemical potential difference for the fluid phase at any time during the deformation is proportional to the difference between fluid pressure and osmotic pressure corresponding to the fixed charge density at that particular deformed state. Further, the incremental change in volumetric water content, $\dot{\zeta}$, can be written in terms of the fluid flux with respect to the fiber network as follows.

$$\dot{\zeta} = \frac{-j_w A}{\rho_w V} \quad (7.54)$$

Where A and V are the area and volume of the RVE and ρ_w is the density of fluid at the pressure of the external bath and the flux, j_w is obtained from Eq.(7.53).

7.4 Comparison of Drained and Undrained Compression

For the examples discussed hereafter, the RVE is subjected to unconfined uniaxial loading in two separate phases: the free-swell phase followed by either drained or undrained loading under uniaxial stress conditions.

7.4.1 Loading Conditions

Free-Swelling

In the free-swell phase, the RVE undergoes pre-strain due to swelling caused by water migration in response to the chemical potential difference between the material and the environment under an overall stress-free condition. The phenomena results in an osmotic pore pressure in the RVE fluid phase. At equilibrium, where chemical potential difference vanishes, osmotic pore pressure, p^c , can be obtained using Donnan's method as follows (Overbeek 1956)

$$p = p^c = RT[(.25C_F^2 + C_o^2)^{1/2} - C_o] \quad (7.55)$$

where C_F is the fixed charge density of the material, C_o is the molarity of the salt solution in which the RVE is immersed, R is the universal gas constant and T is the temperature. The strain and pore pressure increments can now be obtained from Eqs. (7.41) and (7.42) by setting the stress increment to zero, such that

$$\dot{\epsilon}_{kl} = \left(C_{ijkl} + \frac{1}{\Gamma} B_{ij} B_{kl} \right)^{-1} \left(\dot{\sigma}_{ij} + \delta_{rs} L_{rs} \bar{\sigma}_{ij} - \bar{\sigma}_{jm} L_{im} - \bar{\sigma}_{im} L_{jm} + B_{ij} \frac{\dot{\zeta}}{\Gamma} \right) \quad (7.56)$$

where the incremental volumetric water content $\dot{\zeta}$ is specified using suitable step-size. To estimate the step-size, we approximate pre-strain using Eq. (7.41) and the total volumetric water

content change under small-strain linear assumption. The step-size ζ is then taken as a fraction (typically 1/100th) of the approximated total volumetric water content change. The incremental strains are accumulated to obtain the pre-strain corresponding to the equilibrium osmotic pore pressure.

Undrained Loading

During undrained loading there is no ingress or egress of water and the incremental volumetric water content, ζ , is set to zero. Thus from Eqs. (7.41) and (7.42), we get

$$\dot{p} = -\frac{1}{\Gamma} B_{kl} \dot{\epsilon}_{kl} \quad (7.57)$$

$$\dot{\epsilon}_{kl} = \left(C_{ijkl} + \frac{1}{\Gamma} B_{ij} B_{kl} \right)^{-1} \left(\dot{\sigma}_{ij} + \delta_{rs} L_{rs} \bar{\sigma}_{ij} - \bar{\sigma}_{jm} L_{im} - \bar{\sigma}_{im} L_{jm} \right) \quad (7.58)$$

Further, the volume fractions of the constituents change during loading. From Eq. (7.29), the incremental change of porosity is given as

$$\dot{\phi} = -\phi \left(\frac{\dot{p}}{K_f} + \frac{\dot{J}}{J} \right) \quad (7.59)$$

The volume fraction of the fiber is calculated from the identity, $\gamma_f + \phi = 1$, and the increment of fixed charge density is given as

$$\dot{C}_F = -C_F \dot{\epsilon}_{ii}^\phi \quad (7.60)$$

Drained Loading

During drained loading ingress or egress of water is permitted such that when equilibrium is reached for an applied load, the pore pressure is same as the osmotic pore pressure. In this case Eqs. (7.41) and (7.42) apply directly. Further, the incremental change of porosity is obtained from Eq. (7.29) and the increment of fixed charge density is given by Eq. (7.60).

7.5 Results and Discussions

The parameters used for the calculations described below are taken to be as follows: 1-d constitutive law for fiber – $\alpha=0.5$, $C^f=1200$ MPa, fiber volume fraction in the reference state $\gamma_f=0.55$, porosity in the reference state, $\phi=0.45$, fixed charge density in the reference state $C_F=330$ meq/m³, external salt concentration $C_o=15$ meq/m³, fiber material properties – Young's modulus=200 MPa, and Poisson's ratio=0.2, bulk modulus of water $K_f=2200$ MPa, and the probability density function of initially isotropic fiber distribution given by Eq.(7.62). These model parameters are chosen to enable a qualitative comparison with the behavior of articular cartilage which is an example of a chemically active water saturated fibrous material (Oloyede, Flachsmann et al. 1992).

7.5.1 Fiber Stress and Induced Anisotropy

In the free swelling phase, during which water is free to drain, an isotropic pre-strain of 1.27% develops. Thus, at the end of free swelling phase all the fibers in the network are under equal tension as shown in Figure 7-3 which gives the directional fiber stress distribution at 0, 0.8, 2.5 and 10% axial strain, respectively. Under free swelling condition, the fiber network behaves as an isotropic material. As the RVE is subjected to compressive uniaxial stress loading, fibers oriented closer to the loading direction experience unloading while those closer to the lateral direction experience further tensile loading as shown by the directional fiber stress distribution in Figure 7-3. Consequently, the fiber network behaves as a transverse isotropic material although the degree and the nature of this induced anisotropy depends upon the drainage condition. The predicted overall stress-strain behavior and the evolution of material parameters for the two drainage conditions are shown in Figure 7-4 and Figure 7-5. We note that in Figure 7-3 through

Figure 7-6, the axial strain is expressed with respect to the free swollen configuration, such that 0% axial strain corresponds to the end of the free swelling phase.

7.5.2 *Stress-Strain and Pore Pressure-Water Content*

Figure 7-4(a) gives the plot of the axial stress, σ_{11} , with axial strain, ϵ_{11} , and lateral strain, ϵ_{22} , during the uniaxial loading. We observe from Figure 7-4(a) that in the initial stages of loading, for axial strain magnitude, ϵ_{11} , below the tensile pre-strain, the overall stress-strain behavior of the drained and undrained cases are close. However, the drained and undrained behaviors deviate considerably once the fibers oriented closer to the axial direction completely unload. Further, from Figure 7-4(b), we observe that for the drained case, the axial effective stress attributable to the fiber network decreases rapidly from its initial tensile state. In this case, the applied axial stress is increasingly supported by the pore pressure, which for the drained case is contributed exclusively by the osmotic pore pressure as seen from Figure 7-4(c). The rise in osmotic pore pressure for the drained condition is not unexpected since there is a considerable increase in fixed charge density due to the volume compression and change in porosity as shown in Figure 7-4(c).

In contrast, for the undrained case, the axial effective stress first decreases and then begins to increase as seen from Figure 7-4(b). In this case, the large tensile loading that the lateral fibers experience makes increasing contribution to axial component of the effective stress. We further expound on this aspect later in the subsection – Evolution of Stiffness and Poromechanical Parameters. It is also notable that the contribution of the pore pressure in supporting the applied stress is significantly higher for the undrained case as seen from in Figure 7-4(e) and Figure 7-4(f). It is noteworthy however, that in this case the osmotic pore pressure contribution is

insignificant since there is negligible change in fixed charge density and the porosity (Figure 7-4 (c) and Figure 7-4(d), respectively).

The uniaxial stress-strain behavior for the undrained and drained cases closely resemble the bounds of experimental data presented by (Oloyede, Flachsmann et al. 1992) for extremely low (close to drained conditions) and extremely high (close to undrained conditions) loading rates, respectively. The absence of an initially stiff region in the data presented by Oloyede et al is expectantly due to the relatively high bath salt concentration of 0.15 M in their experiments. In our example calculations, given in Figure 7-4, we use a lower bath salt concentration of 0.015 M to demonstrate the effect of higher pre-strain. We obtain similar result as Oloyede et al for higher bath salt concentration. Further, the apparent yielding in the stress-strain curve for drained case predicted by the model has also been observed in experiments on free-swollen articular cartilage (Chahine, Wang et al. 2004). We also note that according to our model prediction the post-yield behavior is primarily governed by the osmotic pressure. Similar post-yield behavior has also been observed in experiments under drained conditions (Chahine, Wang et al. 2004). Moreover, the stiffness in the post-yield regime is found to have a small increase (DiSilvestro, Zhu et al. 2001) which agrees with the prediction shown in Figure 4(a). It is noteworthy, however, that the apparent yielding is absent at higher rate of loading (Li, Buschmann et al. 2003), which is similar to the undrained behavior predicted by our model. Further, the load sharing between the fiber network and the pore-fluid predicted for undrained compression agrees with the well-accepted hypothesis that the pore-pressure largely supports the applied load in the early part of the time response of the articular cartilage (Soltz and Gerard 1998, Li, Buschmann et al. 2003, Li and Herzog 2004).

7.5.3 Evolution of Stiffness and Poromechanical Parameters

We further describe the behavior in the two drainage conditions by considering the evolution of the material parameters during loading. In Figure 7-5(a) through Figure 7-5(c) we give the plots of normalized fiber network stiffnesses, C_{1111} and C_{2222} and Poisson's ratio, ν_{12} , respectively. We also note that the pore pressure in the RVE is governed by the parameter, Γ , while its contribution to the overall stress is modulated by the parameter, B_{ij} . In Figure 7-5(d) through Figure 7-5(f) we give the plot of the evolution of normalized B_{11} and B_{22} and Γ , respectively.

From Figure 7-5(a), we see that the fiber network stiffness C_{1111} decays for both drained and undrained conditions to an asymptotic value. For the drained case the stiffness C_{1111} is generally smaller than that of the undrained case, except in the initial part of the loading. In comparison, we observe from Figure 7-5(b) that fiber network stiffness C_{2222} increases monotonically for the undrained case. For the drained case, C_{2222} first increases and then decreases in a comparatively narrow range. The differences in fiber network stiffness can be attributed to the fiber stress distribution in the two cases shown in Figure 3. In the early stages of loading, the fibers oriented closer to the loading direction resist a significant part of the applied axial stress for the two cases. As the axial strain increases, the fibers oriented close to the loading direction completely unload, while those oriented closer to the lateral direction experience further tensile loading. However, the fiber stresses for the undrained case remain generally larger than that for the drained case as seen from Figure 7-3. The increase in the tensile loading of the fibers oriented laterally is predicted by Eq. (7.41) which says that the pore pressure and the fiber stress must equilibrate each other in the lateral direction in the unconfined case. As a result, the fibers oriented laterally become stiffer. Since, the pore pressure increase is substantially greater in the case of undrained loading; the fiber network stiffness is also larger. For the drained loading case, the stiffening effect in the lateral direction is relatively smaller.

Figure 7-5(c) gives the apparent Poisson's ratio, ν_{12} , for the two drainage conditions. This apparent Poisson's ratio is computed as the ratio of the lateral to the axial strain with reference to the free swollen state as typically done in experiments. For the undrained case, we observe that this Poisson's ratio rapidly asymptotes to 0.5. For the drained case, the apparent Poisson's ratio decreases from a value of ~ 0.3 as fluid is squeezed out during compression. Similar strain-dependence of Poisson's ratio has been reported from drained uniaxial compression of articular cartilage (Chahine, Wang et al. 2004). The decrease in Poisson's ratio is due to the rapid loss in overall stiffness in the direction of loading relative to the lateral direction. The absence of the mechanical pressure in pore-fluid as seen from Figure 7-4(f) also contributes to the loss of stiffness in the drained case.

Figure 7-5(d) and Figure 7-5(e) give a plot of the evolution of parameters B_{11} and B_{22} . We recall from Eq. (7.40) that B_{ij} represents the relative stiffness of the fiber network with respect to the fiber material. When the fiber network stiffness is small relative to the fiber material, B_{ij} tends to identity. Therefore, it is not surprising that in the drained case, both B_{11} and B_{22} , tend to increase as the fiber network stiffness generally decreases with loading. A similar damage induced increase in the values of B_{11} and B_{22} has been predicted for poroelastic solids (Lydzba and Shao 2000). Moreover, B_{11} and B_{22} , reflect the effects of loading induced anisotropy similar to that predicted for linear poroelastic material undergoing damage (Lydzba and Shao 2000). In contrast, for the undrained case, B_{11} increases as the fiber network softens in the axial direction, however B_{22} decreases in response to the stiffening of the fiber network in the lateral direction discussed previously. Similarly, parameter Γ increases for drained case as the fiber network becomes soft and more compressible with loading. However, for the undrained case, parameter Γ first increases but then decreases as the overall compressibility of the fiber network also changes in a similar manner. In this case, the fiber network stiffness in axial direction decreases,

while that in the lateral direction increases. The overall effect of these competing phenomena is represented in parameter Γ . In traditional models for these types of materials, it is typical to assume $B_{ij}=\delta_{ij}$ and $\Gamma=0$. While these may be reasonable approximations at large strains, it is important to have a more accurate value at smaller strains to obtain correct effects of the pore pressure.

7.5.4 *Effect of Fiber Nonlinearity*

We have assumed the fiber to have a nonlinear behavior under tension arising from geometrical effects such as fiber crimping, braiding or folding. Here we explore the effect of fiber nonlinearity by investigating the drained behavior for exponent $\alpha=0, 0.1$ and 0.5 . So that the comparison is on a similar footing, we assume that the fiber behavior is same at fiber strain of 30% as shown in Figure 7-6(a), such that the parameter $C^f = 666.7$ MPa, 827.2 MPa and 1800 MPa, respectively for the three cases. From Figure 7-6(b), we can see that the fiber non-linearity significantly affects the stiffness in the drained condition. Due to different nonlinearity, the pre-strain in the three cases is different. Therefore, the softening of fiber network commences at different applied axial strain as seen from Figure 7-6(c). The behavior of the RVE for linear fiber is stiffer than that of the nonlinear fiber, although the pre-strain for linear fiber is smaller. Such a result is expected since the linear fiber is generally stiffer at small strains compared to nonlinear fiber. In addition we observe from Figure 7-6(b) that the behavior at larger strains is primarily governed by the osmotic pressure and has insignificant influence of the fiber-nonlinearity. Clearly, the fiber stiffness and nonlinearity has impact on the prediction of swelling and stress-strain behavior. Such prediction can be of significance in assessing disease states of soft tissues (Bank, Soudry et al. 2000).

We also observe from Figure 7-6(d) that the lateral stiffness varies little for RVE with nonlinear fiber, but decreases significantly for linear fibers. The lateral stiffness evolution is a complex function of the osmotic pressure and the fiber unloading. Further from Figure 7-6(e) and Figure 7-6(f), we note that the RVE with nonlinear fibers are relative softer than the fiber material, therefore parameter, B_{11} is closer to 1 and parameter Γ larger as the fiber network is more compressible at the pre-strained condition. As the loading progresses, the fibers unload and RVE stiffness becomes smaller for all cases. Thus, parameter, B_{11} , for all the three cases approaches unity. Similarly, the parameter Γ also tends to a common compressibility with loading. The comparison of behavior for different fiber nonlinearity shows that the overall material non-linearity can be attributed to two phenomena: 1) fiber buckling as the fibers unload, and 2) intrinsic fiber non-linearity. We note that the former is a purely micro-structural phenomenon resulting from the high aspect ratio of a fiber whereas the latter is attributable to the non-linearity in the fiber.

7.5.5 *Unconfined Drained Monotonic Compression*

To demonstrate the applicability of the model to steady-state material behavior, the compressive stress-strain behavior of the free-swollen porous material is studied under external salt molarity of 0.015M, 0.15 M and 0.5 M and compared to experimental results for articular cartilage. Figure 7-7(a) through Figure 7-7(g) show the evolution of the stresses, strains, porosity, and fluid pressures associated with the porous material. The porous material shows an initially stiff response, followed by softening, which transitions to a monotonic response with increasing strain. It is observed that both the initial and the post-softening stiffness depend upon the molarity of the bath. In the free swelling phase, during which water is free to drain, an isotropic tensile pre-strain of 1.28%, 0.8% and 0.4% develops under bath molarity of 0.015M, 0.15 M and 0.5 M, respectively. As the uniaxial compression is applied, the tensile strain in the fibers

decreases and the fiber network softens. Consequently, the effective stress decreases rapidly and asymptotes (Figure 7-7(b)). The magnitude of strain at which the material response transitions from the initially stiff to the post-softening regime increases with the pre-strain, or decreases with the external bath molarity. After the fiber network softens, and the effective stress decreases to a minimum, the osmotic pressure (Figure 7-7(c)) becomes the primary load carrying mechanism in the direction of load application. In the lateral direction, the increasing osmotic pressure is balanced by the fiber network stress (Figure 7-7(d)). The osmotic pressure increases with applied strain due to increase in fixed charge density as the material densifies (as shown by decrease of the overall volume in Figure 7-7(e)), caused by a decrease in porosity (Figure 7-7(f)). The softening of the fiber network in the direction of loading coupled with its stiffening in the lateral direction causes the apparent Poisson's ratio (Figure 7-7(g)) to decrease with applied strain. We also note that the osmotic pressures (Figure 7-7(c)) and apparent Poisson's ratio (Figure 7-7(g)) are smaller at higher external bath molarity. The osmotic pressure decreases with external salt concentration, by virtue of a decreased chemical potential difference. Accordingly, the loss of stiffness in the loading direction increases with salt concentration, thereby resulting in a lower value of the apparent Poisson's ratio. We note that the predicted stress-strain and apparent Poisson's ratio behavior are comparable to experimental results for articular cartilage under unconfined drained compression (Chahine, Wang et al. 2004). The following correspondences can be readily observed between the experimental data and the presented results (a) the presence of initially stiff and post-softening regimes (b) the order of material stiffness $0.015\text{ M} > 0.15\text{ M} > 0.5\text{ M}$, and (c) the decrease in apparent Poisson's ratio with loading.

Figure 7-7(h) to Figure 7-7(l) show the evolution of material properties with loading. The loss of fiber network stiffness in the loading direction is shown in Figure 7-7(h). Owing to the fiber non-linearity, C_{III} is stiffer and asymptotes at a larger magnitude of applied strain at lower bath

molarities. The lateral stiffness C_{2222} also decreases with applied strain due to overall softening of the fiber network; however the values of C_{2222} are significantly higher at lower bath molarities both due to higher pre-strain and the less significant effect of fiber unloading in the lateral direction as compared to the loading direction. It is also interesting to note that the poromechanical parameter B differs appreciably from unity. As shown in Figure 7-7(j) and Figure 7-7(k), both B_{11} and B_{22} are higher at higher bath molarity, thus showing that the contribution of fluid pressure to the load bearing increases with bath molarity. Further, it is observed that B_{11} and B_{22} monotonically increase with applied compressive strain. It is seen that the values of B_{11} and B_{22} deviate significantly from unity especially for cases of low bath molarity and need to be explicitly accounted for to obtain an accurate estimate of the load carried by fluid. Figure 7-7(l) shows the evolution of poromechanical parameter Γ , which represents the effective fluid-solid material compressibility. The parameter Γ , is found to increase with both bath molarity and applied strain and is found to be a multiple of water compressibility. We note that the bulk modulus measurements reported for cartilage under large loading rates and confined or unconfined conditions are typically a fraction of the water bulk modulus (Oloyede, Flachsmann et al. 1992, Milentijevic and Torzilli 2005), which agrees with our prediction that parameter Γ is a multiple of water compressibility. The evolution of the poromechanical parameters B and Γ can be attributed to stiffness of the fiber network, which decreases with bath molarity and applied loading and exhibits loading induced anisotropy.

Figure 7-7(m) shows the fiber stress distribution with orientation and its evolution with applied strain. We observe that (a) before the loading commences at 0% strain, the fiber network experiences isotropic pre-strain, which decreases with bath molarity; (b) at 0.5% applied strain, the fibers oriented closer to the loading direction (0° or 180°) are still active for bath molarities of 0.015 M and 0.15 M while they have unloaded for the bath molarity of 0.5 M; and (c) in the

post-softening regime at 1.5% and 5% applied strain, the fiber stress magnitude in the lateral direction follows the order $0.015\text{ M} > 0.15\text{ M} > 0.5\text{ M}$, due to the difference in osmotic pressure. The fiber stress distribution can be directly associated with the effective stress as well as the fiber network stiffness.

7.5.6 Creep Response at Different Stress-Levels

To illustrate the applicability of the model to rate-dependent behavior, we consider the fluid-flow dependent creep of the material under the following applied stress-levels: 0.1, 0.2 and 0.4 MPa, for 0.15 M external bath molarity. In Figure 7-8(a) through Figure 7-8(g), we show the predicted evolution of the strains and fluid pressures. From Figure 7-8(a), the creep strains at equilibrium are found to be 0.7%, 8.7% and 26.6% at 0.1 MPa, 0.2 MPa and 0.4 MPa, respectively, indicating that the creep response is highly non-linear as the load increases from 0.1 to 0.4 MPa. We note from the steady-state stress-strain behavior for the case of 0.15 M external bath (Figure 2(a)) that at a stress of 0.1 MPa the response lies within the initially stiff regime while at 0.2 MPa and 0.4 MPa the response lies in the post-softening regime, thus requiring a large increase in strain to equilibrate to a drained state of loading. When the applied stress lies within the initially stiff regime, the contribution of the fiber network in supporting the load is significant, thereby decreasing the pore pressure rise caused by loading. On the other hand, when the applied stress is in the post-softening regime, the pore pressure high while the fiber network has softened; this leads to large creep strains at equilibrium.

It is also observed that in the case of 0.1 MPa, the creep strain asymptotes in about an hour as compared to several hours for the higher loads (Figure 7-8 (a) and Figure 7-8(b)). However, the rate of creep is highest for 0.4 MPa due to the larger chemical potential difference between the material and the bath. The lateral strain (Figure 7-8(b)) is governed both by the Poisson's effect as well as the shrinkage (Figure 7-8(f)) of the material with drainage. The drainage is the

governing factor at loads below the softening stress, but the lateral strains at higher loads are found to be governed by the Poisson's effect. It is also interesting to note that a majority of the pore pressure equilibrates in less than an hour (Figure 7-8(c)) as the decreasing mechanical pore pressure (Figure 7-8(e)) and increasing osmotic pressure (Figure 7-8(d)) balance each other. However, the creep continues to increase substantially up to 10 hours (Figure 7-8(a) and Figure 7-8(b)) due to the decrease in the mechanical pore pressure. We further observe that for the loads of 0.2 MPa and 0.4 MPa, the shrinkage of the material is substantial as seen from Figure 7-8(f). This corresponds to the increasing creep strains in the axial direction and the decreasing apparent Poisson's ratio. On the other hand, for a load of 0.1 MPa which is in the initial stiff regime, the decrease in apparent Poisson's ratio as well as the magnitude of creep strain is not significant, resulting in negligible shrinkage.

The low creep strain observed at 0.1 MPa applied load is further corroborated by the fiber network stiffnesses C_{ijkl} (Figure 7-8(h) and Figure 7-8(i)), which are generally higher as compared to that at the applied loads of 0.2 MPa and 0.4 MPa, in which cases the fiber network stiffnesses drop significantly and asymptote to a small value. As a result, B_{11} increases and approaches unity (Figure 7-8(j)), while B_{22} increases and approaches a value less than unity (Figure 7-8(k)) at equilibrium. Thus, we see that at higher loads, the contribution of the pore pressure in supporting the load increases not only because of the fiber network softening, but also from an increase in B . Similarly, there is little change in Γ for an applied stress of 0.1 MPa, but a significant change is observed for the other two cases.

The variation in the fiber network stiffness can be understood based on the fiber stress distribution with orientation (Figure 7-8(m)). Since all the loading cases are performed in a bath of the same molarity, the fiber stress distribution before loading is the same. After the instantaneous deformation, active fibers in the direction of loading remain when the applied

stress is 0.1 MPa; however, all the fibers close to the loading direction have unloaded for the cases of 0.2 and 0.4 MPa applied load. As equilibrium is reached within an hour for the 0.1 MPa case of loading, there is no difference between the fiber stress distributions at 1 hour and at 6 hours. On the other hand, for the 0.2 and 0.4 MPa cases, we see that the fiber network stress is progressively transferred to fibers oriented close to the lateral direction; thus imparting induced anisotropy to the material.

7.5.7 Creep Response under Varying Bath Molarity

We further evaluate the rate-dependent behavior of the material by investigating creep under varying external bath concentration. In this case, we apply a constant stress of 0.4 MPa and study the creep response when the material is immersed in bath concentrations of 0.015 M, 0.15 M and 0.5 M. Figure 7-9(a) to Figure 7-9(g) show the evolution of the strains and fluid pressures. Figure 7-9(a) shows the increase in rate of creep and equilibration time with the external salt concentration. The rate of creep increases with the external bath molarity because a smaller osmotic pressure generates a larger chemical potential difference for the same applied load. The larger creep strain at equilibrium follows from the equilibrium strain at steady state behavior (Figure 7-7(a)). The lateral creep strain is shown in Figure 7-9(b), and is a complex phenomenon that depends on the material shrinkage as well as the Poisson's effect. The contribution of the shrinkage is not significant for the lower bath concentrations of 0.015 M and 0.15 M (Figure 7-9(f)). However, in the case of the 0.5 M bath, the material is subjected to a high chemical potential difference due to the low osmotic pressure, and therefore, drains and shrinks substantially. Consequently, the lateral strain rises and then drops down to an equilibrium asymptote. As described in the previous section, the pore pressure (Figure 7-9(c)) experiences a majority of its decrease in the first hour, but equilibrium is achieved only when it equals the osmotic pressure, shown in Figure 7-9(d), that is the mechanical pressure (Figure

7-9(e)) becomes zero. It is noteworthy that though the material starts at a low osmotic pressure for the 0.5 M case, at equilibrium the osmotic pressure has increased significantly due to the material shrinkage (Figure 7-9(f)). Due to the higher creep strains in the loading direction associated with higher bath molarity, the apparent Poisson's ratio (Figure 7-9(g)) decreases with external bath molarity. The results obtained can be qualitatively compared to indentation creep experiments on articular cartilage (Lu, Sun et al. 2004) and condylar cartilage (Lu, Mow et al. 2009) in 2 M and 0.15 M PBS solutions. The trends for increase in creep rate and creep magnitude with bath molarity are correctly predicted by the model.

We further describe the behavior in the three cases by considering the evolution of the material parameters during loading. Since the applied load of 0.4 MPa lies in the post-softening regime under all the bath molarities, there is significant softening of the fiber network, resulting in C_{1111} (Figure 7-9(h)) tending to zero for all the cases. The value of C_{2222} (Figure 4(i)) depends on the bath concentration; clearly when the bath molarity is lower, the material retains a majority of its stiffness in the lateral direction, due to higher contribution from the osmotic pressure in maintaining the fiber network stiffness. Therefore, for lower bath molarities, the values of B_{11} and B_{22} (Figure 7-9(j) and Figure 7-9(k)) are also lower, indicating the increased contribution of the fiber network to load bearing. Similarly, the fluid-solid compressibility Γ (Figure 7-9(l)) is also lower, indicating that it is more difficult to exude fluid under mechanical loading in the case of a lower bath molarity.

The decrease in the fiber network stiffness with loading and bath molarity can be understood from the fiber stress distribution (Figure 7-9(m)). In an unloaded state, there is an isotropic pre-strain in the fiber network whose magnitude depends on the external bath molarity. For this reason, the instantaneous elastic deformation leaves behind a larger number of active fibers in the direction of loading when the bath molarity is lower. Finally, it is interesting to note that, as

the material approaches equilibrium, the fiber stress in the lateral direction decreases due to drainage of fluid and the associated loss of pore pressure. This effect is most prominently seen for the case of 0.5 M bath molarity.

7.5.8 Effect of Confinement on Creep Behavior

Confinement is an important factor that influences the load distribution between the fiber network and the fluid. Figure 5(a) shows the difference in creep behavior under confined and unconfined conditions under an applied load of 0.4 MPa and an external bath molarity of 0.15 M. The instantaneous elastic strains as well as the creep strains are lower in the confined case (Figure 7-10(a)), due to the greater lateral resistance provided under confinement. However, it is only minimally higher than the resistance provided by the fiber network under unconfined conditions; hence the difference in creep strains is small. The major effect on the confinement is on the effective stress. The effective stress in the loading direction $\bar{\sigma}_{11}$ (Figure 7-10(b)) decreases much more rapidly in the confined case because of the absence of contribution from lateral fibers. Correspondingly, the pore pressure (Figure 5(c)) equilibrates much faster in the confined case. The lack of lateral fiber deformation in the confined case also causes the effective stress $\bar{\sigma}_{22}$ to be much smaller (Figure 7-10(d)). The osmotic pressure is marginally higher for the confined case (Figure 7-10(e)) because of a marginally smaller porosity or water volume fraction in the confined case of loading (Figure 7-10(f)). However, it is interesting that the volume change is nearly the same in both cases (Figure 7-10(g)).

Figure 7-10(h) to Figure 7-10(l) display the evolution of the material constants associated with the creep behavior described above. Further, due to confinement, the lateral fibers do not participate in balancing the osmotic pressure and C_{2222} drops rapidly in the confined case (Figure 7-10(i)). Consequently, we observe that B_{11} approaches unity in both the cases (Figure 7-10(j)),

while B_{22} is significantly smaller for the unconfined case of loading (Figure 7-10(k)). Similarly, the lateral fiber contribution results in a smaller compressibility for the unconfined case (Figure 7-10(l)). The fiber stress distribution (Figure 7-10(m)) shows the significant difference in the fiber network stress between the unconfined and confined cases, particularly in the lateral direction, though both the cases have the same distribution before loading.

7.5.9 Stress Relaxation under Variable External Bath Molarity

Finally, we compare the relaxation behavior of the material under varying external bath molarities at an applied strain of 5%. The relaxation happens due to drainage of pore fluid and consequent reduction in the overall stress. From Figure 7-11(a), the stress relaxation is faster and equilibrium stress is lower at higher bath molarities due to higher chemical potential difference. The model prediction agrees with experimental observations that stress relaxation proceeds faster under higher bath molarity for cartilage under unconfined uniaxial compression (June, Mejia et al. 2009). As the relaxation proceeds, the lateral strain ϵ_{22} decreases as the fluid drains and the material shrinks (Figure 7-11 (b) and Figure 7-11(f)). With fluid drainage, the pore pressure decreases (Figure 7-11(c)), however, the decrease in pore pressure increases with the bath molarity due to an increase in chemical potential difference. In contrast to the creep response, the stress and the pore pressure equilibrate at similar times. In stress relaxation, since the axial strain is held constant, the shrinkage of the material is minimal (Figure 7-11(f)), therefore the osmotic pressure does not vary much during relaxation. Consequently, after stress relaxation, the osmotic pressure still follows the order $0.015\text{ M} > 0.15\text{ M} > 0.5\text{ M}$ (Figure 7-11(d)). Similarly, there is a small variation in the mechanical pore pressure, which also remains close to its initial values. Figure 7-11(g) shows the decrease in apparent Poisson's ratio caused primarily by the softening of the fiber network, that is, a decrease in C_{1111} in the direction of loading (Figure 7-11 (h)). We observe that the softening is smaller at lower bath molarity, thus resulting

in a higher apparent Poisson's ratio. C_{2222} undergoes a similar decrease with time. We also note that both C_{1111} and C_{2222} decrease at a slower rate but reach equilibrium faster at lower bath molarity. In Figure 7-11(j) to Figure 7-11(l) we observe that both B and Γ increase as the material softens. Figure 7-11(m) shows the evolution of fiber stress during the relaxation process. During the relaxation phenomenon, the variation in the fiber network stress with time is primarily due to the decrease in ϵ_{22} , resulting in a decrease of fiber stress in the lateral direction. The fiber stresses are observed to decrease faster in the case of high bath molarity contributing to the faster relaxation observed in Figure 7-11(a).

7.6 Summary and Conclusions

We have presented a derivation of poromechanical theory of fluid-saturated chemically active fibrous media. In the derived theory, the tangent stiffness of the dry fiber network is obtained using the framework of granular micromechanics. The poromechanics constitutive relationships are then obtained using Hill's volume averaging principles for strain-free and pore-pressure free conditions. To account for fiber nonlinearity and large deformations, the equations are formulated in an incremental form. The resultant model gives expressions for (1) the fiber network tangent stiffness, C_{ijkl} , in terms of the fiber mechanical properties and fiber directional distribution, (2) the poromechanical parameter, B_{ij} , in terms of the relative stiffness of the fiber network with respect to the fiber material, and (3) the poromechanical parameter, Γ , in terms of the relative compressibility of the fiber network and the fluid phase. The osmotic pressure that develops due to the chemical activity of the fiber network is modeled using Donnan's method. Thus the derived theory provides a method determining the contributions of the mechanical aspects and chemical aspects to the load bearing abilities of these materials.

The applicability of the model is demonstrated by comparison with the observed drained and undrained behaviors of articular cartilage under uniaxial compressive stress. The model predictions are found to show similar trends of stress-strain behavior as experimentally observed. The model is able to predict the apparent yield observed under drained conditions and its absence in the undrained condition. The model also exhibits the post-yield stiffening behavior and the reduction in Poisson's ratio in the drained conditions. We also demonstrate the effect of micro-scale phenomena such as fiber buckling on the macro-scale stiffness tensor and poromechanics parameters. In addition, we demonstrate the effect of fiber nonlinearity on the overall behavior. Traditionally, the constitutive laws used to describe these materials have assumed poromechanical parameter B to be unity and Γ to be zero. In the theory presented here, the poromechanical parameters can be calculated under a given set of loading conditions.

In this paper, we have only presented results for monotonic static loading under drained or undrained conditions. The model can be utilized to obtain the rate-dependent behavior of poromechanical materials. For example, the derived model provides a method for determining the load sharing between the fiber network and the pore-fluid which is of interest in transient behavior of these materials (Li and Herzog 2004). We further note that the analysis presented here is focused on a system where the solid matrix is composed of a fibrous network. However, the presented methodology can be extended to other materials such as clays, polymers, hydrogels. Furthermore, we note that for the porous materials of the type considered here, the behavior may be affected by other micro-scale phenomena, such as capillarity, as well as by occurrence of thin boundary layers which are best modeled using higher-gradient approaches (Madeo, Dell'Isola et al. 2008, Sciarra, Dell'Isola et al. 2008, dell'Isola, Madeo et al. 2009). The present methodology can be potentially applied to obtain the relevant constitutive parameters for these higher-gradient poromechanical theories.

We have derived a poromechanical theory of fluid-saturated chemically active fibrous media by considering the fiber network microstructure, chemical potential driven fluid flow, and micro-poromechanics. In the derived theory, the dry fiber network is modeled using the framework of granular micromechanics. The micro-poromechanics method based upon Hill's volume averaging principles is then utilized to derive expressions for the poromechanical parameters B_{ij} and Γ . The derived equations are formulated in an incremental form to account for fiber nonlinearity, large deformations and rate of fluid-flow. A chemical potential gradient driven transport model is incorporated, which at chemical equilibrium between the material and the surrounding fluid bath yields Donnan's osmotic pressure. In the resultant model: (1) the fiber network tangent stiffness, C_{ijkl} , is obtained in terms of the fiber mechanical properties and fiber directional distribution, (2) the poromechanical parameter, B_{ij} , is obtained in terms of the relative stiffness of the fiber network with respect to the fiber material, and (3) the poromechanical parameter, Γ , is obtained in terms of the relative compressibility of the fiber network and the fluid phase. The fluid-flow and the pore pressure develop both due to chemical activity and mechanical loading. Thus the derived theory provides a method determining the contributions of the mechanical aspects and chemical aspects to the load bearing abilities as well as rate-dependent behavior of these materials.

The applicability of the model is demonstrated by comparison with the experimentally observed behavior of articular cartilage as well as through parametric studies for confined/unconfined uniaxial loading conditions and a variety of surrounding fluid bath molarity. The model predictions are found to show similar trends of stress-strain behavior as experimentally observed. The model: (1) is able to predict the apparent yield observed under drained conditions and the change of stiffness with surrounding fluid bath molarity; (2) exhibits the post-yield stiffening behavior and the reduction in Poisson's ratio in the drained conditions; and (3) shows the

influence of fiber pre-strain and evolution of fiber network structure with loading on the overall behavior and the poromechanical parameters and thus models the phenomenon of induced anisotropy. Traditionally, the constitutive laws used to describe these materials have assumed poromechanical parameter B_{ij} to be unity and Γ to be zero. In the theory presented here, the poromechanical parameters can be calculated under a given set of loading conditions. The evolution of the poromechanical parameters with loading is critical for investigating the solid-fluid interaction in load bearing and deformation. The poromechanical parameter B_{ij} is found to deviate by up to 10% or more from unity, while Γ is found to be a multiple of water compressibility which agrees with the measured bulk modulus of cartilage. Particularly in the case of low surrounding fluid bath molarity, trivial assumptions for poromechanical parameters might lead to erroneous conclusions. Finally we note that in this paper we have presented results for monotonic quasi-static loading under drained conditions as well as fluid flow-dependent creep and relaxation behavior. The model can also be utilized to obtain the rate-dependent behavior of poromechanical materials. The derived model provides a method for determining the load sharing between the fiber network and the pore-fluid which is necessary for describing the transient behavior of these materials.

The results of our simulation show that confinement plays an important role in determining the contribution of the fiber network to load bearing. Therefore, the confining stress can be critical for determination of matrix failure in soft tissues, although these simulations were not presented in this paper. Further, we have only described the cases of creep and relaxation of an initially isotropic fiber network. The model can be used to study mechanical behavior under varying loading rates as well as incorporate inherent fiber anisotropy using fabric tensors (Chang and Misra 1990). We note that the analysis presented here is focused on a system where the solid matrix is composed of a fibrous network. Since the presented methodology relates the effect of

micro-scale interactions on the chemo-poro-mechanical macro-scale behavior, we believe it is relevant to the rate-dependent behavior of different types of porous media such as cement paste, hydrogels, granular soils, rocks and hydrophilic polymers, each of which incorporate grain-grain or molecular interactions at a smaller scale. For these materials as well as for the fibrous materials, the inherent rate-dependence due to fiber or interaction viscous effects and degradation or damage can be potentially incorporated as discussed in (Misra and Singh 2012). Furthermore, we note that for the porous materials of the type considered here, the behavior may be affected by other micro-scale phenomena, such as capillarity, as well as by occurrence of thin boundary layers which are best modeled using higher-gradient approaches (Madeo, Dell'Isola et al. 2008, Sciarra, Dell'Isola et al. 2008, dell'Isola, Madeo et al. 2009). The present methodology can be potentially applied to obtain the relevant constitutive parameters for these higher-gradient poromechanical theories.

Appendix. Fiber orientation density function

The fiber orientation density function expressed in spherical coordinates, $\xi_I(\theta, \phi)$, is written in a discrete form as follows:

$$\xi(n_i) = \frac{1}{M} \sum_{j=1}^M \delta(n_i - n_i^j) \quad (7.61)$$

where, M is the total number of fibers, $\delta(\mathbf{n} - \mathbf{n}^j) = \delta(\theta - \theta^j) \delta(\phi - \phi^j) / \sin \theta$, δ refers to the Dirac delta, and the superscript j refers to the observed fiber directions. The observed discrete directional density of the type given by Eq. (7.61) can be estimated as a smooth orientation distribution function by fitting with parametric forms discussed by (Kanatani 1984), Other forms of smooth orientation distribution functions, particularly exponential forms that appear as extensions of von Mises or Fisher distributions may be used,

especially when we need to represent highly directional data (Federico and Herzog 2008, Federico and Herzog 2008, Cortes, Lake et al.). For practical calculations, transversely isotropic fiber orientation can be expressed as (Chang and Misra 1990):

$$\xi(\theta, \phi) = \frac{1}{4} \frac{1 + \frac{1}{4} a_{20} (3 \cos(2\theta) + 1)}{\pi} \quad (7.62)$$

where a_{20} = the anisotropy factor, such that the isotropic fiber orientation can be expressed as ($a_{20} = 0$)

$$\xi(\theta, \phi) = \frac{1}{4\pi} \quad (7.63)$$

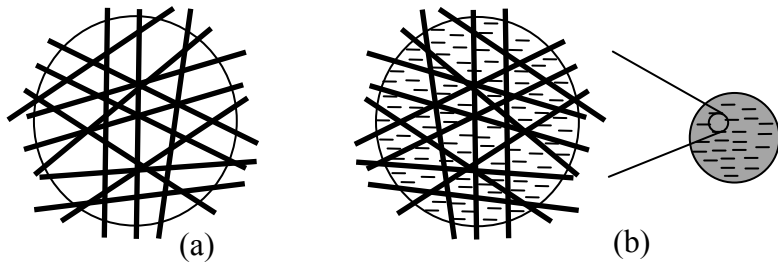


Figure 7-1 (a) Schematic of dry fibrous network at the microscale. (b) Schematic of saturated fibrous network at microscale by zooming in to a homogenized representative volume element at the macroscale.

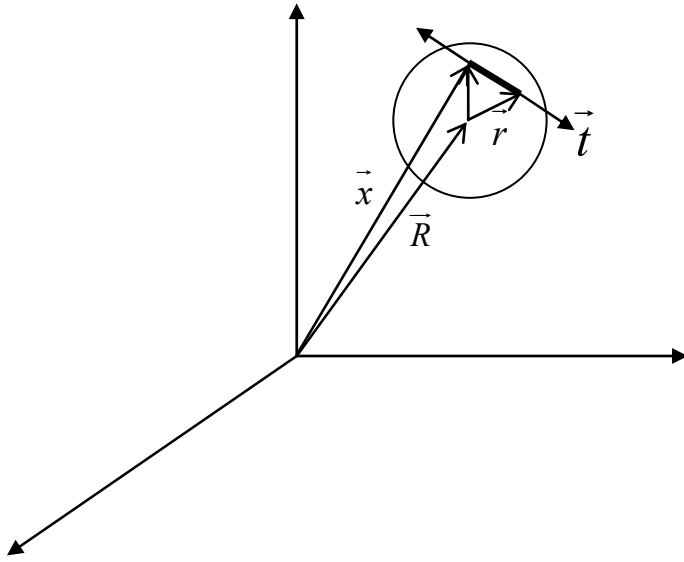


Figure 7-2 Fiber traction in an RVE.

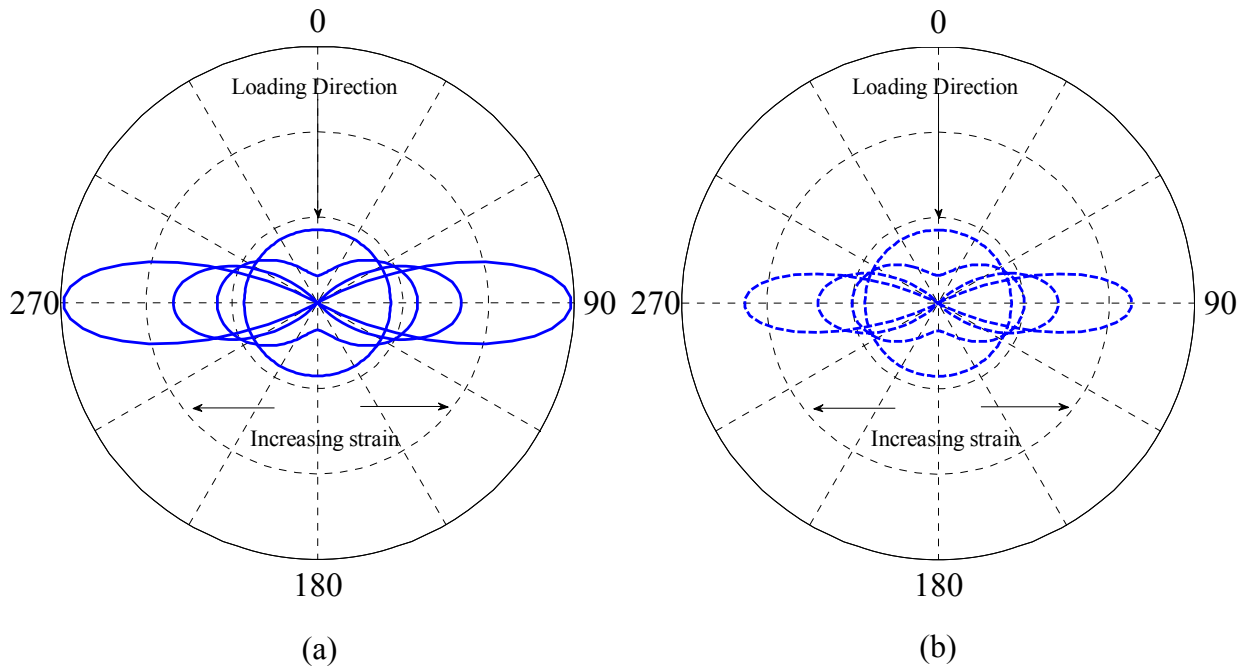


Figure 7-3 Predicted fiber stress distribution with increasing compressive applied strains of 0%, 0.8%, 2.5% and 10% for (a) undrained and (b) drained conditions (plotted to the same scale)..

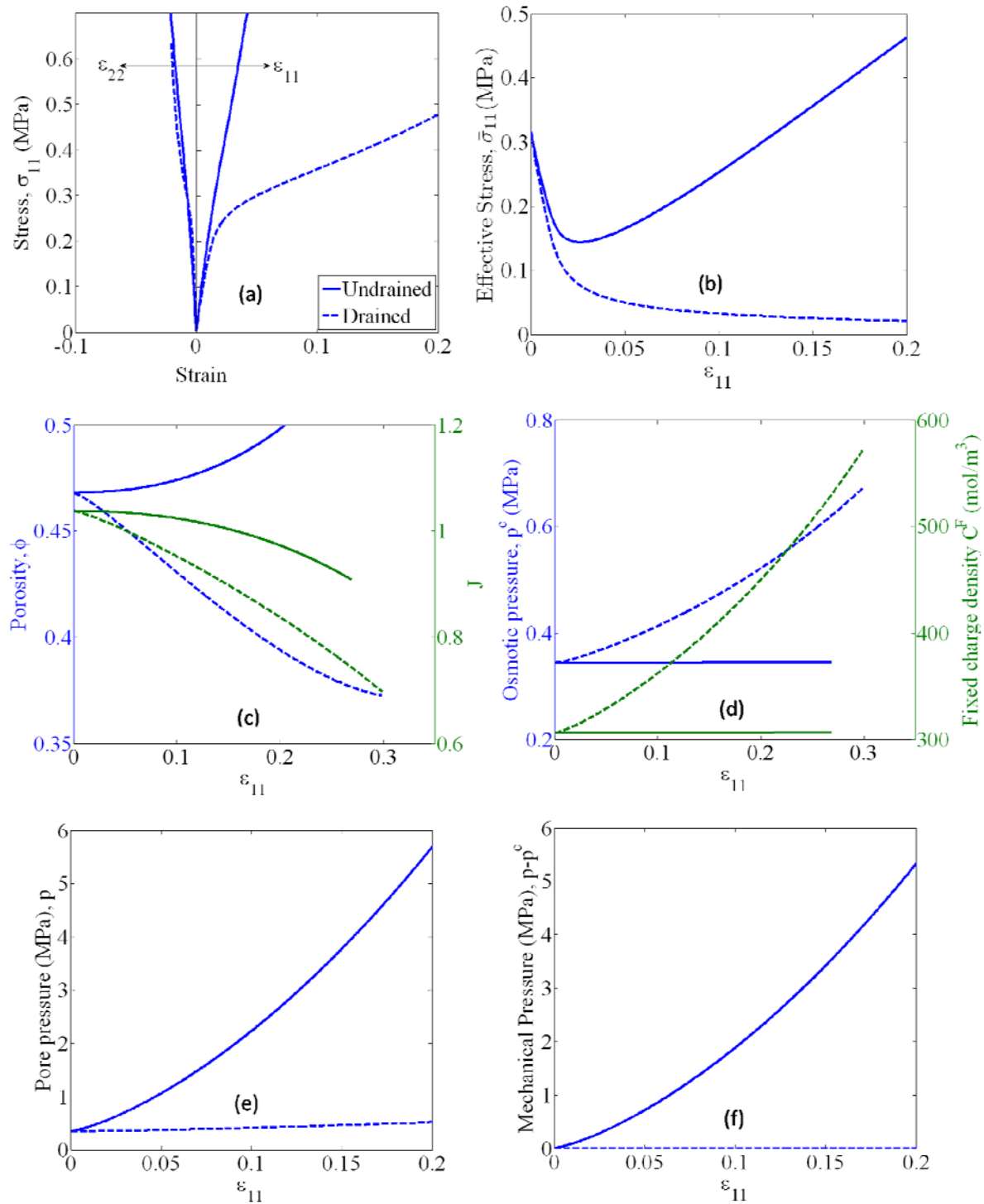


Figure 7-4 Evolution of stress, effective stress, porosity, volume change, pore pressures and fixed charge density under uniaxial compression for drained and undrained cases of loading.

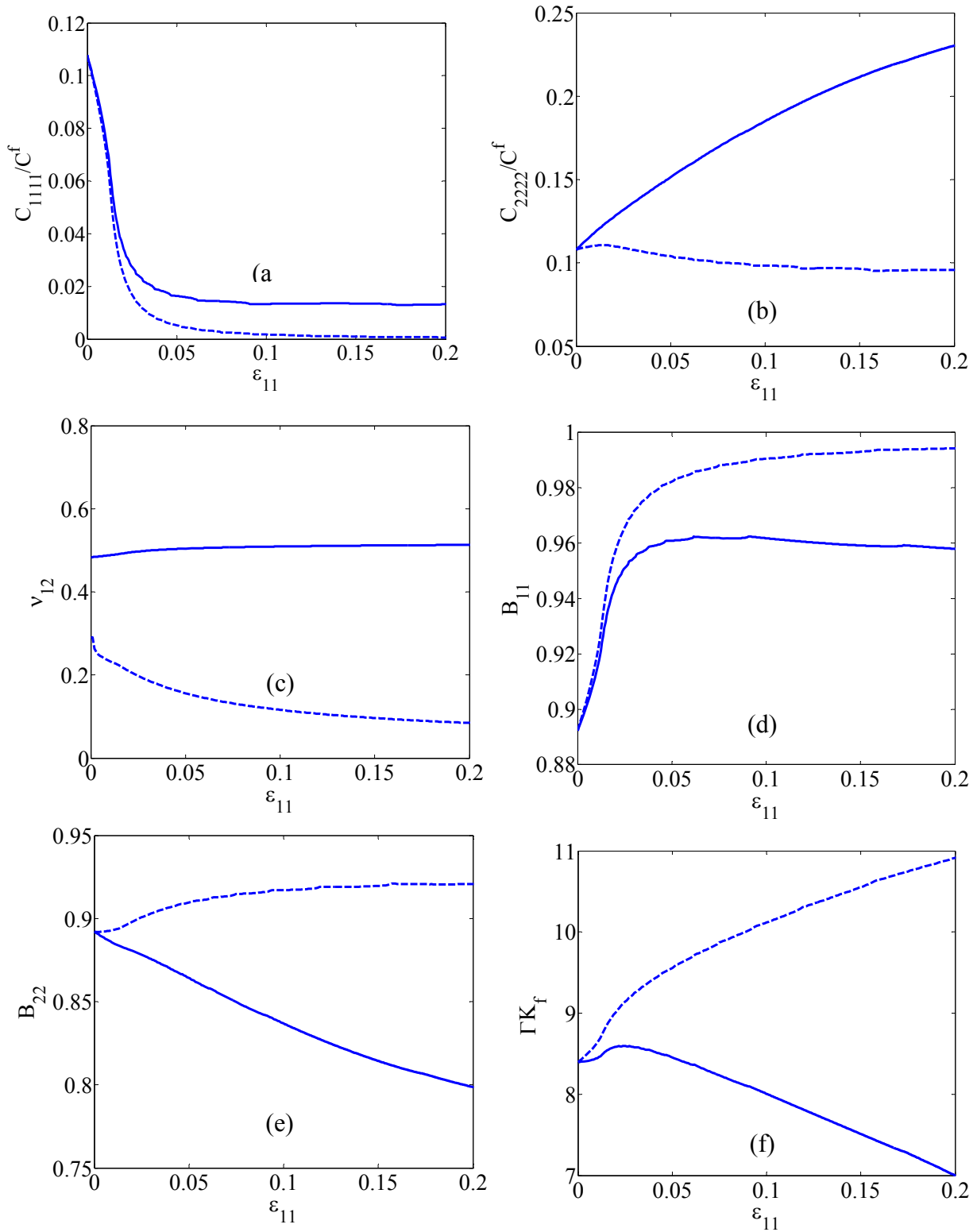


Figure 7-5 Evolution of stiffness and poromechanical parameters under uniaxial compression for drained and undrained cases of loading.

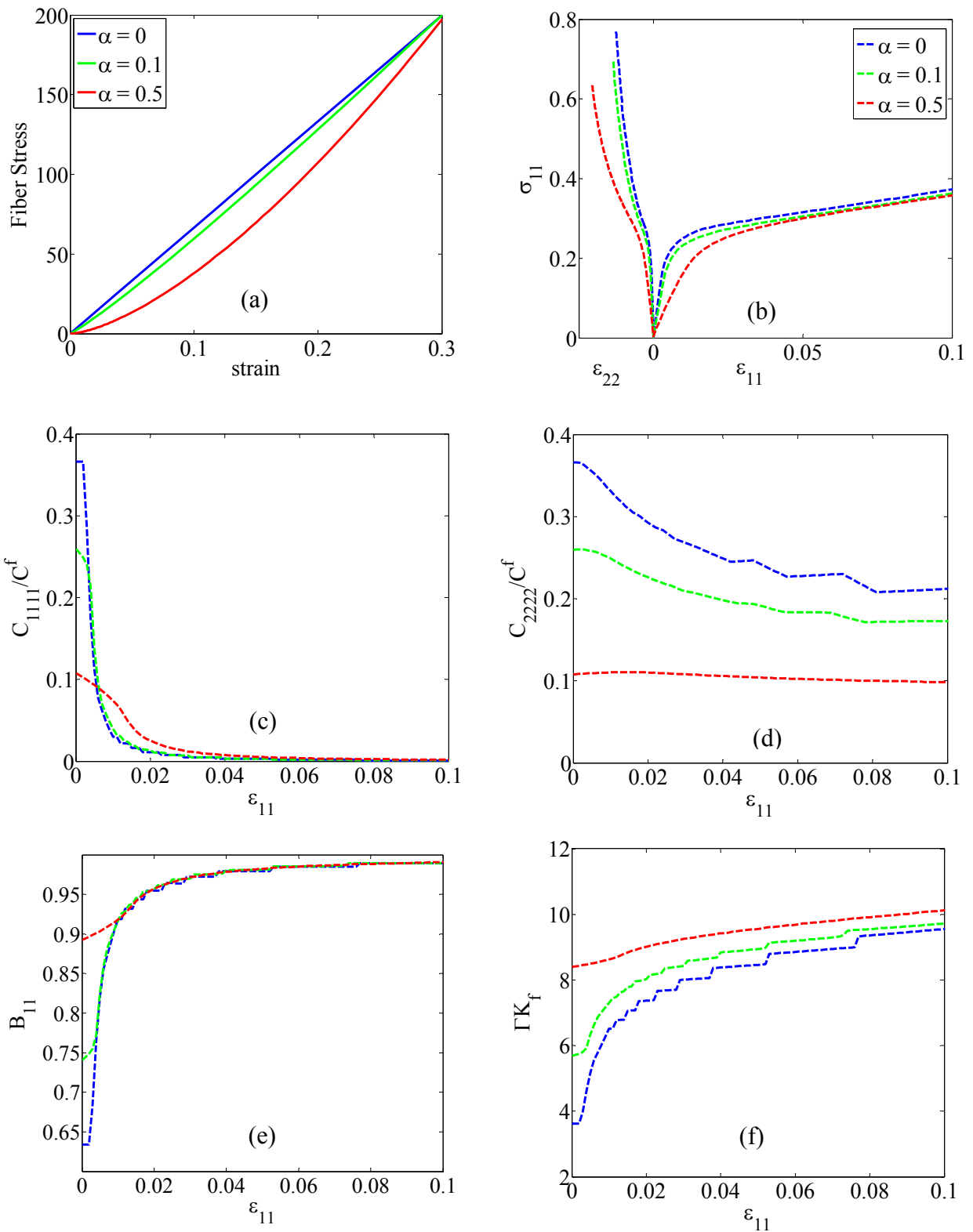


Figure 7-6 Effect of fiber nonlinearity on drained behavior under unconfined compression.

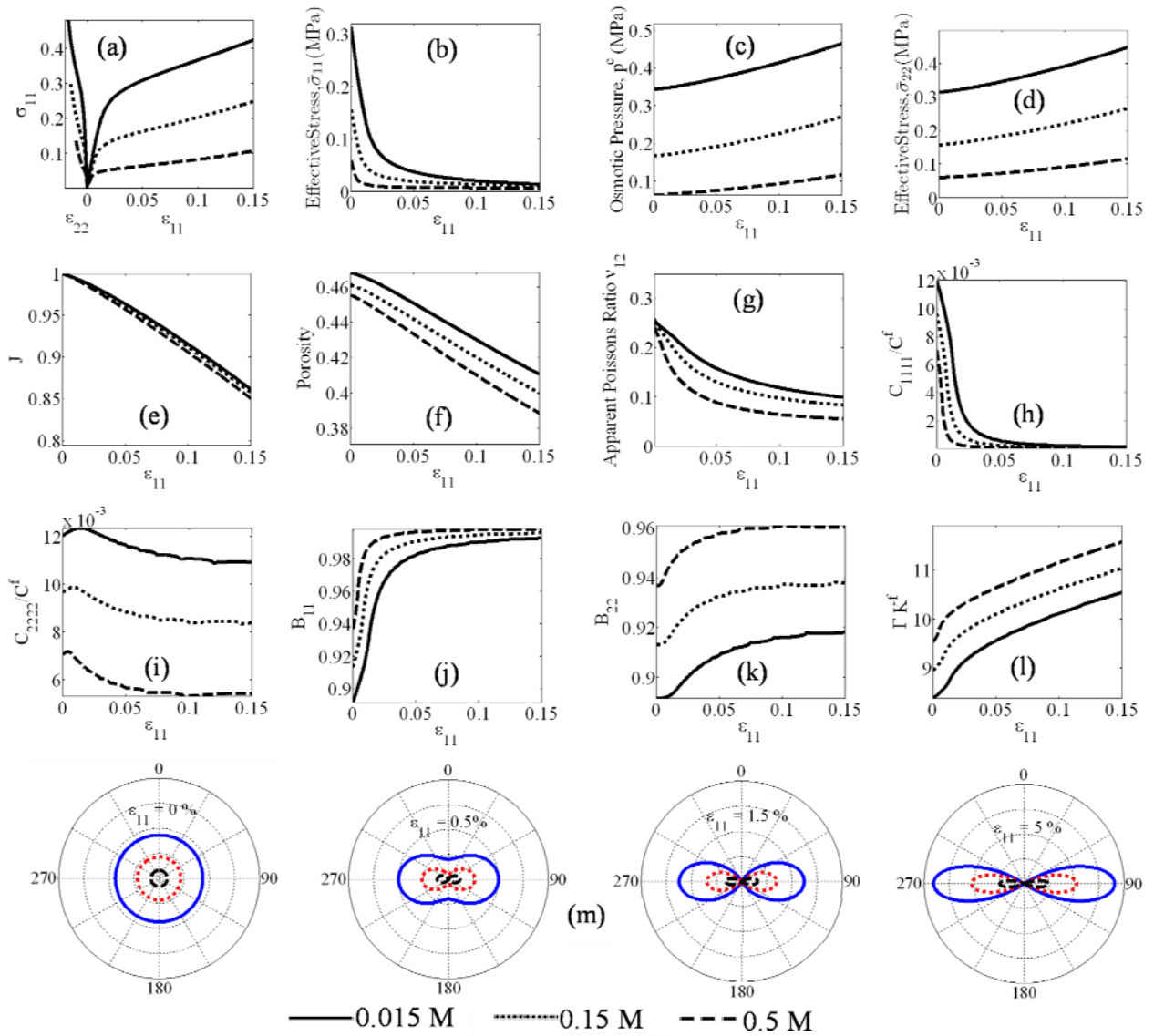


Figure 7-7 Unconfined uniaxial drained monotonic compression: stress-strain behavior under varying external bath molarity (a, b and d), evolution of pore pressure (c), volume change (e), porosity (f), material properties (g-l), and the fiber stress distributions (m).

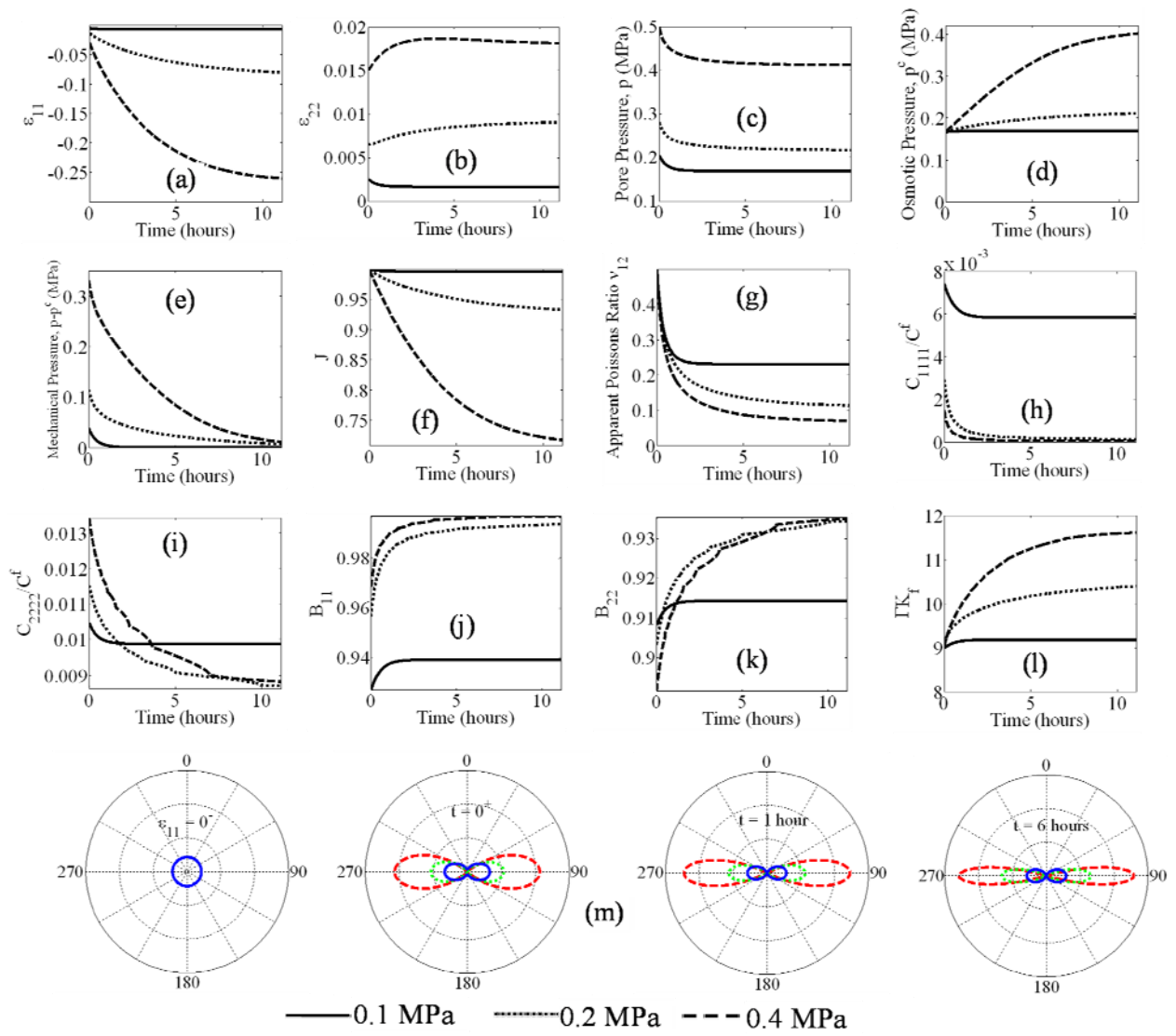


Figure 7-8 Creep response under different axial stress: strain (a, and b), pore pressures (c-e), volume change (f), material properties (g-l), and the fiber stress distributions (m).

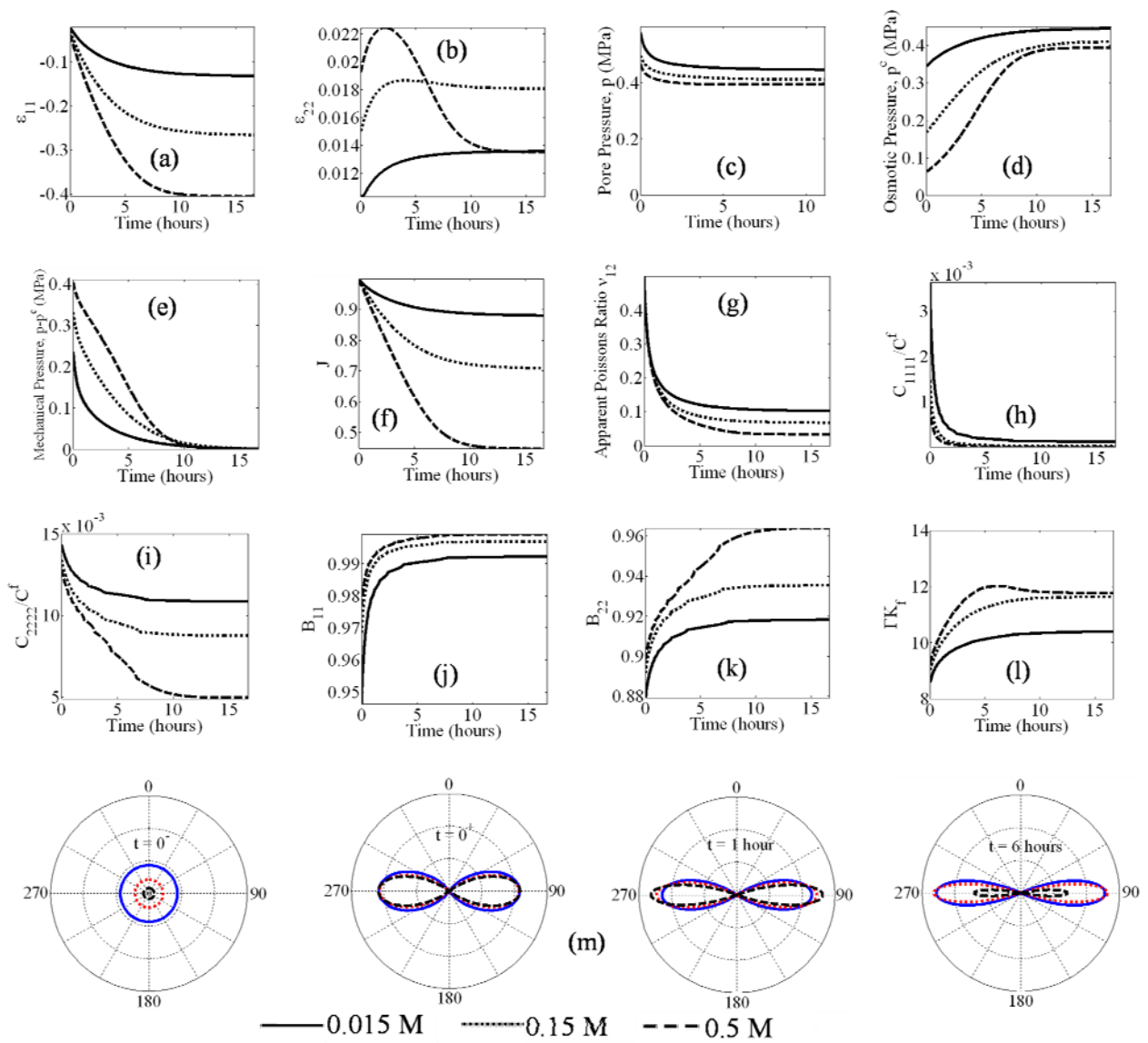


Figure 7-9 Creep response under different external bath molarities: strain (a, and b), pore pressures (c-e), volume change (f), material properties (g-l), and the fiber stress distributions (m).

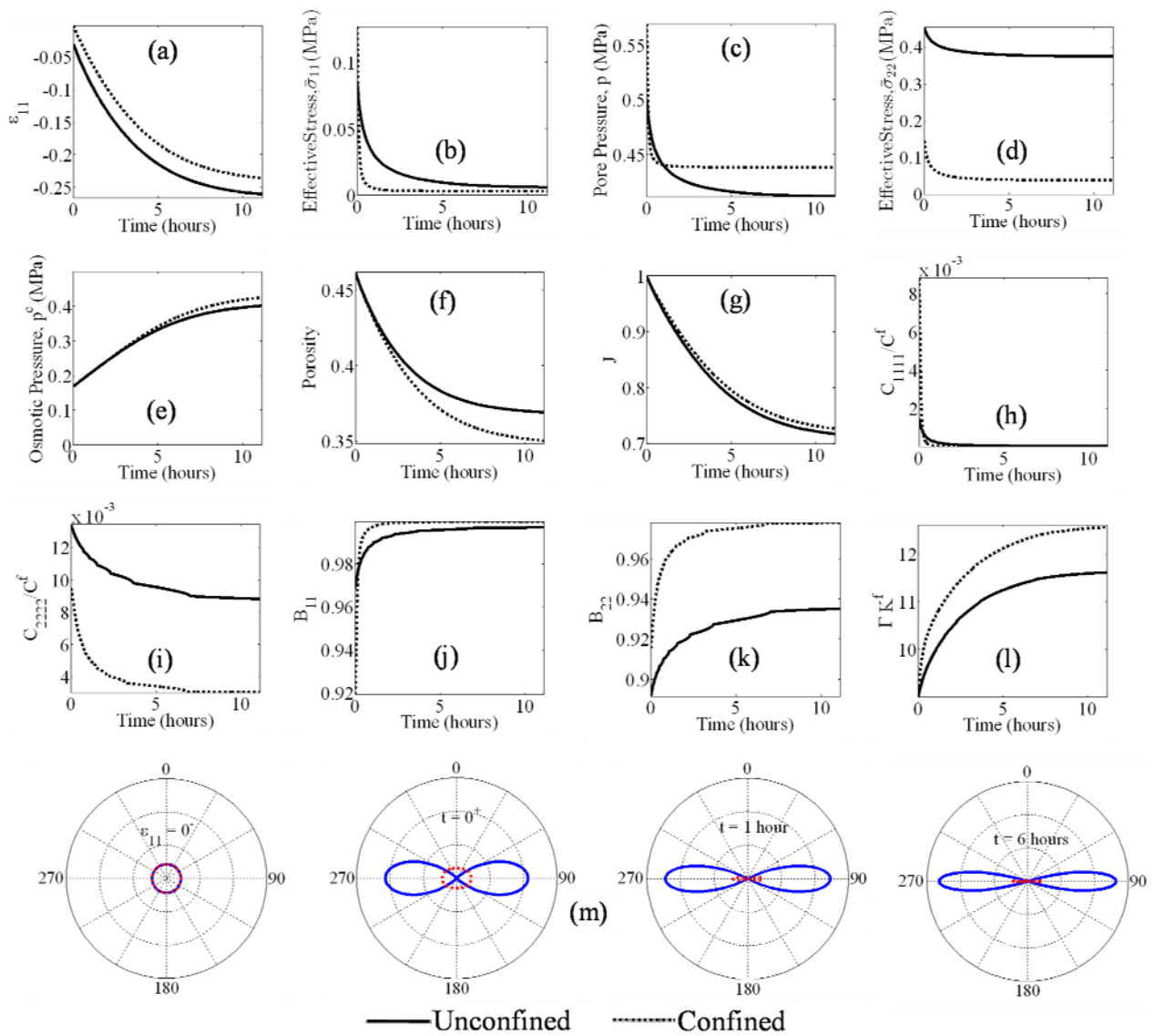


Figure 7-10 Comparison of creep response under confined and unconfined conditions for same applied stress and external bath molarity: strain and effective stress (a, b and d), pore pressures (c and e), porosity (f), volume change (g), material properties (h-l), and the fiber stress distributions (m).

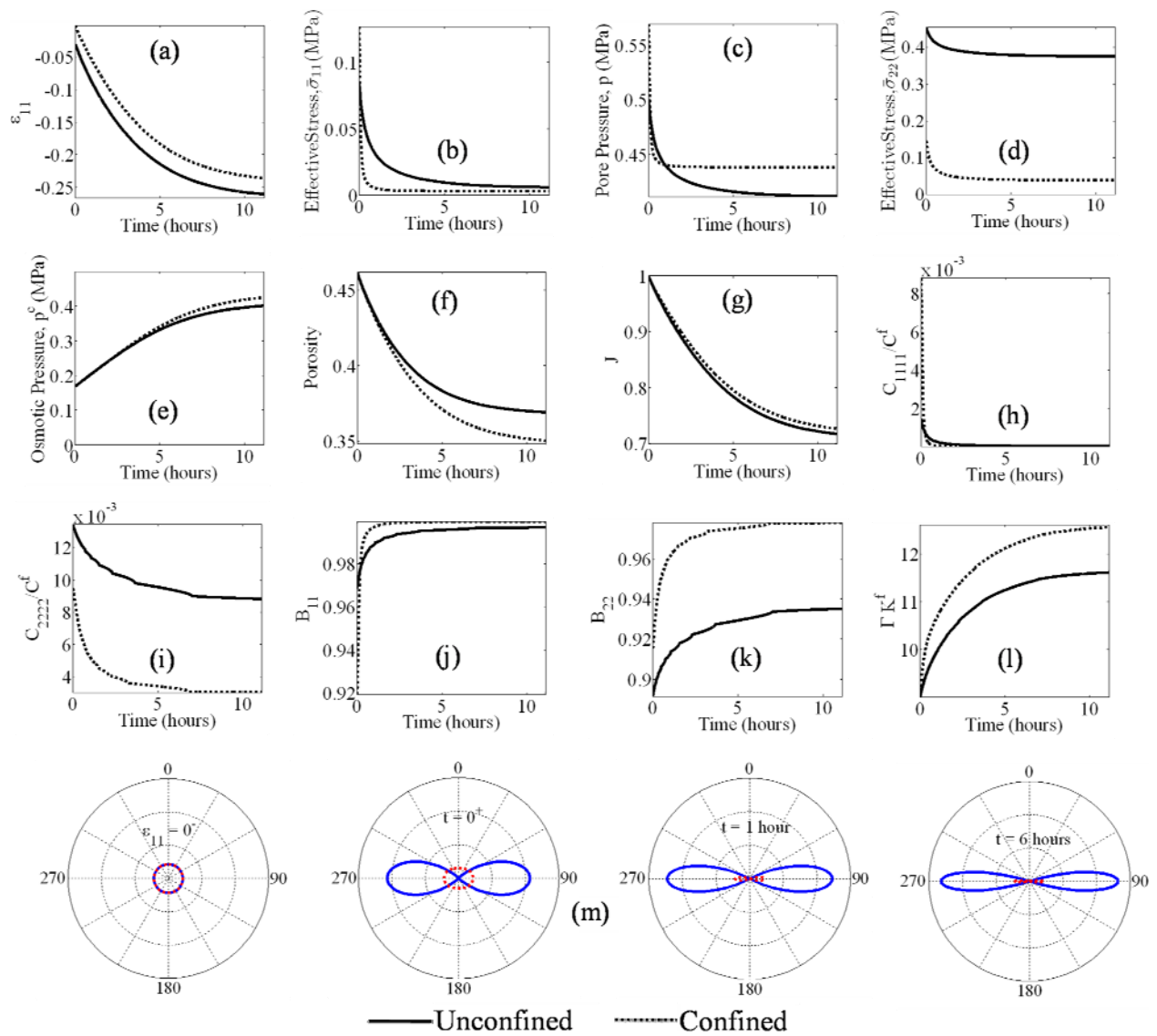


Figure 7-11 Comparison of creep response under confined and unconfined conditions for same applied stress and external bath molarity: strain and effective stress (a, b and d), pore pressures (c and e), porosity (f), volume change (g), material properties (h-l), and the fiber stress distributions (m).

8 CONCLUSIONS AND FUTURE WORK

8.1 Conclusions

Wet bonding is used in clinical restorative dentistry to prevent the collagen network in the demineralized dentin from collapsing, and thus provide adequate porosity for adhesive penetration and micromechanical interlock after polymerization. The presence of water causes phase separation and concomitant composition change of the adhesive when it infiltrates the demineralized dentin. This compositional change of the adhesive monomer has been quantified as part of this research using a ternary phase diagram, which represents thermodynamic equilibrium of a liquid-liquid system. The relationship between polymerization behavior along the adhesive-water phase boundary and the phase composition has also been quantified. The chemical composition and pore structure of the resulting polymer system has also been characterized qualitatively. It has been shown that multi-phase polymer systems formed in the a/d interface can be represented using polymer phases formed along the adhesive-water phase boundary and pore space. Structure-property relationships relating the water diffusion, sorption, elastic moduli and viscoelastic properties to chemical composition have been determined along the water-adhesive phase boundary. It has been verified that covalent crosslinks, not plasticized by water, provide mechanical stiffness under wet conditions. A micromechanics based model has been developed to explain the behavior of the polymer matrices; the model parameters have been linked to chemical structure. The mechanical behavior of wet saturated polymer phases is modeled by incorporating the micromechanical model into a poromechanical framework. The crosslink density, free volume and hydrophilicity are defined as model parameters and their trends along the phase boundary have been determined and verified using independent

experiments. The model predictions such as Poisson's ratio for the hydrophilic-rich phases also match experimental results from literature.

The diffusion of water into the polymer phases and the associated swelling has been modeled using Fick's Law for diffusion and the poro-micromechanical model for mechanical equilibrium. The diffusion coefficients have also been shown to be dependent on the chemical composition along the phase boundary. The developed model allows parametric studies of chemical and mechanical behavior while independently varying crosslink density and hydrophilicity. Such results can be extremely useful in parametrically evaluating diffusion and mechanical behavior before entering the polymer synthesis stage of design. In order to obtain accurate estimates of stress distribution using finite element analysis, an accurate input of material properties is necessary. The results obtained in this research enable determination of the monomer phase composition in the a/d interface, and accurate assignment of poro-micromechanical properties from knowledge of the phase composition. The parametric analysis presented in chapters 6 and 7 also highlights that the effect of microstructural evolution on the overall material behavior is well captured by the model. In particular, the poromechanical parameters have been derived from a micromechanical approach and hence, their evolution with loading can be traced. In conclusion, the dissertation has developed several links between the chemistry and mechanical behavior of dentin adhesive polymers, which should enhance and accelerate the process of adhesive polymer design. The experimental methodology and modeling approach developed can also be used for investigation and development of other hydrogels.

8.2 Future work

The creep behavior of the wet saturated polymer phases along the phase boundary will be predicted using the poro-micromechanical model proposed in chapter 3 and experimentally verified under confined and unconfined conditions. This will provide additional validation to the

model parameters obtained in chapter 3. The adhesive polymer matrix in the dry condition has been shown to be viscoelastic (Singh, Misra et al. 2009, Singh, Misra et al. 2010, Singh, Misra et al. 2011). The Deborah number, that is the ratio of the characteristic times for interaction effects between polymer chains and the characteristic diffusion time, determines whether the viscous interaction effects or the poromechanical effects, or both are important for the boundary value problem in question. In view of this, the polymer matrix will be modeled as a viscoelastic solid, rather than a linear elastic solid, so that poroviscoelastic behavior can be simulated for any value of the Deborah number. The poromechanical behavior of polymer phases formed in the two-phase region of the ternary phase diagram is governed by macro-scale porosity in addition to the spaces between polymer chains at the molecular scale. In order to model the poromechanical behavior through such systems containing porosity at different scales, a dual-porosity model will be formulated by inclusion of macro-scale porosity in the existing model.

Eyring's theory has been proposed to calculate diffusion coefficients where the change in free energy is calculated using the Flory-Rehner theory (Peppas and Reinhart 1983). In chapter 5, the crosslink density dependence of the diffusion coefficients obtained along the phase boundary was observed to follow Eyring's theory. Additional data along the phase boundary will be collected to determine the diffusion coefficient dependence on the polymer-water interaction parameter.

The ternary phase diagram presented in chapter 1 was constructed using tie lines obtained from phase separation experiments and points on the phase boundary using miscibility experiments. The data from the phase separation experiments will be fit using a thermodynamic model such as the non-random two liquid model (Renon and Prausnitz 1968). This will enable automatic generation of tie-lines and minimize the number of experiments to be performed for future studies. In addition, the phase diagram has been developed for the monomer-water system and

the model parameters also have been associated with the composition of the monomer-water phases. The polymer-water phase boundary will be determined in future and the polymer chemo-mechanical properties will be studied with respect to this boundary.

References:

- Amsden, B. (1998). "Solute diffusion within hydrogels. Mechanisms and models." Macromolecules **31**(23): 8382-8395.
- Anderson, J. L. and J. A. Quinn (1974). "Restricted transport in small pores: A model for steric exclusion and hindered particle motion." Biophysical Journal **14**(2): 130-150.
- Anseth, K. S., C. N. Bowman and L. Brannon-Peppas (1996). "Mechanical properties of hydrogels and their experimental determination." Biomaterials **17**(17): 1647-1658.
- Ashby, M. F. and D. R. H. Jones (2012). Engineering Materials 2: An Introduction to Microstructures and Processing, Butterworth-Heinemann.
- Ateshian, G. A. and J. D. Humphrey (2012). Continuum Mixture Models of Biological Growth and Remodeling: Past Successes and Future Opportunities. Annual Review of Biomedical Engineering, Vol 14. M. Yarmush, J. Duncan and M. Gray. Palo Alto, Annual Reviews. **14**: 97-111.
- Ateshian, G. A., V. Rajan, N. O. Chahine, C. E. Canal and C. T. Hung (2009). "Modeling the Matrix of Articular Cartilage using a Continuous Fiber Angular Distribution predicts many observed phenomena." Journal of Biomechanical Engineering **131**(6): 1-10.
- Ausiello, P., A. Apicella and C. L. Davidson (2002). "Effect of adhesive layer properties on stress distribution in composite restorations-a 3D finite element analysis." Dental Materials **18**(4): 295-303.
- Bank, R. A., M. Soudry, A. Maroudas, J. Mizrahi and J. M. TeKoppele (2000). "The increased swelling and instantaneous deformation of osteoarthritic cartilage is highly correlated with collagen degradation." Arthritis and Rheumatism **43**(10): 2202-2210.
- Banks, L. and B. Ellis (1979). "The glass transition temperature of an epoxy resin and the effect of absorbed water." Polymer Bulletin **1**(6): 377-382.
- Banks, L. and B. Ellis (1982). "The glass transition temperatures of highly crosslinked networks: Cured epoxy resins." Polymer **23**(10): 1466-1472.
- Bauwens, J. (1972). "Relation between the compression yield stress and the mechanical loss peak of bisphenol-A-polycarbonate in the β transition range." Journal of Materials Science **7**(5): 577-584.
- Bellenger, V., J. Verdu and E. Morel (1989). "Structure-properties relationships for densely cross-linked epoxide-amine systems based on epoxide or amine mixtures." Journal of materials science **24**(1): 63-68.
- Bennethum, L. S., M. A. Murad and J. H. Cushman (1997). "Modified Darcy's law, Terzaghi's effective stress principle and Fick's law for swelling clay soils." Computers and Geotechnics **20**(3): 245-266.
- Berger, J., M. Reist, J. M. Mayer, O. Felt, N. A. Peppas and R. Gurny (2004). "Structure and interactions in covalently and ionically crosslinked chitosan hydrogels for biomedical applications." European Journal of Pharmaceutics and Biopharmaceutics **57**(1): 19-34.
- Bernardo, M., H. Luis, M. D. Martin, B. G. Leroux, T. Rue, J. Leitão and T. A. DeRouen (2007). "Survival and reasons for failure of amalgam versus composite posterior restorations placed in a randomized clinical trial." The Journal of the American Dental Association **138**(6): 775-783.
- Biot, M. A. (1941). "General theory of three-dimensional consolidation." Journal of applied physics **12**(2): 155-164.
- Biot, M. A. (1956). "Theory of deformation of a porous viscoelastic anisotropic solid." Journal of applied physics **27**(5): 459-467.

- Biot, M. A. (1972). "Theory of finite deformations of porous solids." Indiana University Mathematics Journal **21**(7): 597-620.
- Boudenne, A., L. Ibos, Y. Candau and S. Thomas (2011). Handbook of multiphase polymer systems, Wiley.
- Boudou, T., J. Ohayon, C. Picart and P. Tracqui (2006). "An extended relationship for the characterization of Young's modulus and Poisson's ratio of tunable polyacrylamide gels." Biorheology **43**(6): 721-728.
- Bowen, R. M. (1982). "Compressible porous media models by use of the theory of mixtures." International Journal of Engineering Science **20**(6): 697-735.
- Brandani, V., A. Chianese and M. Rossi (1985). "Ternary liquid-liquid equilibrium data for the water-ethanol-benzene system." Journal of Chemical and Engineering Data **30**(1): 27-29.
- Bursac, P., C. V. McGrath, S. R. Eisenberg and D. Stamenovic (2000). "A Microstructural Model of Elastostatic Properties of Articular Cartilage in Confined Compression." Journal of Biomechanical Engineering **122**(4): 347-353.
- Chahine, N. O., C. C. B. Wang, C. T. Hung and G. A. Ateshian (2004). "Anisotropic Strain Dependent Material Properties of Bovine Articular Cartilage in the Transitional Range from tension to compression." Journal of Biomechanics **37**(8): 1251-1261.
- Chang, C. S., S. J. Chao and Y. Chang (1995). "Estimates of elastic moduli for granular material with anisotropic random packing structure." International journal of solids and structures **32**(14): 1989-2008.
- Chang, C. S. and A. Misra (1989). "Theoretical and experimental study of regular packings of granules." Journal of engineering mechanics **115**(4): 704-720.
- Chang, C. S. and A. Misra (1990). "Packing Structure and Mechanical Properties of Granulates." Journal of Engineering Mechanics **116**(5): 1077-1093.
- Cheng, A. H. D. (1997). "Material coefficients of anisotropic poroelasticity." International Journal of Rock Mechanics and Mining Sciences **34**(2): 199-205.
- Chiaraputt, S., S. Mai, B. P. Huffman, R. Kapur, K. A. Agee, C. K. Y. Yiu, D. C. N. Chan, C. Harnirattisai, D. D. Arola and F. A. Rueggeberg (2008). "Changes in resin-infiltrated dentin stiffness after water storage." Journal of dental research **87**(7): 655-660.
- Chiarelli, P. (2004). "The poro-elastic behavior of a gel thin tube." Materials Science and Engineering: C **24**(4): 463-471.
- Ciucchi, B., S. Bouillaguet, J. Holz and D. Pashley (1995). "Dentinal fluid dynamics in human teeth, in vivo." Journal of Endodontics **21**(4): 191-194.
- Clark, J. M. (1985). "The organization of collagen in cryofractured rabbit articular cartilage: a scanning microscopic study." Journal of Orthopedics Research. **3**(1): 17-29.
- Collins, C. J., R. W. Bryant and K. L. V. Hodge (1998). "A clinical evaluation of posterior composite resin restorations: 8-year findings." Journal of dentistry **26**(4): 311-317.
- Colton, C. K., C. N. Satterfield and C. J. Lai (2004). "Diffusion and partitioning of macromolecules within finely porous glass." AIChE Journal **21**(2): 289-298.
- Cortes, D. H., S. P. Lake, J. A. Kadlowec, L. J. Soslowsky and D. M. Elliott (2010). "Characterizing the mechanical contribution of fiber angular distribution in connective tissue: comparison of two modeling approaches." Biomechanics and modeling in mechanobiology **9**(5): 651-658.
- Costella, A. M., J. L. Trochmann and W. S. Oliveira (2010). "Water sorption and diffusion coefficient through an experimental dental resin." Journal of Materials Science: Materials in Medicine **21**(1): 67-72.
- Coussy, O., L. Dormieux and E. Detournay (1998). "From mixture theory to Biot's approach for porous media." International Journal of Solids and Structures **35**(34): 4619-4635.

Cowin, S. C. (1999). "Bone poroelasticity." Journal of Biomechanics **32**(3): 217-238.

Cowin, S. C. and J. D. Humphrey (2002). Cardiovascular Soft Tissue Mechanics, Springer.

Cui, L. and Y. Abousleiman (2001). "Time-dependent poromechanical responses of saturated cylinders." Journal of engineering mechanics **127**: 391.

dell'Isola, F., M. Guarascio and K. Hutter (2000). "A variational approach for the deformation of a saturated porous solid. A second-gradient theory extending Terzaghi's effective stress principle." Archive of Applied Mechanics **70**(5): 323-337.

dell'Isola, F., A. Madeo and P. Seppecher (2009). "Boundary conditions at fluid-permeable interfaces in porous media: A variational approach." International Journal of Solids and Structures **46**(17): 3150-3164.

dell'Isola, F., G. Sciarra and S. Vidoli (2009). "Generalized Hooke's law for isotropic second gradient materials." Proceedings of the Royal Society a-Mathematical Physical and Engineering Sciences **465**(2107): 2177-2196.

Detamore, M. S. and K. A. Athanasiou (2003). "Structure and function of the temporomandibular joint disc: Implications for tissue engineering." Journal of Oral and Maxillofacial Surgery **61**(4): 494-506.

Dhall, A. and A. K. Datta (2011). "Transport in deformable food materials: A poromechanics approach." Chemical Engineering Science **66**(24): 6482-6497.

DiSilvestro, M. R., Q. L. Zhu and J. K. F. Suh (2001). "Biphasic poroviscoelastic simulation of the unconfined compression of articular cartilage: II - Effect of variable strain rates." Journal of Biomechanical Engineering-Transactions of the Asme **123**(2): 198-200.

Doane, J. W., A. Goleme, J. L. West, J. B. Whitehead Jr and B. G. Wu (1988). "Polymer dispersed liquid crystals for display application." Molecular Crystals and Liquid Crystals **165**(1): 511-532.

Doi, M. (1996). Introduction to polymer physics, Oxford University Press on Demand, Oxford, UK.

Dormieux, L., E. Lemarchand and O. Coussy (2003). "Macroscopic and micromechanical approaches to the modelling of the osmotic swelling in clays." Transport in Porous Media **50**(1-2): 75-91.

Dormieux, L., A. Molinari and D. Kondo (2002). "Micromechanical approach to the behavior of poroelastic materials." Journal of the Mechanics and Physics of Solids **50**(10): 2203-2231.

Eick, J. D., S. J. Robinson, R. P. Chappell, C. M. Cobb and P. Spencer (1993). "The dentinal surface: its influence on dentinal adhesion. Part III." Quintessence international (Berlin, Germany: 1985) **24**(8): 571.

Ellis, T. S. and F. E. Karasz (1984). "Interaction of epoxy resins with water: the depression of glass transition temperature." Polymer **25**(5): 664-669.

Erickson, R. L. (1992). "Surface interactions of dentin adhesive materials." Operative Dentistry: 81.

Eshelby, J. D. (1957). "The determination of the elastic field of an ellipsoidal inclusion, and related problems." Proceedings of the Royal Society of London. Series A. Mathematical and Physical Sciences **241**(1226): 376-396.

Eyring, H. (1936). "Viscosity, plasticity, and diffusion as examples of absolute reaction rates." The Journal of Chemical Physics **4**: 283.

Eyring, H. and T. Ree (1961). "Significant liquid structures, VI. The vacancy theory of liquids." Proceedings of the National Academy of Sciences of the United States of America **47**(4): 526.

Farquhar, T., P. R. Dawson and P. A. Torzilli (1990). "A Microstructural Model for the Anisotropic Drained Stiffness of Articular Cartilage " Journal of Biomechanical Engineering **112**(4): 415-425.

- Federico, S. and W. Herzog (2008). "On the anisotropy and inhomogeneity of permeability in articular cartilage." Biomechanics and modeling in mechanobiology **7**(5): 367-378.
- Federico, S. and W. Herzog (2008). "Towards an analytical model of soft biological tissues." Journal of Biomechanics **41**(16): 3309-3313.
- Ferracane, J. L. (2006). "Hygroscopic and hydrolytic effects in dental polymer networks." Dental Materials **22**(3): 211-222.
- Flory, P. J. (1942). "Thermodynamics of high polymer solutions." The Journal of chemical physics **10**: 51.
- Flory, P. J. (1953). "Phase equilibria in polymer systems." Principles of polymer chemistry: 541-594.
- Fortin, M., J. Soulhat, A. Shirazi-Adl, E. B. Hunziker and M. D. Buschmann (2000). "Unconfined compression of articular cartilage: nonlinear behavior and comparison with a fibril-reinforced biphasic model." Journal of biomechanical engineering **122**(2): 189.
- Freed, K. F. and A. I. Pesci (1989). "Computation of the crosslink dependence of the effective Flory interaction parameter. χ for polymer networks." Macromolecules **22**(10): 4048-4050.
- Gaengler, P., I. Hoyer and R. Montag (2001). "Clinical evaluation of posterior composite restorations: The 10-year report." The journal of adhesive dentistry **3**(2): 185.
- Gao, H. J. and P. Klein (1998). "Numerical simulation of crack growth in an isotropic solid with randomized internal cohesive bonds." Journal of the Mechanics and Physics of Solids **46**(2): 187-218.
- Ghi, P. Y., D. J. T. Hill, D. Maillet and A. K. Whittaker (1997). "Nmr imaging of the diffusion of water into poly (tetrahydrofurfuryl methacrylate-co-hydroxyethyl methacrylate)." Polymer **38**(15): 3985-3989.
- Glasstone, S., K. J. Laidler and H. Eyring (1941). The theory of rate processes: the kinetics of chemical reactions, viscosity, diffusion and electrochemical phenomena, McGraw-Hill Book Company, inc.
- Gong, J. P., Y. Katsuyama, T. Kurokawa and Y. Osada (2003). "Double-Network Hydrogels with Extremely High Mechanical Strength." Advanced Materials **15**(14): 1155-1158.
- Greene, G. W., B. Zappone, O. Söderman, D. Topgaard, G. Rata, H. Zeng and J. N. Israelachvili (2010). "Anisotropic dynamic changes in the pore network structure, fluid diffusion and fluid flow in articular cartilage under compression." Biomaterials **31**(12): 3117-3128.
- Griffiths, P. and J. A. De Haseth (2007). Fourier transform infrared spectrometry, Wiley-Interscience.
- Grillo, A., S. Federico and G. Wittum (2012). "Growth, mass transfer, and remodeling in fiber-reinforced, multi-constituent materials." International Journal of Non-Linear Mechanics **47**(2): 388-401.
- Guggenheim, E. A. (1929). "The conceptions of electrical potential difference between two phases and the individual activities of ions." The Journal of Physical Chemistry **33**(6): 842-849.
- Guo, X., P. Spencer, Y. Wang, Q. Ye, X. Yao and K. Williams (2007). "Effects of a solubility enhancer on penetration of hydrophobic component in model adhesives into wet demineralized dentin." Dental Materials **23**(12): 1473-1481.
- Habeger, C. C., D. W. Coffin and B. Hojjatie (2001). "Influence of humidity cycling parameters on the moisture accelerated creep of polymeric fibers." Journal of Polymer Science Part B: Polymer Physics **39**(17): 2048-2062.
- Hashimoto, M., H. Ohno, K. Endo, M. Kaga, H. Sano and H. Oguchi (2000). "The effect of hybrid layer thickness on bond strength: demineralized dentin zone of the hybrid layer." Dental Materials **16**(6): 406-411.
- Haward, R. N. and R. J. Young (1997). The physics of glassy polymers, Springer.

- Hickel, R. and J. Manhart (2001). "Longevity of restorations in posterior teeth and reasons for failure." The journal of adhesive dentistry **3**(1): 45.
- Hill, D. J. T. and A. K. Whittaker (2011). "Water diffusion into radiation crosslinked PVA-PVP network hydrogels." Radiation Physics and Chemistry.
- Hirschfelder, J. O., C. F. Curtiss and R. B. Bird (1954). Molecular theory of gases and liquids, Wiley New York.
- Hoang, S. K. (2011). Poroviscoelasticity and analytical solutions of selected problems in engineering, THE UNIVERSITY OF OKLAHOMA.
- Hoang, S. K. and Y. N. Abousleiman (2009). "Poroviscoelastic two-dimensional anisotropic solution with application to articular cartilage testing." Journal of engineering mechanics **135**: 367.
- Hoang, S. K. and Y. N. Abousleiman (2012). "Correspondence principle between anisotropic poroviscoelasticity and poroelasticity using micromechanics and application to compression of orthotropic rectangular strips." Journal of applied physics **112**(4): 4907.
- Holzappel, G. A. and R. W. Ogden (2003). Biomechanics of soft tissue in cardiovascular systems, Springer.
- Horkay, F. (2012). "Interactions of cartilage extracellular matrix macromolecules." Journal of Polymer Science Part B: Polymer Physics **50**(24): 1699-1705.
- Horkay, F. and G. McKenna (2007). "Polymer networks and gels." Physical Properties of Polymers Handbook: 497-523.
- Hosaka, K., J. Tagami, Y. Nishitani, M. Yoshiyama, M. Carrilho, F. R. Tay, K. A. Agee and D. H. Pashley (2007). "Effect of wet vs. dry testing on the mechanical properties of hydrophilic self-etching primer polymers." European journal of oral sciences **115**(3): 239-245.
- Huang, C. Y., V. C. Mow and G. A. Ateshian (2001). "The role of flow-independent viscoelasticity in the biphasic tensile and compressive responses of articular cartilage." Journal of biomechanical engineering **123**: 410.
- Huang, Y.-P., S.-Z. Wang, S. Saarakkala and Y.-P. Zheng (2011). "Quantification of Stiffness Change in Degenerated Articular Cartilage Using Optical Coherence Tomography-Based Air-Jet Indentation." Connective Tissue Research **52**(5): 433-443.
- Huggins, M. L. (1941). "Solutions of long chain compounds." The Journal of chemical physics **9**(5): 440-440.
- Huyghe, J. M. (1999). "Intra-extrafibrillar mixture formulation of soft charged hydrated tissues." J Theor Appl Mech **37**(3): 519-536.
- Ito, S., M. Hashimoto, B. Wadgaonkar, N. Svizero, R. M. Carvalho, C. Yiu, F. A. Rueggeberg, S. Foulger, T. Saito and Y. Nishitani (2005). "Effects of resin hydrophilicity on water sorption and changes in modulus of elasticity." Biomaterials **26**(33): 6449-6459.
- Johnson, B., J. M. Bauer, D. J. Niedermaier, W. C. Crone and D. J. Beebe (2004). "Experimental techniques for mechanical characterization of hydrogels at the microscale." Experimental mechanics **44**(1): 21-28.
- June, R. K., K. L. Mejia, J. R. Barone and D. P. Fyhrie (2009). "Cartilage stress-relaxation is affected by both the charge concentration and valence of solution cations." Osteoarthritis and Cartilage **17**(5): 669-676.
- Kanatani, K. I. (1984). "Distribution of Directional-Data and Fabric Tensors." International Journal of Engineering Science **22**(2): 149-164.
- Khonakdar, H. A., J. Morshedjian, U. Wagenknecht and S. H. Jafari (2003). "An investigation of chemical crosslinking effect on properties of high-density polyethylene." Polymer **44**(15): 4301-4309.

- Kim, J. G. and C. M. Chung (2005). "Elution from light-cured dental composites: Comparison of trimethacrylate and dimethacrylate as base monomers." Journal of Biomedical Materials Research Part B: Applied Biomaterials **72**(2): 328-333.
- Korhonen, R. K., M. S. Laasanen, J. Toyras, R. Lappalainen, H. J. Helminen and J. S. Jurvelin (2003). "Fibril reinforced poroelastic model predicts specifically mechanical behavior of normal, proteoglycan depleted and collagen degraded articular cartilage." Journal of Biomechanics **36**(9): 1373-1379.
- Kostoryz, E. L., K. Dharmala, Q. Ye, Y. Wang, J. Huber, J. G. Park, G. Snider, J. L. Katz and P. Spencer (2009). "Enzymatic biodegradation of HEMA/bisGMA adhesives formulated with different water content." Journal of Biomedical Materials Research Part B: Applied Biomaterials **88**(2): 394-401.
- Krongauz, V. V. (2010). "Diffusion in polymers dependence on crosslink density." Journal of thermal analysis and calorimetry **102**(2): 435-445.
- Kubo, S., A. Kawasaki and Y. Hayashi (2011). "Factors associated with the longevity of resin composite restorations." Dental materials journal **30**(3): 374-383.
- Kuboki, T., M. Shinoda, M. G. Orsini and A. Yamashita (1997). "Viscoelastic properties of the pig temporomandibular joint articular soft tissues of the condyle and disc." Journal of Dental Research **76**(11): 1760-1769.
- Lai, W. M., J. S. Hou and V. C. Mow (1991). "A Triphasic Theory for the Swelling and Deformation Behaviors of Articular Cartilage. ." Journal of Biomechanical Engineering. **113**(3): 245-258.
- Lanir, Y. (1987). "Biorheology and Fluid Flux in Swelling Tissues .1. Bicomponent Theory for Small Deformations, Including Concentration Effects." Biorheology **24**(2): 173-187.
- Levin, L., M. Coval and S. B. Geiger (2007). "Cross-sectional radiographic survey of amalgam and resin-based composite posterior restorations." Quintessence international (Berlin, Germany: 1985) **38**(6): 511.
- Li, L. P., M. D. Buschmann and A. Shirazi-Adl (2003). "Strain-rate dependent stiffness of articular cartilage in unconfined compression." Transactions-American Society of Mechanical Engineers Journal of Biomechanical Engineering **125**(2): 161-168.
- Li, L. P., M. D. Buschmann and A. A. Shirazi (1999). "Nonlinear Analysis of Cartilage in Unconfined Ramp Compression Using a Fibril Reinforced Poroelastic Model." Clinical Biomechanics **14**(9): 673-682.
- Li, L. P. and W. Herzog (2004). "Strain-rate dependence of cartilage stiffness in unconfined compression: the role of fibril reinforcement versus tissue volume change in fluid pressurization." Journal of Biomechanics **37**(3): 375-382.
- Lindberg, A., J. W. V. Van Dijken and M. Lindberg (2007). "Nine-year evaluation of a polyacid-modified resin composite/resin composite open sandwich technique in Class II cavities." Journal of dentistry **35**(2): 124-129.
- Loret, B. and F. M. F. Simoes (2003). "Articular Cartilage with intra- and extrafibrillar waters: a chemo-mechanical model." Mechanics of Materials **36**(5-6): 515-541.
- Loret, B. and F. M. F. Simoes (2007). "Articular cartilage with intra-and extrafibrillar waters - mass transfer and generalized diffusion." European Journal of Mechanics-A/Solids **26**(5): 759-788.
- Lou, Y., A. Robisson, S. Cai and Z. Suo (2012). "Swellable elastomers under constraint." Journal of applied physics **112**(3): 034906-034906-034906.
- Lu, X. L., V. C. Mow and X. E. Guo (2009). "Proteoglycans and mechanical behavior of condylar cartilage." Journal of dental research **88**(3): 244-248.

Lu, X. L., D. D. N. Sun, X. E. Guo, F. H. Chen, W. M. Lai and V. C. Mow (2004). "Indentation determined mechano-electrochemical properties and fixed charge density of articular cartilage." Annals of biomedical engineering **32**(3): 370-379.

Luo, Y. and M. S. Shoichet (2004). "A photolabile hydrogel for guided three-dimensional cell growth and migration." Nature Materials **3**(4): 249-253.

Lustig, S. R. and N. A. Peppas (1987). "Solute and penetrant diffusion in swellable polymers. VII. A free volume-based model with mechanical relaxation." Journal of Applied Polymer Science **33**(2): 533-549.

Lydzba, D. and J. Shao (2000). "Study of poroelasticity material coefficients as response of microstructure." Mechanics of Cohesive-frictional Materials **5**(2): 149-171.

Madeo, A., F. Dell'Isola, N. Ianiro and G. Sciarra (2008). "A variational deduction of second gradient poroelasticity II: An application to the consolidation problem." Journal of Mechanics of Materials and Structures **3**(4): 607-625.

Madeo, A., D. George, T. Lekszycki, M. Nierenberger and Y. Rémond (2012). "A second gradient continuum model accounting for some effects of micro-structure on reconstructed bone remodelling." Comptes Rendus Mécanique **340**(8): 575-589.

Madeo, A., T. Lekszycki and F. Dell'Isola (2011). "A continuum model for the bio-mechanical interactions between living tissue and bio-resorbable graft after bone reconstructive surgery." Comptes Rendus Mécanique **339**(10): 625-640.

Magne, P. (2007). "Efficient 3D finite element analysis of dental restorative procedures using micro-CT data." Dental Materials **23**(5): 539-548.

Malacarne, J., R. M. Carvalho, M. F. de Goes, N. Svizero, D. H. Pashley, F. R. Tay, C. K. Yiu and M. R. O. Carrilho (2006). "Water sorption/solubility of dental adhesive resins." Dental Materials **22**(10): 973-980.

Marshall, G. W., S. J. Marshall, J. H. Kinney and M. Balooch (1997). "The dentin substrate: structure and properties related to bonding." Journal of dentistry **25**(6): 441-458.

Mazzobre, M. F., M. V. RomÃ¡n, A. F. Mourelle and H. R. Corti (2005). "Octanol-water partition coefficient of glucose, sucrose, and trehalose." Carbohydrate research **340**(6): 1207-1211.

McCutchen, C. (1982). "Cartilage is poroelastic, not viscoelastic (including and exact theorem about strain energy and viscous loss, and an order of magnitude relation for equilibration time)." Journal of biomechanics **15**(4): 325-327.

Milentijevic, D. and P. A. Torzilli (2005). "Influence of stress rate on water loss, matrix deformation and chondrocyte viability in impacted articular cartilage." Journal of Biomechanics **38**(3): 493-502.

Misra, A. and C. S. Chang (1993). "Effective Elastic-Moduli of Heterogeneous Granular Solids." International Journal of Solids and Structures **30**(18): 2547-2566.

Misra, A., O. Marangos, R. Parthasarathy and P. Spencer (2012). "Micro-scale Analysis of Compositional and Mechanical Properties of Dentin Using Homotopic Measurements." Lecture Notes in Computational Vision and Biomechanics **20**(3): 245-266.

Misra, A., O. Marangos, R. Parthasarathy and P. Spencer (2013). "Micro-scale Analysis of Compositional and Mechanical Properties of Dentin Using Homotopic Measurements." Biomedical Imaging and Computational Modeling in Biomechanics: 131-141.

Misra, A. and V. Singh (2012). "Micromechanical model for viscoelastic materials undergoing damage." Continuum Mechanics and Thermodynamics **25**(2-4): 343-358.

Misra, A. and V. Singh (2013). "Micromechanical model for viscoelastic materials undergoing damage." Continuum Mechanics and Thermodynamics **25**(2-4): 343-358.

- Misra, A., V. Singh, R. Parthasarathy, O. Marangos and P. Spencer (2011). "Mathematical model for anomalous creep in model dentin adhesives." Journal of dental research **90A**: 1708.
- Misra, A., P. Spencer, O. Marangos, Y. Wang and J. L. Katz (2004). "Micromechanical analysis of dentin/adhesive interface by the finite element method." Journal of Biomedical Materials Research Part B: Applied Biomaterials **70**(1): 56-65.
- Misra, A., P. Spencer, O. Marangos, Y. Wang and J. L. Katz (2005). "Parametric study of the effect of phase anisotropy on the micromechanical behaviour of dentin-adhesive interfaces." Journal of the Royal Society Interface **2**(3): 145-157.
- Misra, A. and Y. Yang (2010). "Micromechanical model for cohesive materials based upon pseudo-granular structure." International Journal of Solids and Structures **47**(21): 2970-2981.
- Mjor, I. A., J. E. Dahl and J. E. Moorhead (2000). "Age of restorations at replacement in permanent teeth in general dental practice." Acta Odontologica **58**(3): 97-101.
- Mjor, I. A., C. Shen, S. T. Eliasson and S. Richter (2002). "Placement and replacement of restorations in general dental practice in Iceland." Operative Dentistry **27**(2): 117.
- Mow, V. C., S. C. Kuei, W. M. Lai and C. G. Armstrong (1980). "Biphasic creep and stress relaxation of articular cartilage in compression: Theory and experiments." Journal of Biomechanical Engineering **102**(1): 73-84.
- Mura, T. (1987). Micromechanics of defects in solids, Springer.
- Murray, P. E., L. J. Windsor, T. W. Smyth, A. A. Hafez and C. F. Cox (2002). "Analysis of pulpal reactions to restorative procedures, materials, pulp capping, and future therapies." Critical Reviews in Oral Biology & Medicine **13**(6): 509-520.
- Nia, H. T., L. Han, Y. Li, C. Ortiz and A. Grodzinsky (2012). "Poroelasticity of Cartilage at the Nanoscale." Biophysical Journal **101**(9): 2304-2313.
- Nogueira, P., C. Ramirez, A. Torres, M. Abad, J. Cano, J. Lopez, I. López-Bueno and L. Barral (2001). "Effect of water sorption on the structure and mechanical properties of an epoxy resin system." Journal of Applied Polymer Science **80**(1): 71-80.
- Nordbo, H., J. Leirskar and F. R. Von Der Fehr (1998). "Saucer-shaped cavity preparations for posterior approximal resin composite restorations: Observations up to 10 years." Quintessence international (Berlin, Germany: 1985) **29**(1): 5.
- Nowak, A. P., V. Breedveld, L. Pakstis, B. Ozbas, D. J. Pine, D. Pochan and T. J. Deming (2002). "Rapidly recovering hydrogel scaffolds from self-assembling diblock copolypeptide amphiphiles." Nature **417**(6887): 424-428.
- O'Neil, G. A. and J. M. Torkelson (1999). "Modeling insight into the diffusion-limited cause of the gel effect in free radical polymerization." Macromolecules **32**(2): 411-422.
- Oh, J. and A. D. Rey (2000). "Theory and simulation of polymerization-induced phase separation in polymeric media." Macromolecular theory and simulations **9**(8): 641-660.
- Oloyede, A., R. Flachsmann and N. D. Broom (1992). "The dramatic influence of loading velocity on the compressive response of articular cartilage." Connective tissue research **27**(4): 211-224.
- Opdam, N. J. M., E. M. Bronkhorst, J. M. Roeters and B. A. C. Loomans (2007). "A retrospective clinical study on longevity of posterior composite and amalgam restorations." Dental Materials **23**(1): 2-8.
- Overbeek, J. T. (1956). "The Donnan Equilibrium." Progress in biophysics and biophysical chemistry **6**(1): 57-84.
- Pallesen, U. and V. Qvist (2003). "Composite resin fillings and inlays. An 11-year evaluation." Clinical oral investigations **7**(2): 71-79.

Pappa, G. D., G. M. Kontogeorgis and D. P. Tassios (1997). "Prediction of ternary liquid-liquid equilibria in polymer-solvent-solvent systems." Industrial & engineering chemistry research **36**(12): 5461-5466.

Park, G. S. and J. Crank (1968). "Diffusion in polymers."

Park, J., J. Eslick, Q. Ye, A. Misra and P. Spencer (2011). "The influence of chemical structure on the properties in methacrylate-based dentin adhesives." Dental Materials **27**(11): 1086-1093.

Park, J. G., Q. Ye, E. M. Topp, E. L. Kostoryz, Y. Wang, S. L. Kieweg and P. Spencer (2008). "Preparation and properties of novel dentin adhesives with esterase resistance." Journal of Applied Polymer Science **107**(6): 3588-3597.

Park, J. G., Q. Ye, E. M. Topp, C. H. Lee, E. L. Kostoryz, A. Misra and P. Spencer (2009). "Dynamic mechanical analysis and esterase degradation of dentin adhesives containing a branched methacrylate." Journal of Biomedical Materials Research Part B: Applied Biomaterials **91**(1): 61-70.

Park, J. G., Q. Ye, E. M. Topp, A. Misra and P. Spencer (2009). "Water sorption and dynamic mechanical properties of dentin adhesives with a urethane-based multifunctional methacrylate monomer." Dental Materials **25**(12): 1569-1575.

Parthasarathy, R., A. Misra, J. Park, Q. Ye and P. Spencer (2012). "Diffusion coefficients of water and leachables in methacrylate-based crosslinked polymers using absorption experiments." Journal of Materials Science: Materials in Medicine: 1-16.

Parthasarathy, R., A. Misra and P. Spencer (2011). "Application of soft tissue micromechanics model to condylar cartilage." Journal of dental research **90A**: 3610.

Pashley, E. L. and Y. Zhang (1998). "Effects of HEMA on water evaporation from water-HEMA mixtures." Dental Materials **14**(1): 6-10.

Peppas, N. A. and C. T. Reinhart (1983). "Solute diffusion in swollen membranes. Part I. A new theory." Journal of membrane science **15**(3): 275-287.

Perdigao, J. and M. Lopes (2001). "The effect of etching time on dentin demineralization." Quintessence Int **32**(1): 19-26.

Pereira, P. N. R., M. Okuda, H. Sano, T. Yoshikawa, M. F. Burrow and J. Tagami (1999). "Effect of intrinsic wetness and regional difference on dentin bond strength." Dental Materials **15**(1): 46-53.

Petite, H., V. Viateau, W. Bensaid, A. Meunier, C. de Pollak, M. Bourguignon, K. Oudina, L. Sedel and G. Guillemain (2000). "Tissue-engineered bone regeneration." Nature biotechnology **18**(9): 959-963.

Pusch, W. and A. Walch (1982). "Membrane structure and its correlation with membrane permeability." Journal of membrane science **10**(2): 325-360.

Quiligotti, S., G. A. Maugin and F. dell'Isola (2003). "An Eshelbian approach to the nonlinear mechanics of constrained solid-fluid mixtures." Acta Mechanica **160**(1-2): 45-60.

Quinn, T. M. and V. Morel (2007). "Microstructural Modeling of Collagen Network Mechanics and Interactions with the Proteoglycan Gel in Articular Cartilage " Journal of Biomechanics and Modeling in Mechanobiology **6**(1-2): 73-82.

Rakesh, V. and A. K. Datta (2013). "Transport in deformable hygroscopic porous media during microwave puffing." AICHE Journal.

Reinhart, C. T. and N. A. Peppas (1984). "Solute diffusion in swollen membranes. Part II. Influence of crosslinking on diffusive properties." Journal of membrane science **18**: 227-239.

Renon, H. and J. M. Prausnitz (1968). "Local compositions in thermodynamic excess functions for liquid mixtures." AICHE Journal **14**(1): 135-144.

Rosoff, M. (1989). Controlled release of drugs: polymers and aggregate systems, Wiley-VCH.

- Roulet, J. F. and M. Degrange (2000). Adhesion: The silent revolution in dentistry, Quintessence Pub Co.
- Roy, S. and W. Xu (2001). "Modeling of diffusion in the presence of damage in polymer matrix composites." International Journal of Solids and Structures **38**(1): 115-126.
- Rudakova, T. E. and G. E. Zaikov (1988). "Stressed polymers in physically active media." Polymer degradation and stability **21**(2): 105-120.
- Rudakova, T. Y. and G. Y. Zaikov (1987). "Effect of an aggressive medium and mechanical stress on polymers. Review." Polymer Science USSR **29**(1): 1-19.
- Sacks, M. S., W. D. Merryman and D. E. Schmidt (2009). "On the biomechanics of heart valve function." Journal of Biomechanics **42**(12): 1804-1824.
- Safranski, D. L. and K. Gall (2008). "Effect of chemical structure and crosslinking density on the thermo-mechanical properties and toughness of (meth) acrylate shape memory polymer networks." Polymer **49**(20): 4446-4455.
- Sar, B. E., S. Freour, P. Davies and F. Jacquemin (2012). "Coupling moisture diffusion and internal mechanical states in polymers - A thermodynamical approach." European Journal of Mechanics-A/Solids.
- Schapery, R. (2000). "Nonlinear viscoelastic solids." International journal of solids and structures **37**(1): 359-366.
- Schweickl, H., G. Spagnuolo and G. Schmalz (2006). "Genetic and cellular toxicology of dental resin monomers." Journal of Dental Research **85**(10): 870-877.
- Sciarra, G., F. dell'Isola and K. Hutter (2001). "A solid-fluid mixture model allowing for solid dilatation under external pressure." Continuum Mechanics and Thermodynamics **13**(5): 287-306.
- Sciarra, G., F. Dell'Isola, N. Ianiro and A. Madeo (2008). "A variational deduction of second gradient poroelasticity part I: General theory." Journal of Mechanics of Materials and Structures **3**(3): 507-526.
- Senol, A. (2006). "Liquid-liquid equilibria for the system (water+ carboxylic acid+ chloroform): thermodynamic modeling." Fluid phase equilibria **243**(1): 51-56.
- Shimizu, T., T. Kitano, M. Inoue, K. Narikawa and B. Fujii (1995). "Ten-year longitudinal clinical evaluation of a visible light cured posterior composite resin." Dental materials journal **14**(2): 120.
- Shraiman, B. I. (2005). "Mechanical feedback as a possible regulator of tissue growth." Proceedings of the National Academy of Sciences of the United States of America **102**(9): 3318-3323.
- Sideridou, I. D. and M. M. Karabela (2008). "Characteristics of the sorption of water and an ethanol/water solution by light cured copolymers of 2 hydroxyethyl methacrylate with dental dimethacrylates." Journal of Applied Polymer Science **109**(4): 2503-2512.
- Sideridou, I. D. and M. M. Karabela (2011). "Sorption of water, ethanol or ethanol/water solutions by light-cured dental dimethacrylate resins." Dental Materials **27**(10): 1003-1010.
- Sideridou, I. D., M. M. Karabela, E. C. Vouvoudi and G. E. Papanastasiou (2008). "Sorption and desorption parameters of water or ethanol in light cured dental dimethacrylate resins." Journal of Applied Polymer Science **107**(1): 463-475.
- Sideridou, I. D. and G. E. Papanastasiou (2007). "Water sorption kinetics in light cured poly HEMA and poly (HEMA co TEGDMA); determination of the self diffusion coefficient by new iterative methods." Journal of Applied Polymer Science **106**(4): 2380-2390.
- Signorini, A. (1932). "Sollecitazioni Iperstatiche." Rend. Inst. Lombardo **2**(65): 1-7.
- Simecek, J. W., K. E. Diefenderfer and M. E. Cohen (2009). "An evaluation of replacement rates for posterior resin-based composite and amalgam restorations in US Navy and Marine Corps recruits." The Journal of the American Dental Association **140**(2): 200-209.

Singh, M. and M. S. Detamore (2008). "Tensile properties of the mandibular condylar cartilage." Journal of Biomechanical Engineering-Transactions of the Asme **130**(1).

Singh, V., A. Misra, O. Marangos, J. Park, Q. Ye, S. Kieweg and P. Spencer (2011). "Anomalous creep in model dentin adhesive under changing moisture conditions " Journal of Dental Research **90A** (1708).

Singh, V., A. Misra, O. Marangos, J. Park, Q. Ye, S. L. Kieweg and P. Spencer (2009). "Viscoelastic and fatigue properties of model methacrylate-based dentin adhesives." Journal of Biomedical Materials Research Part B: Applied Biomaterials **95**(2): 283-290.

Singh, V., A. Misra, O. Marangos, J. Park, Q. Ye, S. L. Kieweg and P. Spencer (2010). "Viscoelastic and fatigue properties of model methacrylate based dentin adhesives." Journal of Biomedical Materials Research Part B: Applied Biomaterials **95**(2): 283-290.

Singh, V., A. Misra, O. Marangos, J. Park, Q. Ye, S. L. Kieweg and P. Spencer (2011). "Fatigue life prediction of dentin-adhesive interface using micromechanical stress analysis." Dental Materials **27**(9): E187-E195.

Singh, V., A. Misra, R. Parthasarathy, Q. Ye, J. Park and P. Spencer (2013). "Mechanical properties of methacrylate-based model dentin adhesives: Effect of loading rate and moisture exposure." Journal of Biomedical Materials Research Part B: Applied Biomaterials.

Soltz, M. A. and A. A. Gerard (1998). "Experimental verification and theoretical prediction of cartilage interstitial fluid pressurization at an impermeable contact interface in confined compression." Journal of Biomechanics **31**(10): 927-934.

Soncini, J. A., N. N. Maserejian, F. Trachtenberg, M. Tavares and C. Hayes (2007). "The longevity of amalgam versus compomer/composite restorations in posterior primary and permanent teeth: findings from the New England Children's Amalgam Trial." The Journal of the American Dental Association **138**(6): 763-772.

Spencer, P. and J. R. Swafford (1999). "Unprotected protein at the dentin-adhesive interface." Quintessence international (Berlin, Germany: 1985) **30**(7): 501.

Spencer, P. and Y. Wang (2002). "Adhesive phase separation at the dentin interface under wet bonding conditions." Journal of biomedical materials research **62**(3): 447-456.

Spencer, P., Y. Wang and B. Bohaty (2006). "Interfacial chemistry of moisture-aged class II composite restorations." Journal of Biomedical Materials Research Part B: Applied Biomaterials **77**(2): 234-240.

Spencer, P., Y. Wang, M. P. Walker, D. M. Wieliczka and J. R. Swafford (2000). "Interfacial chemistry of the dentin/adhesive bond." Journal of dental research **79**(7): 1458-1463.

Spencer, P., Q. Ye, J. Park, E. M. Topp, A. Misra, O. Marangos, Y. Wang, B. S. Bohaty, V. Singh and F. Sene (2010). "Adhesive/dentin interface: the weak link in the composite restoration." Annals of biomedical engineering **38**(6): 1989-2003.

Sperling, L. H. (1997). Polymeric multicomponent materials: an introduction. New York, NY, Wiley-Interscience.

Sun, J.-Y., X. Zhao, W. R. K. Illeperuma, O. Chaudhuri, K. H. Oh, D. J. Mooney, J. J. Vlassak and Z. Suo (2012). "Highly stretchable and tough hydrogels." Nature **489**(7414): 133-136.

Tauer, K., A. I. Ali and M. Sedlak (2005). "On the preparation of stable poly (2-hydroxyethyl methacrylate) nanoparticles." Colloid and Polymer Science **283**(4): 351-358.

Tham, W. L., W. S. Chow and Z. A. M. Ishak (2010). "Simulated body fluid and water absorption effects on poly (methyl methacrylate)/hydroxyapatite denture base composites." Express Polymer Letters **4**(9): 517-528.

Thominette, F., E. Gaudichet-Maurin and J. Verdu (2007). "Effect of structure on water diffusion in hydrophilic polymers." Defect and Diffusion Forum **258-260**: 442-446.

- Toledano, M., M. Yamauti, E. Osorio, F. Monticelli and R. Osorio (2012). "Characterization of Micro-and Nanophase Separation of Dentin Bonding Agents by Stereoscopy and Atomic Force Microscopy." Microscopy and Microanalysis **18**(2): 279.
- Truesdell, C. and R. Toupin (1960). The classical field theories, Springer.
- Unemori, M., Y. Matsuya, S. Matsuya, A. Akashi and A. Akamine (2003). "Water absorption of poly (methyl methacrylate) containing 4-methacryloxyethyl trimellitic anhydride." Biomaterials **24**(8): 1381-1387.
- Van Dijken, J. W. V. (2000). "Direct resin composite inlays/onlays: an 11 year follow-up." Journal of dentistry **28**(5): 299-306.
- Vriens, G. N. and E. C. Medcalf (1953). "Correlation of Ternary Liquid-Liquid Equilibria." Industrial & Engineering Chemistry **45**(5): 1098-1104.
- Wang, J. and W. Wu (2005). "Swelling behaviors, tensile properties and thermodynamic studies of water sorption of 2-hydroxyethyl methacrylate/epoxy methacrylate copolymeric hydrogels." European polymer journal **41**(5): 1143-1151.
- Wang, X. and W. Hong (2012). "A visco-poroelastic theory for polymeric gels." Proceedings of the Royal Society A: Mathematical, Physical and Engineering Science.
- Wang, Y. and P. Spencer (2003). "Hybridization efficiency of the adhesive/dentin interface with wet bonding." Journal of dental research **82**(2): 141-145.
- Wang, Y., P. Spencer, C. Hager and B. Bohaty (2006). "Comparison of interfacial characteristics of adhesive bonding to superficial versus deep dentine using SEM and staining techniques." Journal of dentistry **34**(1): 26-34.
- Wen, Q., A. Basu, P. A. Janmey and A. G. Yodh (2012). "Non-affine deformations in polymer hydrogels." Soft Matter **8**(31): 8039-8049.
- West, J. L. (1988). "Phase separation of liquid crystals in polymers." Molecular Crystals and Liquid Crystals Incorporating Nonlinear Optics **157**(1): 427-441.
- Wilson , W., C. C. V. Donkelaar, B. V. Rietbergen, K. Ito and R. Huiskes (2004). "Stresses in the Local Collagen Network of Articular Cartilage: A Poroviscoelastic Fibril-Reinforced Finite Element Study." Journal of Biomechanics **37**(3): 357-366.
- Wilson , W., C. C. V. Donkelaar, B. V. Rietbergen, K. Ito and R. Huiskes (2005). "A fibril-Reinforced Poroviscoelastic swelling model for Articular Cartilage." Journal of biomechanics **38**(6): 1195-1204.
- Wold, S., M. Sjostrom and L. Eriksson (2001). "PLS-regression: a basic tool of chemometrics." Chemometrics and intelligent laboratory systems **58**(2): 109-130.
- Wu, Y., S. Joseph and N. R. Aluru (2009). "Effect of cross-linking on the diffusion of water, ions, and small molecules in hydrogels." The Journal of Physical Chemistry B **113**(11): 3512-3520.
- Xu, X., A. V. Goponenko and S. A. Asher (2008). "Polymerized polyHEMA photonic crystals: pH and ethanol sensor materials." Journal of the American Chemical Society **130**(10): 3113-3119.
- Yang, Y. and A. Misra (2012). "Micromechanics based second gradient continuum theory for shear band modeling in cohesive granular materials following damage elasticity." International Journal of Solids and Structures **49**(18): 2500-2514.
- Yasuda, H., A. Peterlin, C. K. Colton, K. A. Smith and E. W. Merrill (2003). "Permeability of solutes through hydrated polymer membranes. Part III. Theoretical background for the selectivity of dialysis membranes." Die Makromolekulare Chemie **126**(1): 177-186.
- Ye, Q., J. Park, J. S. Laurence, R. Parthasarathy, A. Misra and P. Spencer (2011). "Ternary phase diagram of model dentin adhesive exposed to over-wet environments." Journal of dental research **90**(12): 1434-1438.

- Ye, Q., J. Park, F. Pamatmat, A. Misra, R. Parthasarathy, O. Marangos and P. Spencer (2011, Under Review). "Quantitative analysis of aqueous phase composition of model dentin adhesives experiencing phase separation." Acta Biomaterialia.
- Ye, Q., J. G. Park, E. Topp, Y. Wang, A. Misra and P. Spencer (2008). "In vitro performance of nano-heterogeneous dentin adhesive." Journal of dental research **87**(9): 829-833.
- Ye, Q., P. Spencer, R. Parthasarathy, J. Park, J. S. Laurence and A. Misra (2011). Multivariate spectral analysis of phase partitioning in methacrylate-based dentin adhesive. 46th Midwest 39th Great Lakes Joint Regional ACS Meeting. L. O'Brien. Saint Louis, MO.
- Ye, Q., Y. Wang and P. Spencer (2009). "Nanophase separation of polymers exposed to simulated bonding conditions." Journal of Biomedical Materials Research Part B: Applied Biomaterials **88**(2): 339-348.
- Yiu, C. K. Y., N. M. King, M. R. O. Carrilho, S. Sauro, F. A. Rueggeberg, C. Prati, R. M. Carvalho, D. H. Pashley and F. R. Tay (2006). "Effect of resin hydrophilicity and temperature on water sorption of dental adhesive resins." Biomaterials **27**(9): 1695-1703.
- Yoon, J., S. Cai, Z. Suo and R. C. Hayward (2010). "Poroelastic swelling kinetics of thin hydrogel layers: comparison of theory and experiment." Soft Matter **6**(23): 6004-6012.
- Zhang, J., J. L. Chai, G. Z. Li, G. Y. Zhang and K. C. Xie (2004). "Phase Behavior of the APG/Alcohol/Alkane/H₂O System." Journal of dispersion science and technology **25**(1): 27-34.
- Zou, Y. (2007). Adhesive resin conversion and composition in the hybrid layer of the resin-dentin bond. Doctor of Philosophy, University of Iowa.
- Zou, Y., S. R. Armstrong and J. L. P. Jessop (2010). "Quantitative analysis of adhesive resin in the hybrid layer using Raman spectroscopy." Journal of Biomedical Materials Research Part A **94**(1): 288-297.
- Zustiak, S. P. and J. B. Leach (2011). "Characterization of protein release from hydrolytically degradable poly (ethylene glycol) hydrogels." Biotechnology and bioengineering.